THÈSE

En vue de l'obtention du

DOCTORAT DE L'UNIVERSITÉ DE TOULOUSE

Délivré par :

Institut National Polytechnique de Toulouse (INP Toulouse)

Discipline ou spécialité :

Science et Génie des Matériaux

Présentée et soutenue par :

Mme JYOTI GUPTA

le jeudi 7 avril 2016

Titre :

INTERGRANULAR STRESS CORROSION CRACKING OF ION IRRADIATED 304L STAINLESS STEEL IN PWR ENVIRONMENT

Ecole doctorale :

Sciences de la Matière (SDM)

Unité de recherche :

Centre Interuniversitaire de Recherche et d'Ingénierie des Matériaux (C.I.R.I.M.A.T.)

Directeur(s) de Thèse :

M. ERIC ANDRIEU

MME LYDIA LAFFONT

Rapporteurs :

M. JÉROME CREPIN, MINESPARISTECH

M. VIVEKANAND KAIN, ATOMIC RESEARCH CENTRE MUMBAI

Membre(s) du jury :

M. PHILIPPE PAREIGE, UNIVERSITE DE ROUEN, Président

M. BENOIT TANGUY, CEA SACLAY, Membre

M. ERIC ANDRIEU, INP TOULOUSE, Membre

M. JOËL ALEXIS, ECOLE NATIONALE D'INGENIEUR DE TARBES, Membre

Mme LYDIA LAFFONT, INP TOULOUSE, Membre

M. STEPHANE PERRIN, CEA SACLAY, Membre

ACKNOWLEDGMENT

Firstly, I would like to express my sincere gratitude to my advisors Prof. Eric Andrieu, Prof. Lydia Laffont and Dr. Benoit Tanguy for providing me the opportunity to work on such an interesting topic. I would like to thank Dr. Jérémy Hure for showing interest in my work and providing necessary guidance in times of hardship. I could not have imagined having better mentors for my PhD study. Their continuous support, patience, immense knowledge and motivation have helped me in all the time of research and writing of this thesis.

I would like to thank Prof. Philippe Pareige for accepting to head my dissertation committee. I would like to extend my gratitude to all the members of committee, Dr. Jérôme Crepin, Prof. Vivekanand Kain, Prof. Joël Alexis and Stéphane Perrin not only for their time and patience, but also for their insightful comments and encouragement which contributed to my development as a scientist.

During the thesis, I got the opportunity of working in Toulouse (CIRIMAT) as well as in Paris (CEA Saclay). I am glad that I got the chance to meet many people with varied skills at both places. I would like to thank all my colleagues of CIRIMAT and CEA for their encouragement and assistance. Special thanks to Clement Berne, Deni Ferdian, Tristant Jezequel and Vincent Mcdonalds for bearing me and answering all my relevant or irrelevant questions patiently. For their assistance during irradiation campaign, I would like to thank Yves Serruys, Eric Bordas and team JANNuS (DMN/SRMP/JANNUS). I am indepted to Marie-Christine Lafont, who taught me about the TEM sample preparation techniques and spent numerous hours on TEM to get beautiful pictures of “defects” for my thesis. I would also like to acknowledge Matthias Rousseau and Holande Aurore (DPC/LECA) for carrying out the mechanical tests. I would like to thank Sylvie Poissonnet (DMN/SRMP) and Joël Alexis (INP-Tarbes) for conducting nano-hardness tests. For his supervision and guidance during FIB sessions, I would like to acknowledge Mickel Jublot (DMN/LM2E). I would like to thank Francoise Barcelo (DMN/SRMA) for conducting EBSD analysis. I would also like to thank team MEMO of CIRIMAT, SEMI of CEA.

Last but not the least, I would like to express my heartfelt gratitude to my parents (Mukesh Kumar and Hemlata Gupta) and brother (Pulkit Gupta) for their confidence and continuous support. Finally, there are my friends (Neetu Gupta and Nitendra Singh) with whom I was able to talk happily and endlessly about anything other than my research. Thanks for being that “zaroori” friend.

I could not have completed my research without the support of all these wonderful people.

Dedicated to Mumma, Papa, Pulkit and boss

Table of Contents

LIST OF FIGURES

LIST OF TABLES

ACRONYMS

APPM	Atomic Parts Per Million
APT	Atom Probe Tomography
ASTM	American Society for Testing and Materials
BCC	Body Centered Cubic
BF	Bright Field
BFB	Baffle Former Bolts
BSE	Back Scattered Electron
BWR	Boiling Water Reactor
CERT	Constant Extension Rate Tensile
CSL	Coincident Site Lattice
CW	Cold Work
DF	Dark Field
DPA	Displacement Per Atom
EBSD	Electron Back Scattered Diffraction
EELS	Electron Energy Loss Spectroscopy
EDS	Electron Dispersion Spectroscopy
FBR	Fast Breeder Reactor
FC	Full Cascade
FCC	Face Centered Cubic
FFT	Fast Fourier Transforms
FIB	Focused Ion Beam
FP	Frenkel Pair
FSE	ForeScattered electron
GB	Grain Boundary
GDMS	Glow Discharge Mass Spectrometry
HFW	Horizontal Full Width
HRTEM	High Resolution Transmission Electron Microscopy
IASCC	Irradiation Assisted Stress Corrosion Cracking
ICP-AES	Inductively Coupled Plasma Atomic Emission Spectroscopy and
IGSCC	Inter Granular Stress Corrosion Cracking
JIS	Japanese Industrial Standards
KP	Kinchin and Pease
LAGB	Low Angle Grain Boundaries
LTO	Long Term Operation
LVDT	Linear Variable Displacement Transducer
LWR	Light Water reactor
NRT	Norgett – Robinson – Torrens
PIA	Post Irradiation Annealing
PIPS	Precision Ion Polishing System
PKA	Primary Knock-on Atoms
PT	Pressure – Temperature
PWR	Pressurized Water Reactor

RIS	Radiation Induced Segregation
R&D	Research and Development
RHAB	Randomly High Angle Grain Boundary
SA	Solution Annealed
SAED	Selected Area Electron Diffraction
SCC	Stress Corrosion Cracking
SCW	Super Critical Water
SE	Secondary Electron
SEM	Scanning Electron Microscope
SF	Schmid Factor
SFE	Stacking Fault Energy
SFT	Stacking Fault Tetrahedra
SHE	Standard Hydrogen Electrode
SRIM	Stopping and Range of Ions in Matter
SS	Stainless Steel
SSRT	Slow Strain Rate Test
STP	Standard Temperature and Pressure
SUS	Steel Use Stainless
TEM	Transmission Electron Microscope
TGSCC	Trans Granular Stress Corrosion Cracking
UHP	Ultra High Purity

RESUME

En France, le secteur de l'électricité est dominé par l'énergie nucléaire, qui représente plus de 75% de la production totale d'électricité du pays. Le parc nucléaire électrogène français est constitué de réacteurs à eau pressurisés (REP). Ces dernières années, d'importants efforts ont été consentis pour prolonger la durée de fonctionnement des réacteurs de 40 à 60 ans.. Les structures internes du cœur du réacteur sont une partie essentielle des REP, car ils fournissent un support au cœur (ensembles combustibles et 'instrumentation) et elles canalisent la circulation du fluide caloporteur. L'intégrité de ces structures internes qui sont proches du combustible et en contact direct avec l'eau du circuit primaire doit être démontrée pendant toute la durée de fonctionnement du réacteur. Les aciers inoxydables austénitiques sont utilisés pour ces structures car ils sont résistants à la corrosion et en particulier à la corrosion sous contrainte. Les cloisons et renforts qui composent les structures internes sont constituées d'un acier austénitique hypertrempé 304 et / ou 304 L tandis que les vis sont constitués d'un acier 316 écroui (CW 316) et / ou 316 (CW 316L). Certains de ces composants, du fait de leur proximité avec le cœur, sont soumis à de fortes doses d'irradiation qui peuvent dépasser ~ 80 dpa (déplacement par atome) pour 40 années de service. Du fait du vieillissement des centrales nucléaires, ces composants accumulent des doses d'irradiation importantes et à terme peuvent devenir sensibles au phénomène de corrosion sous contrainte assistée par irradiation (IASCC). Plusieurs cas de défaillance de vis par IASSC ont été rapportés en France, en Belgique, et aux États-Unis (Figure 1). Bien que l'intégrité des internes puisse être garantie avec environ 1/3 des vis (sur un total d'environ 1000 vis), le temps de maintenance et l'optimisation des coûts au cours des inspections sont des problématiques importantes et ont conduit les opérateurs à s'intéresser à l'IASCC.

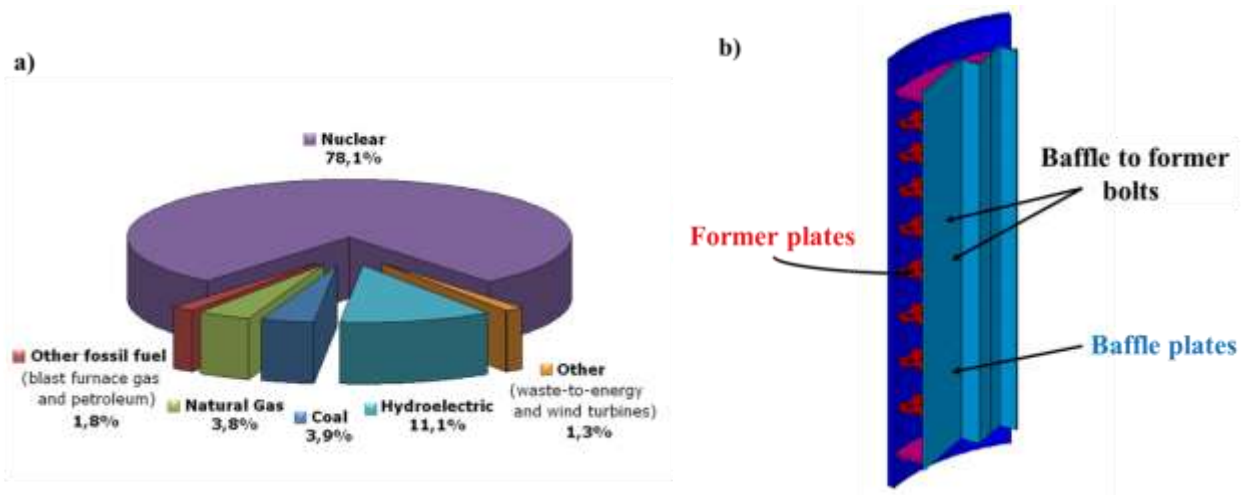

Figure 1: a) Diagramme représentant la contribution des différentes ressources d'énergie dans la production totale d'énergie en France. b) Schéma illustrant la manière dont les cloisons sont reliées aux renforts par l'intermédiaire des vis.

L'IASCC est un mécanisme de fissuration intergranulaire par corrosion sous contrainte (IGCSC) induite par l'irradiation. C'est un phénomène complexe qui se produit par la combinaison de

plusieurs facteurs (le matériau, l'état de contrainte, l'environnement corrosif et l'irradiation). L'exposition aux neutrons est connue pour entraîner une modification de la microstructure et de la microchimie du matériau en induisant des défauts telle que des boucles de Frank, de la ségrégation induite par la radiation (RIS), de la précipitation et des cavités. Ces changements modifient les propriétés mécaniques du matériau. L'augmentation importante de la limite d'élasticité et la diminution de la ductilité avec l'irradiation ont été rapportées pour les aciers inoxydables austénitiques. Ces modifications induisent ou augmente la sensibilité à la CSC dans ces aciers en milieu REP Un seuil de fluence critique de ~ 2×10^{25} n/m² (≈ 3 dpa) à la fissuration a été proposé en dessous duquel 304 SS et 316 SS sont considérés comme immunes vis-à-vis de l'IASCC dans les REP.

Des recherches approfondies dans ce domaine ont montré que plusieurs facteurs (tels que la microstructure induite par l'irradiation, le durcissement par l'irradiation, RIS, etc.) contribuent à l'IASCC, mais aucun d'entre eux, n'est capable, seul, d'initier l'IASCC. L'effet prépondérant serait le mode de déformation des aciers inoxydables austénitiques irradiés et ces facteurs pourraient servir de contributeurs secondaires. A 300°C, la déformation se produit principalement dans des bandes de glissement. L'interaction de ces bandes avec les joints de grains est identifiée comme un facteur prépondérant dans l'amorçage des fissures dans le matériau irradié. Lorsqu'une bande de glissement interagit avec la surface libre ou avec les joints de grains, il en résulte la formation de marches. Ces marches sont caractérisées par la hauteur, la largeur et l'espacement et peuvent donner des informations quantitatives et qualitatives sur le degré de localisation de la déformation dans le matériau. Par ailleurs, la déformation localisée en environnement corrosif est identifiée comme une condition nécessaire pour la fissuration intergranulaire. L'irradiation peut également influer sur la chimie de l'eau, soit par radiolyse ou en modifiant la cinétique d'oxydation à la surface du métal. La radiolyse en milieu hydrogéné ne peut pas entraîner des changements importants dans le potentiel de corrosion et donc, n'apparait pas comme un facteur prépondérant pour l'IASCC en conditions REP. Cependant, les défauts induits par l'irradiation peuvent influencer la cinétique d'oxydation. Il a ainsi été montré que l'irradiation pouvait affecter la couche interne d'oxyde en modifiant son épaisseur et en induisant un enrichissement en Cr. Mais l'effet de l'irradiation sur la formation d'oxyde n'est pas encore clairement appréhendé et il reste encore un sujet ouvert à discussions.

Des études réalisées sur des échantillons irradiés aux neutrons ont servi d'étape préliminaire à l'identification des divers facteurs qui influent sur la sensibilité à la fissuration par IASCC. Mais, il reste encore des questions pour expliciter les mécanismes de dégradation et prédire leur évolution. Il est donc nécessaire d'effectuer des essais sur le matériau irradié en explorant divers facteurs sur une large gamme de dose d'irradiation et pour une large gamme de conditions (irradiation, chargement, environnement, etc.). La complexité associée à la conduite de caractérisations sur matériau irradié aux neutrons rend difficilement réalisable des études exhaustives. Les irradiations aux ions sont utilisées pour conduire des études analytiques sur les effets de l'irradiation. En utilisant des changements de température adéquats, l'irradiation aux

ions peut être un outil efficace pour isoler l'effet des divers paramètres dans l'IASSC. En effet, l'irradiation aux protons a été utilisée avec succès dans plusieurs études pour étudier la sensibilité à la fissuration du matériau dans différents milieux (REB, REP, environnement inerte). Cependant, peu d'études ont utilisé l'irradiation aux ions lourds.. Ainsi avec l'aide de la littérature actuellement disponible, nous avons mis l'accent, dans cette étude, sur le potentiel des ions lourds pour l'étude de l'IASCC.

L'objectif de cette thèse est d'étudier la fissuration intergranulaire par corrosion sous contrainte d'un acier inoxydable austénitique SA 304L irradié aux ions en milieu REP. Trois axes principaux ont été étudiés (i) l'impact de la microstructure induite par l'irradiation, (ii) l'impact de l'état de surface et (iii) l'effet du type de chargement mécanique sur la sensibilité de l'acier inoxydable austénitique 304L à la fissuration intergranulaire. Une méthodologie spécifique a été développée pour répondre aux objectifs de la thèse, qui comprenait la réalisation des irradiations, la caractérisation de la microstructure avant et après l'irradiation, suivis par des sollicitations mécaniques et les caractérisations de surface après ces dernières.

Un acier 304L hypertrempé (SA 304L) a été utilisé dans cette étude en raison de sa sensibilité à l'IGCSC légèrement plus élevée que le 316 et sa microstructure initiale simple par rapport à un acier écroui (état utilisé pour les vis de REP). Le matériau contient 19% en poids de Cr et 9 % en poids de Ni et l'énergie de défaut d'empilement (EDE) du matériau est de 23 mJ/m². La microstructure du matériau utilisé est constituée majoritairement d'austénite et d'une faible quantité de ferrite (~ 2 – 6%). La taille moyenne des grains est d'environ 27µm. Deux géométries différentes de échantillons ont été utilisées : des échantillons de traction (utilisés pour effectuer des essais mécaniques) et des barres (utilisées pour caractériser la microstructure, effectuer des essais de dureté et d'oxydation). La caractérisation de la surface par MET a révélé la présence de grains d'austénite de taille standard avec quelques grains de ferrite.

Les deux types d'échantillons ont été irradiés à JANNuS (CEA Saclay) en utilisant des ions 10 MeV Fe^{5+} à 450 °C avec deux doses différentes : 5 dpa et 10 dpa. Une irradiation complémentaire à 450°C en utilisant 10 MeV Fe^{5+} et 1 MeV He^{+} avec une dose de 5 dpa a également été réalisée. Avec cette énergie, la profondeur de pénétration des ions fer a été calculée à l'aide du logiciel SRIM. Elle est d'environ 2,5 µm. La région irradiée consiste en une zone dont le dommage croie continument avec un pic d'irradiation à environ 2 µm. En parallèle, une campagne d'irradiation aux protons a été réalisée au Michigan Ion Beam Laboratory (MBIL, Université du Michigan, USA) en utilisant des protons 2 MeV à 350 °C à une dose de 2 dpa. La région irradiée dans le matériau atteint une profondeur environ de 20 µm et se compose d'une région de dommage constante suivie par un pic d'irradiation à 19 µm. Le choix de la température pour les deux irradiations (fer et proton) a été choisi pour obtenir des microstructures et des mécanismes représentatifs de ceux observés pour des irradiations aux neutrons.

La caractérisation des microstructures des échantillons irradiés aux ions fer a été effectuée à l'extrême surface d'irradiation alors que pour les échantillons irradiés aux protons, la caractérisation a été effectuée à l'extrême surface d'irradiation ainsi qu'au pic d'irradiation. La caractérisation a été réalisée en utilisant le MET et a révélé principalement la présence de boucles de Frank induites par l'irradiation pour les deux types d'irradiations.

La quantification de la densité des boucles de Frank a été réalisée sur 3 images différentes pour chaque dose. Pour estimer la densité, l'épaisseur moyenne supposée des lames minces est de 100 nm. Les résultats de cette évaluation quantitative sont détaillés dans le Table 1. La quantification de ces défauts est en bon accord avec la littérature pour les échantillons irradiés aux protons, ainsi que pour l'échantillon 10 dpa – Fe. Une densité plus faible d'un facteur 20 a été observée dans l'échantillon 5 dpa – Fe. Ceci est probablement dû à une sous-estimation de la densité des boucles de Frank. Cette hypothèse a été vérifiée en effectuant des mesures de densité de boucles de Frank sur l'échantillon 5 dpa – FeHe. Sur cet échantillon, une densité de $2{,}2 \times 10^{22}$ boucles/m^3 a été estimée ce qui est en bon accord avec la valeur déterminée pour l'échantillon 10 dpa – Fe et supérieur à la valeur de l'échantillon 5 dpa – Fe.

Irradiation	Dommage (dpa K-P)	densité des boucles de Frank (x 10^{22} m^{-3})	Taille des boucles de Frank (nm)	Augmentation du durcissement (%)
5 dpa – Fe	5	0,50 ± 0,31	13,4 ± 1,9	54
10 dpa – Fe	10	2,55 ± 1,05	14,9 ± 3,6	67
2 dpa – H	2	3,60 ± 1,50	13,8 ± 4,8	120

Table 1: Résumé de la microstructure induite par l'irradiation, du durcissement induit par l'irradiation observée dans le matériau après l'irradiation aux ions fer et aux protons.

Pour déterminer l'augmentation de la dureté sur l'échantillon irradié aux ions, un essaide nanodureté a été utilisé en raison des faibles profondeurs de pénétration des ions dans le matériau. Des indentations 'Berkovich' ont été réalisées à différentes profondeurs, et la dureté a été déterminée en utilisant la relation 'Nix – Gao' qui donne la courbe de la dureté² en fonction de l'inverse de la profondeur. Compte des interactions possibles entre les zones non irradiée et irradiée en fonction de la profondeur d'indentation, une attention particulière a été portée sur la détermination de la dureté pour les échantillons irradiés aux ions fer. Bien que la détermination de la dureté pour le matériau irradié aux ions fer ait été effectué jusqu'à une profondeur d'irradiation de 2,5 µm, seuls les résultats de l'indentation à la profondeur de $d \leq 0{,}5$ µm ont été utilisés afin d'éviter de prendre en compte une contribution de la partie non irradiée (Figure 2). Ces difficultés ne sont pas rencontrées pour l'échantillon irradié aux protons (profondeur d'irradiation ~ 20 µm) en raison de leur pénétration plus profonde.

L'augmentation relative de la dureté dans l'échantillon irradié aux ions fer est de 54 à 67%, ce qui est inférieur d'un facteur 2 par rapport à la littérature concernant l'irradiation aux neutrons pour

une dose similaire, mais en excellent accord avec la littérature concernant l'irradiation au fer. Une augmentation relative de 120 – 130% est observée dans l'échantillon irradié aux protons, ce qui est en bon accord avec la littérature concernant les neutrons et les protons. Le résumé de ces résultats est rapporté dans Table 1. En utilisant d'une part un modèle de durcissement de type « barrière dispersée » pour évaluer l'augmentation de la limité d'élasticité et d'autre part et en évaluant l'augmentation de la limite d'élasticité à partir des valeurs de dureté mesurées, une corrélation linéaire entre l'augmentation de la dureté mesurée et la racine carrée du produit de la densité et de la taille des boucles de Frank induit par l'irradiation est obtenue (Figure 3).

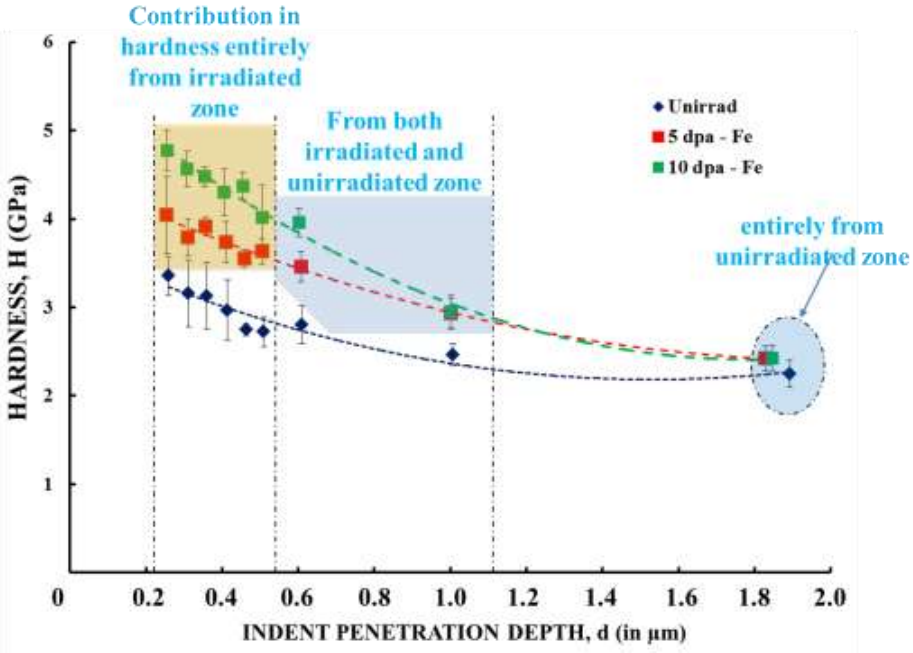

Figure 2: Profil de dureté montrant la comparaison de la dureté obtenue pour les échantillons non irradiées (bleu), 5 dpa - Fe (en rouge) et 10 dpa - Fe (en vert) en utilisant les essais de nano indentation.

Une différence de dureté a été observé pour les échantillons irradiés 10 dpa – Fe et 2 dpa – H alors que la densité des boucles de Frank est similaire. Une explication potentielle est le rôle des défauts dont la taille est inférieure à la résolution du moyen de caractérisation (MET) utilisé dans cette étude. Il a été suggéré que la densité de ces défauts était plus élevée dans l'échantillon 2 dpa – H conduisant à une augmentation de la dureté plus importante. Mais la validité de cette hypothèse doit être vérifiée à l'aide d'outils de modélisation tels que la dynamique moléculaire, la cinétique de Monte Carlo et de la dynamique d'amas.

Les résultats de la caractérisation des microstructures et de la mesure de dureté ont suggéré que les conditions d'irradiation au fer, utilisées dans cette étude, étaient appropriées pour imiter l'irradiation ionique rapportée dans la littérature. Le défi était de vérifier la possibilité d'utiliser l'irradiation au fer pour étudier l'effet des dommages induits par l'irradiation sur la sensibilité à la

fissuration du matériau dans des conditions différentes. Pour atteindre cet objectif, des échantillons de traction irradiés ont été soumis à des essais de traction lente SSRT (Slow Strain Rate Test) dans différents environnements et les essais ont été interrompus après une déformation plastique de 4%.

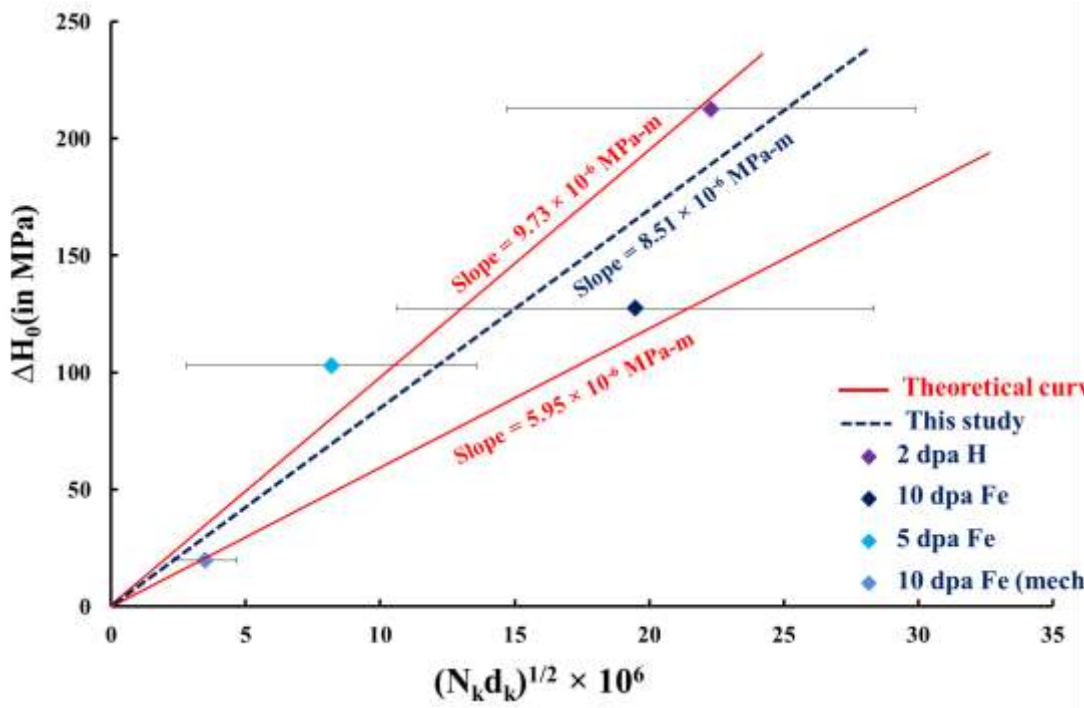

Figure 3: Augmentation de la dureté tracée en fonction de la densité des boucles de Frank pour toutes les doses d'irradiation

- <u>Possibilité d'utiliser l'irradiation au fer pour étudier la fissuration inter granulaire de l'acier inoxydable austénitique irradié.</u>

  Tout d'abord, l'essai a été effectué sur l'échantillon 5 dpa – Fe à la fois en environnement inerte (argon) et en milieu corrosif (milieu REP). La surface des échantillons a été analysée à l'aide du MEB. Sur la surface de l'échantillon testé dans un environnement inerte, aucune fissure n'a été observée. Alors que dans la région irradiée de l'échantillon testé dans l'environnement corrosif, de nombreuses fissures ont été observées (Figure 4). Ce résultat, montrant que l'environnement corrosif est une condition préalable indispensable à la fissuration inter granulaire de l'acier inoxydable austénitique 304L irradié à faible dose, était attendu.

  Comme toute la longueur des échantillons de traction n'a pas été irradiée, une analyse de surface a été réalisée dans la région non irradiée des échantillons pour observer les fissures (le cas échéant). La majeure partie de la zone non irradiée de l'échantillon 5 dpa – Fe ne présentait aucune fissure. Cependant, une inspection approfondie a révélé la

présence de quelques petites fissures intergranulaires. Par la suite, les échantillons 10 dpa – Fe et 2 dpa – H ont été également testés en et analysés en utilisant le MEB. Dans les deux échantillons, quelques fissures ont été observées dans la région non irradiée alors que de nombreuses fissures ont été observées dans les régions irradiées. La nature de ces fissures inter granulaires a été déterminée grâce à plusieurs cartographies de surface dans la région irradiée en utilisant le système d'imagerie FSE (Forescattered Electron) de l'EBSD. En outre, et une coupe transversale a été réalisée par FIB et analysée à l'aide de l'EBSD sur une fissure choisie dans la région irradiée de l'échantillon 5 dpa – Fe. L'analyse a confirmé le nature inter granulaire de la fissure analysée.

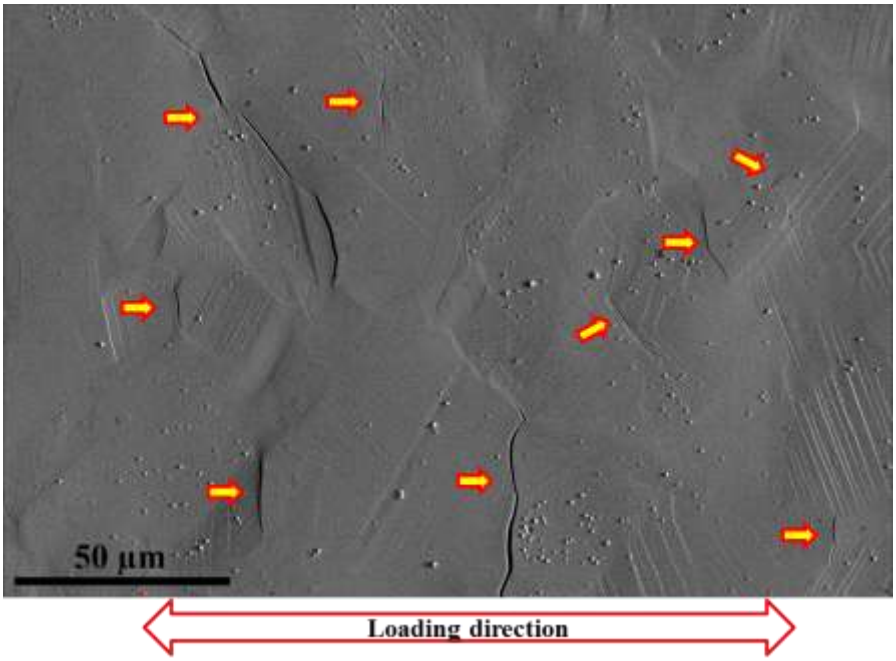

Figure 4: image MEB de la région irradiée de l'échantillon 5 dpa - Fe après l'essai SSRT réalisé en milieu REP. La direction de chargement est indiquée sur l'image.

Pour des études comparatives, des informations quantitatives (à savoir la longueur et densité moyenne de la fissure) ont été déterminées. Une zone de 1 mm² (2mm x 0,5 mm) a été scannée dans la partie centrale de la région irradiée de l'échantillon en utilisant le MEB. La densité des fissures a été obtenue pour deux zones irradiées différentes. La densité moyenne des fissures et l'erreur ont été estimées. La longueur des fissures a été estimée à l'aide du logiciel ImageJ. Les résultats de l'analyse quantitative effectuée sur les échantillons sont résumés dans le Table 3-1. La reproductibilité de ces résultats a été confirmée en comparant la densité et la taille moyenne pour les deux 'essais SSRT sur échantillons irradiés 5 dpa – Fe.

échantillons	régions non irradiées		régions irradiées	
	densité de fissures (fissures/mm²)	longueur de fissure moyenne (µm)	densité de fissures (fissures/mm²)	longueur de fissure moyenne (µm)
5 dpa – Fe	99 ± 18	12 ± 2	302 ± 23	17 ± 2
10 dpa – Fe	64 ± 12	12 ± 2	293 ± 18	16 ± 2
2 dpa – H	71 ± 13	12 ± 2	316 ± 30	17 ± 2

Table 2 : Résumé de l'analyse quantitative réalisée dans les régions non irradiées et irradiées des échantillons 5 dpa - Fe, 10 dpa - Fe et 2 dpa - H.

De toute évidence, une forte influence de l'irradiation sur la susceptibilité de fissuration de l'acier inoxydable austénitique en milieu REP a été observée pour tous les échantillons. En dépit de la faible profondeur de pénétration des ions fer dans le matériau, la densité des fissures est semblable dans l'échantillon irradié au fer par rapport à l'échantillon irradié aux protons. Cela implique que l'irradiation au fer est un bon outil pour étudier l'IGCSC de l'acier inoxydable austénitique irradié.

Néanmoins, il est nécessaire de vérifier si le mécanisme de fissuration dans l'échantillon irradié au fer est le même que celui rapporté dans la littérature pour l'échantillon irradié aux protons.. A cet effet, une corrélation entre la sensibilité à la fissuration et la déformation localisée a été étudiée pour les échantillons irradiés au fer et aux protons. Une augmentation du degré de déformation localisée ayant été suggérée comme étant le facteur principal contribuant à la fissuration du matériau irradié aux protons.. L'espacement des lignes de glissement a été utilisé dans notre étude comme un indicateur quantitatif du degré de localisation.

L'analyse de surface par MEB a confirmé la présence de fines lignes de glissement à l'intérieur des grains dans les deux régions (non irradiés et irradiés) de tous les échantillons. Pour chaque échantillon, l'espacement des lignes de glissement a été calculé sur 10 images (environ 25 grains) pour les régions non irradiées et irradiées. Pour tous les échantillons, une valeur moyenne de l'espacement des lignes de glissement a été obtenue, elle est plus élevée dans la région irradiée par rapport à la région non irradiée impliquant un plus haut degré de localisation dans la région irradiée des échantillons. Pour les échantillons irradiés au fer, dans la région irradiée, la valeur moyenne de l'espacement dans l'échantillon 10 dpa – Fe est similaire à celle de l'échantillon 5 dpa – Fe, indiquant que cet espacement est indépendant de la dose entre 5 et 10 dpa.

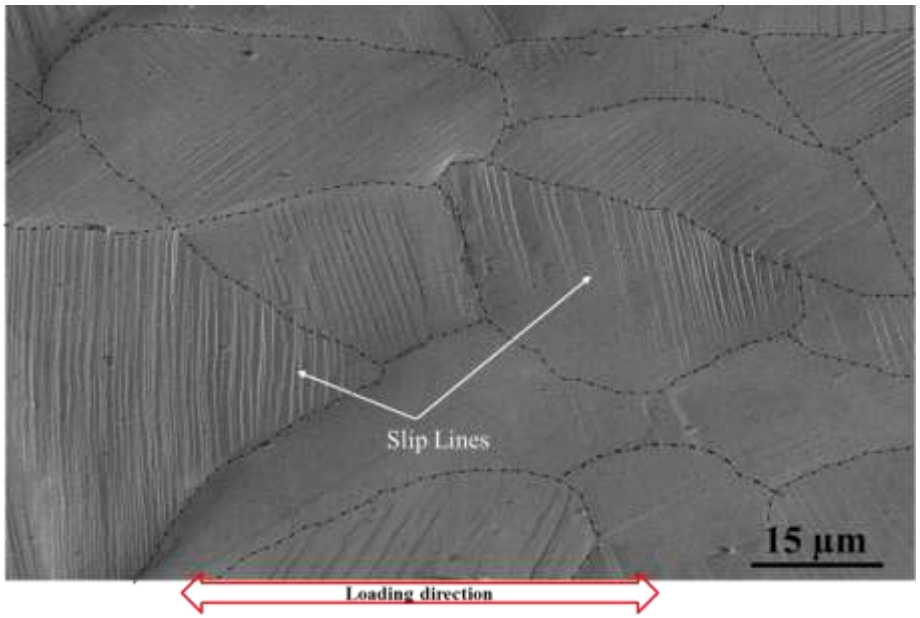

Figure 5: Image MEB dans la région irradiée de l'échantillon 5 dpa – Fe après l'essai de corrosion dans un environnement inerte jusqu'à la déformation plastique de 4%. La présence de lignes de glissement sur la surface de l'échantillon est clairement visible. Certains des joints de grains sont marqués par une ligne noire (en pointillés). La direction de chargement est indiquée dans l'image.

La valeur d'espacement moyen dans la région irradiée de l'échantillon 2 dpa – H est beaucoup plus élevée que celle des échantillons 10 dpa – Fe et 5 dpa – Fe, indiquant un degré de localisation plus élevé pour les irradiations aux protons bien que la dose soit plus faible... Bien que le degré de localisation soit plus élevé dans l'échantillon 2 dpa – H, la densité de fissures est la même dans tous les échantillons (5 dpa – Fe, 10 dpa – Fe et 2 dpa – H). Ces observations indiquent que pour les conditions d'irradiation et le taux de déformation utilisés dans cette étude, le degré de localisation n'est pas le seul facteur prépondérant dans la fissuration inter granulaire. Il est très plausible que des facteurs tels que le RIS et/ou l'oxydation inter granulaire ont contribué à dégrader la résistance des joints de grains, ce qui affecte la sensibilité à la fissuration intergranulaire. Le RIS et l'oxydation inter granulaire n'ont pas été examinés dans cette étude. Mais l'oxydation à la surface du matériau a été étudiée pour comprendre l'impact de l'irradiation sur l'oxydation de l'acier inoxydable austénitique.

Tout d'abord, les échantillons préparés par FIB à partir des régions non irradiée et irradiée de l'échantillon 5 dpa – Fe testés en milieu primaire simulé à 340 °C après un essai de traction lente SSRT ont été analysés par MET. La couche d'oxyde formée sur les deux régions a été caractérisée comme une couche duplex constituée d'une couche d'oxyde externe (discontinue) et une couche d'oxyde interne (continue). L'oxyde externe observé sur la région non irradiée et irradiée de l'échantillon est constitué de cristallites riches en Fe tandis que la couche intérieure est composée de spinelle de type ((Fe, Ni)Cr_2O_4 riche en Cr. Les couches d'oxyde (externe et interne) formées sur l'échantillon non irradié

étaient plus épaisses que les couches d'oxyde formées sur l'échantillon irradié. Cela indique que l'irradiation a entrainé une diminution de la taille des deux couches d'oxyde. La teneur en Cr de la couche interne de l'échantillon non irradié est également plus élevée. Ce qui suggère que l'irradiation a modifié l'oxyde formé sur l'acier inoxydable austénitique. Afin d'obtenir d'avantage d'informations sur les couches d'oxydes, des essais d'oxydation ont ensuite été conduits dans des autoclaves (en acier inoxydable).

Deux essais d'oxydation ont été réalisées pour 360 h chacun dans un milieu primaire simulé à 340 °C dans deux autoclaves de différents volumes (0,38 L et 5L). De façon surprenante, les échantillons non irradiés et irradiés ont révélé une tendance opposée à celle observée pour l'éprouvette de traction 5 dpa - Fe après l'oxydation dans l'autoclave de petit volume. En effet, une augmentation de l'épaisseur de la couche interne et un enrichissement en Cr avec l'irradiation a été observée dans les échantillons oxydés (Table 3-2). Il y avait peu de différences entre les deux essais à savoir, la durée, le volume du milieu corrosif et la contrainte. L'augmentation de l'épaisseur de la couche interne avec la durée de l'essai et l'application d'une contrainte a été rapportée dans la littérature pour les matériaux non irradiés. Cependant, peu de résultats sont connus pour l'état irradié. Pour étudier l'effet du volume du milieu corrosif sur les échantillons irradiés, des échantillons irradiés à 5 dpa - FeHe oxydés dans des autoclaves de 5L et 0,38 L ont été étudiés. Avec l'augmentation du volume des milieux corrosifs, nous observons une augmentation de l'épaisseur de la couche d'oxyde interne dans le matériau irradié. Cependant, l'effet du temps et de la contrainte appliquée n'ont pas pu être examiné dans cette étude. Aucun effet concluant de l'irradiation sur l'oxydation n'a pu être mis en évidence et le manque d'information dans ce domaine suggère que d'autres études devront être menées pour comprendre le processus d'oxydation et les facteurs affectant ce dernier.

L'échantillon	**Epaisseur**	
	Couche externe (nm)	**Couche interne (nm)**
Non irradiée	20 – 100	5 – 6
5 dpa – Fe	1 – 3	10 – 20

Table 3 : Epaisseur des couches d'oxyde formées sur les échantillons non irradiées et irradiés à 5 dpa – Fe après l'essai d'oxydation dans le milieu REP simulé à 340 °C pendant 360 h.

Néanmoins, il est évident que l'irradiation a augmenté le degré de localisation de la déformation plastique et a modifié la formation de l'oxyde dans le matériau SA 304L. Ces changements (hors l'effet du RIS dans cette étude) pourraient conduire à des joints de grains d'une part plus fragiles et d'autre part plus sollicités entraînant une augmentation de la densité de fissures par rapport au matériau non irradié. Cependant, dans la région

irradiée, tous les joints de grains ne sont pas fissurés ce qui indique que toutes les conditions qui amène un joint de grain à fissurer ne sont remplies.

Pour commencer, les sites de fissure ont été classés en deux catégories: interaction continue (transfert du glissement à travers le joint de grain) et interaction discontinue (pas de transmission évidente de glissement à travers le joint de grain) basé sur l'interaction des lignes de glissement avec les joints de grains. Parmi tous les joints de grains fissurés observés, 30 – 40 % appartenaient à une interaction continue tandis que 50 – 60 % appartenaient à la catégorie discontinue. Environ 10% appartenaient à la catégorie où aucune ligne de glissement n'a été observée de chaque côté du joint de grain fissuré. Dans le cas de l'interaction discontinue, l'accumulation de contraintes au joint de grain est élevée en raison de l'accumulation de dislocations qui augmentent la le chargement mécanique du joint de grain.. Par conséquent, le nombre de joints de grain fissurés qui correspond à cette catégorie est légèrement plus élevé. Mais, sur la base de ces résultats, on ne peut pas conclure que l'interaction discontinue est un critère suffisant pour qu'un joint de grain fissure.

Il a été proposé dans la littérature que ; dans l'acier inoxydable austénitique irradié aux protons et déformé dans l'eau supercritique et en milieu REB (réacteur à eau bouillante), les joints de grain qui sont plus sensibles à la fissuration présentent les critères suivants :

- la nature du joint général
- inclinés à des angles plus élevés (supérieur à 70°) par rapport à la direction de traction
- adjacents aux grains à faible facteur Schmid ($FS \leq 0,44$)
- classés en catégorie « interaction continue ».

Dans notre étude, la validité de ces critères a été étudiée pour les échantillons irradiés à 5 dpa – Fe et 2 dpa – H et les conditions de déformations (dans un milieu REP) utilisées. Pour cela, une surface de 0,1 mm² a été scannée à l'aide de l'EBSD et les informations sur FS ont été obtenues. Les valeurs de FS obtenues ont été classés en trois catégories différentes: haut ($0,47 < FS \leq 0,50$), Moyenne ($0,44 < FS \leq 0,47$) et faible ($FS \leq 0,44$).
Le pourcentage de joints de grain fissurés qui satisfont tous les critères proposés a été calculé à partir de la zone de 0,1 mm² de la région irradiée pour l'échantillon 5 dpa – Fe. Il est intéressant de remarquer que seulement 32 % des joints de grains fissurés observé satisfaisaient de toutes les conditions proposées. Une analyse similaire a été effectuée sur l'échantillon 2 dpa - H et des résultats similaires ont été obtenus. Cela implique que, indépendamment du type d'irradiation utilisé, ces conditions ne sont pas suffisantes pour décrire totalement le critère de fissuration dans les aciers inoxydables austénitiques irradiés avec les conditions de déformation utilisées dans cette étude. Aucune étude détaillée sur la répartition des contraintes et la déformation locale n'a été menée dans cette étude. Cependant, en prenant en compte les joints de grains inclinés à un angle supérieur ou égal à 50 °, une corrélation entre l'orientation des joints de grains par rapport à l'axe de traction et la fissuration inter granulaire a été observée et améliorée de 68% à

90%. Cela implique que, les joints de grain qui sont inclinés à un angle inférieur à 50° par rapport à l'axe de traction deviennent plus sensibles à la fissuration quand ils ont été irradiés. Mais cette corrélation doit encore être explorée.
Ces résultats ont mis en évidence la possibilité d'utiliser l'irradiation aux ions fer pour étudier l'IGCSC sur l'acier inoxydable austénitique irradié. La majorité des données existantes sur la fissuration inter granulaire d'échantillon irradié aux ions est basée sur l'utilisation de l'irradiation aux protons. Mais la limitation de l'irradiation aux protons est liée à la difficulté d'obtenir des doses très élevées par rapport aux ions lourds. Comme proposé dans cette étude, l'irradiation au fer pourrait être utilisée à des doses plus élevées, pour améliorer la compréhension de l'IGCSC pour l'acier inoxydable austénitique irradié et enrichir la littérature.

- Effet de la préparation surface sur la sensibilité de la fissuration inter granulaire de l'acier inoxydable austénitique irradié aux fers.

En utilisant l'irradiation au fer, quelques aspects de l'IGCSC sur l'acier inoxydable austénitique irradiés ont été étudiés dans cette thèse. Tout d'abord, l'effet de la préparation de surface sur la sensibilité du matériau à la fissuration. L'objectif était de relier les résultats obtenus en laboratoire avec le scénario réel dans le milieu REP. Le matériau utilisé dans les vis des internes de cœur de REP a une couche écrouie de surface, durcie, en raison de l'usinage. Mais la majorité des études faites dans les laboratoires, pour étudier la sensibilité à la fissuration d'un matériau irradié aux ions, utilise des échantillons électropolis et donc sans surface écrouie. Comme l'amorçage de la fissuration inter granulaire est un phénomène de surface, cette différence pourrait avoir des effets conséquents sur les mécanismes mis en jeux.

Pour étudier cet effet, deux préparations de surface différentes ont été utilisées, à savoir, un polissage mécanique et un vibro-polissage. La caractérisation par MET de l'échantillon poli mécaniquement et non irradié a révélé la présence d'une couche durcie en surface constituée de nanograins jusqu'à une profondeur d'environ 500 nm. La microstructure de l'échantillon vibro-poli est quant à elle libre de toute couche de surface écrouie et contient des grains de taille standard. En raison de la présence de la couche de surface durcie, la valeur de dureté de l'échantillon poli mécaniquement est plus élevée (~ + 28%) que l'échantillon vibro-poli.

Les deux échantillons ont été irradiés à une même dose (10 dpa) aux ions fer à 450°C. Dans l'échantillon irradié à 10 dpa au Fe (échantillon vibro-poli), la profondeur d'irradiation se situe dans les grains de taille standard. Alors que dans l'échantillon 10 dpa – Fe (mech.) (échantillon poli mécaniquement), la zone irradiée se situe partiellement dans la zone avec des nanograins, c'est-à-dire la couche écrouie (Figure 4-1).

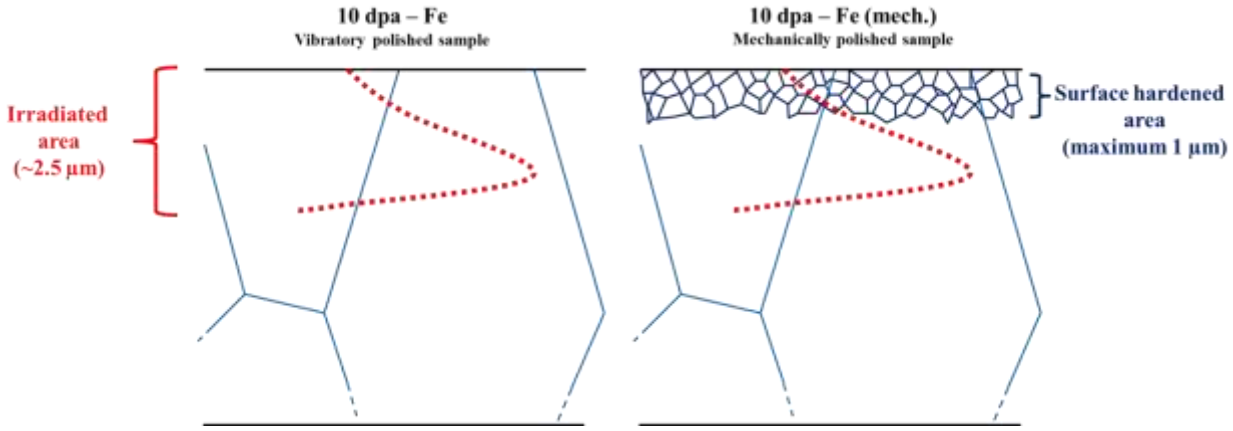

Figure 6 : Schémas illustrant la profondeur de la zone irradiée dans les échantillons 10 dpa - Fe et 10 dpa - Fe (mech.). Le profil de dommage est représenté en pointillé rouge et les joints de grains en bleu.

Après l'irradiation, la microstructure a été caractérisée et a révélé la présence de boucles de Frank dans les deux échantillons (Figure 7). Dans les échantillons polis mécaniquement, il est difficile d'observer les défauts dû à la petite taille des grains, mais une observation approfondie a révélé la présence de ces défauts dans quelques nanograins d'austénite. L'analyse quantitative a montré que la densité des défauts d'irradiation dans l'échantillon poli mécaniquement (échantillon 10 dpa – Fe (mech.)) est plus faible d'un facteur de 40 par rapport à son homologue vibro-poli. Cela est attribué à la fraction volumique plus élevée des joints de grains dans l'échantillon 10 dpa – Fe (mech.) qui agissent comme des puits de défauts. L'augmentation de la dureté avec l'irradiation est plus faible aussi dans l'échantillon 10 dpa – Fe (mech.) par rapport à l'échantillon 10 dpa – Fe.

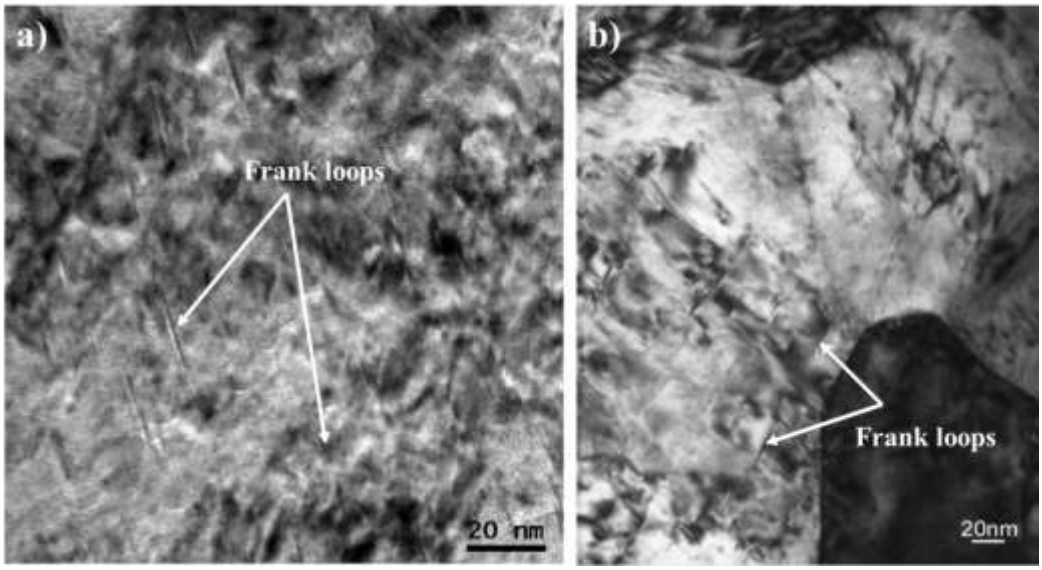

Figure 7: Images en champ clair obtenues au MET montrant les défauts d'irradiation observés dans l' échantillon a) vibro-poli b) poli mécaniquement après l'irradiation au fer à une dose de 10 dpa.

Après avoir caractérisé les dommages d'irradiation, les échantillons de traction ont été ensuite soumis à l'essai SSRT jusqu'à 4% de déformation plastique dans un milieu primaire simulé à 340 °C. Cela a conduit à l'apparition de fissures et de lignes de glissement à la surface des échantillons. Comme indiqué précédemment, quelques fissures dans la région non irradiée et de nombreuses fissures dans la région irradiée de l'échantillon 10 dpa – Fe ont été observées. Par contre peu de fissures ont été observées dans la région irradiées de l'échantillon 10 dpa – Fe (mech.).

L'analyse quantitative a révélé une augmentation de la sensibilité à la fissuration dans les deux échantillons après l'irradiation (Table 4). Cependant, l'augmentation est beaucoup plus faible dans l'échantillon 10 dpa - Fe (mech.). Les résultats ont également montré que la densité de fissures dans la région non irradiée de l'échantillon 10 dpa – Fe (mech.) était légèrement plus élevé que dans la région non irradiée de l'échantillon 10 dpa – Fe. Ceci suggère que la présence de la couche de surface écrouie a augmenté la sensibilité à la fissuration inter granulaire du matériau non irradié.

Au contraire, dans les régions irradiées, la densité de fissures et la longueur moyenne de la fissure sont plus élevées pour l'échantillon 10 dpa – Fe. L'analyse qualitative a montré que les fissures sont plus larges sur l'échantillon 10 dpa – Fe par rapport à l'échantillon 10 dpa – Fe (mech.). Cela montre que pour le matériau irradié, la fissuration a été plus sévère pour l'échantillon vibro-poli. En d'autres termes, la présence de nanograins a diminué de manière significative la sensibilité à la fissuration du matériau irradié. Cet effet inverse de l'état de surface dans les matériaux irradiés signifie aussi que la sensibilité à la fissuration du matériau irradié dépend de plusieurs facteurs, qu'il convient de pouvoir étudier séparément.

échantillons	**régions non irradiées**			**régions irradiées**		
	densité de fissures (fissures/mm²)	**longueur de fissure moyenne (µm)**	**l'espacement des lignes de glissement moyenne (µm)**	**densité de fissures (fissures/mm²)**	**longueur de fissure moyenne (µm)**	**l'espacement des lignes de glissement moyenne (µm)**
10 dpa – Fe	64 ± 12	12 ± 2	0.9 ± 0.2	293 ± 18	16 ± 2	1.7 ± 0.1
10 dpa – Fe (mech.)	82 ± 6	8 ± 1	0.8 ± 0.2	115 ± 9	11 ± 1	1.3 ± 0.1

Table 4: Comparaison de l'analyse quantitative réalisée dans les régions non irradiées et irradiées des échantillons 10 dpa - Fe et 10 dpa – Fe (mech.).

La région écrouie de surface et les défauts ponctuels induits par l'irradiation sont des sources de durcissement. Dans l'échantillon 10 dpa – Fe, seuls les défauts induits par l'irradiation ont contribué à l'augmentation de la dureté tandis que dans l'échantillon 10 dpa – Fe (mech.), le durcissement est le résultat de deux effets. Pourtant, l'augmentation

nette est beaucoup plus faible sur l'échantillon 10 dpa – Fe (mech.) que sur l'échantillon 10 dpa – Fe, principalement en raison de la densité beaucoup plus faible de défauts induits par l'irradiation sur cet échantillon. Cette augmentation plus faible de la dureté est cohérente avec l'observation d'une densité de fissures plus faibles dans l'échantillon 10 dpa – Fe (mech.).

Comme indiqué précédemment, les lignes de glissement ont été observées à la surface des échantillons. L'espacement entre ces lignes a été utilisé comme un indicateur du degré de localisation pour établir une corrélation entre le degré de localisation et la sensibilité à la fissuration inter-granulaire. Dans les deux échantillons (10 dpa – Fe et 10 dpa – Fe (mech.)), l'espacement moyen des lignes de glissement est plus élevé dans la région irradiée que dans la région non irradiée. Ceci implique que, indépendamment de l'état de surface, l'irradiation augmente la probabilité de déformation localisée d'un matériau. Un espacement plus élevé signifie un plus haut degré de localisation et, par conséquent, une bonne corrélation avec la densité plus élevée des fissures observées dans la région irradiée. Dans les régions non irradiées des deux échantillons, aucune différence significative n'a été observée sur les valeurs d'espacement des lignes de glissement, impliquant un effet nul de la couche écrouie de surface sur l'espacement entre les lignes de glissement. Dans les régions irradiées des deux échantillons, les valeurs d'espacement sont un peu plus élevées dans l'échantillon 10 dpa – Fe (Table 4). Par compte l'augmentation de la densité de fissures est beaucoup plus importante dans l'échantillon vibropoli (facteur ~2.5), ce qui semble montrer que la localisation de la plasticité induite par l'irradiation, bien que jouant un rôle, n'est pas le seul facteur affectant la fissuration intergranulaire. D'autres facteurs tels que le RIS et l'oxydation intergranulaire n'ont pas été étudiés ; ici, nous avons choisi de caractériser l'oxydation de surface.

Les échantillons non irradiés vibro-poli, poli mécaniquement et irradiés 10 dpa – Fe (mech.) sont oxydés en autoclave pendant 360 h en milieu REP. Quel que soit l'état de surface, la couche d'oxyde duplex est observée. Les cristallites d'oxyde externe observés sur l'échantillon vibro-poli sont de plus grande taille que ceux de l'échantillon poli mécaniquement (figure 8). Grâce aux analyses MET, il est montré que la couche interne formée sur l'échantillon poli-vibro est plus mince et moins enrichi en Cr montrant son caractère moins protecteur. En raison de la présence de nanograins dans l'échantillon poli mécaniquement, la fraction volumique des joints de grains est plus élevée. La diffusion de l'oxygène et / ou des atomes métalliques est plus rapide le long des joints de grains, la fraction volumique plus élevée des joints de grain devrait globalement améliorer la diffusion vers le substrat de l'oxygène et la diffusion vers l'oxyde du Fe entraînant la formation d'une couche interne plus épaisse et plus enrichie en chrome.

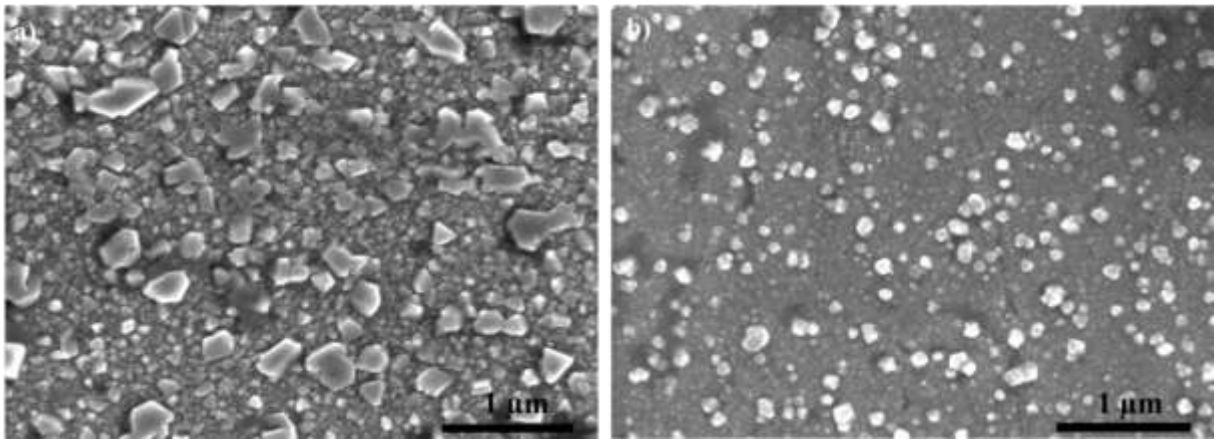

Figure 8 : Micrographes MEB des échantillons non irradiés oxydés en autoclave pendant 360 h en milieu REP a) vibro-poli b) poli mécaniquement.

Enfin, l'effet de l'irradiation sur l'oxydation de l'échantillon poli mécaniquement a été étudié. Les résultats ont montré que la taille des cristallites d'oxyde externe diminue avec l'irradiation. En outre, la couche interne formée sur la région irradiée de l'échantillon 10 dpa – Fe (mech.) a été caractérisée et présente une teneur en Cr inférieure, par conséquent, moins protectrice que la couche formée sur l'échantillon non irradié (mécaniquement poli) (Table 4-3).

échantillon	**Region**	**composition chimique**			**épaisseur (nm)**
		Cr (relatif at. %)	**Ni (relatif at. %)**	**Fe (relatif at. %)**	
Poli Mech. Non irradiée	Couche externe	16	1	83	10 – 35
	Couche interne	56	1	43	10 – 12
	Substrat (nanograins – Ferrite)	28	3	69	650
10 dpa – Fe (mech.)	Couche externe	33	7	60	2 – 20
	Couche interne	36	7	57	10 – 15
	Substrat (nanograins – Austenite)	20	7-14	66-73	200 – 250

Table 5 : Comparaison des couches d'oxyde formées sur les échantillons non irradiée et 10 dpa – Fe (mech.) après 360 h d'oxydation en milieu REP.

Le substrat de l'échantillon non irradié poli mécaniquement contient des grains de ferrite. Malheureusement, notre échantillon présente grains de ferrite oxydé contrairement à l'échantillon vibro-poli et l'échantillon 10 dpa – Fe (mech.) qui présentent grains

d’austénite. Cela peut affecter de manière significative l’oxydation de ces échantillons. Par conséquent, aucune conclusion de l’effet de l’irradiation sur l’oxydation en fonction de l’état de surface n’a pu être faite, mais ces résultats signifient que l'irradiation modifie l'oxydation de l'acier inoxydable austénitique, indépendamment de l'état de surface. Par conséquent, cette question devra être abordée dans les études futures.

En conclusion, les résultats de ces travaux suggèrent que la présence de la couche de surface écrouie peut limiter la sensibilité à l’IGCSC de l’acier austénitique 304L irradié aux ions. A noter que, dans notre étude, la profondeur de la région irradiée est légèrement supérieure à la profondeur de la couche écrouie de surface. Cependant, dans le cas d’une irradiation aux neutrons, la région irradiée est beaucoup plus profonde que la couche écrouie de surface. Ainsi, il est nécessaire de confirmer les résultats de cette étude dans le cas d’une zone irradiée plus profonde que la couche écrouie de surface, par exemple en utilisant dans un premier temps une irradiation aux protons.

- <u>Effet de la trajectoire de chargement sur la sensibilité à la fissuration intergranulaire de l’acier inoxydable austénitique irradié au fer</u>

Le troisième aspect abordé dans cette étude a été l'effet de la trajectoire de chargement sur l’IGCSC de l’acier inoxydable austénitique irradié. Les données d'amorçage en IACSC existantes dans la littérature préconisent la présence d'un seuil de contrainte pour une fluence neutronique (dose) donnée au-dessous duquel l’IACSC ne se produira pas en milieu REP. Ces évaluations sont basées sur l'utilisation d'essais à charge constante sur les aciers inoxydables austénitiques irradiés aux neutrons pour obtenir un seuil de contrainte – dose (à savoir le seuil de contrainte pour l'initiation des fissures en fonction de la dose). Cependant, la représentativité de ces essais pour les conditions de fonctionnement doit encore être validée. Les contraintes thermiques que subissent les vis en milieu REP pendant leur fonctionnement en service (par exemple lors de l'arrêt et le redémarrage du réacteur pour la maintenance) est plus complexe qu'une charge constante. Elles peuvent être décrites comme un chargement cyclique avec des périodes de détention longues. La température varie pendant le chargement cyclique conduisant à amplifier la variation. La question de l'effet d’un chargement cyclique sur la propension à l’amorçage des fissures doit être soulevée et des efforts ont été faits dans cette étude pour répondre à cette question.

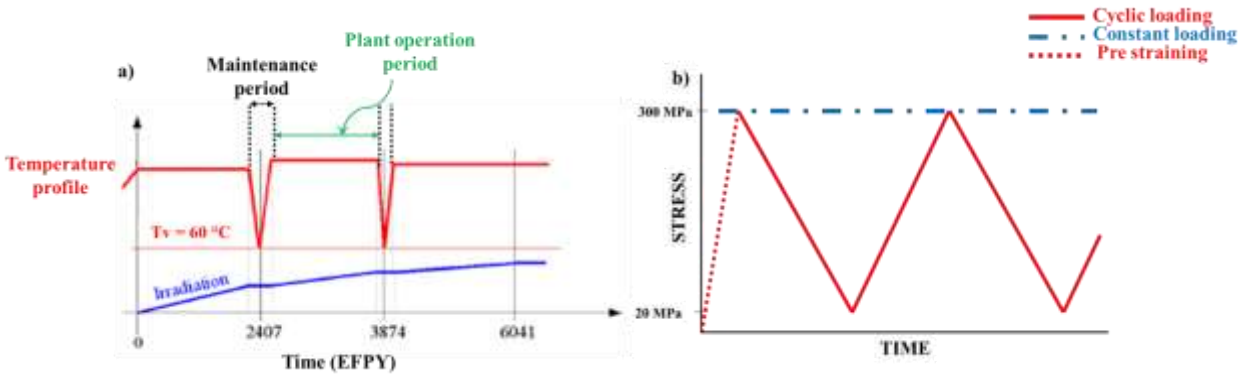

Figure 9: a) Schéma illustrant le cycle de température pendant le fonctionnement normal et la période de maintenance (source EDF). b) Graphique de la contrainte en fonction du temps pour les conditions de chargement cycliques (en trait plein rouge) et constant (en traits pointillés bleu) utilisés. Pré-déformation appliqué avant le chargement est représenté en pointillé rouge.

Dans une première approche, le chargement complexe réel de la vis a été simplifié et modélisé par un chargement cyclique. La première condition de charge a consisté à appliquer une charge cyclique variant de 20 MPa (σ_{min}) à 300 MPa (σ_{max}) avec une fréquence de 2 cycles/jour. Pour étudier le rôle du chemin de chargement sur l'amorçage des fissures du SA 304L irradiée au fer, il a été proposé de comparer les chargements cycliques et constants. Pendant le chargement constant, la charge a été maintenue à 300 MPa pendant 360 h. Ces différents chemins de chargement ont été appliqués sur un échantillon irradié 5 dpa - Fe en milieu REP. La contrainte maximale choisie pour les deux conditions était de 300 MPa et la déformation plastique à la fin de l'essai était de 6,5%. Une pré-déformation identique (chargement rapide de 0 MPa à 300 MPa, avec une sollicitation de 5×10^{-4} s^{-1} jusqu'à 4% de déformation plastique) a été utilisée avant d'appliquer les chargements cycliques et constants. Les échantillons ont été pré-déformés avant le chargement cyclique afin d''avoir un état de référence identique au début des deux essais. Pour comprendre les conséquences de cette pré-déformation, une charge de traction rapide avec la même sollicitation et déformation plastique a été effectuée sur l'échantillon 10 dpa – Fe.

Cet échantillon (10 dpa – Fe soumis à une charge de traction rapide) a été comparé avec l'autre échantillon 10 dpa – Fe soumis à l'essai de SSRT avec un taux de déformation 5×10^{-8} s^{-1}. La déformation plastique à la fin des deux essais était la même. Pourtant, aucune fissure n'a été observée après le chargement rapide tandis que de nombreuses fissures ont été observées après l'essai de SSRT. Ceci implique que la sensibilité à la fissuration diminue avec l'augmentation de la vitesse de déformation. Cette observation peut être expliquée par l'hypothèse selon laquelle l'effet du milieu dans l'amorçage de la fissuration intergranulaire n'a pas le temps de se produire lors d'une vitesse de déformation rapide. Ainsi, le matériau est insensible à la fissuration en milieu corrosif avec ce taux de déformation rapide comme celle du matériau dans un environnement

inerte.. L’essai de charge de traction rapide menée était identique à la pré-déformation pour les conditions de chargement cycliques et constantes utilisées dans cette étude, ce qui implique que les fissures observées dans les échantillons (le cas échéant) après chargement cyclique et constant ont été amorcées au cours du chargement et pas pendant la pré – déformation.

L'analyse de surface des échantillons irradiés 5 dpa - Fe après les différents chargements mécaniques (cyclique et constant) a révélé la présence de fissures intergranulaires. Seules les régions irradiées de ces échantillons ont été analysées. La quantification de ces fissures suggère que la longueur moyenne et la densité des fissures pour les deux cas sont similaires malgré les différents chemins de charge. Les résultats sont résumés dans le Table 5-2. On peut conclure que pour les conditions d'irradiation et les conditions de chargement utilisées dans cette étude, le chemin de chargement n'a pas modifié l'amorçage et la propagation de la fissure dans le matériau irradié. En d'autres termes, la charge maximale appliquée apparait comme un paramètre plus influent que le chemin de chargement.

échantillons	**Type de chargement**	**densité de fissures (cracks/mm²)**	**longueur moyenne de fissure (µm)**
5 dpa – Fe_ Cy	Cyclique	153	12
5 dpa – Fe_ Co	Constant	166	12

Table 6 : Comparaison de l'analyse quantitative réalisée sur les échantillons irradiée aux fers et suivant différentes conditions de chargement.

Ces résultats ne semblent pas en accord avec la littérature ou les résultats montrent que l’application d’un chargement cyclique accélère la propagation de fissure. La raison de cette tendance inverse n’est pas claire. Par conséquent, pour mieux comprendre les différents facteurs possibles qui contribuent à la fissuration intergranulaire du matériau et leur corrélation avec les différents chemins de chargement ont été explorés.

La déformation localisée dans les deux échantillons a été estimée en mesurant l'espacement des lignes de glissement après le chargement La valeur de l'espacement des lignes de glissement est très semblable. Une même valeur d'espacement implique un degré de localisation proche. Cela semble être en accord avec la même densité de fissures observées dans les deux échantillons. Mais, l'évolution de l'oxydation avec le chemin de chargement pour les échantillons irradiés au fer dans un environnement REP est encore à étudier. Néanmoins, les résultats de cette étude suggèrent que le chemin de chargement n'a pas d'impact sur la susceptibilité à la fissuration des échantillons irradiés au fer. Ce résultat est contraire à la littérature et doit encore être étudié.

Pour conclure, la possibilité d'utiliser l'irradiation aux ions lourds (en particulier, l'irradiation au fer) pour étudier l'IGCSC en milieu REP d'un acier inoxydable austénitique a été explorée dans cette étude. De plus, quelques aspects de l'IGCSC ont été analysés avec succès en utilisant l'irradiation au fer comme outil. Cette étude propose donc la possibilité d'utiliser l'irradiation au fer comme un outil pour conforter la littérature actuelle de l'IGCSC des aciers inoxydables austénitiques irradiés au fer en particulier à des doses plus élevées, pour améliorer la compréhension du mécanisme de l'IGCSC sur les aciers inoxydables austénitiques irradiés.

INTRODUCTION

With the potential to fulfil the increasing energy demands of world while keeping the carbon dioxide emissions low, nuclear energy has gained new interest. In order to account for this rapid expansion and increased scrutiny; safe, economic and reliable operation of Light Water Reactors (LWRs) will become highly necessary which implies the need to improve the reliability of technical solutions implemented along with development of mitigation strategies. LWRs include both Pressurized Water Reactors (PWRs) and Boiling Water Reactors (BWRs) and constitute the major part of the nuclear fleet of the world. However, in this study, only PWRs will be considered as all the French units are PWRs. In recent years, significant efforts are led to the lengthening of the duration of the operating cycles of the reactors from 40 years to 60 years, which requires control of the properties of service structures and the materials constituting them in severe operating conditions [1 – 3]. As the reactor internals provide support to the core, distribute the coolant flow through the core and guide and protect the rod cluster assemblies and in core instrumentations, their integrity must be maintained in all operating and accident conditions to achieve this Long Term Operation (LTO) objective.

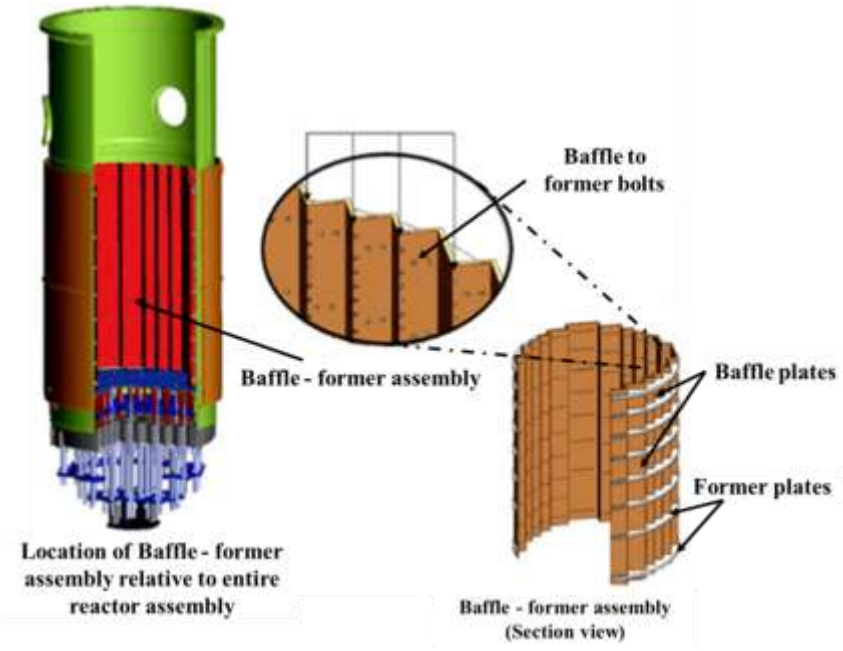

Figure 10: Baffle former assembly locations and views for a CP0 900 MWe PWR [4].

The core baffle is a part of the reactor lower internals which consists of vertical baffle plates maintained by 8 horizontal former plates (Figure 10). The baffles plates are bolted to former plates and these bolts are called baffle to former bolts (or baffle bolts). In CP0 900 MWe PWRs, there are 957 bolts including 832 baffle-former bolts, 104 bolts around the periphery of the baffle plates in each octant; 13 bolts at each of the 8 former levels in each octant [4]. These internals are intended to remain for the full life of the reactor, so the choice of material non sensitive to stress corrosion cracking is made based on their position (direct contact to primary water) in the vessel.

As a consequence, austenitic stainless steels are used, due to their good mechanical properties and corrosion resistance. The baffle and former plates are made of solution annealed austenitic 304 and/or 304 L while bolts are made of cold worked 316 (CW 316) and/or 316L (CW 316L). In normal operating conditions, the average temperature of the these components in PWR is around 300 to 330 °C but it can reach locally to 360 °C due to gamma heating. Besides, being in the vicinity of the core, some of these components can experience a dose as high as ~ 80 dpa during their in – service (40 years) lifetime (Table 7) [3].

Component	**Material**	**Operating temperature**	**Maximum dose (after 40 years of in-service life)**
Baffle plate	SA 304L	~300 – 380 °C	80 dpa
Former Plate	SA 304L	~300 – 380 °C	60 dpa
Bolts	CW 316	~300 – 370 °C	80 dpa

Table 7: Irradiation conditions of the core internals of a PWR [1].

In-service inspection of these core internals in CP0 design revealed the susceptibility of baffle to former bolts to aging mechanism. The first failure of the bolts was reported in 1989 at Bugey 2 power plant in France. The detailed investigation revealed that all bolts were located in high neutron irradiation fluence and high temperature regions and some of them were in high stress region. The cracks were observed at the bolt head-shank interface (Figure 11). The cracking was attributed to Irradiation Assisted Stress Corrosion Cracking (IASCC) [5].

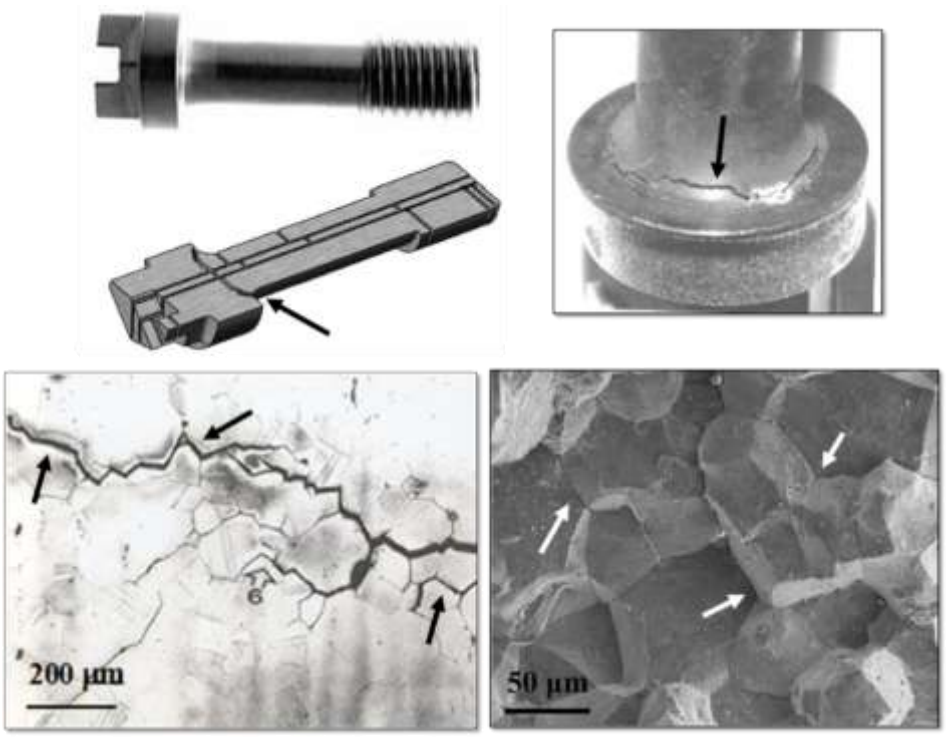

Figure 11: Intergranular cracks (indicated by arrows) observed on the neutron irradiated baffle former bolts of the PWRs [source EDF].

Since then, such incidents have occurred in a number of plants in France, Belgium, Japan and United States (Figure 12) [6]. To address this problem, standard utilities strategy is to replace the bolts found cracked during inspection. Although the integrity of internals can be maintained by about 1/3 of the bolts (from a total of 960 bolts), the maintenance time and cost optimization during inspections has led operators to become interested in the IASCC issue. Besides bolt replacement, mitigation strategies have been adopted to resolve the problem which includes changing the direction of coolant flow[1] from "down flow" to "up flow" in order to suppress the difference of pressure on each side of the baffle plates, making a provision to cool the bolts (i.e. making holes in the bolts to allow a water flow on the bolt shaft) and modifying the head to shank design to reduce the stress concentration (Figure 13) [7, 8]. These provisions, have contributed to strongly reduce the cracking for now. However, with the plans to extend the lifetime of reactors, it is important to anticipate if the onset of cracking due to IASCC could occurs for higher doses. Hence, an extensive R&D is essential to understand the IASCC mechanisms that could cause cracking of the bolts.

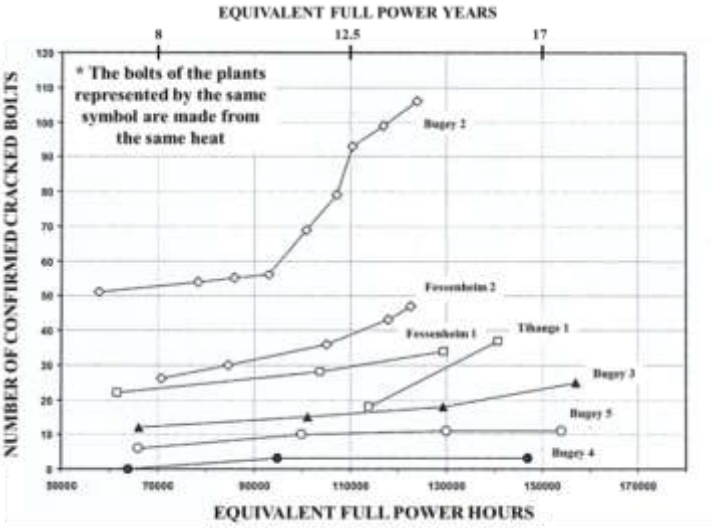

Figure 12: Summary of the inspection results for baffle bolts of CP0 PWRs that have been confirmed detective [6].

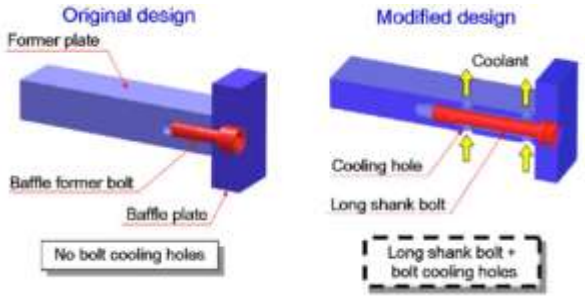

Figure 13: Few modifications incorporated in the design of baffle bolts to suppress cracking in PWR environment [7].

[1] Bypass flow of coolant though the space between the core barrel and core baffle plates. This bypass flow cools these components as they are subjected to significant gamma heating.

IASCC is the irradiation enhanced or induced intergranular stress corrosion cracking of the material. It is a complex phenomenon that occurs with the combination of several factors (Figure 14).

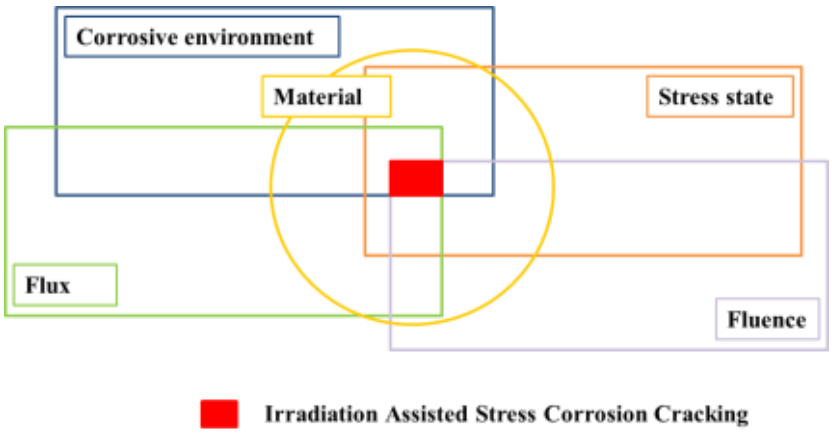

Figure 14: Venn diagram of the factors contributing to the Irradiation Assisted Stress Corrosion Cracking of the material [3].

Irradiation with neutrons leads to the production of point defects, point defect clusters, and transmutation products. The rearrangement of these defects results in the formation of observable defects in microstructure (such as, Frank loops, cavities), Radiation Induced Segregation (RIS) and precipitation (such as Ni_3Si). These changes in microstructure, in consequence, alter the mechanical properties of the material [9 – 11]. Prominent increase in yield strength and decrease in ductility with irradiation have been reported for austenitic stainless steel. A critical fluence threshold of ~2 $\times 10^{25}$ n/m² (≈ 3 dpa[2]) to cracking has been proposed below which 304 SS and 316 SS are considered immune to IASCC in PWRs. Previously, this enhancement of cracking with irradiation was believed to be caused due to depletion of chromium at the grain boundaries with irradiation. However, it is now strongly inferred based on post irradiation annealing studies that grain boundary segregation is not the sole contributor [13]. In fact, several factors (such as irradiation hardening, irradiation induced microstructure, etc.) have been identified to contribute to IASCC and efforts should be made to account for the major contributor. Recent studies based on proton irradiation have evidenced localization of deformation to have the maximum correlation with IGSCC [14]. Irradiation changes the deformation mode from homogeneous (where many slip systems are active) to heterogeneous (where dislocation channels are formed leading to the localization of the deformation). In other words, irradiation modifies the microstructure, mechanical properties and deformation mechanism of material, but these changes are not sufficient for initiating IGSCC. Some studies [15, 16] have reported to observe intergranular cracking in highly irradiated stainless steel in the absence of corrosive environment but others have reported to observe no cracking in irradiated material (to lower dose) deformed in

[2] Using the conversion factor of 1 dpa = 7 × 10^{24} n/m² (for PWR neutron spectra and E > 1 MeV) based on a displacement energy of 40 eV as recommended in ASTM E 521 – 89 [12] for stainless steels.

argon and intergranular cracking on the same material (for the same amount of deformation and irradiation) when deformed in PWR environment [17]. This suggests that embrittlement of grain boundary is necessary which could either be achieved via RIS in highly irradiated material or via oxidation. This implies the necessity to study the of role corrosive environment in enhancing the propensity of the material to intergranular cracking.

Exposure of austenitic stainless steel to aqueous medium leads to formation of duplex oxide layer namely, outer layer and inner layer. The thin protective inner oxide layer commonly called "passive film" makes it highly corrosion resistance even in aqueous medium [3]. Irradiation induced defects, however, have been shown to modify the oxidation kinetics of the material. Perrin et al. observed that irradiation resulted in formation of a thinner and more protective inner layer [18]. On contrary, Fukuya et al. [19] observed an increase in inner layer thickness with neutron irradiation. These conflicting results indicate that the effect of irradiation on oxidation kinetics is still poorly understood. It has been proposed that the embrittlement of the grain boundaries is necessary for cracking which could either be provided by the corrosive environment or by RIS induced by high irradiation doses or by the combination of two. This suggests that it is as important to understand the effect of irradiation on oxidation (and correlating it to cracking) as it is to understand the effect of irradiation on deformation mechanism.

Apart from the irradiation, another dominating parameter is the stress state. Baffle-former bolts begin their service history with a design preload that induces stresses in the bolts in the elastic range of the unirradiated material. During their lifetime, they might further experience different types of stresses [4]:

1. Thermally induced stress, induced by thermal expansion of the material or by a thermal gradient
2. Stresses induced by the pressure difference between the surfaces inside and outside the baffles[3].
3. Irradiation relaxation.
4. Void swelling of baffles.

These stresses when coupled with PWR corrosive environment could result in intergranular SCC of the austenitic stainless steel which otherwise was considered as immune to SCC. A stress threshold for crack initiation has also been proposed based on the constant load SCC initiation tests conducted in simulated PWR environment on irradiated austenitic steel. For materials irradiated to 10 dpa, a threshold of 50 % of the yield strength was proposed suggesting below this value no initiation occurs [20]. These curves are updated timely by adding new information on crack initiation data. But a better correlation can only be obtained with a better understanding of IASCC mechanism.

[3] These stresses have been suppressed by changing the direction of coolant from “down flow” to “up flow”.

Work hardening that could be induced during fabrication or mounting of the bolts has been shown to enhance the cracking susceptibility of unirradiated austenitic steels in PWR environment [21]. In their recent study, Courant et al. [22] revealed that the strain path has an influence on cracking susceptibility of unirradiated austenitic stainless steel in PWR environment. They observed higher cracking susceptibility under dynamic deformation conditions (such as Slow Strain Rate Test) compared to static deformation conditions (such as constant loading). Their results show that the change in strain path can enhance the strain concentration at grain boundaries which results in increase in susceptibility to cracking. Though effect of work hardening and dynamic strain paths on cracking susceptibility of unirradiated austenitic stainless steel has been studied but lack of data implies further investigation required for the better understanding. Besides, there is no information on the effect of strain path and work hardening on irradiated austenitic stainless steel. From structural analysis, it is inferred that the irradiated baffle former bolts are subjected to transient loading conditions in PWRs, especially during the startup and shut down of the reactor. Hence, the impact of these transient loading conditions on the cracking susceptibility of irradiated austenitic stainless steels is of interest to IASCC understanding.

In conclusion, several studies and research programs have been conducted to handle the problem of IASCC since its first observation. These studies have served as the preliminary steps towards the understanding of various factors influencing the extent of cracking. Still, several questions required to be solved to ameliorate the present understanding of degradation mechanisms, prediction of their evolution and to explore the possibility of new (and important) contributing factors.

Objectives of this study

Understanding of IASCC mechanism requires correct interpretation of the impact of all potential contributors individually and in combination. It is difficult to obtain all information from a single study but can be achieved by focusing few parameters at a time. This study aims to focus on some of the open questions related to the impact of irradiation induced microstructure and strain paths on intergranular cracking susceptibility of austenitic stainless steel.

As neutron irradiation is time consuming and expensive, ion irradiation (proton and iron irradiation) was used in this study to surrogate the effect of neutron irradiation. Moreover, observation of comparable threshold fluence for IASCC susceptibility for both, in service core component cracking and during ex-situ post irradiation slow strain rate SCC testing, has suggested that while in situ effects such as radiolysis are potential contributing factors, only persistent radiation effects (material changes) are sufficient to reproduce high IASCC susceptibility. And hence, post irradiation tests in PWR environment were conducted in this study.

Solution Annealed 304L was used in this study due to its higher susceptibility to IGSCC and simpler initial microstructure compared to CW 316. To achieve the objective, a specific methodology was developed which included microstructural characterization pre and post to irradiations, followed by mechanical loadings in PWR environments and surface characterizations post to the mechanical loadings.

For ease of comprehension, results are summarized in five chapters. The first chapter is a bibliographic review which will give an introduction to SCC and IASCC. It will provide a synopsis on what is known so far including the recent results and questions which still remain open. It will help to develop a basic understanding of the problem.

Second chapter will provide information on the (initial) reference state of the material used which will include the initial microstructure and mechanical properties of SA 304L. Along with it, the conditions of irradiations conducted (proton and iron irradiations) will be summarized. Post irradiation, microstructure characterized using TEM and mechanical properties estimated using different mechanical tests will help to provide a comparison of the reference state and post irradiation state. Comparison with literature will also be provided.

In the third chapter, impact of irradiation induced defects on the cracking susceptibility will be studied. Based on the results of the Slow Strain Rate Tensile (SSRT) tests conducted on the irradiated materials in different (PWR and argon) environment, influence of ion irradiations on cracking susceptibility of material was estimated. To correlate the differences observed, impact of different ion irradiations (proton and heavy ions) on degree of localization and bulk oxidation

will also be discussed. In the last part, criteria proposed in literature for cracking in BWR environment was verified for cracking observed in ion irradiated SA 304L in PWR environment.

Fourth chapter will present the result of surface state cracking susceptibility of the austenitic steel. In this chapter, two different surface finishes (with and without surface hardened zone) will be studied and compared. Comparison will also include the impact of surface state on the localized deformation and bulk oxidation of irradiated material with different surface finishes.

In the last chapter, impact of loading path on the cracking susceptibility of iron irradiated austenitic steel will be outlined. This chapter will summarize the results of two different loading conditions namely, Cyclic loading and Constant loading, conducted on iron irradiated 304L SS samples in PWR environment. Surface characterization done post to the loadings will illustrate the difference in cracking susceptibility and localized deformation for different loading paths.

At the end conclusions of all these results will be given along with some future prospective.

REFERENCES

1. B. Tanguy, F. Sefta, P. Joly, "Le vieillissement des internes de cuve. Programme de recherche", Revue Générale du Nucléaire, in the proceedings of la durée de functionnement des reacteurs REP, Revue Nucleaire, 3 (2015) 56 – 63.
2. B. Tanguy, "Corrosion sous contrainte assiste par l'irradiation des aciers austénitique (IASCC) ", Revue de Métallurgie 108 (2011) 39 – 46.
3. D. Féron, E. Herms, B. Tanguy, "Behavior of stainless steel in pressurized water reactor primary circuits", J. Nucl. Mat. 427 (2012) 364 – 377.
4. T. J. Griesbach, G. J. Licina, P. C. Riccardella, J. R. Rashid, R. E. Nickell, "A probabilistic approach to baffle bolt IASCC prediction", in the proceedings of 3rd International conference on nuclear power plant life management (PLiM) for long term operations (LTO), (2012).
5. E. Wachi, J. Nishitani, K. Okimura, "Maintenance technology and its applications for PWR plants", in the proceedings of 3rd International conference on nuclear power plant life management (PLiM) for long term operations (LTO), (2012).
6. P. M. Scott, M.-C. Meunier, D. Deydier, S. Silvestre, A. Trenty, "An analysis of baffle/former bolt cracking in French PWRs", Environmentally Assisted Cracking: Predictive methods for risk assessment and evaluation of materials, equipment and structures, ASTM STP 1401, R.D. Kane, Ed., American society for testing and materials, (2000).
7. K. Ikeda, T. Ishikawa, T. Miyoshi, T. Takagi, "Reactor core internals replacement of Ikata units 1 and 2", in the proceedings of 3rd International conference on nuclear power plant life management (PLiM) for long term operations (LTO), (2012).
8. R. Gérard, D. Bertolis, S. Vissers, "Aging management of the reactors internals in Belgian nuclear units in view of Long Term Operations", in the proceedings of 3rd International conference on nuclear power plant life management (PLiM) for long term operations (LTO), (2012).
9. G. Was, "Fundamentals of Radiation Materials Science: Metals and Alloys", Springer, (2007).
10. S.M. Bruemmer, E.P. Simonen, P.M. Scott, P.L. Andersen, G.S. Was, J.L. Nelson, "Radiation induced material changes and susceptibility to intergranular failure of light water reactor core internals", J. Nucl. Mat. 274 (1999) 299.
11. O.K. Chopra, A.S. Rao, "A review of irradiation effects on LWR core internal materials – IASCC susceptibility and crack growth rates of austenitic stainless steels", J. Nucl. Mat. 409 (2011) 235 – 256.
12. "Standard practice for neutron radiation damage simulation by charged particle irradiation", ASTM Designation E 521-89, Annual Book of ASTM Standards, vol. 12.02, American Society for Testing and Materials, (1989).

13. J. T. Busby, G. S. Was, E. A. Kenik, "Isolating the effect of radiation induced segregation in irradiation assisted stress corrosion cracking of austenitic stainless steels", J. Nucl. Mat. 302 (2002) 20 – 40.
14. W. Karlsen, G. Diego, B. Devrient, "Localized deformation as a key precursor to initiation of intergranular stress corrosion cracking of the austenitic stainless steels employed in nuclear power plants", J. Nucl. Mat. 406 (2010) 138-151.
15. K. Fukuya, M. Nakano, K. Fujii, T. Torimaru, "IASCC susceptibility and slow tensile properties of highly irradiated 316 stainless steels", J. Nucl. Sci. and Tech. 41 (2004) 673 – 681.
16. C. Bailat, F. Gröschel, "Deformation mode of proton and neutron irradiated stainless steels", J. Nucl. Mat. 276 (2000) 283 – 288.
17. Z. Jiao, G. S. Was, "Impact of localized deformation on IASCC in austenitic stainless steels", J. Nucl. Sci. and Tech. 408 (2011) 246.
18. S. Perrin, L. Marchetti, C. Duhamel, M. Sennour, F. Jomard, "Influence of irradiation on the oxide film formed on 316 L stainless steel in PWR Primary water", Oxidation of Metals 80 (2013) 623 – 633.
19. K. Fukuya, H. Nishioka, K. Fujii, Y. Kitsunai, "Characterization of surface oxides formed on irradiated stainless steels in simulated PWR primary water", in proceedings of Fontevraud 8 International Symposium: Contribution of Materials Investigations and Operating Experience to LWRs' Safety, Performance and Reliability, Avignon (2014).
20. S. Fyfitchl, H. Xu, P. Scott, L. Fournier, A. Demma, "Criteria for initiation of Irradiation Assisted Stress Corrosion Cracking in stainless steels in PWR systems", in the proceedings of 14th international conference on Environmental degradation of materials in nuclear power systems, (2009).
21. O. Raquet, E. Herms, F. Vaillant, T. Couvant, "SCC of cold worked austenitic stainless steels in PWR conditions", Advances in materials science 7 (2007) 33 – 45.
22. T. Couvant, F. Vaillant, J. M. Boursier, D. Delafosse, "Effect of strain-path on stress corrosion cracking of AISI 304L stainless steel in PWR primary environment at 360°C", in Proceedings of Eurocorr (2004).

CHAPTER 1. LITERATURE SURVEY

1.1. INTRODUCTION

Austenitic stainless steel is the structural material used to fabricate the core internals of a Pressurized Water Reactor (PWR). Not only it has good mechanical properties but it is highly corrosion resistant in many varied corrosion conditions without the need for additional protective measures [1]. As core components are designed to stay in the reactor for the lifetime, these two qualities of austenitic stainless steel makes it an optimum choice. During their service lifetime, they are exposed to a corrosive environment which consists of demineralized water (with some traces of B, Li and H) maintained at high temperature range (280 – 340 °C) and pressure of 155 bars. Though austenitic stainless steel is corrosion resistant in hydrogenated water, some recent studies [2, 3, 4] have shown that high amount of cold working (e.g. due to improper manufacturing) and subjection to dynamic loadings can make it vulnerable to Stress Corrosion Cracking (SCC). In a PWR, some of the core internals are cold worked and are subjected to constant loads with sudden and sharp load transient. Under extreme conditions, the conditions used in above studies can be a representative of the actual scenario. Besides, the core components are in close vicinity to reactive core and hence, are subjected to severe neutron damage. Irradiation is known to enhance (and/or induce) the SCC susceptibility of material. This special form of corrosion is called Irradiation Assisted Stress Corrosion Cracking (IASCC).

IASCC is a materials degradation phenomenon which has been known to affect the lifetime of core internals such as baffle-former bolts (BFBs). It can also lead to increase in duration and cost of maintenance operation of these internals, therefore, has come up as one of the main concerns for the presently working PWRs. IASCC results from the coupling of various factors namely, susceptible material, stress state, irradiation and corrosive environment (Figure 1-1) [5]. Elimination of either of these factors can highly reduce or suppress IASCC.

Several incidents of IASCC have been reported to occur in both BWR (Boiling Water Reactor) and PWRs. Based on the experience with Intergranular stress corrosion cracking (IGSCC) of non-irradiated stainless steel in BWR water environment, information on radiation induced microstructure and microchemistry, Bruemmer et al. [6] proposed a schematic (Figure 1-2) illustrating the mechanistic issues believed to influence crack initiation and propagation during IASCC of austenitic stainless steel in Light Water Reactors (LWRs).

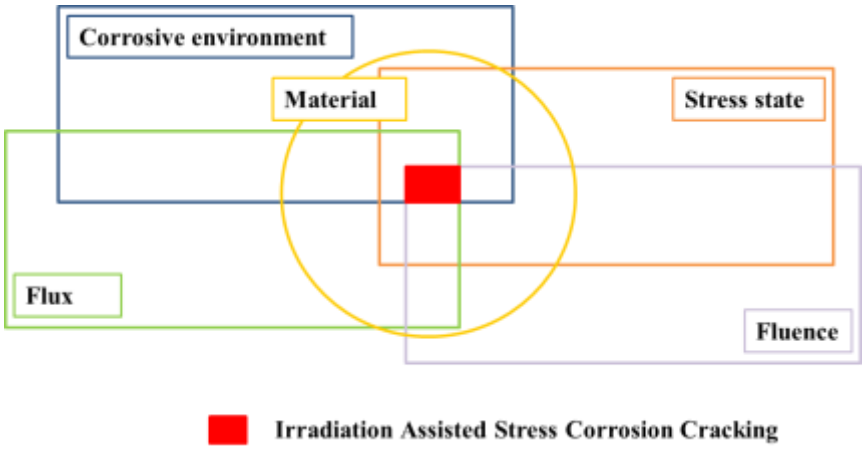

Figure 1-1 : Venn diagram to represent the different factors contributing in the IGSCC of material [25].

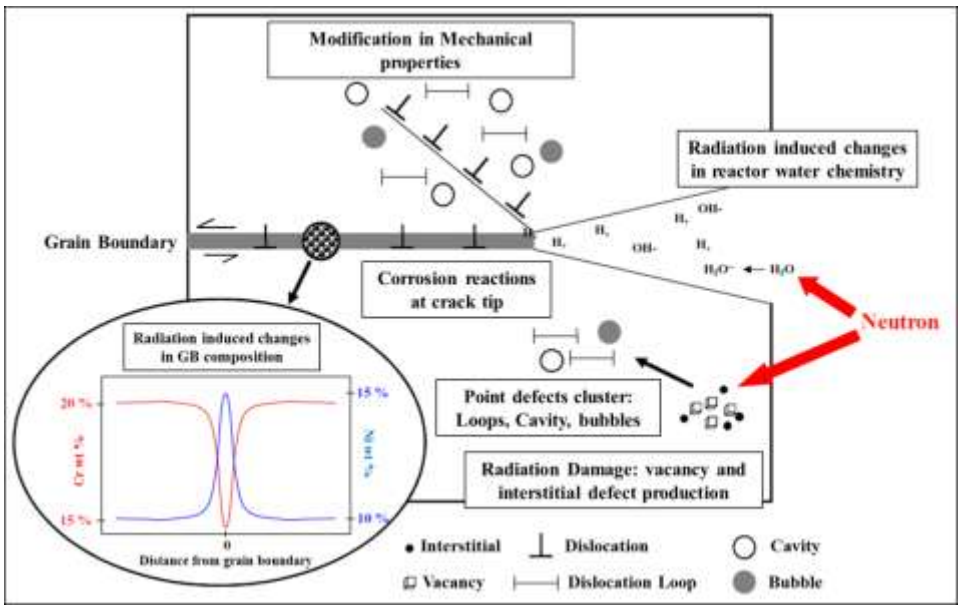

Figure 1-2 : Schematic depicting all possible mechanistic issues believed to influence crack advance during IASCC of austenitic stainless steels in LWRs [6].

However the processes dominating SCC mechanism (and hence, IASCC) in PWR and BWR environments are different. For example, the increase in quantity of dissolved oxygen and depletion of chromium at the grain boundaries can efficiently explain the SCC of austenitic steel in BWR environment but these are not sufficient conditions in PWR environment. Hence, further work is required for better understanding of the IASCC phenomenon in PWR environment.

Nevertheless, the schematic depicts the complex coupling of the various parameters which makes the comprehension of the IASCC phenomenon very difficult. And hence, despite of the enormous research and efforts in this field, the basic phenomenon of IASCC is still unclear. It is inevitably necessary to assess the impact of each of these

parameters, individually as well as when coupled, on IASCC for the comprehension. Going with this approach, this chapter will first summarize the SCC susceptibility of the unirradiated material which will cover the importance of each contributing parameters as well as different conditions or requirements which are known to enhance/suppress the cracking. In second part, contribution of irradiation over several parameters will be illustrated and at the end mechanisms that have been proposed so far to describe the occurrence of IASCC in PWR environment will be provided.

This study will be restricted solely to degradation (with main focus on crack initiation) of austenitic stainless steel in PWR corrosive environment.

1.2. SCC OF AUSTENITIC STAINLESS STEEL IN PWR ENVIRONMENT

Stress Corrosion Cracking (SCC) is a corrosion phenomenon leading to the crack initiation under the influence of tensile loading and corrosive environment. All the three conditions; a susceptible material, a tensile stress component and a corrosive environment (Figure 1-3) must be present simultaneously for SCC to occur and propagate. The elimination or reduction of any one of these three factors below some threshold level can prevent SCC [7].

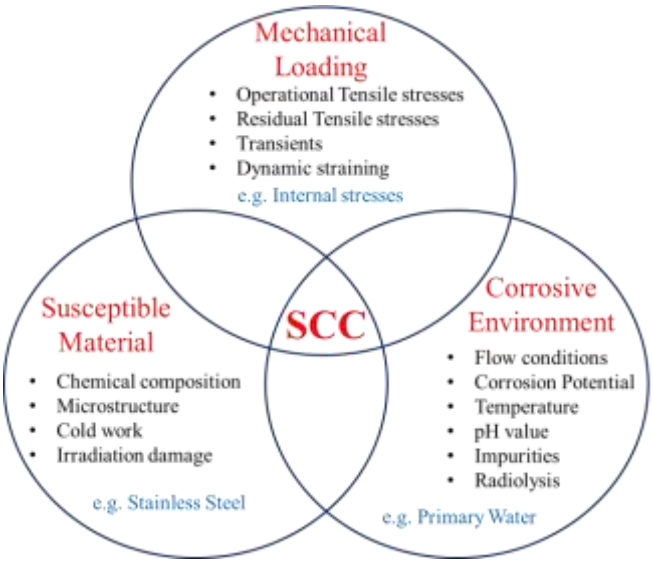

Figure 1-3 : Conditions necessary for Stress Corrosion Cracking (SCC) [7].

The susceptible material here is the austenitic stainless steel and the corrosive environment it experiences in PWR consists of the demineralized primary water which is maintained at high temperature range (280 – 340 °C) and pressure of 155 bars during the reactor operation. It contains small traces of boron (1000 ppm B), lithium (2 ppm Li) and

dissolved hydrogen (25 – 35cc/kg H_2 STP[4]). Boron is added in the form of boric acid (H_3BO_3 or $B(OH)_3$) and is used as neutron poison (or neutron absorber) to slow down the fission reaction rate. Lithium is added, in the form of lithium hydroxide (LiOH), to balance the pH of the coolant around 7. Hydrogen is added to prevent the radiolysis of water that produces oxidative chemical species. This also maintains a low corrosion potential (< – 500 mV_{SHE}[5]). Though 304L and 316L austenitic stainless steels don't readily corrode in such conditions, some recent studies [2, 3] have shown that high amount of cold working in combination with dynamic loading in PWR primary water environment can make them vulnerable to SCC.

Before detailing the SCC mechanism of material known so far, it is therefore necessary to have some insight on the possible effects of individual offenders (susceptible material, oxidation and stress state).

1.2.1. SUSCEPTIBLE MATERIAL

Stainless steel is essentially a low carbon steel which contains a minimum of 12 wt. % chromium. Depending on their crystalline structure stainless steels are classified as: austenitic, ferritic, martensitic, duplex and precipitation hardening martensitic. Austenitic stainless steel is the most common and familiar type of stainless steel. As name suggests, it crystalizes in Face Centered Cubic (FCC) system and usually contains between about 16 and 25 % chromium. This high chromium (Cr) content gives them their excellent corrosion resistance [8]. Besides Cr, the other alloying elements that a commercial grade stainless steel contains are nickel, manganese, tungsten, molybdenum, carbon, vanadium and silicon. These secondary elements can drastically alter some of the properties of these steels such as enhanced weldability and formability. Austenitic stainless steel also benefit from very high ductility and toughness. Their excellent corrosion resistance and good mechanical strength made them the prime choice as the structural material in PWRs.

The alloying elements can be divided into two groups: alpha-genic elements such as Cr, Si and Mo which promotes ferrite (Body Centered Cubic) phase formation and gamma-genic elements such as Ni, C or N promotes austenite (FCC) phase. It is the combination of nickel and chromium that allows the austenitic stainless steel to be FCC from absolute zero to the melting point. Carbon is an interstitial alloying element. As a result it can diffuse rapidly through the structure and concentrate on the grain boundaries. A detrimental effect of this is precipitation of chromium carbide. Formation of chromium carbide ($Cr_{23}C_6$) at grain boundaries depletes the grain boundaries of chromium, thus

[4] STP stands for Standard Temperature and Pressure
[5] Volts against the Standard Hydrogen Electrode (SHE).

decreasing the corrosion resistance and enhancing susceptibility of material to localized (intergranular) corrosion at the grain boundaries. Other secondary phases that have been reported frequently to occur in austenitic stainless steel (due to addition of alloying elements) are:

1. $M_{23}C_6$ – it is the most widely observed precipitate and occurs as a result of heating solution annealed SSs to 500 – 950°C.
2. M_6C – it is usually observed in the grades containing molybdenum or niobium additions on heating to 600°C. They usually precipitate intergranularly.
3. MC – it is a very stable precipitate and is usually observed in steels containing titanium or niobium.
4. η (Laves) – it forms after long term high temperature (650 – 900°C) exposure of steel. It precipitates intergranularly and exists as globular particles [8, 9].

In addition to these phases, the orthorhombic M_7C_3 carbide can occur in austenitic SS with higher bulk carbon content, e.g. mass fraction of 0.3-0.6% [8, 9]. To avoid the formation of these precipitates, and achieve a stable microstructure, austenitic stainless steels are solution heat treated and annealed at controlled temperatures followed by rapid quenching.

Austenitic stainless steels are metallurgical simple alloys. They are either 100% austenite or austenite with a small amount of ferrite in the form of delta ferrite. Delta ferrite forms during solidification of austenitic stainless steel and is retained in the structure at room temperature. Based on the composition of alloy, the amount of delta ferrite in the material can be estimated using Schaeffler – DeLong diagram (Figure 1-4). The Schaeffler – DeLong diagram divides the alloying elements into two groups, namely ferrite and austenite stabilizers, whose effects could be predicted by formulas of chromium and nickel equivalent, respectively. The intersection point of chromium and nickel equivalent on the diagram provides the information on the amount and type of phases present in the alloy. The delta ferrite transforms to intermetallic phases, notably sigma phase, faster than austenite during high temperature services. Sigma phase is very brittle and hence has a deleterious effect upon mechanical properties (such as decrease in ductility and increase in potential for fracture). Higher the amount of delta ferrite a nominally austenitic stainless steel has, the more vulnerable it will be to sigma phase formation which will lead to decrease in ductility and increase in potential for fracture. And hence, amount of delta ferrite is usually controlled (preferably below 10 %) in material [10].

Austenitic stainless steels are generally stable at room temperature and will only form martensite upon cooling to subzero temperatures. The spontaneous martensite transformation starts at the temperatures below M_s given by:

$$Ms\ (°C) = 502 - 810 \times (C\%) - 1230 \times (N\%) - 13 \times (Mn\%) - 30 \times (Ni\%) - 12 \times (Cr\%) - 54 \times (Cu\%) - 46 \times (Mo\%) \quad \text{..... (I.1)}$$

where, the concentration is in mass % [11].

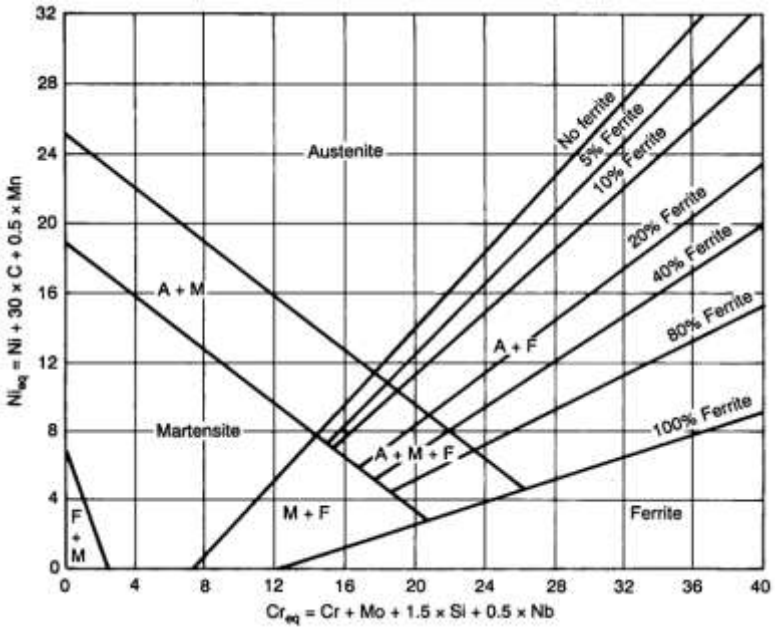

Figure 1-4 : Schaeffler – DeLong diagram [1].

1.2.1.1. GRADES 304L AND 316L OF AUSTENITIC STAINLESS STEEL

Depending on different weight percentage of different alloying elements, several variants of austenitic stainless steel exists. The most common amongst them are 304 SS and 316 SS. Majority of the core internals of a PWR are, indeed, made of Solution Annealed (SA) 304L and Cold worked (CW) 316L. The cold worked material is dominated by high density dislocations and deformation twins compared to solution annealed state. The letter L is used with these grades (e.g. 304L) when the carbon content in these grades is lower than 0.03 wt. %. The composition of the two grades as per the ASTM standard is given in Table 1-1 [12].

Material	Cr	Ni	Mo	Si	Mn	C	P	S	Fe
SS 304L	18 – 20	8 – 12	< 2	< 1	< 2	< 0.03	0.045	0.3	Bal.
SS 316L	16 – 18	10 – 14	2 – 3	< 1	2	< 0.03	0.045	0.3	Bal.

Table 1-1 : Chemical composition (in wt %) of 304L and 316L austenitic stainless steel as per ASTM standards [12].

The minimum mechanical properties (at room temperature) requisite by ASTM for 304L and 316L are given in Table 1-2 below [12]. They exhibit good mechanical properties.

Material	Yield strength, $\sigma_{0.2\%}$ (in MPa)	Ultimate tensile strength, σ_{UTS} (in MPa)	% elongation
SS 304L	170	485	40
SS 316L	170	485	40

Table 1-2 : Mechanical properties (minimum values) of 304L and 316L austenitic stainless steel at room temperature as per ASTM standards [12].

1.2.1.2. DEFORMATION MODES OF AUSTENITIC STAINLESS STEEL

The most common modes of deformation observed in austenitic stainless steel upon plastic deformation are [13]:

1. Slip
2. Twinning
3. Deformation induced martensite transformation

The deformation process can induce the formation of α' martensite (i.e. $\gamma \rightarrow \alpha'$) in the austenitic stainless steel which means that for temperatures above M_s, deformation will contribute to initiate transformation. The amount of deformation induced martensite is dependent on various factors such as material composition, temperature, deformation mode, etc. Angel et al. [14] studied the dependence of temperature with composition for different steels and provide following formula (eq. I.2) to estimate the M_{d30} temperature which corresponds to the temperature at which 50 % α' martensite is present after a tensile deformation of 30 %.

$$M_{d30}\,(°C) = 413 - 462 \times (C\% + N\%) - 9.2 \times (Si\%) - 8.1 \times (Mn\%) - 9.5 \times (Ni\%) - 13.7 \times (Cr\%) - 18.5 \times (Mo\%) \quad \text{(I.2)}$$

where, the concentration is in mass % [14].
The martensite is harder and stronger than austenite and hence, the increase of α' martensite causes a change in physical properties of austenitic stainless steels.

Out of twinning and slip deformation, the deformation mode material will predominantly adopt is dependent on the stress state, temperature and the strain rate. For high strain rates and/or low temperatures, twinning is dominant while for low strain rates and/or high temperatures slip dominates [15, 16]. In fact slip is by far the most common mechanism and occurs by dislocation glide within a slip plane. Slip could either be planar or cross slip and is dependent on the stacking fault energy (SFE) of the material. SFE is a material property and can be estimated using Pickering's formula [10]:

$$\text{SFE}\left(\frac{\text{mJ}}{\text{m}^2}\right) = 25.7 + 2 \times (\text{Ni}\%) + 410 \times (\text{C}\%) - 0.9 \times (\text{Cr}\%) - 77 \times (\text{N}\%) - 13 \times (\text{Si}\%) - 1.2 \times (\text{Mn}\%) \quad \text{(I.3)}$$

Due to slight differences in chemical compositions, 304L and 316L have different stacking fault energies. In general, 304 SS has a SFE in the range of about 17 – 26 mJ/m² which is slightly lower than that of 316 SS (25 – 64 mJ/m²) [17]. The SFE for these austenitic stainless steels belong to Low SFE category. Hence, they exhibit planar slip which is characterized by the evenly spaced slip bands. Slip occurs on {111} planes along <110> directions. In a FCC crystal structure, there are 4 {111} octahedral planes and 6 <110> directions in each octahedral plane resulting in a total of 24 slip planes for dislocation movement. Due to geometrical symmetry, number of slip planes can be reduced to 12 (Table 1-3).

Slip systems	1	2	3	4	5	6	7	8	9	10	11	12
Slip planes	(111)			$(1\bar{1}1)$			$(\bar{1}11)$			$(\bar{1}\bar{1}1)$		
Slip direction	$[\bar{1}01]$	$[0\bar{1}1]$	$[\bar{1}10]$	$[\bar{1}01]$	[011]	[110]	$[0\bar{1}1]$	[110]	[101]	$[\bar{1}10]$	[101]	[011]

Table 1-3 : Slip systems possible in austenitic stainless steel (FCC) [18].

Deformation in stainless steel is very heterogeneous and these numerous slip planes available for dislocation movement combined with low level of interstitial elements give these materials their good ductility. However, this mode of deformation could be responsible for intergranular cracking of the material because of the high stress concentrations produced between a grain boundary and an impinging slip band [19]. Thompson [20] also has suggested an inverse relation between the SCC susceptibility and SFE. This suggests that the austenitic stainless steel is indeed vulnerable to SCC.

1.2.2. CORROSIVE ENVIRONMENT

In general, exposure of austenitic stainless to aqueous medium results in the formation of a thin protective oxide layer (called passive layer) which imparts high corrosion resistance to the steel. In conditions close to that of PWRs, however, formation of duplex oxide layer (i.e. outer and inner oxide layers) has been reported [21–24]. The inner layer has been reported to be a continuous layer rich in chromium which grows into the alloy surface. The outer layer is iron rich discontinuous, porous layer formed on the surface of the metal and grows outwards into the solution.

Though the composition of the oxide layer formed on austenitic stainless steel is very sensitive to the environment, majority of the studies agrees that the two oxide layers formed have a Me_3O_4 spinel type structure. The dominant composition for outer oxide is magnetite, Fe_3O_4 and AB_2O_4 in which Fe (III) is the main constituent for B and Fe (II) also takes the majority parts over Ni (II) for A. Inner layer is mostly chromite, Cr_2O_3 and AB_2O_4 where, Cr (III) is the main constituent for B and Fe (II) takes the dominant position against Ni (II) for A. In short, composition of outer and inner oxide can be summarized as: $(Ni_{1-x}Fe_x)(Fe_yCr_{1-y})O_4$, with x ,y > 0.5, and y can even be 1 for outer oxide; x > 0.5 and y < 0.25 for inner oxide [5, 25 – 26]. In addition to this duplex layer, nickel enrichment at the metal-oxide interface has been identified as well [24].

The corrosion experiments performed by Lister et al. [27] on 304 SS in high temperature lithium containing water proved that the formation of outer layer is bonded to the saturation of the medium and is inhibited in corrosion product free water. Besides, the inner layer, once formed, prevents the formation of the outer layer. These results led to the conclusion that the outer oxide crystallites are formed by the diffusion of the cations through the inner layer. Besides, there is a competition between dissolution and precipitation which governs the germination and growth of the outer oxide crystallites.

Terachi et al. [25] hypothesized that the inner layer is formed by anionic diffusion. This was later proven by Perrin et al. [23] using isotropic tracing method. But neither of them gave any information on the different phases of this process. Soulas [28] studied the evolution of the inner and outer oxide in the early stages of oxidation and provided the oxide layer formation mechanism as shown in Figure 1-5. The author proposed that the double oxide layer is formed within the first minute of oxidation. An increase in the thickness of the oxide layer and average crystallite size with exposure time to the PWR water has been reported (Figure 1-6a) [29]. During first 10 hours, oxide layer thickness increases sharply and reaches a first maximum. In next 14 hours, the dissolution and re-precipitation compete with each other so a decrease is observed in the curve. From 24 to 48 hours, the thickness of oxide layers increases sharply again. Afterwards, a dynamic balance between precipitation and dissolution is reached which stabilizes the growth of the oxide film.

Crystallographic orientation can have an influence on the nucleation and growth of the oxide (Figure 1-6b). Soulas [28] has proven that the crystallization of the inner oxide layer is faster and thickness of inner layer is utmost for the grain orientation [111] compared to [100] and [110]. The maximum outer oxide crystallites size reported was for grain orientation [110]. Besides grain orientation, grain size can influence the oxide layer nucleation and growth as well.

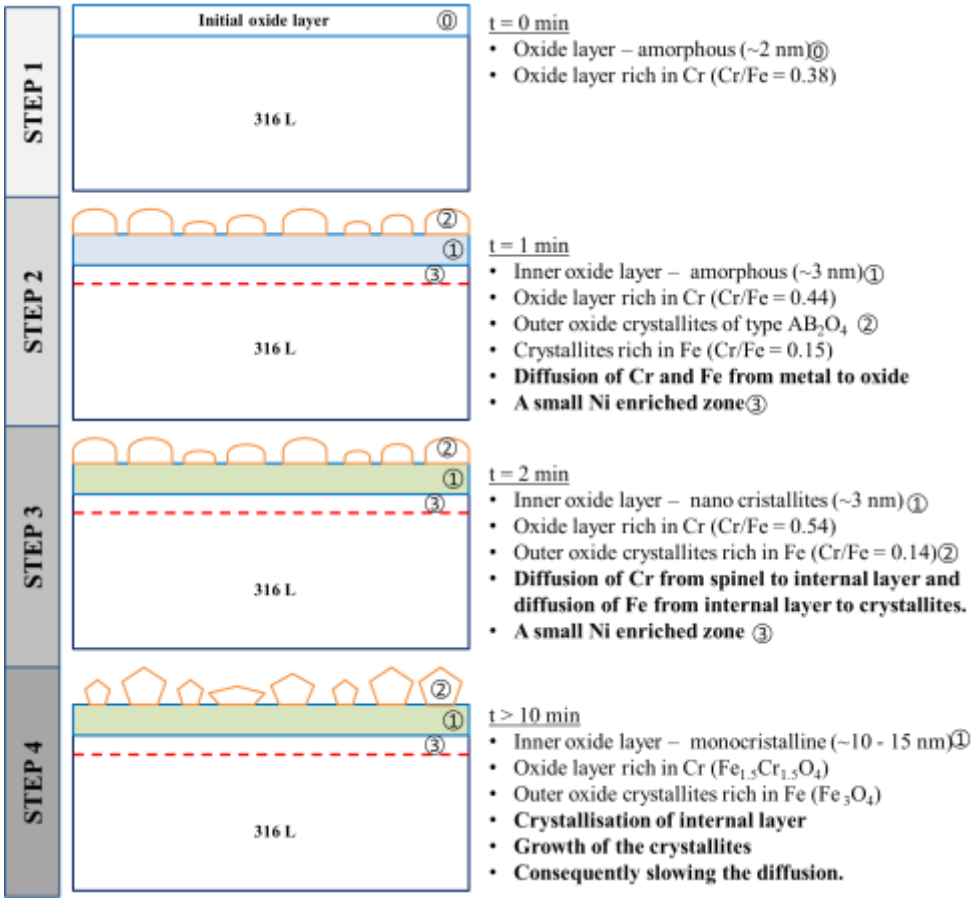

Figure 1-5 : Schematics representing the evolution of outer and inner oxide of 316 SS in PWR environment with time of exposure [28].

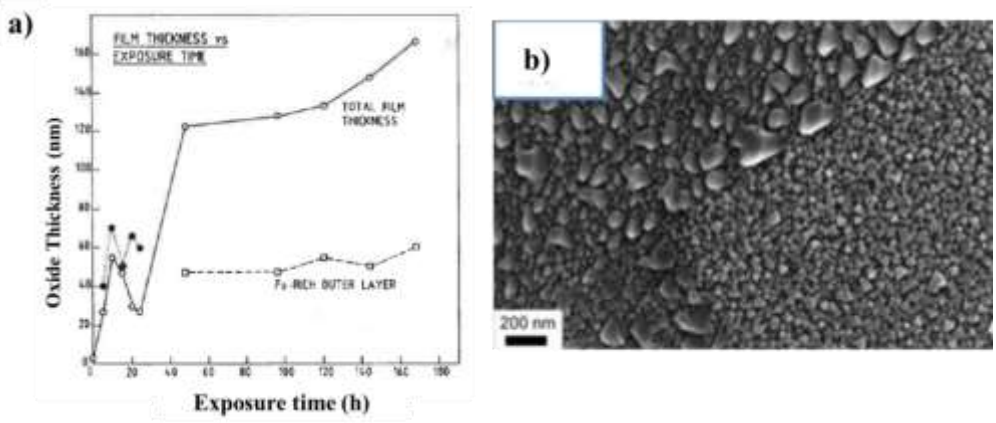

Figure 1-6 : a) Oxide thickness (for polished surface) plotted as a function of exposure time [29] b) effect of crystallographic orientation apparent on 316 L samples after an oxidation of 24 h in PWR environment [28].

- **Effect of surface preparation on oxide layer thickness**

Different surface state can result in different substructures in the metal beneath. For example, presence of recrystallized area has been reported in mechanically polished and

ground surfaces while no such area is present in samples electro polished. This recrystallized area consists of nano-grains and the area affected (depth of this zone) is dependent on the surface preparation. Cisse et al. [30] reported to observe oxide layers (outer and inner) relatively thinner for a rough surface (i.e. larger recrystallized area) compared to polished surface (Figure 1-7). The authors concluded that the larger recrystallized area results in larger number of grain boundaries which can enhance the flow of chromium in the inner layer and hence, leading to formation of a thinner and more protective inner layer. Similar results have been reported by other authors [31].

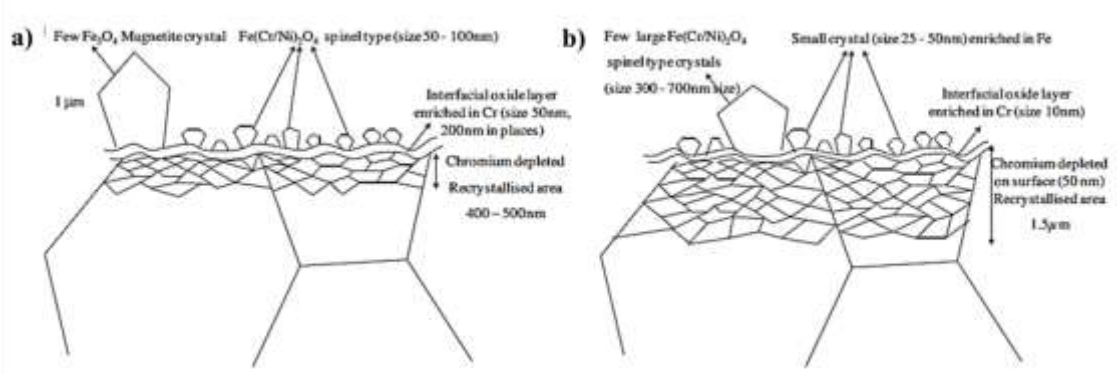

Figure 1-7 : Schematics illustrating the oxide formed on 304 L sample under simulated PWR primary water at 340 °C for 500 hours: a) polished surface b) ground surface [30].

Other factors such as chromium content of the alloy, lithium and boron concentration of medium, dissolved hydrogen content in medium, temperature and pH can influence the oxide formation as well but will not be discussed in this study. It is to be noted that the double oxide layer structure is maintained in each case; however, these factors just influence the thickness and effective protectiveness (Cr and Fe content) of the oxide layers.

- **Effect of strain on oxide layer thickness**

Herbelin et al. [32] used cross shaped SA 304 and SA 316 SS specimens loaded in simulated PWR environment to study the effect of strain on oxide layer growth. Cross shaped specimens helped to localize the strain during complex loading paths. An increase in oxide penetration with increasing deformation level was reported with a sharp increase around 10 % cumulated deformation. The author concluded that the preferential oxidation along the deformation structures was responsible for this increase. The increase in thickness of chromium rich layer can be interpreted as increasing susceptibility of material towards SCC with deformation.

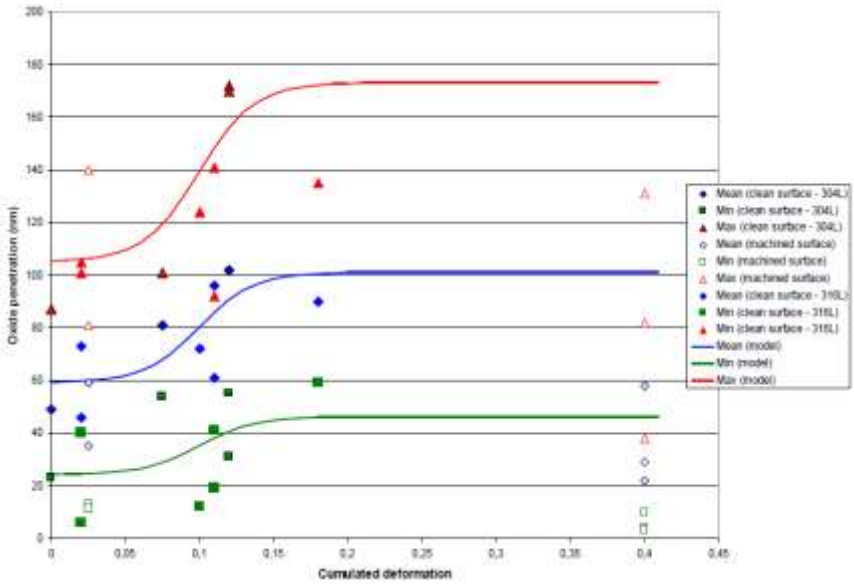

Figure 1-8 : Evolution of inner oxide thickness as a function of cumulated deformation [32].

1.2.3. SCC MECHANISM

SCC is a deceitful corrosion as it can bring a remarkable loss of mechanical strength with little metal loss. In consequence, the damage of SCC is not evident from inspection, but it can trigger mechanical fast fracture and catastrophic failure of components and structures.

It is characterized by intergranular and trans-granular cracks occurring in the same alloy, depending on the microstructure, the stress/strain state or the environment. For example, 304 SS can have trans-granular crack in boiling $MgCl_2$ at 154 °C and intergranular cracks in 288 °C water [33]. Considering PWR corrosive environment, SCC of austenitic stainless steel majorly leads to intergranular (IG) cracks in the material. Hence, only intergranular stress corrosion cracking (IGSCC) of austenitic stainless steel in PWR environment will be discussed. Development of IG cracks takes places in two steps: initiation and propagation. Cracking generally starts at local defects, which may arise from surface features (such as preexisting grooves, corrosion induced pits) or may be microstructural features (such as sensitization of material). After initiating, it develops through various stages of growth including: i) formation of multiple short cracks, ii) coalescence of these cracks and ultimately iii) generation of a dominant long crack leading to failure [34]. IGSCC usually propagates perpendicular to the principal tensile stress. Cracks can also vary in the degree of branching.

Understanding of the crack initiation phase is extremely important. However, the complexity of the process, trouble in defining the initiation phase and inability to distinct between initiation and propagation phase makes it a challenging task [33]. The crack tips

of active intergranular cracks have been main focus for the understanding of crack initiation while oxidation has been held responsible for the propagation of the cracks.

IGSCC is an electrochemical process involving oxidation and reduction with their thermodynamic tendency described by the Nernst equation. Several tests and experiments have been conducted on different materials and a wide range of conditions, yet no general model capable of predicting (quantitatively) IGSCC has been proposed. The most prominent models that are in general used in concern to IGSCC are active path IGSCC and the film rupture model [33]. In active path SCC model, it is hypothesized that the applied stress opens the crack tip exposing the fresh metal to dissolution which then causes preferential dissolution along the grain boundary. This theory suggests preferred dissolution occurs at slip planes and hence, plastic deformation enhances the susceptibility of material to corrosion. However, this theory also suggests that electrochemical dissolution at crack tip should result in blunting and not contribute in its advance. Hence, it is not valid theory for the propagation of IGSCC cracks observed. The second model, film rupture model is based on the rupture of protective oxide layer. This model suggests that under sufficient stress, the shear stress on properly oriented glide planes can either ruptures the protective layer formed on the material in aqueous medium or can damage it, thereby revealing the bare metal to corrosive medium. Exposure of bare metal will lead to formation of new passive layer which will again be ruptured by the applied stress. Crack will grow in discrete steps as the cycle repeats. Some mechanical failure models such as film induced cleavage, tarnish rupture model (or brittle film model), corrosion tunnel model, etc. have been proposed as well which explains cracking by mechanical fracture processes but these will not be discussed in this study.

Anderson [35] has proved that the film rupture model, also called slip dissolution model, can efficiently describe the intergranular crack propagation in austenitic stainless steel at PWR relevant conditions. Terachi et al. [24] investigated the stress corrosion behavior and in particular the crack tips of cold worked SUS[6] 316 SS in simulated PWR primary water post to a Constant Extension Rate Tensile test (CERT). They observed slip step like patterns (Figure 1-9) on the crack surface and concluded that slip phenomenon (such as grain boundary sliding) affect crack propagation, hence, slip dissolution model can be used to explain SCC in austenitic stainless steel in PWR environment.

[6] SUS stands for Steel Use Stainless and is an acronym for stainless steel from Japanese Industrial Standards (JIS)

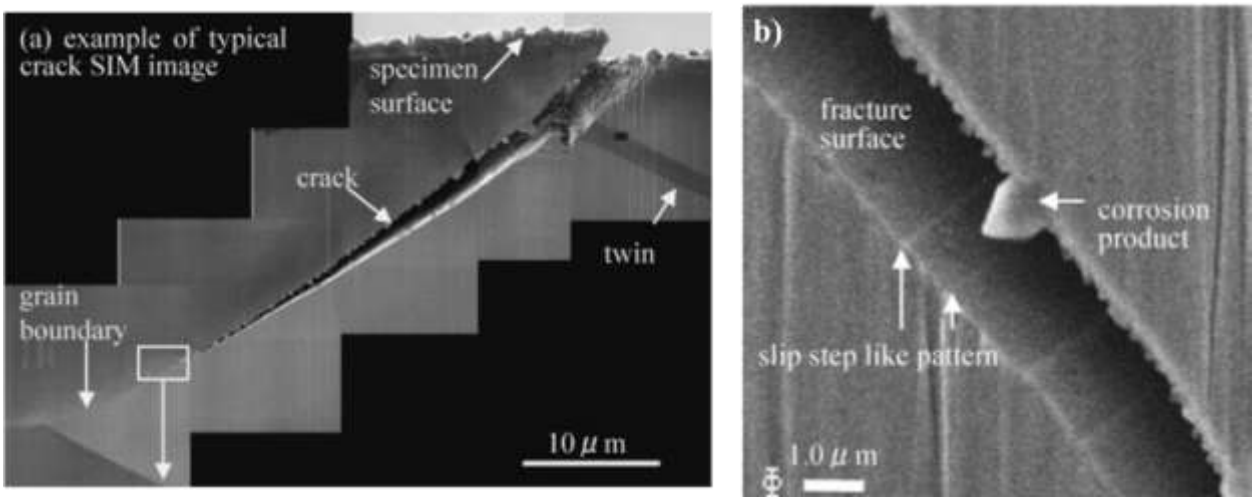

Figure 1-9 : SEM image of a) the crack observed b) zoomed image indicating the slip step like pattern observed in SUS 316 SS post to CERT in PWR environment [24].

1.2.3.1. EFFECT OF GRAIN BOUNDARY TYPE

It has been hypothesized that oxidation leads to crack propagation but the propagation may stop at special grain boundaries. Special grain boundaries are the Coincident Site Lattice (CSL) boundaries. The grains adjacent to these GBs have misorientation where some of the atoms are at coincident lattice points. The value of reciprocal of density of coincident sites (Σ) is generally used to label these boundaries. For example, Σ1 represents a perfect lattice without any coincidental sites while Σ3 corresponds to a twin boundary in FCC structures. However, few studies [20, 36] reported that these boundaries are not always cracking resistant. They might require higher stress intensities to crack but they eventually crack [36]. Later Gertsman and Bruemmer [37] showed that except Σ3 CSL no other boundary is resistant to IGSCC in high temperature water environments and stress states. Observation of cracks along the favourably oriented grain boundaries led them to hypothesize that indeed it is the orientation of grain boundaries with respect to the applied stress which is more important. The resistance of the boundary to a particular type of degradation could be associated to the aggressiveness of the environment [38].

1.2.3.2. EFFECT OF COLD WORK

Cold working or strain hardening is plastic deformation of material at low temperature resulting in the dislocation motion and dislocation generation within the material. These dislocations accumulate, interact with one another and serve as obstacles to their motion. This results in increase in yield strength and subsequently increases hardness. Due to cold working internal stresses (or residual stresses) are developed which, like an externally applied stress, can result in stress corrosion cracking. This suggests that amount of cold working will have significant effect on IGSCC. In fact, relatively few cases of material

suffering from IGSCC have been reported in PWR systems compared to BWR systems and those that have occurred have been credited to the combination of an inadvertent presence of oxygen trapped in stagnant regions combined with cold work.

The corrosion potential at the surface of austenitic stainless steels in PWR conditions is considerably low compared to the potential in oxygenated water and hence, they are generally immune to cracking. But some recent studies showed that highly cold worked austenitic stainless steel on exposure to CERT are susceptible to IGSCC. They also reported to observe increase in cracking susceptibility with increase in amount of cold work for a given cold work technique. The nature of cold working process is important as well regarding the susceptibility to IGSCC of austenitic stainless steel in PWR conditions [2]. Observation of Trans-granular SCC (TGSCC) in rolling cold worked specimen while intergranular in tensile cold worked specimen by Tribouilly et al. [3] further verified the argument. They also reported that a required level of cold work is prerequisite for cracking. Some studies have shown that a minimum hardness of 310 $HV_{0.1}$ is required for crack propagation and a minimum cold work threshold of 240 $HV_{0.1}$ is necessary to see some initiation of cracking.

For crack initiation, the stress level at the surface is a trigger and these stresses may be either applied or residual. Apart from bulk cold working, surface finishing operations such as grinding can also results in residual stresses. Such surface preparation techniques induces a surface hardened layer in material that depends on the precise surface preparation mode, strain rate and deformation temperature at the surface. Most of the deformation in this layer occurs as cold work. It can result in local near surface stresses which remarkably exceed the original yield strength of the bulk material, thereby, having detrimental effect on the IGSCC resistance of material [6, 39, 40].

1.2.3.3. EFFECT OF LOADING PATH

Intergranular cracking of cold worked stainless steels has never been observed when using constant load or deformation tests. Raquet et al. [2] studied the effect of loading path on the IGSCC susceptibility of austenitic stainless steel in PWR environment and reported that indeed, the dynamic loading conditions (such as CERT, cyclic loading) are prerequisite. The author also emphasized that majority of the IGSCC propagation studies conducted on austenitic stainless steel in PWR environment are indeed under dynamic deformation conditions. In a study conducted by Couvant et al. [4], TGSCC was observed post to monotonic strain path while IGSCC was obtained post to complex loading paths in SA 304 L and SA 316 L. The authors further suggested that high levels of deformation are not required to initiate the cracks. In fact, it is the intergranular stress due to strain incompatibilities which affects the susceptibility of the material to IGSCC.

CERT test is the most preferred test conducted to study the susceptibility of material to cracking. However, the strain rate used is of great importance for this type of dynamic loading. If the strain rate is too high, no impact of environment can be seen as the time available for corrosion is reduced. While if the strain rate is too low, ductility of the material will increase as the strain rate will be too slow to keep up with the effect of the environment. Hence, an optimal choice of strain rate is necessary to study the effect of all the influencing mechanism [33].

1.2.4. SUMMARY

Austenitic stainless steels are well known for their corrosion resistance but some recent studies have shown that they are prone to IGSCC in PWR environments.

1. Exposure to corrosive primary water (280 – 340 °C, 155 bars and < - 500 mV) results in formation of duplex oxide layer: Fe rich outer layer and Cr rich inner layer (also called protective layer). The protective inner layer imparts corrosion resistance to steel. The thinner, more enriched in Cr inner layer is, the more protective it is. Various parameters such as grain orientation, surface finish, applied stress and environmental conditions can influence the thickness of the outer and oxide layer.
2. Intergranular Stress Corrosion cracking (IGSCC) of austenitic stainless steel in PWR environment can be explained by the film rupture model. Increase in SFE of alloy results in lower cracking susceptibility.
3. IGSCC has been reported in heavily cold worked (minimum cold work threshold of 240 $HV_{0.1}$ for crack initiation and 310 $HV_{0.1}$ for crack propagation) austenitic stainless steel under dynamic loading conditions.

1.3. IGSCC OF IRRADIATED AUSTENITIC STAINLESS STEEL IN PWR ENVIRONMENT

Nuclear power plant operating environments create material degradation mechanisms that may be unique or environmentally exacerbated. The concept of IGSCC immunity is very attractive; however, previous section has demonstrated that it might not be the case always for austenitic stainless steel (especially in PWR environment). Besides, in PWRs, most of the core structural components are in a close vicinity of the core. They are exposed to a high neutron damage which results in the modification of their microstructure, microchemistry, mechanical properties and deformation modes. Irradiation not only modifies the material properties but also modifies the environment (e.g. water radiolysis). It is known to enhance and/or induce IGSCC in austenitic stainless steels in PWR environment thereby reducing the lifetime of the core internals. This section will provide in detail the effect of irradiation on material, environment and lastly

on intergranular stress corrosion cracking of austenitic stainless steels that has been reported in literature.

1.3.1. EFFECT OF IRRADIATION ON AUSTENITIC STAINLESS STEEL

In a PWR, the production of energy takes place by nuclear fission of the radioactive fuel. This also leads to the production of neutrons. A part of these neutrons maintain the fission reaction, while other escapes out of the core region toward the core internals and the Reactor Pressure Vessel. These fission produced neutrons are characterized by a spectrum (called fission spectrum) which defines the distribution of the neutron flux according to their energy, at a given location in the reactor (Figure 1-10) [41]. The fission spectrum is divided in three parts namely thermal neutrons, epithermal neutrons and fast neutrons.

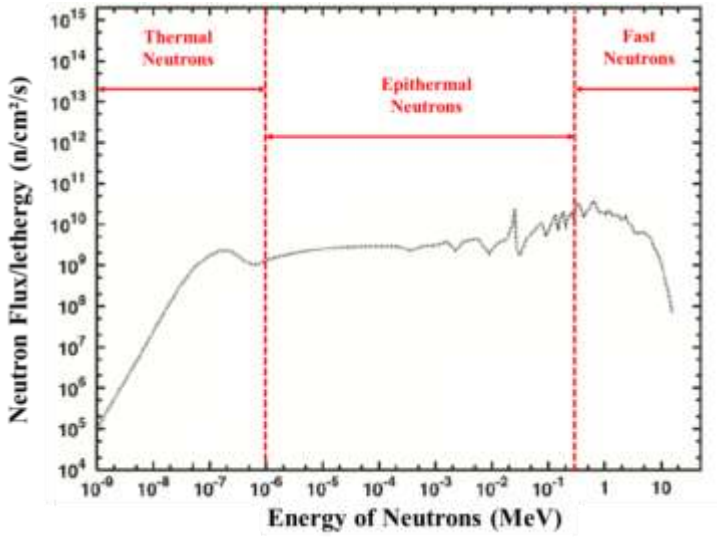

Figure 1-10 : Fission spectrum in a Pressurized Water Reactor [41].

Neutrons are uncharged and hence, can travel appreciable distance in matter. They interact with the material resulting in the modification of the properties of the material by inducing the microstructural defects in the lattice. During their (or other energetic particles like protons, ions etc.) elastic collision with the atom of lattice, they transfer some of their energy to the atom. If the energy transferred is less than displacement threshold (E_d ~ 40 eV for iron), the struck atom will vibrate about its equilibrium position but will not be displaced. While if the energy transferred is greater than the E_d, it can knock the atom out of the lattice resulting in the formation of primary knock-on atoms (PKA). This knocked out atom leaves behind a vacancy thus creating Frenkel Pair (FP). The primary knock-on atom generally possesses sufficient kinetic energy to initiate further atomic displacements and hereby initiating a collision cascade which is a spatial cluster of FPs. Displacement cascades cannot be observed experimentally because of their short duration (few picoseconds). During each collision, neutrons and displaced atoms

lose energy which eventually slows them. When their energy becomes too low, the collision phase ends and ballistic peak (Bragg peak) is reached [33, 42]. The characteristic time of the defects production in irradiated material is very short and given in Table 1-4.

Time (s)	Event	Result
10^{-18}	Energy transfer from the incident particle	Creation of a primary knock-on atom (PKA)
10^{-13}	Displacement of lattice atoms by the PKA	Displacement cascade
10^{-11}	Energy dissipation, spontaneous recombination and clustering	Stable Frenkel pairs (single interstitial atoms (SIA) and vacancies) and defect clusters
$> 10^{-8}$	Defect reactions by thermal migration	SIA and vacancy recombination, clustering, trapping, defect emission

Table 1-4 : Approximate time scale for the production of defects in irradiated metals [33].

Most of the displaced atoms (~ 90 – 99%) ultimately recombine to the vacant lattice positions. However, it is the microstructural rearrangement of the remaining incorrectly placed displaced atoms which contributes to the changes in properties of the material upon irradiation. The surviving defects rearrange into more stable configurations such as dislocation loops, network dislocations, precipitates, and cavities (or voids) (Figure 1-11), or migrate to sinks such as grain boundaries or surfaces of second phase particles [43, 44]. The production, annihilation, and migration of the point defects lead to alteration of the dislocation and dislocation loop structures, and produces defect-impurity and defect cluster-impurity complexes, leading to radiation-induced hardening and plasticity localization via dislocation channelling under straining. Irradiation also leads to changes in the stability of second–phase precipitates and the local alloy chemistry near all trap-like defects (dislocations, grain boundaries, precipitates, and defect clusters) [43]. This results in the changes in the microstructure and microchemistry of the material.

Neutrons can also interact with the nuclei of material, giving rise to a transmutation reaction in which the target nucleus changes from one element to other. These reactions are most likely to occur when energy of the incident neutron is between few MeV and several tens of MeV. In austenitic steel core internals, the typical transmutation reaction that occurs is $^{58}Ni + n \rightarrow {}^{59}Ni + \gamma$ followed by $^{59}Ni + n \rightarrow {}^{56}Fe + {}^{4}He$ leading to formation of helium. The amount of helium generated in PWR is around 10 – 20 appm/dpa. Solubility of helium is very low in steel, thus helium transmutation yields creation of helium bubbles in the matrix. These bubbles can exert pressure and thereby contributing in the swelling of material. Production of hydrogen via (n, p) reactions takes place as well. Moreover, these reactions also lead to activation of the material [45].

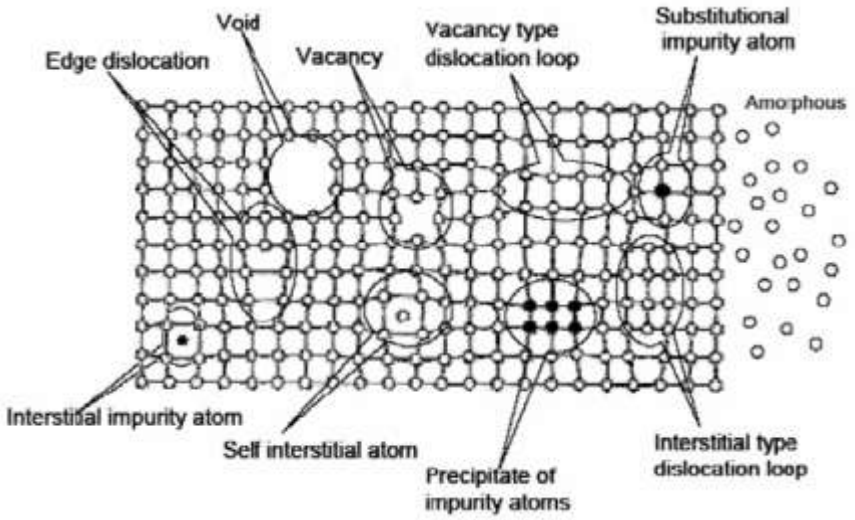

Figure 1-11 : Defects in the lattice structure of materials that can change their mechanical properties [44].

Irradiation-induced defects resulting from displacement damage are critical for understanding degradation in structural materials. The degradations are dependent on fluence and operating temperature. These operating parameters are highly geometrically dependent and strongly vary within the pressure vessel. So, a common parameter is needed to quantify the damage induced by neutron. This is possible either by using neutron fluence or using unit of displacement per atom (dpa). By definition, dpa gives the number of times that an atom is moved on average from its initial site by collision. It depends on the particle interaction cross section-area, diffusion centers (material's characteristics) and fluence. As it is directly related to the total number of Frenkel pairs produced for a given energy transferred to the primary knock-on atom, it provides a better measure of irradiation damage. Neutron fluence can be converted to dpa using a conversion factor of 1 dpa = 7×10^{24} n/m² (PWR neutron spectra and E > 1 MeV) based on a displacement energy of 40 eV as recommended in ASTM E 521 – 89 [46, 47] for stainless steels.

To be precise, dpa_{NRT} i.e. the dpa calculated using the Norgett – Robinson – Torrens (NRT) model, is commonly used as it provides a nuclear reactor environment-independent radiation exposure parameter. dpa_{NRT} can scale radiation doses or fluence between different kinds of irradiations. And hence, it is used as the standard unit in commercial nuclear and research communities to address the damage induced by neutrons. The same unit (designated as "dpa" hereafter) will be used in this study.

1.3.1.1. MICROSTRUCTURE

Core internals of PWRs are subjected to the neutron irradiation at temperature between 270 °C and 380 °C and receive a maximum dose of 80 dpa during their in-service lifetime (40 years). At these operating conditions, the cascade damage produced by neutron consists of both interstitial and vacancy type defects and clusters [48]. The migration and interaction of these defects and their clusters influence the material properties. Typical radiation-induced microstructural features in austenitic stainless steels are:

1. Black dots
2. Dislocation loops
3. Cavities (bubbles and/or voids)
4. Precipitates
5. Stacking Fault Tetrahedra[7]

These defects are dependent on initial microstructure, irradiation temperature and neutron fluence. The LWR operating temperature range represents a transition region between low-temperature (50 – 300°C) and high-temperature (300 – 700°C) suggesting an evident microstructural evolution between the two regions (Figure 1-12). Detailed description of these irradiation induced defects with current information on their evolution is presented in the following sections.

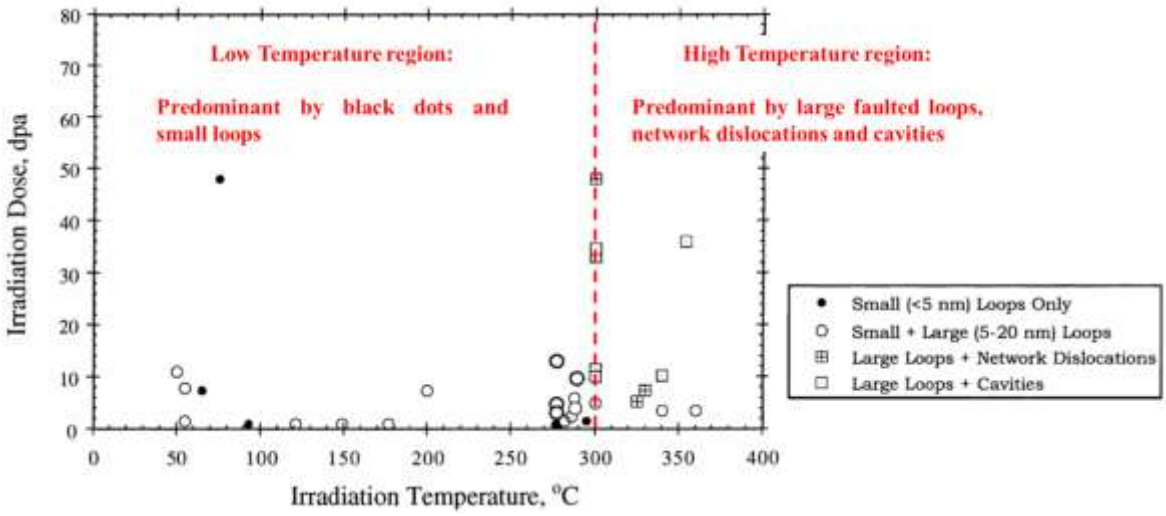

Figure 1-12 : Defects reported to be observed in austenitic stainless steel as a function of irradiation dose and temperature [6].

[7] Not observed in commercial grade austenitic stainless steel irradiated in PWR.

- **BLACK DOTS**

Black dots (or black spots) are the small loops or clusters (defects smaller than 2 – 3 nm) that have been observed in early stages of irradiation. They appear as small black dots in bright field TEM micrographs and hence the name. They are dominant microstructural features for low temperature irradiation region and are created directly in the damage cascade. Their density saturates around $2 – 4 \times 10^{23}$ m^{-3} which is attained after doses of about 0.1 dpa. The observable density of black dots is nearly independent of irradiation temperature in the low-temperature regime. However, as the irradiation temperature increases above 300 °C, a decreasing trend in the black dots density has been reported. This decrease in density has been associated with the recovery of the damage and replacement via voids or precipitates (depending on the temperature and irradiation dose). Due to their small size, nature of these defects remains unclear. Some studies have proposed that black dots are small dislocation loops of interstitial type [49, 50], while others suggested that these defects are mixed and consist of vacancy and interstitials type defects [6, 51]. However, some recent studies [52] have proved that the black dots are indeed a combination of edge-on Frank loops (that are more easily distinguishable at larger sizes) and the inclined variants (that appear as small round defects). In other words, black dots and Frank loops are one single defect seen under different contrast conditions.

- **FRANK LOOPS**

Frank loops have been reported as the major irradiation defect observed in neutron irradiated steel for all irradiation doses at LWR operating temperatures. Frank loops are the faulted dislocation loops lying on the (111) planes in the austenitic structure with a Burgers vector of a/3[111] in lattice with a lattice parameter a. These dislocation loops can be either interstitial type (extrinsic defects) or vacancy type (intrinsic defect). Their formation is mainly governed by condensation of vacancies and interstitials in (111) type planes of the FCC lattice. However, majority of the faulted loops formed during neutron irradiation in austenitic steels that are larger than 10 nm in diameter have been reported in literature to be interstitial in nature [54].

Frank loops are sessile, meaning they do not slip in their plane. They are major obstacles to the dislocation motion henceforth inducing hardening of the material. As they are partly responsible for microstructural changes, observation of these defects in irradiated material is of great interest. The rel-rod Dark Field technique can be applied to observe these defects. In an irradiated stainless steel with a well-developed loop microstructure, very distinct streaks will be present in the diffraction pattern (Figure 1-13a) if any edge-on loops are present at a given orientation due to presence of the {1 1 1} stacking faults in the loops. A relevant diffraction condition can be obtained by tilting the sample close to the g = [311] two-beam condition near the zone axis [011], and the rel-rod DF images can

be formed by selecting the rel-rod streak with the objective aperture. One of the four variants of Frank loops can be observed in a single rel-rod picture [55]. Assuming an isotropic distribution at all orientations, the density of Frank loops can be determined. A typical image of Frank loops obtained by TEM for Solution Annealed 304L SS neutron irradiated to 36 dpa at 390 °C is given in Figure 1-13b.

The appearance of these defects, their size and density, however are strongly dependent on irradiation conditions (flux, temperature), irradiation dose and the chemical composition of material.

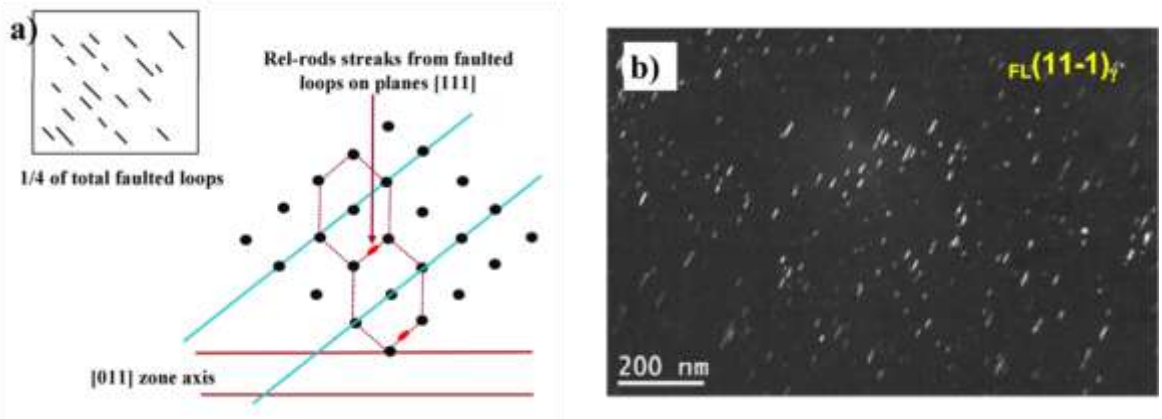

Figure 1-13 : a) Diffraction condition to obtain rel –rod image of one of the families of the Frank loops [55] b) A typical TEM Dark Field micrograph of the family of the Frank loops observed in SA 304L irradiated to 36 dpa at 390 °C in PHENIX Fast Breeder reactor (FBR) [55].

A fairly sharp transition in the loop density and size occurs between the low temperature and the high temperature regimes for a given dose (Figure 1-14). The density increases with increasing irradiation temperature in the low temperature region and was reported to be highest for irradiation temperatures between 300 – 360 °C. The temperature influence on the density and average size of Frank loops in this temperature range (290 – 360 °C) is prominent in cold worked states but has been reported to be insignificant in solution annealed stainless steel.

As the irradiation temperature increases beyond 400 °C, decrease in the density and increase in loop size has been reported in literature [6, 49]. As the loop size increases with temperature, the loop unfaulting rate increases and hence a decrease in density with increasing temperature is observed. The energy associated to a faulted Frank loop is the sum of the energy of the dislocation line (E_d) and stacking fault (E_γ). When the size of the loops grows beyond a diameter of 50 to 100 nm, they tend to unfault (i.e. removal of stacking fault) to form the lower-energy (E'_d) perfect loop configuration.

$$E_{\text{Frank loops}} = E_\gamma + E_d > E'_d \text{ (or } E_{\text{Perfect loops}}) \quad \text{(I.4)}$$

As the formation of perfect loops is less energy favorable, their proportion is generally low. Moreover, these perfect loops, unlike faulted loops, are glissile and can glide to interact and form network dislocations.

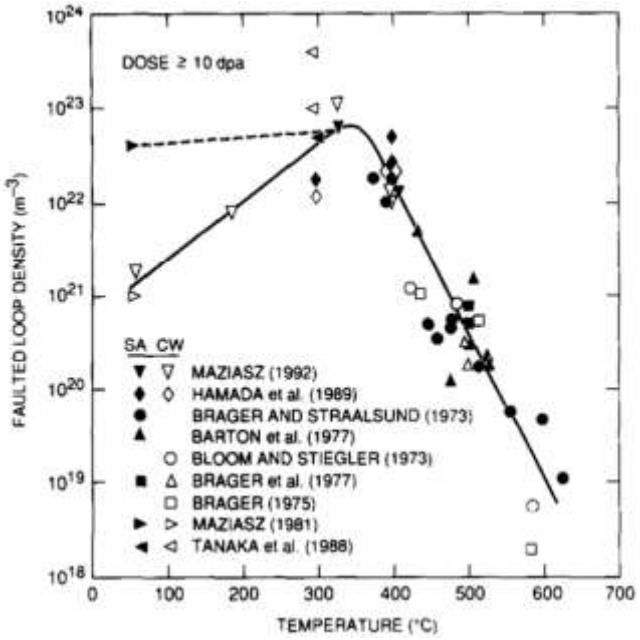

Figure 1-14 : Evolution of faulted Frank loops density with irradiation temperature in a neutron irradiated austenitic stainless steel [49].

An increase in average loops size and density with dose for initial low dose values followed by saturation for the higher doses has also been reported for all temperature regions (Figure 1-15). The initial increase is associated to the high mobility of interstitial resulting in nucleation and growth of the large faulted dislocation loops. Increasing dose enhances the vacancy migration resulting in an increase in annihilation of interstitials. And when the adsorption of vacancy and interstitial equalizes, a saturation in density and size is observed. For PWR relevant temperatures, saturation of Frank loop density to a value of order 1×10^{23} m^{-3} occurs at very low doses (~1 dpa). The average loop size saturates at ~ 5 dpa [57]. In addition, for all doses, a distribution of Frank loops size exists due to the presence of loops of different sizes at a given dose. This distribution tends to be narrow Gaussian distributions for low doses that eventually broaden to asymmetric distribution for higher doses (Figure 1-16).

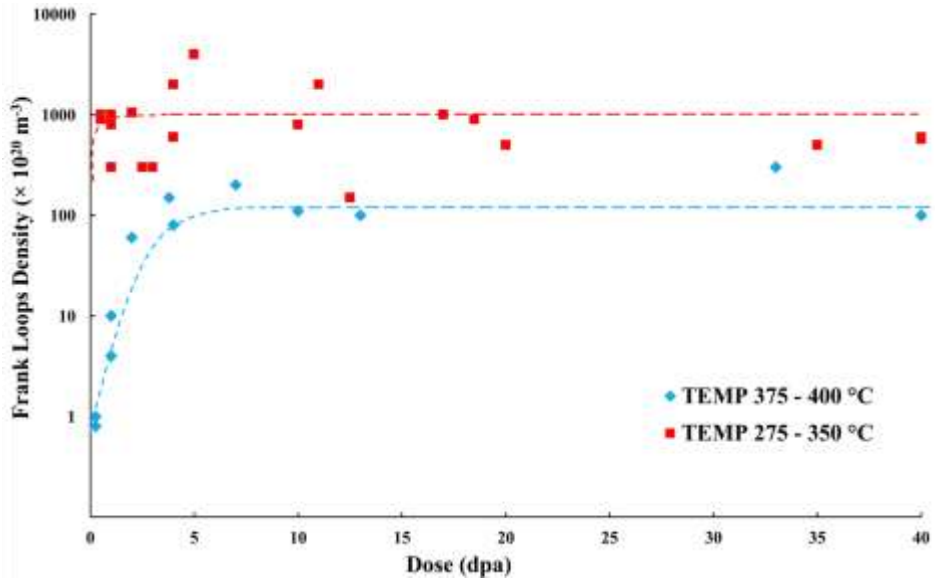

Figure 1-15 : Evolution of Frank loops density with dose in neutron irradiated austenitic stainless steel for different irradiation temperatures [6, 49 - 53].

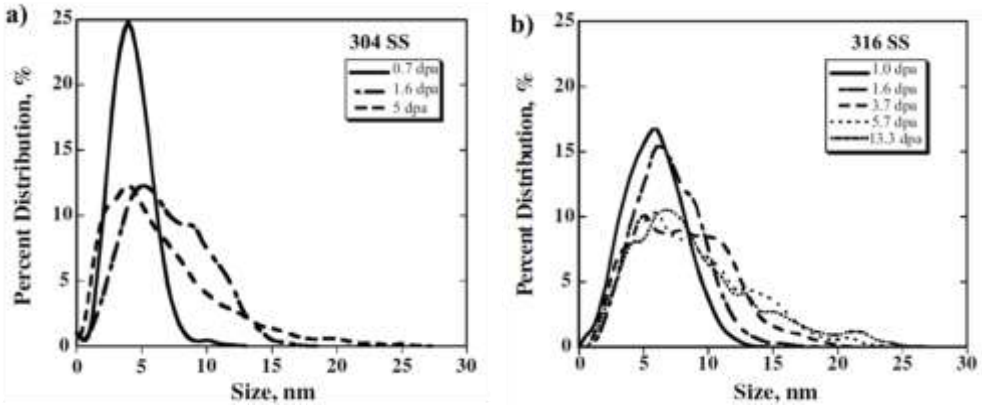

Figure 1-16 : Frank loop size distribution in a) 304 SS b) 316 SS for different doses irradiated at an in-core position at 275 °C in the Barsebäck BWR [50].

A large scatter in dose dependence of the Frank loops density and size for neutron irradiation exists and is shown in Figure 1-17 and Figure 1-18. Moreover, the observable faulted loop density in the low-temperature regime for cold work steel is slightly lower than for solution annealed material for low damage levels (< 5 dpa). This is due to the presence of dense dislocation network in cold worked material which increases the sink strength [57]. At higher doses, this difference vanishes. Also, the density and size of Frank loops in 316 L and 304 L are identical and within the scatter of the data.

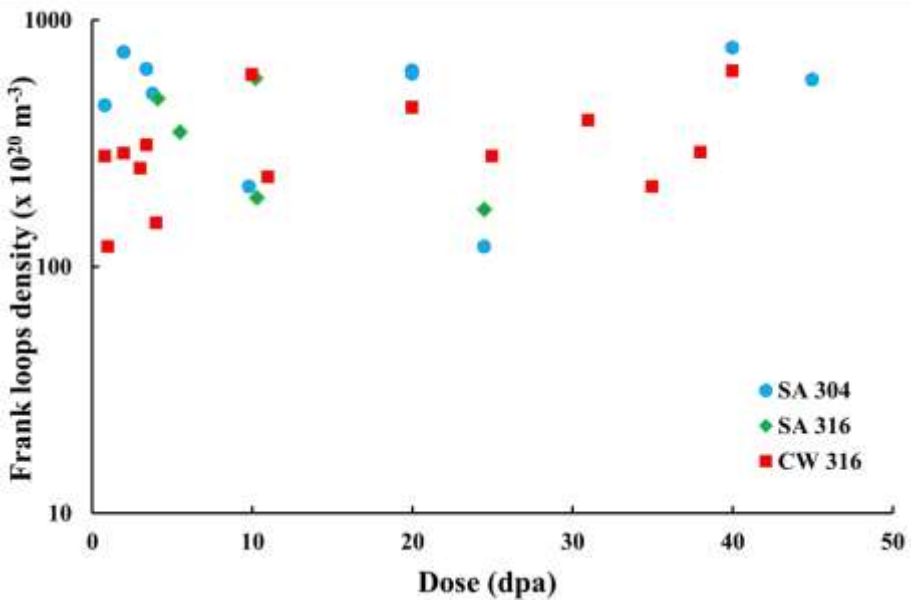

Figure 1-17 : Evolution of Frank loops density with dose for an irradiation temperature range of about 290 – 360 °C in different neutron irradiated austenitic stainless steel [6, 49, 50, 52 - 60].

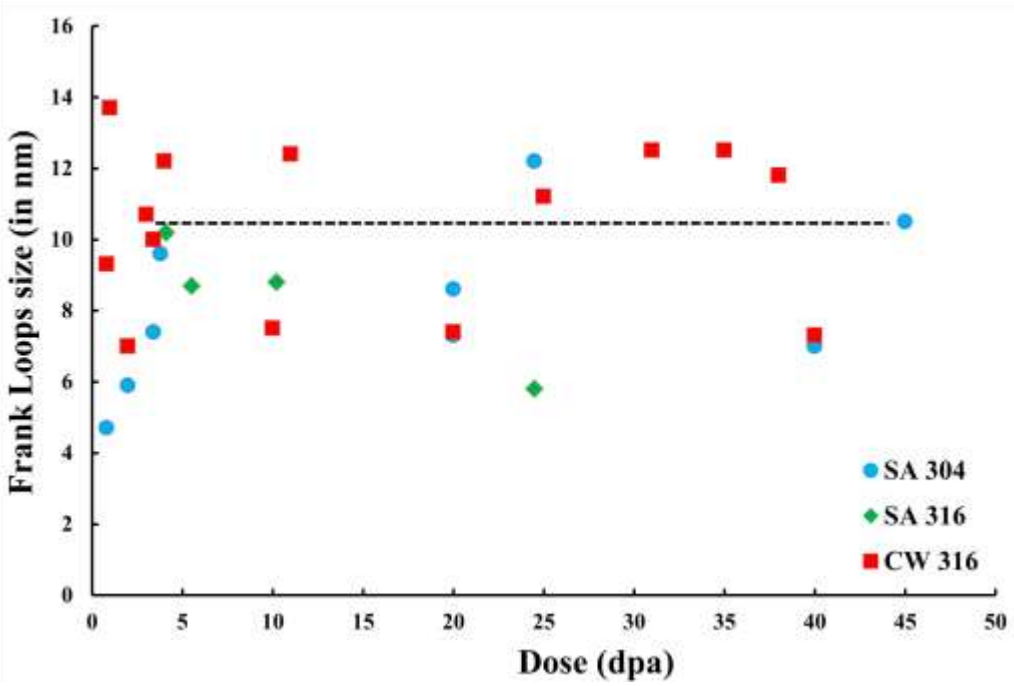

Figure 1-18 : Evolution of Frank loops size with dose for an irradiation temperature range of about 290 – 360 °C in different neutron irradiated austenitic stainless steel [6, 49, 50, 52 - 58].

Effect of grain size on the Frank loops density has been studied by Radiguet et al. [61] using ion irradiation (see §1.4). Observation of a drastic decrease in the Frank loop density with decreasing grain size was reported. As the grain boundaries acts as sinks to

these defects, increase in volume fraction of grain boundaries (due to nano sized grains) will enhance the annhiliation resulting in a decrease in density of defects.

Alloying element has an influence on the density and size of the loops. Miwa et al. [59] studied the effect of various alloying elements on the Frank loops density and size in 316 model alloys neutron irradiated at 240 °C to 1 dpa. They reported that the addition of Mo, C and Si decreased the average size of the loops. Addition of Mo and Si also decreases the average number density while C increases the average number density of loops in irradiated alloy.

- **CAVITIES**

Cavities are three dimensional vacancy clusters which grow by absorbing vacancies and shrink by vacancy emission and interstitial absorption. Cavities can be distinguished into two categories of voids and bubbles dependent on the gas content in them.

A void is an agglomeration of irradiation induced vacancies while a bubble is a cavity stabilized by gas atom present in it. In a PWR, helium atoms are generated continuously in structural materials through nuclear transmutation reaction (n, α) as explained in section 1.3.1. As solubility of helium in steels is very low, thus helium transmutation yields creation of helium bubbles in the matrix. The bubble stability is usually maintained by an internal gas pressure. In general, the bubbles produced in reactor irradiations tend to be small with radius less than 2.5 nm, unlike voids which can range in size from the smallest observable to greater than 1000 Å [62, 63]. Voids and bubbles can be distinguished based on their shapes as bubbles are perfect spherical in shape whereas voids are crystallographically faceted. A typical image of cavities is shown in Figure 1-19a.

An evident cavity formation occurs in steel irradiated to high temperature or at very high doses in low temperature region. However, post irradiation examination of core components has demonstrated the presence of cavities in neutron irradiated steel at irradiation temperatures below 300 °C at a dose of 8.5 dpa [57]. At the macroscopic scale, presence of cavities may lead to dimensional changes known as swelling which is a potential concern for these components. Hence, it is necessary to study the evolution of these defects in relation to LWRs as well. Note that issues of swelling will not be discussed in this study.

Cavities below a certain size are unstable as they emit vacancies faster than they absorb them. They require internal gas pressure to exist and hence, grow as bubbles. The size of the bubbles increases with increasing temperature. After reaching the critical size (radius) of stability, vacancy absorption overrides emission and hence, began to grow more

rapidly as voids [49, 62 – 64]. Voids and bubbles can coexist. However, the temperature range of coexistence is a strong function of He/dpa ratio, damage rate and alloy composition.

The density of bubbles and cavity is a function of irradiation temperature too. In low temperature region, formation of He bubbles is possible as vacancies are mobile in austenitic steels at temperatures above 50 °C. But high sink densities suppress the vacancy supersaturation and thereby inhibit bubble nucleation and growth. And majority of the remaining vacancies are in sessile vacancy cluster. As a consequence, only a small fraction of vacancies survives which are free to migrate to form He bubbles. Evolution of their density with irradiation temperature is presented in Figure 1-19b. For irradiation temperature greater than 450 °C, their density decreases rapidly with increasing temperature.

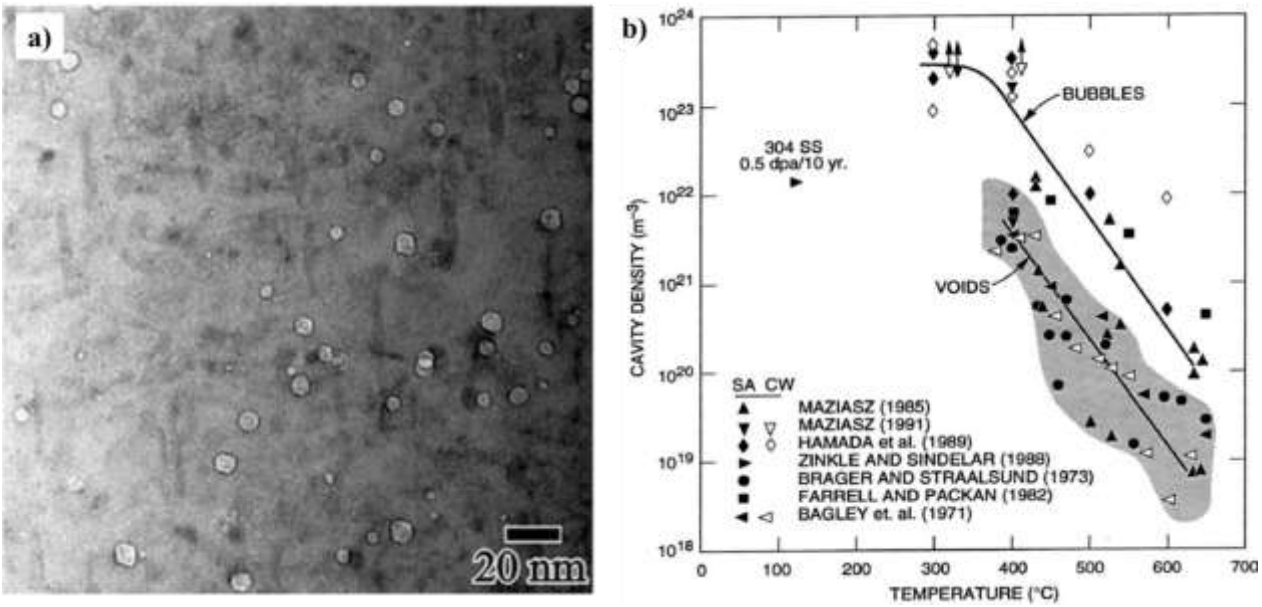

Figure 1-19 : a) A typical TEM image of the cavities observed in baffle former bolt of Tihange - 1 PWR [55] b) Effect of neutron irradiation temperature on the cavity density observed in austenitic stainless steel [49].

For a given temperature, initial increase and subsequent saturation in void density with neutron fluence has been reported. The void density saturates at doses of less than 0.5 dpa during irradiation near 400 °C. As the irradiation temperature increases, higher doses of 15 – 20 dpa are required to achieve this saturation [49].

Like Frank loops, cavity formation is dependent on initial microstructure and alloy composition. It has been shown that solutes such as Si impede void formation by increasing vacancy diffusion and reducing vacancy supersaturation [65].

Majority of the information on cavities formation known has been obtained from fast reactors. However, the He/dpa ratio is very different in PWRs (10 – 20 appm/dpa) and fast reactors (0.1 – 1 appm/dpa). As helium can enhance cavity formation, this suggests that the density and size information obtained from the two types of reactors are not coherent [65, 67].

- **STACKING FAULT TETRAHEDRA**

An SFT is a tetrahedron of intrinsic stacking faults on {111} planes with dislocations along the edges of the tetrahedron. They are the most stable geometries for vacancy cluster for low stacking fault energy material [68]. Horiki and Kiritani [69] reported to observe these defects in low dose neutron irradiated (100 – 400 °C) high purity Fe16Ni15Cr alloy. They suggested that these effects were formed directly from the cascade collapse. While studies by Maziasz and Zinkle et al. [49, 51] showed that the SFTs are not present in high irradiation temperature region while their density is very low: ~1 % of the observed defects in commercial alloys in low irradiation temperature region. In agreement with these findings, Edward et al. [50] reported to observe a very small density (~ 5 % of the observed defects) of SFTs in high purity 304 alloy (Figure 1-20a) and no SFTs in commercial purity 304 and 316 SS. They, however, also pointed out the possibility of mistaking small Frank loops and partially dissociated Frank loops for SFTs. Recent study from Zouari [70] reported to observe SFTs in commercial purity 304L irradiated at 320 °C to 46 dpa in Swedish fast reactor Bor – 60 (Figure 1-20b). However, within author's knowledge no observation of SFTs in commercial grade austenitic stainless steel irradiated in PWR has been reported so far.

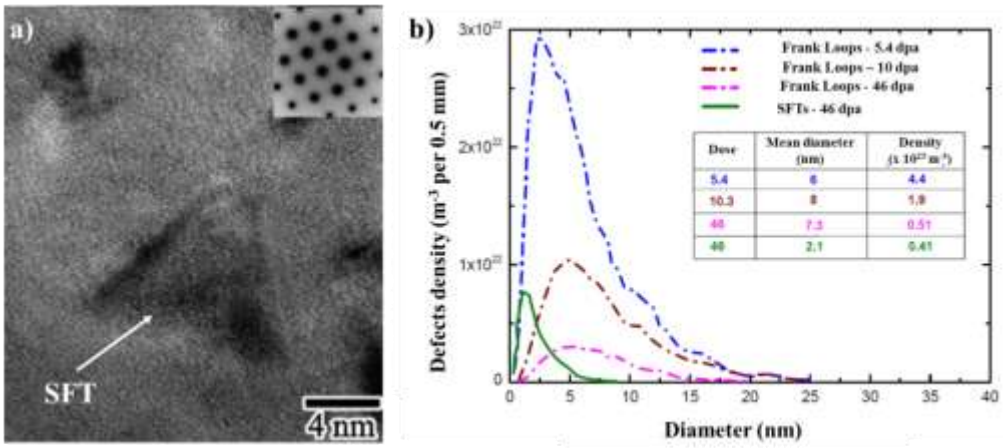

Figure 1-20 : a) TEM lattice image of SFE observed in high purity 304SS neutron irradiated at 1.2 dpa at 275 °C in Barsebäck BWR reactor [58]. b) Size distribution of Frank loops (dotted line) and SFTs (solid line) observed in SA 304L irradiated in BOR 60 FBR at 320 °C with a dose rate of 9.4 x 10^{-7} dpa/s at different doses [72].

1.3.1.2. MICROCHEMISTRY

Radiation induced segregation (RIS) is the preferential migration of atoms in a point defect flux (i.e. vacancies and self – interstitials) directed away from or towards point defect sinks. The flow of defects to sinks (such as surfaces, grain boundaries and dislocations) results in the loss or enrichment of local elements leading to non – equilibrium segregation. As this segregation is driven by the flux of radiation produced defects to sink, it is fundamentally different form thermal segregation process.

Different species diffuses at different rates. Species with slow diffusing rate are enriched while species with faster diffusing rate are depleted. The directions of segregation are dependent upon the atomic volume of the solute. The undersized atoms (e.g. Ni in austenitic steel) migrate towards while oversized atoms (e.g. Cr) migrate away from sinks. RIS thus can produce large compositional change on a local scale. In austenitic stainless steel, phenomena of RIS can be well understood by two major mechanisms which are solute concentration dependent and occur at various times. These are:

1. Interstitial association Segregation (or Solute – defect bindings)

   This mechanism is based on the formation of interstitial – solute complex in low solute concentration alloys. The self – interstitial binds with an undersized solute atoms such as Si and P, and if their (interstitial – solute complex) migration energy is less than dissociation energy, they become mobile. The complex diffuses towards the sink where interstitial gets eliminated (Figure 1-21a). Thus, a concentration gradient is established causing enrichment of the solute elements around the sinks.

2. Inverse Kirkendall effect

   Vacancies produced in the damage cascade require exchanging positions with atoms in lattice in order to diffuse to sink. They preferentially exchange with faster diffusing species which results in the depletion of faster diffusing species (such as Cr in austenitic stainless steels) at the sinks. This is counterbalanced by the enrichment of slower diffusing species (such as Ni) at sinks. The motion of atoms is opposite to that of vacancies (Figure 1-21b).

   Inverse Kirkendall effect occurs for interstitial as well. In the case of interstitial, the motion of atoms is in same direction as that of interstitial. The faster diffusing species in this case results in enrichment.

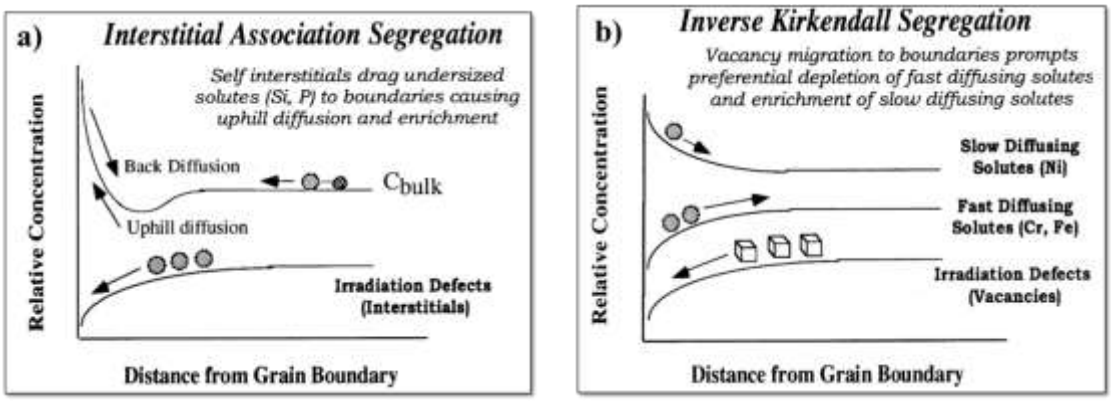

Figure 1-21 : Schematics showing the flow of defects and changes in composition at sink for a) Interstitial association Segregation b) Inverse Kirkendall Segregation mechanisms of irradiation induced segregation [6].

- **SEGREGATION OF ALLOYING ELEMENTS**

In austenitic steels, inverse Kirkendall mechanism effectively explains the observed major element segregation [71 - 73]. Neutron irradiation of austenitic stainless steel at LWR operating temperatures results in redistribution of the major alloying elements and segregation of impurities. Depletion of chromium and iron and enrichment of nickel at grain boundaries has been observed in 304 and 316 stainless steels after neutron irradiation. RIS increases with dose and saturates at 3 – 5 dpa at irradiation temperature of 300 °C. A typical RIS profile for Cr, Ni and Fe at the grain boundary of a neutron irradiated sample is presented in Figure 1-22. A basic characteristic of RIS profiles is their narrowness (typically on the order of 5 – 10 nm at the grain boundaries). Figure 1-23 shows grain boundary chromium depletion and nickel enrichment in austenitic stainless steel as a function of dose. Jacob et al. [74, 75] reported to observe Ni enrichment of 1.75 times the bulk and Cr depletion to 0.75 – 0.85 times the bulk level in a commercial purity 304 SS irradiated to 4 – 5 dpa. Chromium imparts corrosion resistance to the grain boundaries and its significant depletion could lead to intergranular stress corrosion cracking of the material.

In addition to major alloying element, segregation of minor alloying elements such as depletion of Mn, Mo and enrichment of Si and P has been reported as well. The extent of segregation is dependent on matrix composition. Increase in Ni matrix content enhances the enrichment of Ni and depletion of Cr, while increase in Cr matrix content diminishes it. Addition of Mo and P reduces the segregation as well.

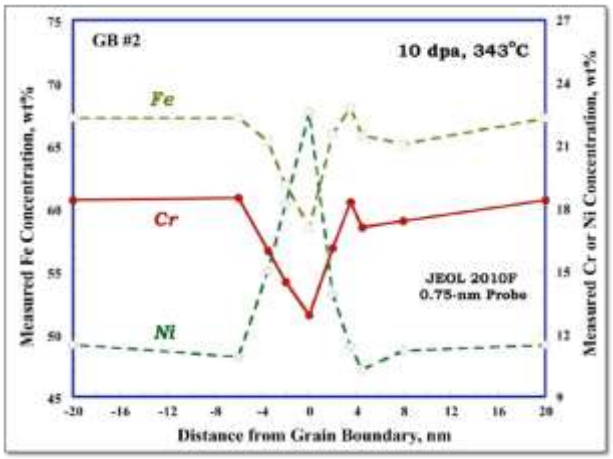

Figure 1-22 : Concentration Profile plotted as a function of distance from grain boundary observed in a baffle former bolt taken from Tihange PWR and irradiated to a dose of 10 dpa [50, 76].

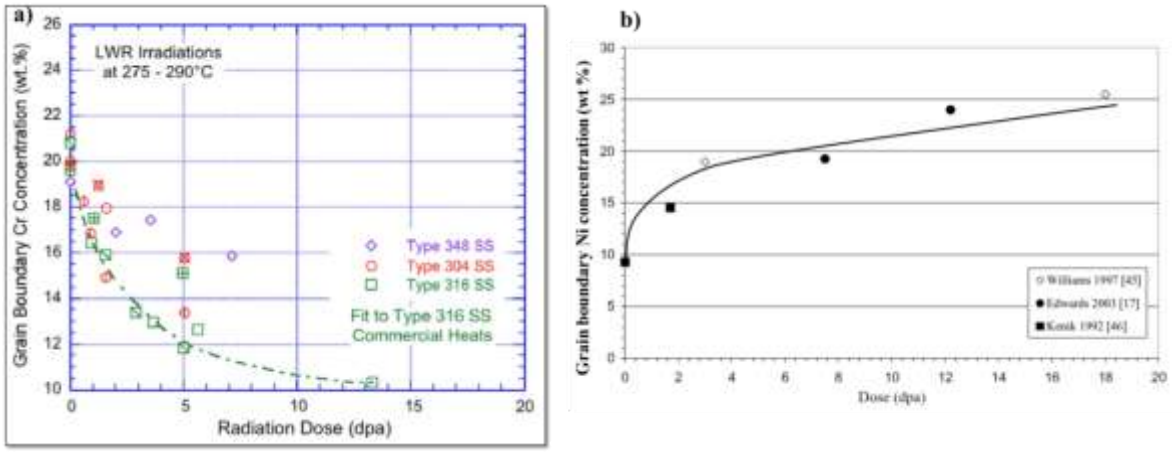

Figure 1-23 : Concentration profile of a) Cr b) Ni of grain boundary in irradiated stainless steel plotted as a function of dose [76, 77].

Several studies have reported to observe the segregation at the grain boundaries, however, only few reported to observe the segregation on voids and loops. Kenik and Hojou [78] were the first to observe Ni and Si enrichment on both sides of the loop on edge – on position. Fukuya et al. [60] also studied the segregation at edge on Frank loops (Figure 1-24) as a function of dose in CW 316 flux thimble tubes irradiated in a PWR and observed no significant segregation at the loops. They used spot analyses (using TEM with energy dispersive X ray spectroscopy, EDS) to estimate the segregation. The problem with this technique is the undesired strong signal from the matrix making the estimation of the real segregation at the loops difficult. However, few studies have shown Ni and Si segregation at the loops using Atom Probe Tomography (APT) analysis on ion irradiated austenitic stainless steels.

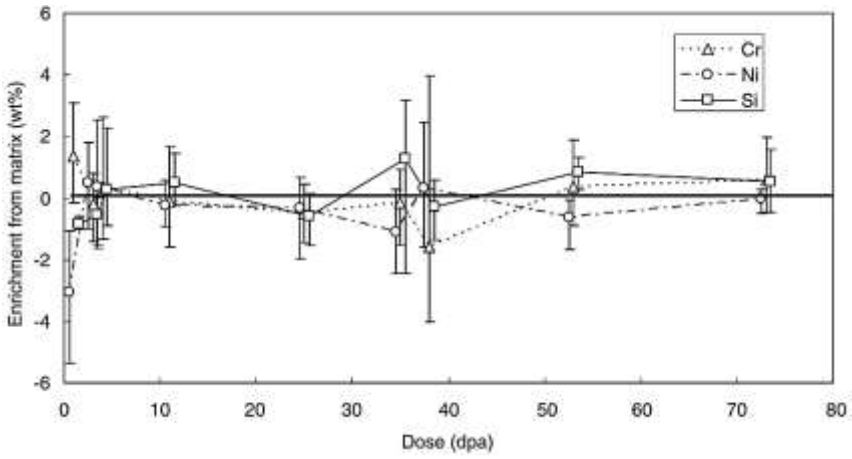

Figure 1-24 : Enrichment of Cr, Ni and Si from matrix level at edge on Frank loops in PWR irradiated CW 316 SS [60].

Temperature and flux are the primary factors controlling RIS. For a given neutron fluence (LWR relevant), at low temperatures (< 80 °C), mobility of the defects is low. While at high temperatures (> 500 °C), recombination dominates. RIS is low for both of these temperature ranges. RIS dominates at intermediate temperature which corresponds to the LWR operating conditions [33, 79]. Decrease in dose rate shift the temperature dependence of RIS to lower temperatures. Lower dose rate implies a lower point defect generation rate which increases the probability of finding a sink over recombination resulting in higher segregation. This argument is in agreement with the results obtained by Allen et al. [80]. They witnessed greater chromium depletion and nickel enrichment for samples irradiated at lower displacement rate.

- **PRECIPITATION**

In addition to producing local chemical composition changes, migration of alloying element to sinks can also lead to phase change or acceleration of phase formation. If the solute enrichment caused by RIS exceeds the solubility limit of alloying elements at the defect sinks, precipitation of the second phase occurs. Indeed, the precipitates form in austenitic steels during irradiation can be classified in three categories, namely Radiation enhanced (/retarded) phases, radiation modified phases and radiation induced phases [50]. Radiation enhanced (/retarded) phases includes the thermal phases (τ ($M_{23}C_6$), η (M_6C), MC, laves, σ, χ) which are present in the material before irradiation. They have the same composition after irradiation but their abundance is accelerated (/retarded) by irradiation. This means that they are present in the irradiated material at temperatures where they are not present under thermal aging.

Radiation modified phases are the phases that have same crystal structure after irradiation as the corresponding phase formed during aging, but their composition is different (i.e.

wt. % of their constituting elements is different) for the two conditions. These are η (M_6C), laves, M_2P.

Radiation induced phases are the phases that are unique to the irradiation conditions such as G ($M_6Ni_{16}Si_7$), γ' (Ni_3Si), MP, M_2P, M_3P. These phases are not observed during aging treatment at any temperatures.

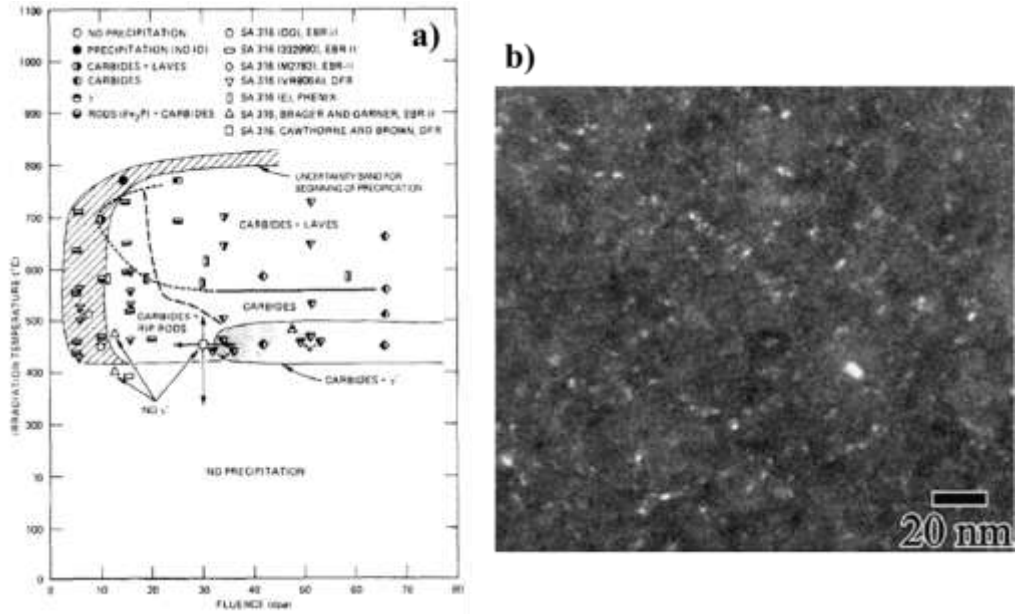

Figure 1-25 : a) Temperature and dose regime where precipitation is observed in SA 316 irradiated in Fast neutron fission reactor [49]. b) BF TEM image of γ'observed in a CW 316 baffle former bolt irradiated at 8.5 dpa at 300 °C in Tihange – 1 PWR [57].

The phase evolution in stainless steel is sensitive to several factors such as alloy composition, irradiation conditions etc. Zinkle et al. [49] reported that precipitation in austenitic steel generally occurs for irradiation temperature range of 400 – 800 °C and for doses over 1 – 10 dpa (Figure 1-25a). They also reported that the observation of radiation modified or induced phases during irradiation temperatures of 450 – 600 °C indicates higher segregation during irradiation and hence, is a sign of poor radiation resistance whereas presence of radiation enhanced (/retarded) phases is an indicator of radiation resistant microstructure.

In contradiction, Hashimoto et al. [81] witnessed presence of low density precipitates formed in stainless steel irradiated at 200 °C. Observation of γ' (Figure 1-25b) in a CW 316 baffle-former bolt irradiated at a temperature of 300 °C in PWR to a dose of 8.5 dpa has been stated by Thomas et al. [82]. In addition to radiation enhanced (/retarded) phases, Renault et al. [55] also detected the presence of radiation induced phases in SA 304L irradiated in PHENIX Fast Breeder Reactor to a dose of 36 dpa at 390°C. They also

reported to observe γ' attached to cavities. Other studies have also reported to observe γ' at dislocation loops and cavities in stainless steels irradiated at higher temperature (> 380 °C) and to higher doses (> 20 dpa) [50].

1.3.1.3. MECHANICAL PROPERTIES

Defects induced by irradiation affect the mechanical properties of the material through interaction with dislocations. These defects cause stress fields which are responsible for impeding dislocation glide, resulting in an increase in yield strength and a subsequent reduction in ductility and fracture toughness of the materials. An increase in yield strength and reduction in ductility with irradiation dose and saturation at around 5 – 10 dpa has been observed (Figure 1-26). An increase of 80 % in yield strength corresponding to a dose of 0.15 dpa for 304 L has been reported by Bailat et al. [83]. In addition to dose, irradiation temperature influences the increase in yield strength as well. For a given dose, maximum increase in yield strength and loss of ductility occurs at irradiation temperatures near 300 °C.

The increase in yield strength is due to irradiation induced defects and is dependent on the population of these defects (such as faulted Frank loops with density N_k, and mean diameter d_k). The increase in yield strength in irradiated stainless steel due to these radiation induced defects can be calculated using the dispersed barrier hardening model [85]:

$$\Delta\sigma_{ys} = (\Sigma\Delta\sigma_k^2)^{1/2} \text{ and } \Delta\sigma_k = \alpha M \mu b (N_k d_k)^{1/2} \quad \text{.....(I.5)}$$

Where, k = Frank loops, black dots, cavities and γ' precipitates, M is the Taylor factor (3.06), μ is the shear modulus (72 – 84 GPa), b is the Burgers vector (0.248 – 0.255 nm), and N_k and d_k are the number density (m^{-3}) and the mean diameter (nm) of type k defects, respectively [84, 85]. The α is the hardening coefficient which is dependent on the type of defects. In general, cavities (or voids) are strong barriers, large faulted Frank loops are intermediate barriers, and small loops and bubbles are weak barriers to dislocation motion. For stainless steels, the α values are 0.2, 0.2 and 0.4 for black dots, cavities and γ' precipitates, respectively. Several studies have reported that the α value for dislocation loops ranges between 0.4 – 0.6 (i.e. < 300 °C) for low irradiation temperature region and 0.33 – 0.45 for high temperature region (i.e. > 300 °C) [86, 87]. Dislocation loops are regarded as the significant contributor in hardening of irradiated materials.

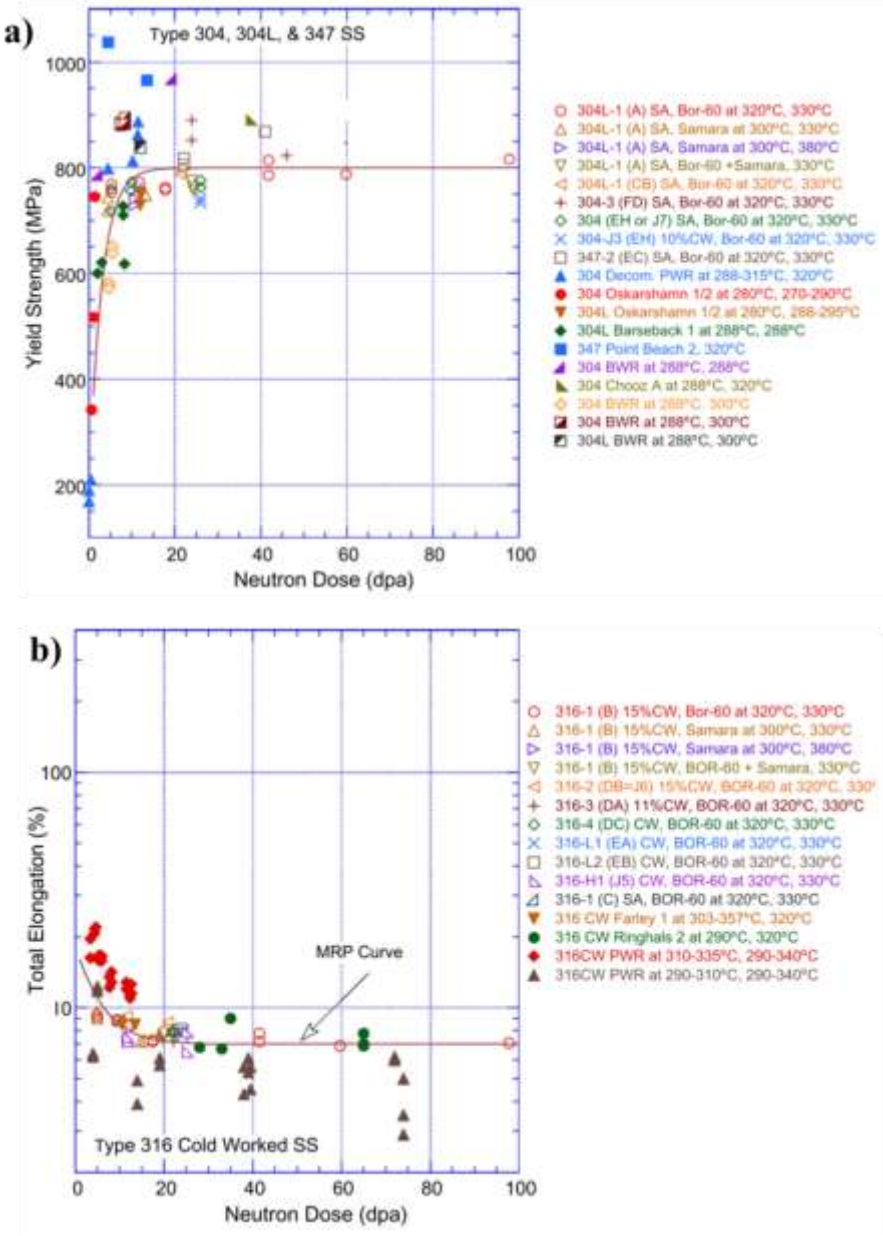

Figure 1-26 : Evolution of Yield strength and total elongation with dose for solution annealed stainless steels neutron irradiated at 270 – 380 °C [77].

The expression in eq. (I.5) implicitly assumes that the density of dislocation remained after irradiation is lower compared to density of Frank loops induced after irradiation, resulting in a negligible contribution in hardening by former. This is true only for solution annealed (SA) material and not for Cold Worked material. Assuming ρ_0 to be initial dislocation density of cold work and ρ_d to be dislocation density remained after irradiation, equation (I.5) can be modified to

$$\Delta\sigma_k = M\mu b[\alpha_k(N_k d_k)^{1/2} + \alpha(\rho_d)^{1/2} - \alpha(\rho_o)^{1/2}] \text{ ……………………………..…(I.6)}$$

where α describes the strength of obstacles created by dislocation network [84]. Since, in this study, solution annealed material is used and ρ_0 and ρ_d are not considered, eq. (I.5) will be used.

Increase in yield strength is measurable directly in a tensile test. However, handling and testing of highly irradiated samples is quite troublesome. Besides, not enough neutron irradiated samples are available. So, an indirect measurement can be performed by conducting indentation hardness measurement tests. Indeed, irradiation hardening is defined as the increase in yield strength due to irradiation induced defects. Several studies have studied the correlation between the measured hardness and increase in yield strength. Out of the several available relationships, the most promising is the one proposed by Busby et al. [88] as it relates the increase in measured hardness with increase in yield strength independent of alloy composition or test temperature.

$$\Delta\sigma_v = 3.03\,\Delta H_v \quad \text{(I.7)}$$

where $\Delta\sigma_v$ is increase in yield strength (in MPa) and ΔH_v is increase in measured Vickers hardness. They compared the increase in yield strength obtained from measured hardness obtained using the relation with the literature and obtained a good agreement.

A rapid increase in measured hardness with dose has been reported at low doses which is consistent with increase in defect density with dose. When creation of defects is balanced by destruction of defects, saturation is reached. Saturation in hardness has been observed at doses above 5 dpa for SA 304 SS. Like dose, irradiation hardening is dependent on irradiation temperature. For a given dose, hardening is significant corresponding to the irradiation temperature of 300 °C at which density of dislocation loops is maximum. Decrease in measured hardness with increasing test temperature has been reported as well.

Apart from irradiation hardening, stainless steels exhibits strain softening and little or no uniform elongation at irradiation doses above 3 – 5 dpa. This is due to the change in deformation mode in the material at these doses [77] discussed in the following section.

1.3.1.4. DEFORMATION MODE

Plastic deformation produces a wide variety of microstructures such as tangled dislocations, dislocation pileups, stacking faults, twins, dislocation channels and martensite formations in austenitic stainless steel depending on the material and testing conditions (deformation temperature, strain rate). Amongst these, dislocation channeling and twinning are prominent deformation microstructure reported to be observed in irradiated austenitic stainless steels in various studies [15, 16, 90]. While channeling dominates at temperatures near 300 °C at low strain rate, twinning dominates at low

temperature and high strain rates. Deformation mode map proposed by Byun et al. [16] for austenitic stainless steel also proposes that for higher stresses and higher doses the microscopic deformation is dependent on the nature of irradiation induced defects. Creation of non-removable defects (such as dense tangles and gas bubbles) favors twinning whereas removable defects (such as Frank loops) promote channeling. In PWRs, the core components experiences a strain rate of 10^{-10} /s which is very low and the irradiation temperature is around 300 °C suggesting the dominance of dislocation channeling in these components and will be described in detailed in the following section. Indeed, several studies [16, 17, 83, 89 – 91] have proved that dislocation channeling is the prime deformation mode for neutron irradiated austenitic steel at LWR relevant temperatures.

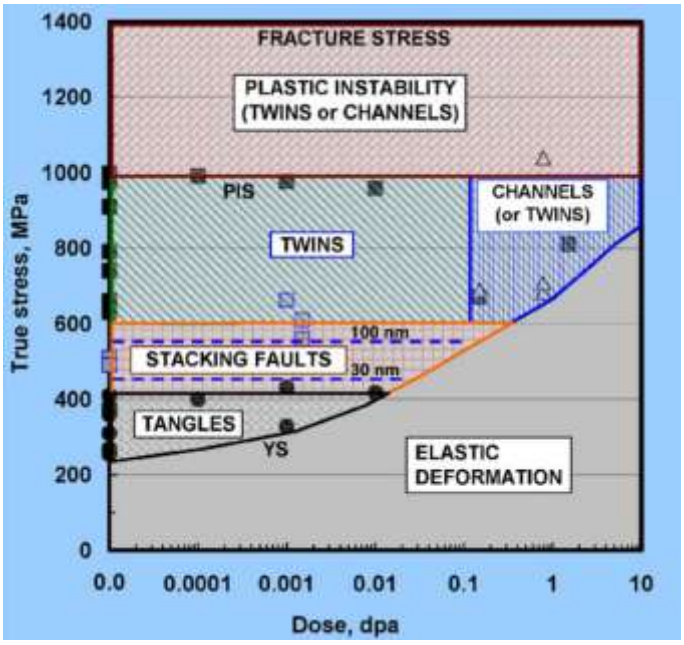

Figure 1-27 : Deformation mode map for 316 and 316 LN stainless steels in true stress – dose space [16].

Irradiation induced defect clusters (such as loops, cavities) acts as obstacle to the dislocation motion. Under dynamic straining, annihilation of these defects occurs during the motion of dislocations in a particular slip plane. This clears the path for subsequent dislocations and results in formation of highly localized deformation band also called dislocation channel (Figure 1-28a). The channels are very narrow (< 100 nm) and closely spaced (< 1 µm) and typically run the entire length of the grain, terminating at the grain boundaries.

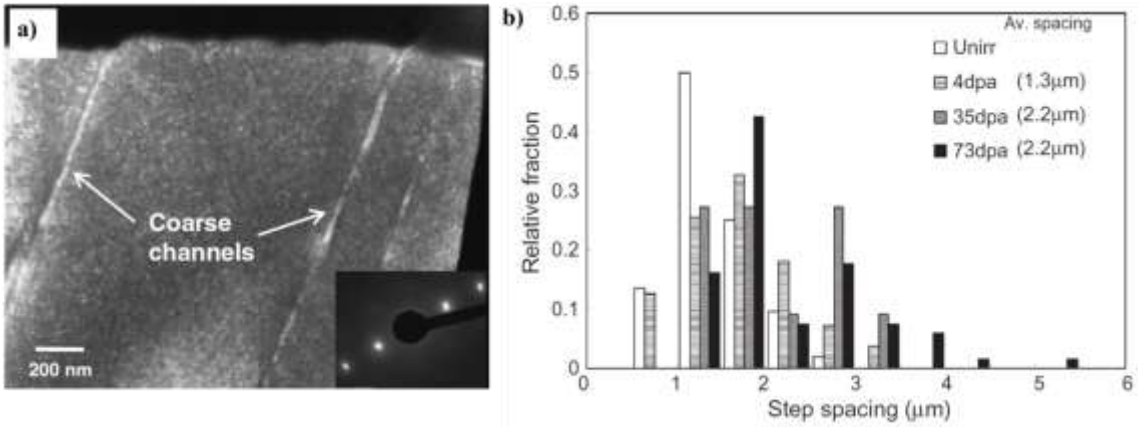

Figure 1-28 : a) Dark Field image of coarse dislocation channels observed b) Average step spacing distribution obtained in 35 dpa neutron irradiated SUS 316 austenitic steel deformed at slow strain rate to 13 % plastic strain [89].

Formation of these deformation bands leads to heterogeneous deformation strain within the grain and has recently drawn a lot of attention as it holds the potential to unveil the underlying principle of IASCC. Termination of deformation bands at free surfaces results in formation of steps (or slip lines). The amount of strain accumulated in channel (γ) is believed to be proportional to the height of these steps (h) and inversely proportional to the spacing (w).

$$\gamma \approx \frac{Displacement\ on\ one\ slip\ plane}{plannar\ spacing} = \frac{h}{w} \quad \text{.....(I.8)}$$

Hence, to characterize the degree of deformation, quantities such as slip line height, spacing, and width are used. Nishioka et al. [89] observed an increase in average slip line spacing with increasing dose for neutron irradiated SUS 316 (Figure 1-28b). Higher dose implies a higher degree of localized deformation suggesting that these parameters can be used to characterize the degree of localization.

Several factors such as dose, SFE, irradiation hardening (indirectly irradiation induced microstructure) have been known to influence the degree of localization. Farrell et al. [92] studied the evolution of dislocation channeling in irradiated austenitic steel as a function of dose. They observed that increasing dose decreased the work hardening and the volume of material occupied by channels increased suggesting a sharp increase in localized deformation with dose. SFE is known to influence the slip mechanism. High SFE results in wavy slip consisting of a web of tangles while low SFE promotes planar slip which enhances localized deformation [33, 90, 94]. Decrease in average step height with increasing SFE provides the evidence for the argument (Figure 1-29).

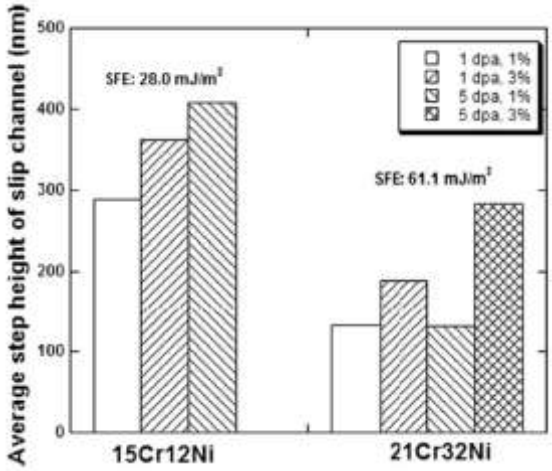

Figure 1-29 : Average step height in the slip channels in alloys with different SFE at two doses and strain levels [90].

Dislocation loops are the dominant irradiation induced defects in austenitic stainless steel irradiated by neutrons at LWR irradiation temperatures. Few cavities have been reported as well at these irradiation temperatures. Cavities are harder obstacle to dislocations compared to dislocation loops [95]. Hence, dislocations can easily annihilate the loops while cavities cannot be removed by gliding dislocations and hence, cavities alone cannot produce defect channels during deformation. They can however, may promote dislocation cross slips. This suggests the dependence of localized deformation on irradiation induced microstructure. Indeed an increase in average channel height with increasing density of loops while a decrease in channel height with increasing void density has been observed (Figure 1-30) [95].

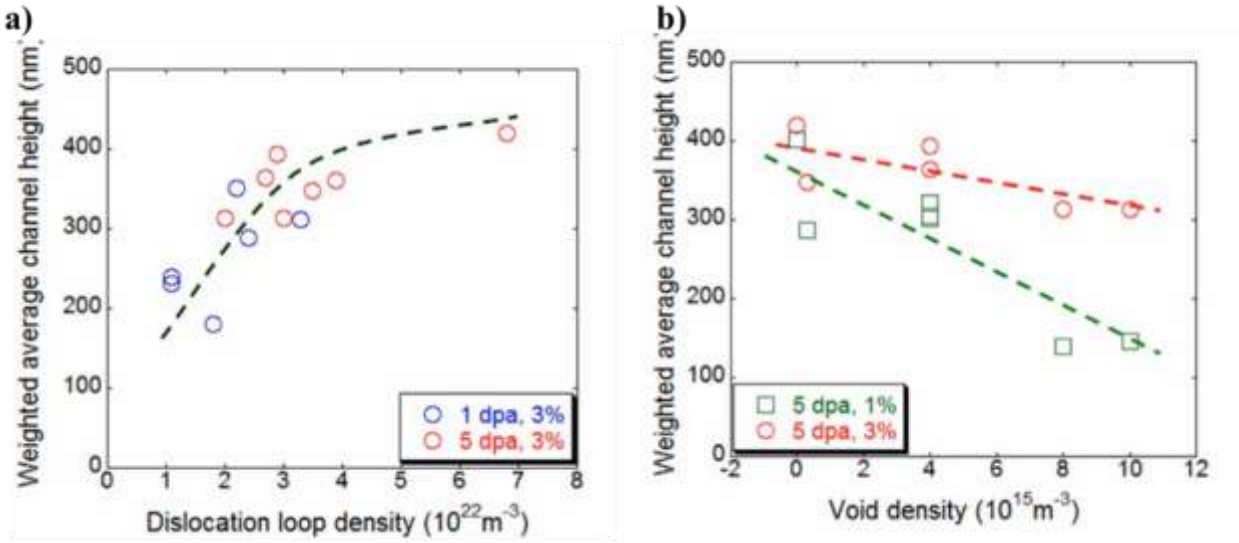

Figure 1-30 : Dependence of average channel height on a) dislocation loop density b) void density for different doses and strain rates [95].

1.3.2. EFFECT OF IRRADIATION ON OXIDATION

Exposure of austenitic stainless steel to aqueous medium leads to formation of duplex oxide layer (§ 1.2.2). The thin protective inner oxide layer commonly called "passive film" makes it highly corrosion resistance. Irradiation can, however, change oxidation kinetics by either water radiolysis or changing material properties through damage production.

Due to irradiation, water molecules dissociate into ions and radicals which interact to form H_2O_2, H_2 and O_2. This phenomenon is called radiolysis. This can influence the susceptibility by increasing the corrosion reactions. However, recent results showed that this elevation in corrosion potential induced by radiation (via radiolysis) is significantly low [33]. Moreover in PWRs, hydrogen is added to suppress the formation of oxygen due to radiolysis of water. This further suppresses the elevation of corrosion potential via irradiation. Hence, it could be concluded that the water radiolysis is not a prime factor influencing the crack propagation in PWR environments.

The other way in which irradiation can change oxidation kinetics is by inducing defects in the material microstructure. Few studies [96, 97] conducted on irradiated samples gave a mixed response on effect of irradiation on oxidation kinetics. However, the environment and irradiation conditions in these studies were quite different amongst themselves and also from a PWR environment. Perrin et al. [23] conducted an oxidation test on mirror polished unirradiated and proton irradiated samples (see §1.4) in simulated PWR primary water environment at 325 °C and 155 bars pressure to study the role of irradiation induced defects on the oxidation kinetics. They compared the oxides formed on unirradiated and irradiated samples after 1024 h (3 different corrosion sequences in two different autoclaves). They observed that the outer oxide crystallites were bigger on unirradiated sample while the crystallites were smaller (hence, in higher number density) on proton irradiated sample (Figure 1-31).

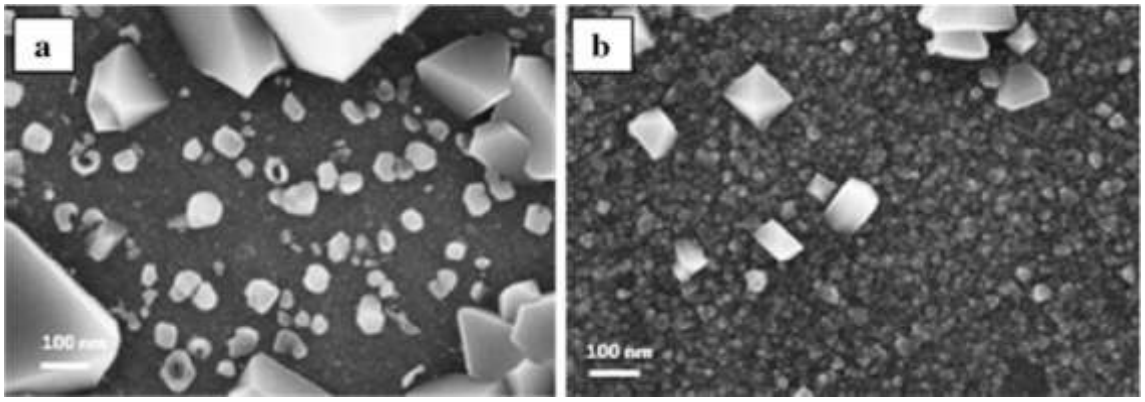

Figure 1-31 : Comparison of the morphology of the outer oxide observed in a) unirradiated b) proton irradiated austenitic stainless steel after corrosion for 1024 h in simulated PWR primary water [23].

The inner layer was thinner and more enriched in chromium as well for the proton irradiated sample. This led the authors to conclude that the irradiation induced defects (such as dislocation loops, cavities) acted as a preferential site of nucleation for the external layer. In addition, these irradiation induced defects enhanced the diffusion of chromium resulting in an inner layer richer in chromium and hence, more protective. The authors, however, insisted on further investigations as these results did not incorporate the effect of crystal orientation.

Same research group, in other study, also reported to observe a thinner and more Cr enriched inner oxide layer in mirror polished irradiated sample compared to the unirradiated state after 600 h corrosion in simulated PWR environment (Figure 1-32) [98]. They, on contrary, also reported to observe less number of outer oxide crystallites in case of irradiated samples. The author argued that the presence of defects modifies the chromium content in the inner layer which in consequence affects the cation diffusion of Fe. This strongly influences the size and growth of the outer oxide crystallites.

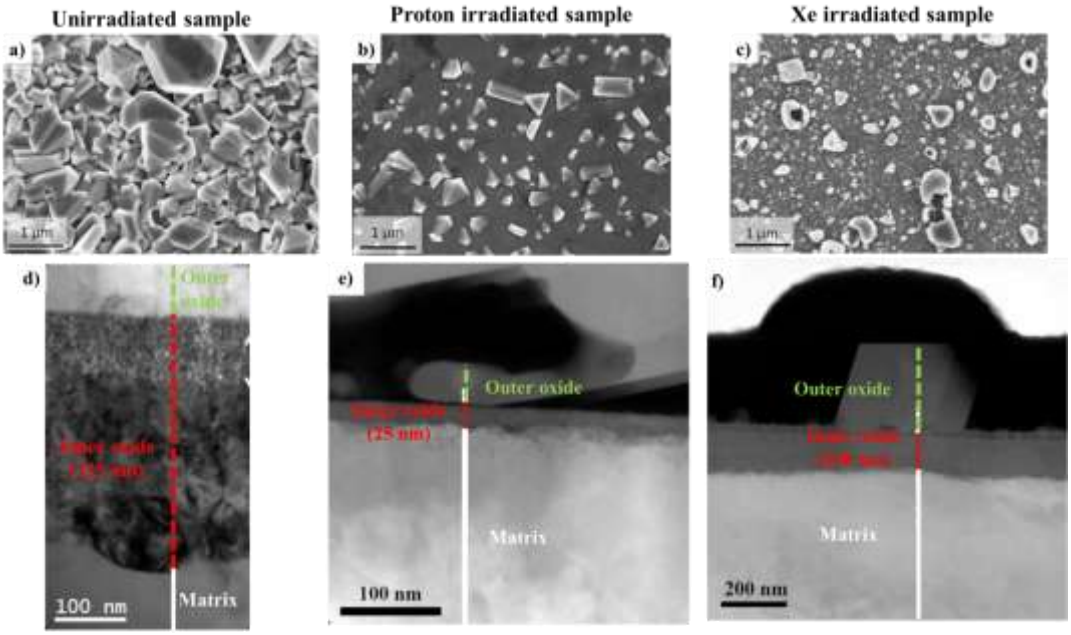

Figure 1-32 : Comparison of morphology of outer oxide (a – c) and thickness of inner oxide (d – f) in unirradiated, proton and xenon irradiated 316 L after corrosion for 600 h in simulated PWR primary water [98].

Fukuya et al. [99] conducted the corrosion test on mirror polished PWR flux thimble tubes (irradiated to different doses at 300 °C) in simulated PWR primary water at 320 °C for 1200 h. They observed, that the inner layer was thicker for irradiated sample (contrary to [23, 98]) compared to unirradiated sample and concluded that neutron irradiation doesn't alter the oxidation process but oxidation rate. These contradictory results in different studies suggest that the mechanism by which irradiation influences the oxidation

is poorly known and hints towards the need of further investigation required in this direction.

1.3.3. IGSCC OF AUSTENITIC STAINLESS STEEL

On subjection to irradiation, susceptibility of austenitic stainless steel towards SCC enhances. This degradation mechanism of core internals is often referred as Irradiation Assisted Stress Corrosion Cracking. IASCC is also characterized by intergranular crack initiation and propagation but there are some differences between IASCC and IGSCC. IGSCC is a well-established and much studied phenomenon. As shown previously, IGSCC of austenitic stainless steel can occur in absence of irradiation. On the other hand, IASCC is highly dependent on neutron fluence exposure level. Indeed, laboratory SSRT (Slow Strain Rate Tensile testing) data suggested that the intergranular SCC in austenitic stainless steels is promoted only when critical threshold fluence (~ 10^{24} n/m²) is reached (Figure 1-33). The critical threshold is dependent on material and environmental parameters. The existence of this threshold suggests that though in-situ effects (corrosion potential, etc.) are important, persistent radiation effects such as microstructural and microchemical effects can be responsible for the behavior in post irradiation tests. Furthermore, Was et al. [100] have proposed that there exists a common link between IGSCC and IASCC making intergranular cracking in irradiated material an analogue to the unirradiated case. So, the cracking observed in post irradiated tests is generally addressed as IGSCC of irradiated austenitic stainless. However, the studies dealing with in situ cracking still address it as IASCC.

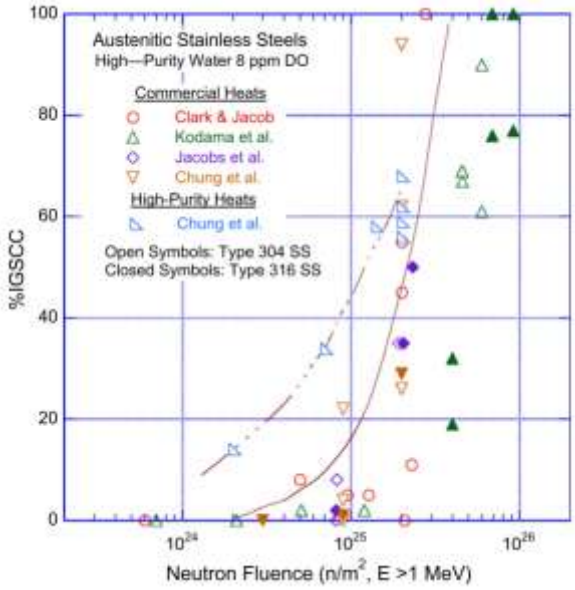

Figure 1-33 : Dependence of intergranular stress corrosion cracking in neutron-irradiated 304 SS and 316 SS as a function of neutron fluence in high dissolved oxygen water [77].

Like classical SCC behavior, environment chemistry and stress/strain conditions strongly influence the IASCC susceptibility. A baffle-former bolt begins its service life with a designed preload that induced stresses in the bolt in the elastic region of the unirradiated material. During the course of its service, it might experience different types of stresses. These stresses when coupled with PWR corrosive environment and susceptible material (due to irradiation) results in intergranular SCC of the material. IASCC initiation data on irradiated austenitic stainless steel has been obtained by conducting constant load tests in a simulated PWR environment in which the specimens had been tested as a function of fluence and applied stress. Applied stress normalized by irradiated yield stress plotted as a function of time (Figure 1-34a) disclosed that crack initiation can occur very quickly (within 500 h) in highly irradiated material. Several studies [77] have also reported to observe a stress threshold (Figure 1-34b) corresponding to about 50 % of the yield strength for the material.

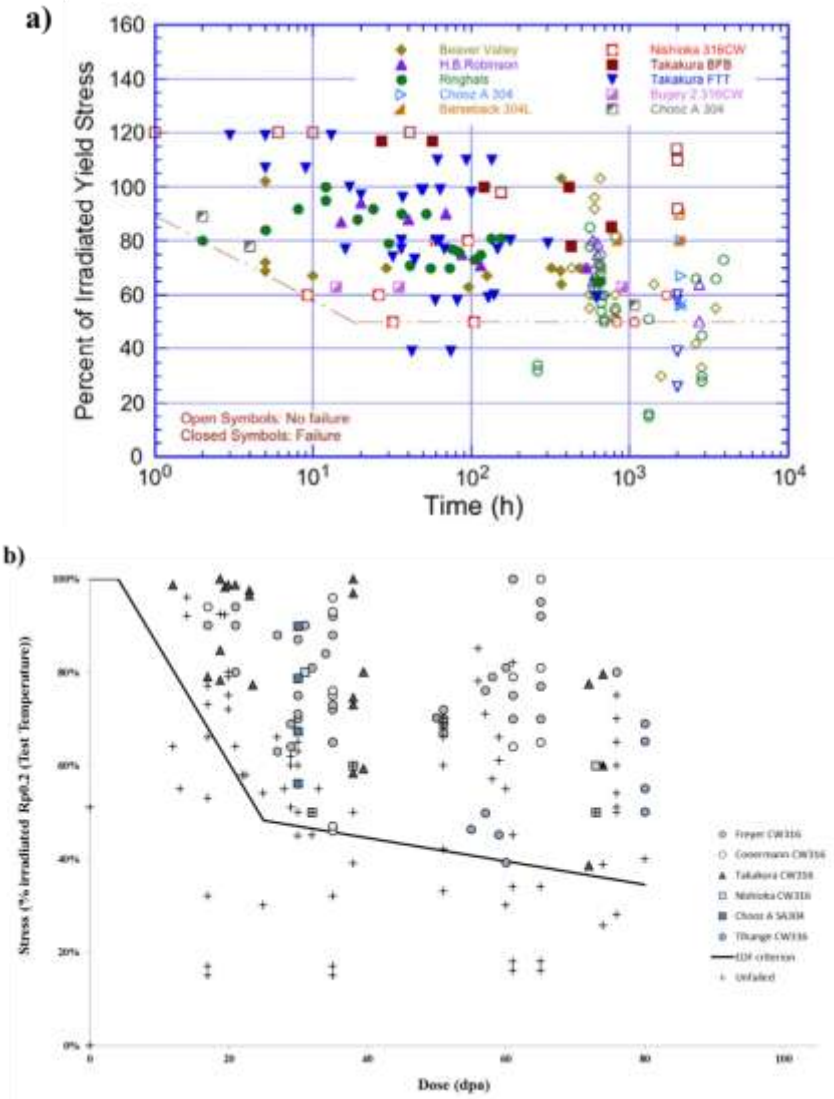

Figure 1-34 : Stress as percent of the irradiated yield stress vs. a) time b) dose for IASCC initiation in austenitic stainless steels in a PWR environment [extracted from 77].

For higher doses, however, some samples cracked for values below 50 % suggesting an overestimation for these samples by the criterion. These results are used to obtain a lower bound for stress and fluence below which a core internal will not experience IASCC during its in service lifetime. The IASCC initiation data, however, corresponds to different tests conducted on different material (different initial states). All of these can have a significant effect on the crack initiation susceptibility. Indeed, recently, K. Takakura [101] have proposed that due to slight differences[8] in the material used to fabricate baffle former bolts (BFBs) and Flux thimble tubes (FTT) of a PWR, the SCC initiation time for BFBs is longer than that for a FTT at lower applied stress value (Figure 1-35) but the difference vanishes at higher stress level. As FTTs have higher doses than BFBs due to different location in a reactor, most of the present work on SCC initiation has been done performed and reported for FTTs. As a consequence, there exists a significant scatter in IASCC initiation data with respect to failure and non-failure as well as the time of failure.

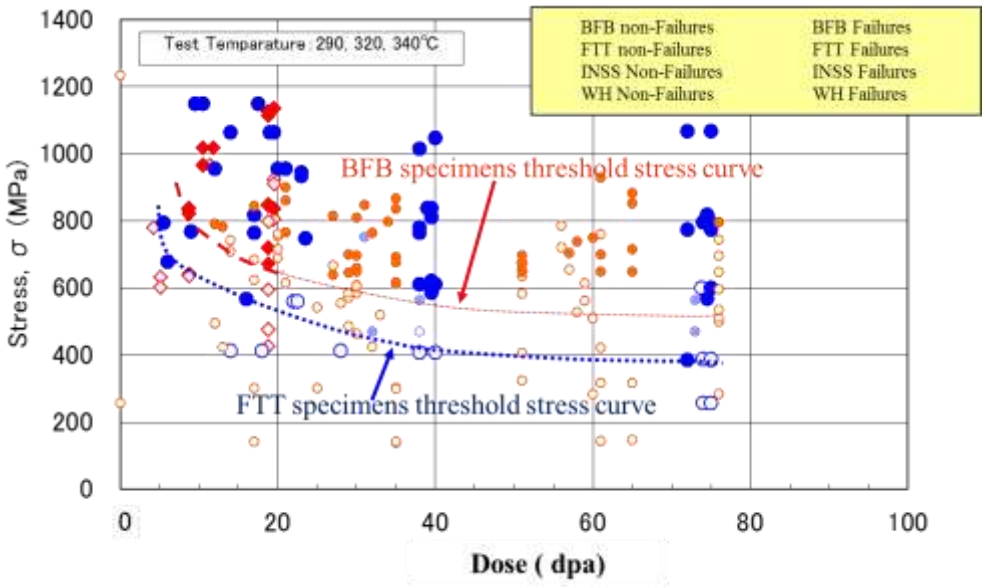

Figure 1-35 : Stress vs. dose curve for IASCC initiation in austenitic stainless steels in a PWR environment indicating the different threshold stress curve for BFBs and FTTs [101].

These curves are updated timely by adding new information on crack initiation data and the threshold stress below which IASCC is considered unlikely has been decreased from 50 % to 40 %. A better correlation can only be obtained with a better understanding of IASCC mechanism.

Bruemmer et al. [6] emphasized on the need of accurate prediction of microstructures, microchemistries and mechanical property changes in austenitic steels during irradiation

[8] Presence of hardening layer on the surface of FTTs prior and post to irradiation but not in BFBs.

at PWR temperatures for better understanding of the phenomenon. Since then, several studies have been conducted to study the role of various parameters individually and in combination. In early 1980s, several in-field and laboratory tests conducted on irradiated steels concluded that RIS at grain boundaries, radiation hardening and deformation mode are amongst the most significant contributors (Figure 1-36) in IGSCC of stainless steel in PWR environment.

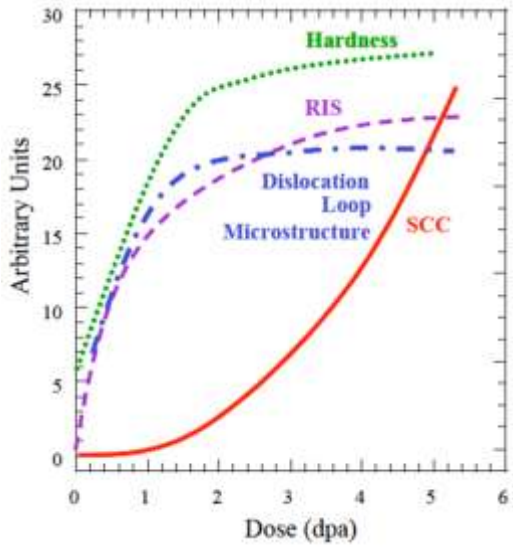

Figure 1-36 : Schematic showing the increase in RIS, Frank Loop line length, hardness and SCC susceptibility with dose in PWR [33, 95].

As stated before, segregation of alloying elements results in depletion of Fe and Cr and enrichment of Ni at the grain boundaries. Chromium imparts passivity and its depletion (due to segregation) makes grain boundaries susceptible to corrosion. Irradiation induced defects such as faulted loops, cavities result in irradiation hardening. Irradiation results in change in deformation mode enhancing the localization of deformation. All these parameters can highly influence the susceptibility of the material towards cracking. The problem lies in the coupling of these parameters which makes the assessment of IASCC highly complicated.

Few studies have also reported that SFE can influence the localization of deformation and IASCC susceptibility. With increase in stacking fault a decrease in SCC susceptibility has been reported by Thompson [20] in unirradiated stainless steel. Interpreting from the results of Rhodes [102] and Schramm [103] and considering that IASCC is the irradiation enhanced SCC, Was [72] proposed a similar inverse relation between SFE and IASCC. Though, some scatter has been observed at low stacking fault values. It has been proposed that low SFE and high irradiation dose promotes IGSCC. As SFE influences the cracking susceptibility of material indirectly via influencing the deformation mode, it questions the potential of SFE as a sole contributor to IASCC.

Fukuya et al. [104] conducted Post Irradiation Annealing (PIA) experiments on CW 316 SS, neutron irradiated to 25 dpa, to isolate the microstructural and micro-chemical effects on IASCC in simulated primary water. For the purpose, they estimated and plotted the recovery of IASCC susceptibility, microstructure, hardness and RIS against the iron diffusing distance $\sqrt{Dt}$, where t is the annealing time and $D = D_o \exp(-Q/kT)$, D_o is the iron self-diffusing coefficient, Q is the migrating energy and T is annealing temperature. They reported that the RIS was slowest to recover and hence was not a controlling factor while microstructure and hardening could be the potential factors. Several studies [105, 106] conducted using different type of irradiations yielded similar results (Figure 1-37).

In all these studies, for small diffusion distances, very small recovery in hardness profile was observed. Though, hardness and cracking reduces with annealing temperature, hardness was unable to fully explain the response. Hash et al. [106] demonstrated that hardness alone is not sufficient for IASCC by conducting tests on series of CP 304 SS samples with same hardness. For the purpose, authors conducted SSRT in BWR environment on 5 samples; 35 % CW (no irradiation), 1.67 dpa (no cold work) and three other samples having varying degree of cold work and irradiation but same hardness. They observed that the cracking was not same as would be expected if hardness was the only factor. In combination with the annealing results, they suggested that other factors besides hardness such as deformation mode could be the key role players.

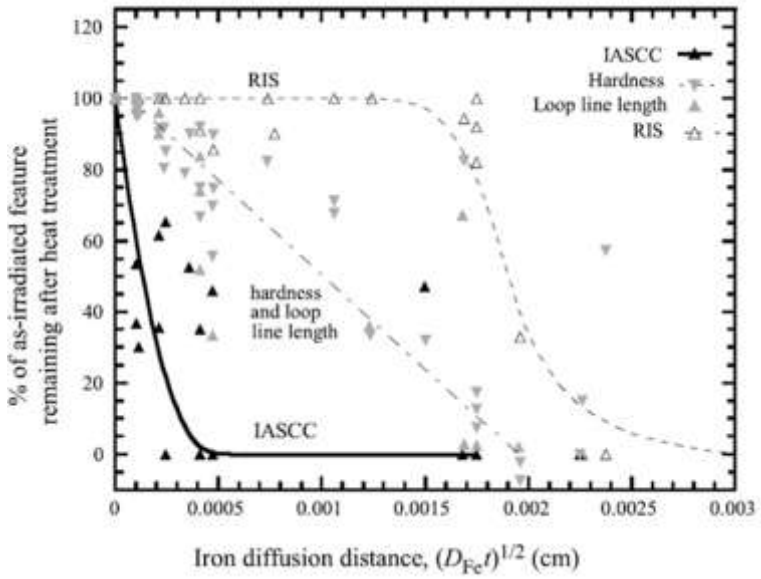

Figure 1-37 : Removal of RIS, dislocation microstructure (measured by loop line length) and hardness as a function of iron diffusing distance ($\sqrt{Dt}$). The data for the graph was taken from different studies conducted on neutron (BWR and PWR environment) and proton irradiated stainless steel (tested in BWR environment) [104].

For better understanding of basic processes, Thomas et al. [82] characterized the crack tip in a cold-worked 316SS baffle-former bolt (Figure 1-38a) irradiated to 8.5 dpa after 20

years of service in a PWR. The crack under study was intergranular in nature, branched near the tip and was filled with oxide corrosion products (i.e. nano-porous, fine grained spinel). They argued that the RIS altered grain boundaries chemistry and irradiation induced fine defects hardened the material but these changes were not necessarily the cause of IASCC. These results are in accordance with the PIA results. They also observed that deformation structures near the crack tip consisted of high density of dislocations and shear bands (planar faults). The crack narrowed to the steps coincident with the slip band intersection suggesting that the flow of dislocations along the slip steps and into the grain boundary may have been responsible for discontinuous growth of the crack along the grain boundary (Figure 1-38b). Absence of these steps like structure at the crack wall in unirradiated steel exposed to high temperature water environment points towards the difference in cracking mechanism for in core irradiated components and unirradiated SS. Based on their finding they proposed that crack initiation in irradiated material could be a consequence of a dislocation based mechanism. While the stresses generated by the growth of oxide layer formed behind the crack tip resulted in the crack propagation.

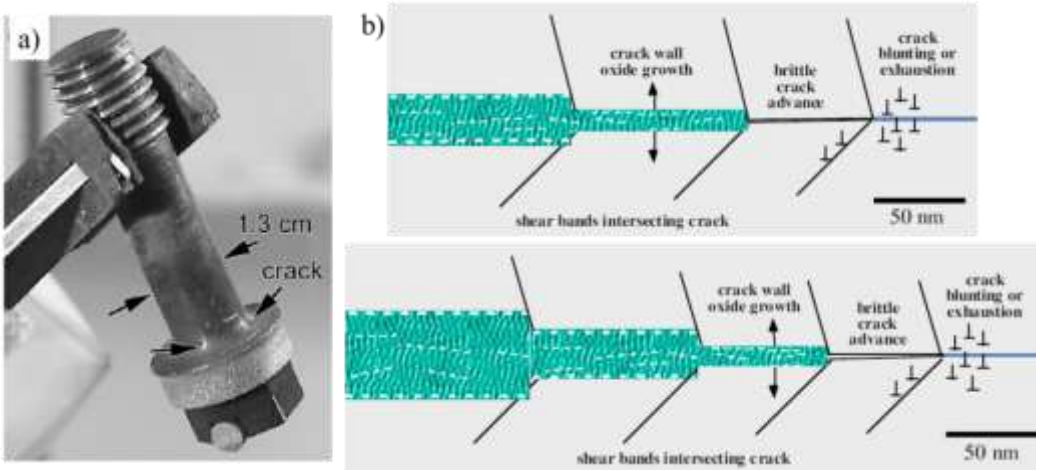

Figure 1-38 : a) Cracks observed on in-service bolt b) Discontinuous cracking mechanism in PWR baffle bolt proposed by Thomas et al.. Crack proceeds in steps of brittle cracking along metal grain boundary followed by oxide formation to fill crack [82].

In post irradiation constant load test conducted on 15 % CW SUS 316 PWR flux thimble tube irradiated to 38 dpa, Fukuya et al. [108] reported to observe a high stress and strain field near the tip along with twins in high stress regions but no evidence of oxides near the crack tip. This led them to conclude that unlike SCC in PWR environment, slip oxidation can't explain the IASCC mechanism as the cracks in latter can propagate without oxides. They also claimed that the crack investigated by Thomas and Bruemmer was an arrested subcrack i.e. it was not active, hence they observed the thin oxide layer continuing up to the crack tip. He also proposed schematics to differentiate amongst the active and arrested crack as shown in Figure 1-39.

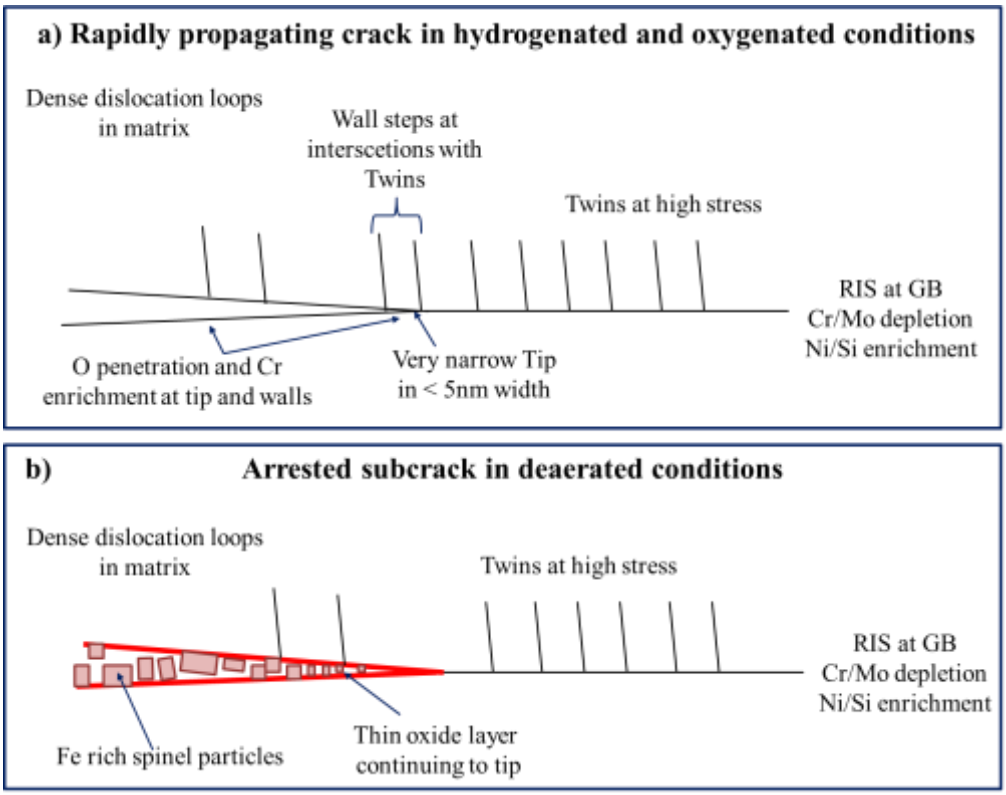

Figure 1-39 : Schematics illustrating a) rapidly growing crack in hydrogenated and oxygenated conditions b) arrested subcrack in deaerated conditions [108].

Not many studies have been done to characterize the crack tip which makes it difficult to conclude the exact role of oxide in crack propagation in IASCC. Nevertheless, it could be concluded that corrosive environment is not sufficient to initiate cracking in the austenitic stainless steel. Interestingly, both studies reported to observe a region of high stress and strain in the vicinity of crack tip pointing towards the possibility of dislocation based mechanism playing the key role. Since then, several studies[9] have proposed localized deformation as one of the key contributor to IASCC. Jiao et al [91] examined the correlation of several factors (SFE, microstructure, localized deformation) with cracking behavior to determine their importance in IASCC by conducting CERT test on proton irradiated austenitic stainless steel in BWR and argon environments. They reported that the correlation strength of SFE with IASCC was 0.5, while that of hardness and RIS was 0.54 and 0.4 respectively. This suggests that SFE and hardness contributes in cracking but are not dominant factor. They found that the maximum correlation strength was of localized deformation (0.88) with IASCC signifying the potential of localized deformation as a prime contributor in IASCC. It cannot be denied that factors such as SFE, microstructure, etc. can influence the degree of localized deformation, thereby indirectly influencing IASCC susceptibility. Hence, though the correlation strength is maximum for the localized deformation, contribution of other factors cannot be ignored.

[9] All these studies are based on dynamic tests (i.e. CERT or SSRT tests).

Was [95] summarized the combination of these various factors to IASCC initiation roughly as per Figure 1-40.

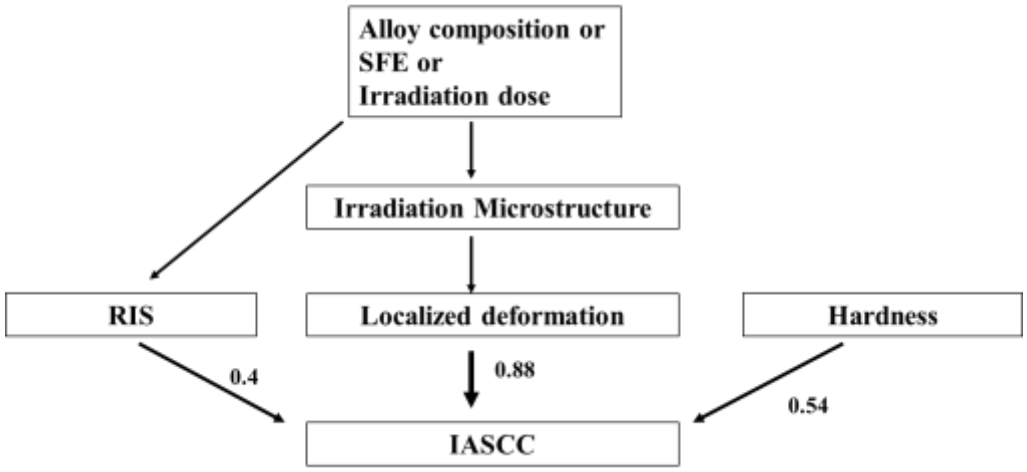

Figure 1-40 : Contribution of SFE, RIS, Hardness and Localized deformation to IASCC initiation. [95].

To pursue further, studies have suggested that the interaction of slip localization with grain boundary is of great interest concerning the intergranular crack initiation in irradiated material. During plastic deformation, channels fed the dislocations to the grain boundaries. This pileup of the dislocation creates higher stresses at the grain boundaries which must be accommodated by the boundary either by transfer of slip across the boundary or by cross slip in the grain boundary region (Figure 1-41).

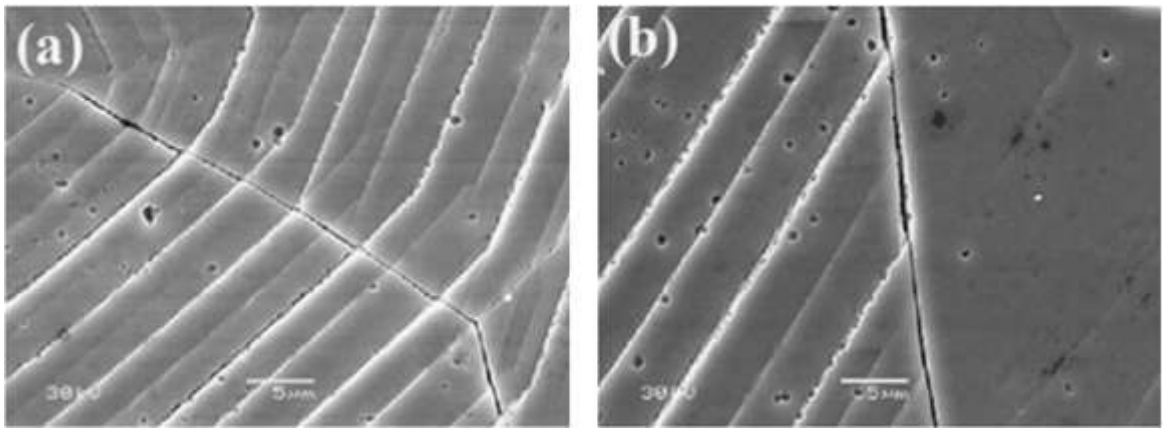

Figure 1-41 : Example of a) slip transfer (or slip continuity) b) no transfer of slip (slip discontinuity) at grain boundaries of proton irradiated 316L specimen following straining to 5 % in 400 °C SCW [109].

There exists another possibility of accommodation of stress by interaction between dislocations in channel and grain boundary dislocations leading to formation of a dislocation in grain boundary plane which is capable to slide the grain boundary if it is mobile. The sliding of the grain boundary will rupture the oxide film above it resulting in

exposure of metal beneath to the solution. This will promote IASCC by slip oxidation type process as presented in Figure 1-42.

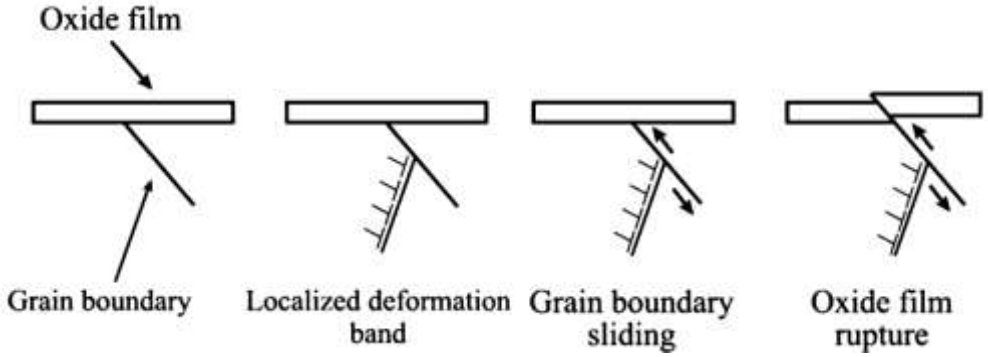

Figure 1-42 : Schematics representing the transfer of slip by dislocation channel to grain boundary resulting in the rupture of oxide film at the grain boundary and causing IGSCC [33].

However, if there is no transfer of slip, the stress at the grain boundaries (due to dislocation pileups) can exceed the grain boundary strength and separation of grain boundaries could occur resulting in formation of wedge cracks. Creation of step also generates shear strain at the grain boundary. Because of this stress/strain concentration, cracks have been observed to initiate at these steps and propagate along the grain boundaries until it meets another step. Nishioka et al. [88, 108] reported that in neutron irradiated austenitic stainless steel, grain boundary separation occurred when the slip lines were discontinuous i.e. one side grain was less deformed and other grain had coarse dislocation channels leading to dislocation pile up at the boundary (Figure 1-43a). They also hypothesized that, in addition to dislocation pileup, high normal stress resolved from tensile stress on the grain boundary plane is a must for the separation to occur (Figure 1-43b). In addition they also found that the separation was prominent for slow strain rate test compared to fast strain rate.

To account for normal stress resolved from tensile stress on the grain boundary plane, as pointed by Nishioka et al. [89], correlation of Schmid Factor (SF) of the grains adjacent to the grain boundaries are used. SF relates the tensile stress to the resolved shear stress in a slip system (Figure 1-44), and appears more promising in interpreting IASCC susceptibility. SF is defined as the product of cosine of the angle with the glide plane (φ) and cosine of the angle with the glide direction (λ) i.e. $f = \cos\varphi \times \cos\lambda$.

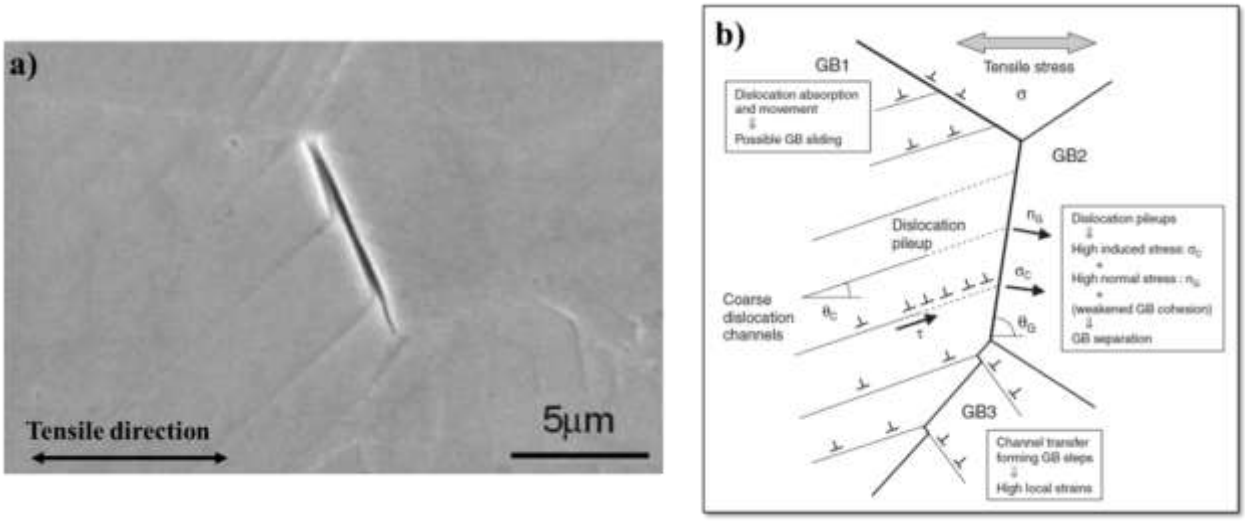

Figure 1-43 : a) crack observed along a grain boundary with slip discontinuity in 73 dpa neutron irradiated austenitic stainless steel [106] b) schematic illustrating the interaction between dislocation channels and grain boundaries [89].

In a FCC, as reported before, there are 12 slip systems and conventionally the SF given to a grain corresponds to the value of the slip system with the highest SF. A high SF values implies that slip will be activated at lower tensile stress. Incompatibility of SF between adjacent grains can lead to stress and strain heterogeneity at grain boundaries and hence has been of great interest. Nishioka [89] hypothesized that in neutron irradiated austenitic stainless steel cracking occurs more readily on the boundaries with a larger difference in SF. They supported this argument by saying that it is due to the higher possibility of deformation occurring in grain with higher SF on one side and no deformation on the other grain with low SF resulting in dislocation pileups.

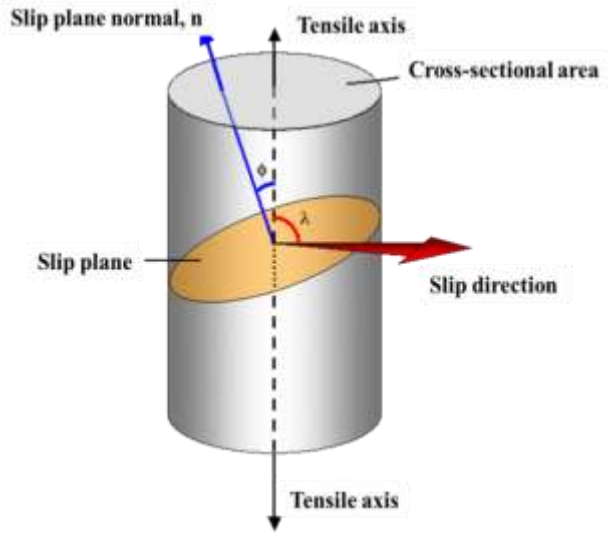

Figure 1-44 : Schematic representation of the Schmid law [18].

As not many studies have been conducted using neutron irradiated material, it poses a problem to validate the hypothesis. To overcome this problem, ion irradiations have been used.

1.3.4. SUMMARY

IASCC is a degradation mechanism resulting from the complex coupling of various parameters. It is necessary to study the effect of each parameter on:

1. Interaction of material with neutrons (or heavy ions, protons, electrons) results in the formation of defect clusters including both interstitial and vacancy types of defects. Majority of the defects recombine and remaining few rearranges themselves to form observable point defects. The microstructural and microchemical defects induced by irradiation includes: Black dots, Frank loops, cavities, precipitates and segregation of alloying elements. All these defects evolve with irradiation dose, temperature and have an influence of initial microstructure
2. At PWR relevant temperatures (290 – 360 °C), irradiation induced microstructure is dominated by Frank loops. Their density and size increase with dose and saturate at 1 – 5 dpa. Cavities and few precipitates have also been reported at this temperature range. Radiation induced segregation results in the depletion of Cr, Fe and enrichment of Ni at the grain boundaries. Depletion of Cr at grain boundaries can enhance the susceptibility to intergranular cracking of the material.
3. These point defects act as an obstacle to dislocation motion resulting in increase in yield strength and reduction in ductility of the material. Yield strength (and hence, hardening) increases with increasing irradiation dose and saturates at around 5 – 10 dpa.
4. Irradiation can modify the oxidation kinetics or by inducing defects in the microstructure of the material which changes the thickness and Cr content in the inner layer thereby, influencing the crack propagation. However, the exact effect of irradiation on oxide formation is still not well understood.
5. Post irradiation annealing performed to investigate the contribution of various parameters to IASCC suggested that neither radiation Induced segregation, nor irradiation microstructure nor irradiation hardening are sole sufficient to initiate IASCC. Deformation mode could be an important controlling parameter.
6. SFE, irradiation induced defects and hardening can influence localized deformation and hence, susceptibility to IASCC. However, correlation of localized deformation with IASCC is the maximum suggesting it could be the prime contributor. Though it is not the sole contributor.

7. Plasticity localization is the most dominant deformation mode observed in irradiated austenitic stainless steel at 300 °C. When slip bands intersect with free surface or grain boundaries, a step is formed. These steps can be characterized by their height, width and spacing.
8. Increase in slip line spacing (hence, degree of localization of deformation) with increasing dose has been reported in neutron irradiated sample.
9. Randomly high angle grain boundaries with high strain incompatibility are more prone to cracking. Further investigation is required in this direction.

1.4. EMULATION OF NEUTRON DAMAGE USING ION IRRADIATION

A thorough understanding of microstructural evolution of materials under irradiation is still required to develop and validate the modelling of irradiation effects and thus maintaining the integrity of reactor core components. This point towards the necessity of conducting more experiments at different damage levels and at different irradiation temperature regions. This will require long term neutron irradiation experiments as in thermal test reactors, damage could be accumulated at a rate of 3 – 5 dpa/year. This delay can highly limit the pace of research. Using fast reactors, a maximum dose rate of 20 dpa/year could be achieved but it has its own drawbacks. The difference in the neutron spectrum could lead to higher defect survival rates whereas difference in flux and temperature could lead to lower defect survivals in PWRs compared to fast reactors. In addition, there persist differences in helium generation rates, radiation induced segregation and radiation hardening.

Besides, handling of highly radioactive samples makes the research programs extremely costly. And very few laboratories are able to carry out experiments with high definition analysis (SEM and APT) on neuron irradiated samples. Ion irradiations have been proposed as one of the possible solution to these problems. Ion irradiation are conducted at high damage rate and are capable of producing damage levels in only few hours that are equivalent to years of reactor exposure with no or little residual radioactivity of the material. Hence, it has an advantage over both time and money. As ion irradiation can be conducted at a well-defined energy, dose rate and temperature, it results in very well controlled experiments. In past, proton, electrons and heavy ion (such as Ni, Fe, Xe) irradiations have been used to replicate some aspects of the neutron damage. The damage state and microstructure resulting from ion irradiation depends on the particle type, the irradiation temperature and the damage rate.

Damage produced by ions is very different from the damage produced by neutrons as well, resulting in very different recoil spectra and hence, different deposited energy. To overcome these differences dpa K-P i.e. the damage calculated using Kinchin and Pease is generally used to address damage induced by ions. Different studies have shown that the

dpa K-P calculated for ion irradiation is in the closest conformity with the dpa_{NRT} for neutron irradiation. Moreover, to obtain the damage profile of ion irradiation, Monte Carlo simulation based software SRIM (The Stopping and Range of Ions in Matter) is used [48]. Using SRIM with the "quick damage" option, dpa K-P for ion irradiation can be calculated. The same will be used in this study to calculate the damage induced by ion irradiations in austenitic stainless steels. The damage induced by ion irradiation will be represented in dpa K-P and damage induced by neutron will be represented in dpa_{NRT} (or simply dpa).

Ion irradiations have some drawbacks too. First being the small penetration depths i.e. displacement damage created by ions is confined to a very small volume of material. The depth profile for proton and heavy ions in comparison to neutrons is shown in Figure 1-45. Heavy ions form displacement cascade similar to neutron but their penetration depth (for 10 MeV) is the least (~2 µm) and the profile is strongly peaked i.e. the damage rate continuously varies. Protons, on the other hand, form smaller displacement cascades compared to neutron but have a relatively flat profile and the penetration depth (for 3.2 MeV) can exceed upto 40 µm. The damaged depth is indeed a function of particle energy and can be increased by increasing particle energy. However, particle energy is indirectly limited by the possibility of activation of sample [111, 112].

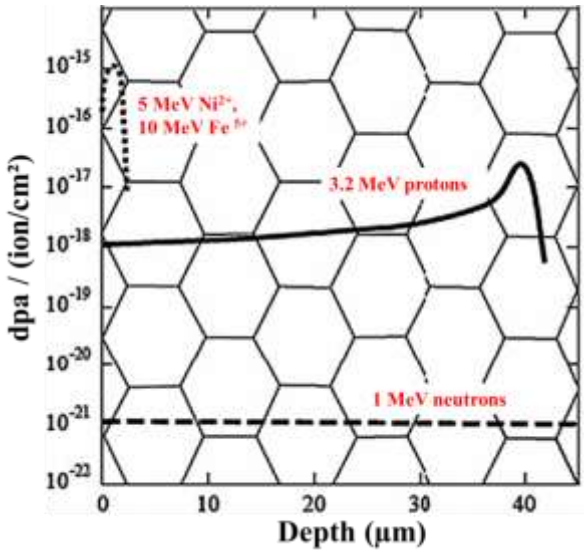

Figure 1-45 : Comparison of irradiation depth profile in austenitic stainless steel of Heavy ions and protons with neutron [112].

High damage rate benefits in gaining time but at the same time raises an issue of "temperature shift" to be addressed to preserve the aggregate behavior of defects during irradiation. This shift is in accordance to the invariance theory proposed by Mansur [113], which suggests that any change in the value of an irradiation variable from reactor conditions needs to be accommodated by a shift in other variable. Based on this theory,

relations between ion irradiation temperature and dose rate for a given dose have been derived to obtain microstructure and microchemistry similar to neutron irradiation and are presented in equations (I.9) and (I.10) respectively [33].

$$T_2 - T_1 = \frac{\frac{kT_1^2}{E_m^v + 2E_f^v} ln\frac{K_{0_2}}{K_{0_1}}}{1 - \frac{kT_1}{E_m^v + 2E_f^v} ln\frac{K_{0_2}}{K_{0_1}}} \quad \text{.....(I.9)}$$

$$T_2 - T_1 = \frac{\frac{kT_1^2}{E_m^v} ln\frac{K_{0_2}}{K_{0_1}}}{1 - \frac{kT_1}{E_m^v} ln\frac{K_{0_2}}{K_{0_1}}} \quad \text{.....(I.10)}$$

Where, T_1 is the neutron irradiation temperature, T_2 is ion irradiation temperature, K_{0_1}, K_{0_2} are the damage rate for neutron and ion irradiations, k is Boltzmann constant, E_m^v is the vacancy migration energy and E_f^v is the vacancy formation energy.

The damage rate for neutron irradiation is of the order 10^{-8} – 10^{-7} dpa/s while for proton and heavy ion irradiations are of the order 10^{-6} dpa/s and 10^{-3} dpa/s. Using a vacancy migration energy of 1.2 eV and vacancy formation energy of 1.8 eV, these formulas yield a temperature shift of 15 °C to obtain similar microstructure and of 63 °C to obtain similar microchemistry using proton irradiation (with damage rate of 10^{-6} dpa/s). As a compromise between the two factors, proton irradiations are generally conducted at a temperature of 350 – 360 °C to imitate neutron damage at ~ 320 °C. Similar arguments yield a temperature shift of around 60 – 80 °C to obtain similar microstructure and around 200 °C to obtain similar microchemistry using heavy ion irradiations.

Incorporating this temperature shifts, several studies [65, 93, 94, 114–124] supported the arguments of possibility of imitating neutron damage using ion irradiations.

Carter et al. [114] studied the microstructure and microchemistry of ultrahigh purity (UHP) 304L irradiated using 3.4 MeV proton at 400°C to a dose of 1 dpa. They observed that the microstructure after proton irradiation consisted of black dots and small faulted loop similar to what has been reported after neutron irradiation. They also reported that the loop size and density was smaller for proton irradiation and attributed the difference to higher irradiation temperature used in the study. Ni enrichment and Cr depletion they observed after proton irradiation were also in accordance with neutron literature [114]. Was et al. [47] compared the microstructure of 3.2 MeV proton irradiated (at 360 °C) 304L and 316L spanning a dose range from 0.3 dpa to 5 dpa with neutron irradiation conducted in Barsebäck boiling water reactor (BWR) at 290 °C. They observed that for all doses, the microstructure consisted of small (< 10 nm) faulted loops for both

irradiations. They agreed with on the observation of smaller Loop size and density after proton irradiation compared to neutron irradiation. However, in both of these studies, full cascade (FC) damage option was used to calculate the damage induced by proton irradiation which is twice the dpa K-P value generally used to compare with neutron damage (dpa NRT). In other study, Cole et al. [93] were successful in inducing microstructure similar to neutron using 5 MeV Ni^{2+} irradiation conducted at 500 °C. Comparison of irradiation induced microstructure for proton, heavy ion and neutron irradiations obtained in various studies is presented in Figure 1-46. As evident, both Frank loops size and density for ion irradiations are in a very good agreement with neutron irradiation especially at low doses. Comparison of irradiation induced microchemistry for proton and neutron irradiated austenitic steel is presented in Figure 1-47.

Beside microstructure and microchemistry, ion irradiation is capable of mimicking irradiation induced changes in mechanical properties (such as radiation hardening, increase in yield strength, etc.). As an example, comparison of percentage increase in hardness observed in neutron and ion irradiated austenitic stainless steels in various studies has been reported in Figure 1-48. Hardness for neutron irradiated material can be evaluated using micro-Vickers hardness test (with a load of 500 g). However, nano indentation tests were used for ion irradiations because of their confined (small) zone of irradiation. As evident, values for proton irradiation are in good accordance while for Fe irradiation the increase was much smaller compared to both neutron and proton irradiation.

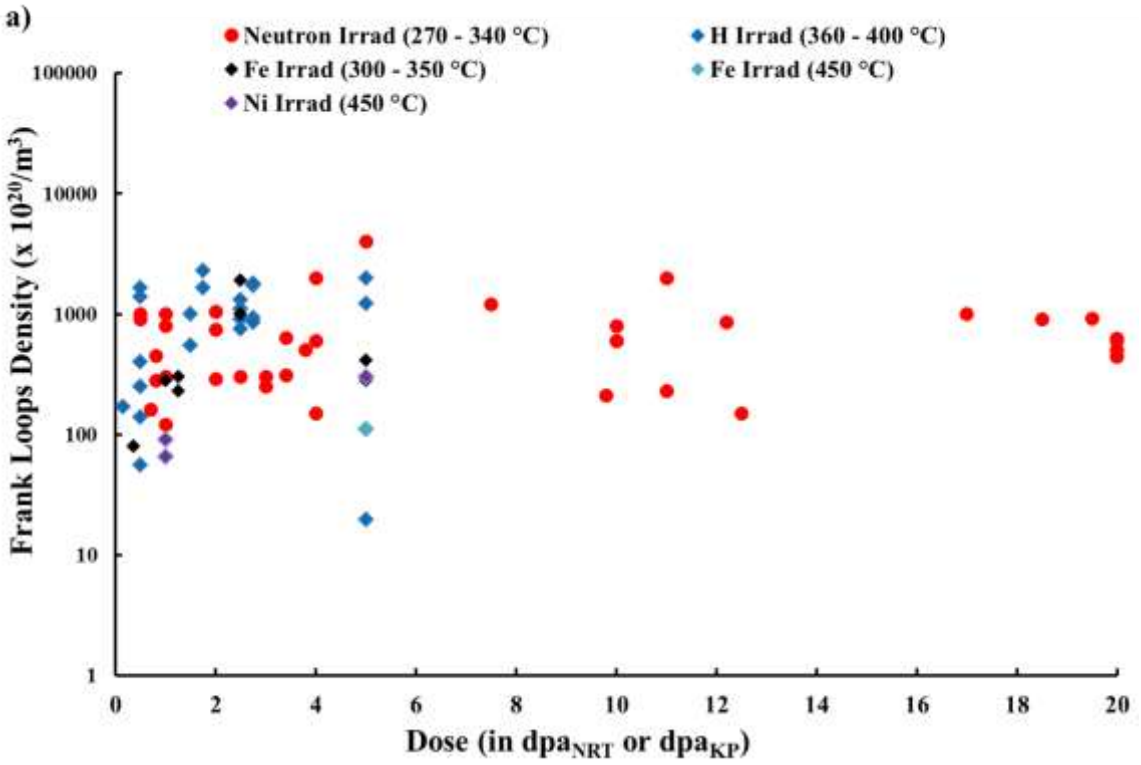

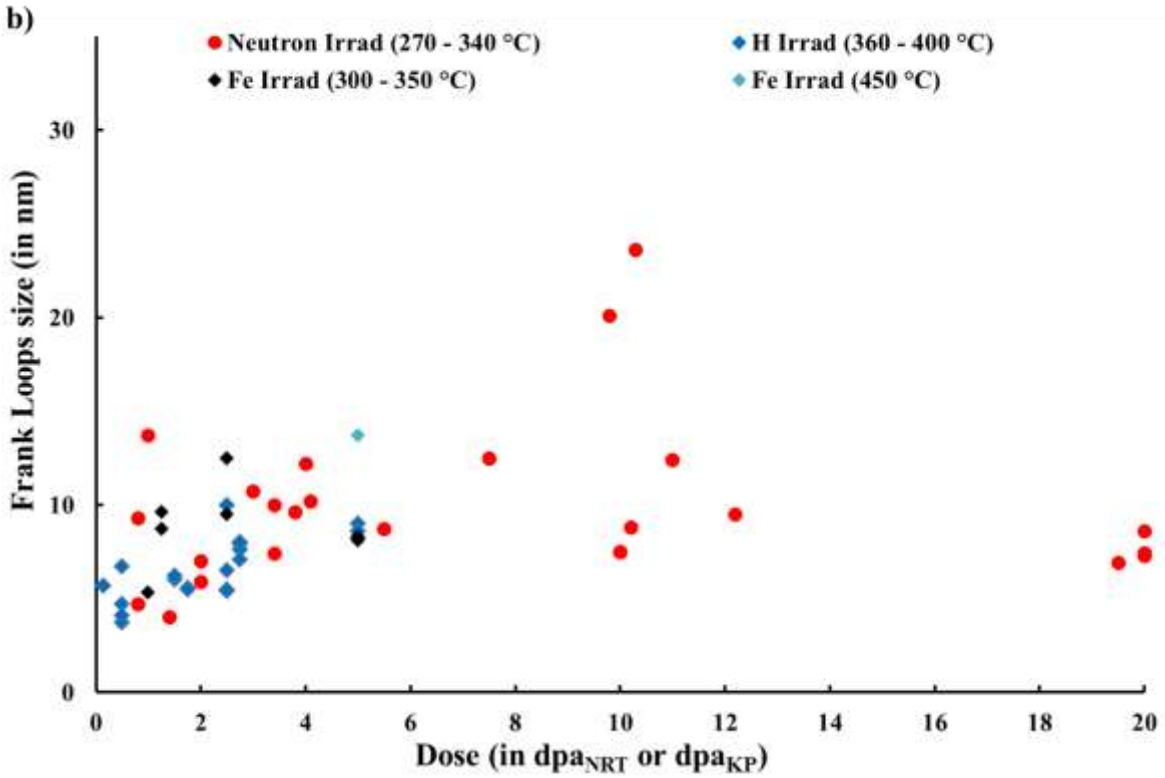

Figure 1-46 : Comparison of the dose dependence of a) Frank Loop density and b) size for austenitic stainless steel irradiated with neutrons at 270 – 340 °C and with protons at 360 – 400 °C and heavy ions at 300 – 500 °C [6, 47- 55, 65, 94, 95, 114 - 119].

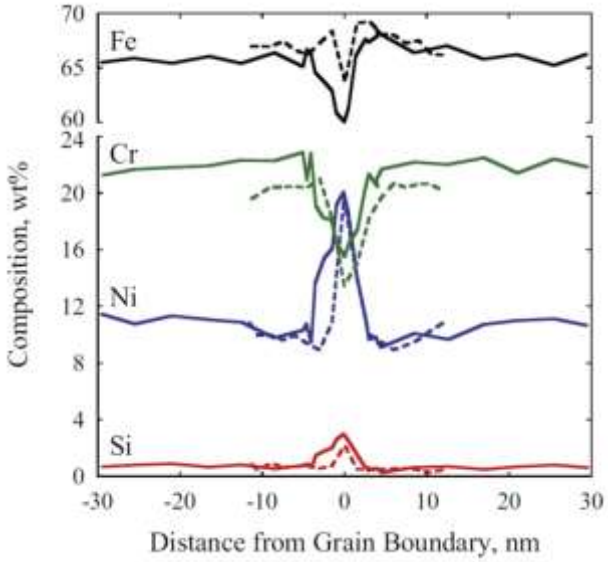

Figure 1-47 : Comparison of grain boundary composition profile for CP 304L post to 5.5 dpa neutron irradiation in BOR-60 fast reactor (solid line) and 5.5 dpa[10] proton irradiation at 360 °C (dashed line) [65].

[10] The author used full cascade damage option while computing the damage using SRIM and therefore, the corresponding dpa – KP value should be ~3 dpa – KP.

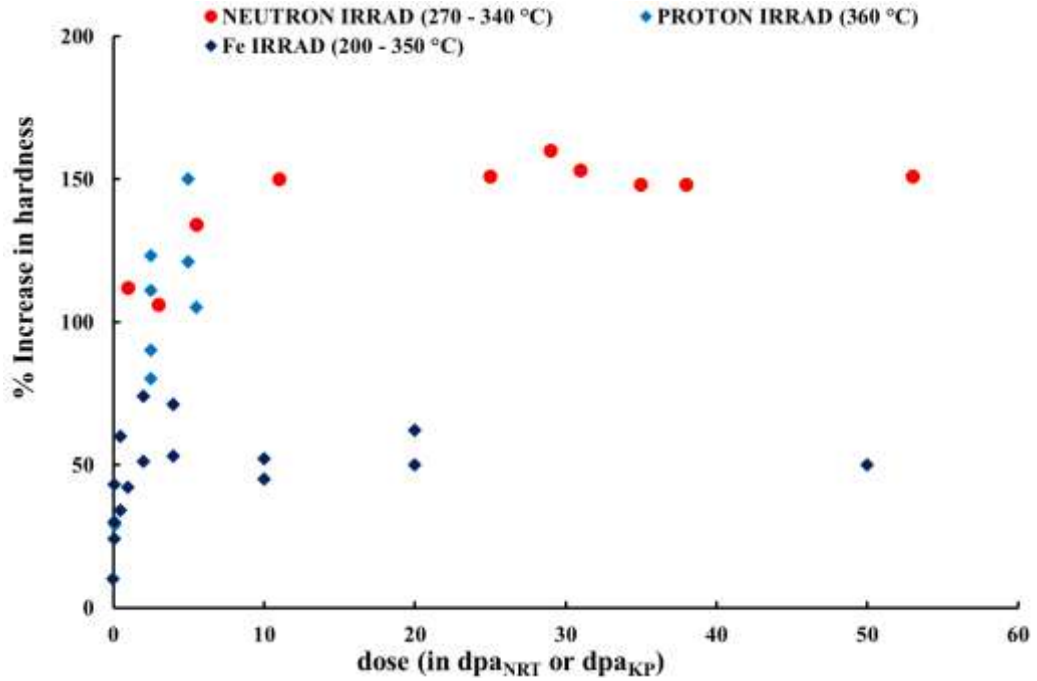

Figure 1-48 : Comparison of the dose dependence of irradiation hardening for austenitic stainless steel irradiated with neutrons at 270 – 340 °C, and with protons at 360 °C and iron ions at 200 – 350 °C[61, 66, 119–124].

Ion irradiation has proved its utility in almost every aspect. However, if ion irradiation needs to be used to study the intergranular cracking of irradiated austenitic stainless steel, it must also result in the deformation mode similar to that in neutron irradiated stainless steel post to dynamic straining. Several studies have proved that dislocation channeling is, indeed, the prime deformation mode for proton and heavy ion (Fe) irradiated austenitic steel at LWR relevant temperatures (Figure 1-49b).

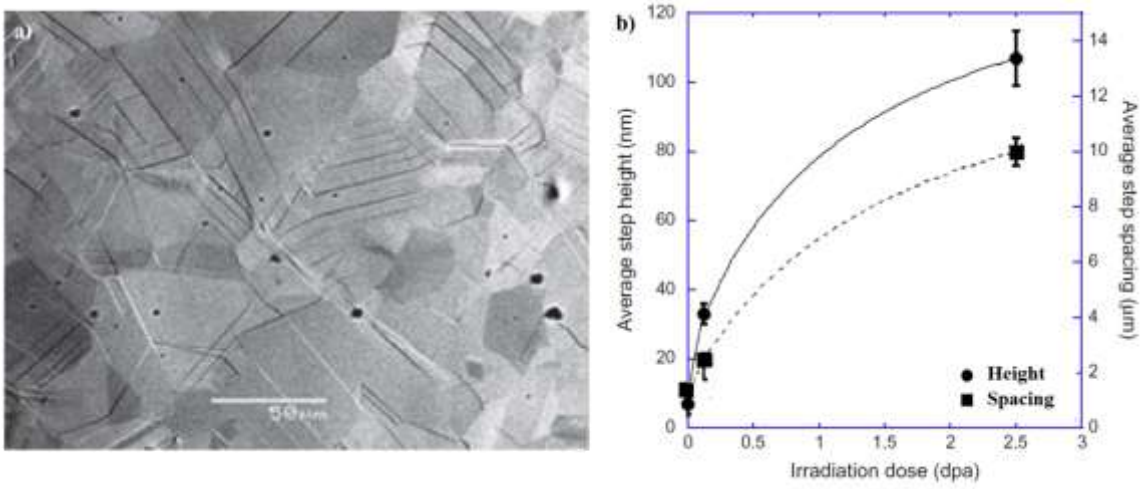

Figure 1-49 : a) Surface slip step morphology b) Average step height and spacing as a function of irradiation dose reported in SUS 304 after 2 MeV proton irradiation to 2.5 dpa at 300 °C and straining in argon at 300 °C to 2 % [121].

Jiao et al. [91] noticed that in proton irradiated austenitic steel strained to 1 %, slip lines spacing and height varied from one grain to another grain as well as within the grain. As the straining was increased (3 %), both channel height and spacing tend to be homogeneous. In other study, Jiao et al. [121] observed increase in step spacing and height with dose for proton irradiated sample similar to what has been reported for neutron irradiated material. In addition, several studies [47, 65] have reported to observe a remarkable agreement between neutron and proton irradiated alloys in correspondence to relative variation in IASCC susceptibility (measured by %IG). These results suggest that the proton irradiation can be used to study the IGSCC of irradiated austenitic steel.

However, within author's knowledge, no study has investigated the mechanisms of IGSCC and the contribution of localized deformation in intergranular cracking of irradiated austenitic stainless steels in PWR environment using heavy ion irradiation. With the possibility to attain high doses (in very less time), heavy ion irradiation offers an ample opportunity which yet has to be explored.

1.4.1. SUMMARY

Dealing with neutron irradiated samples is quite problematic. Need of quick and easy availability of irradiated samples to understand the IASCC has shifted the focus from neutron irradiation to ion irradiation. Taken in account the correct temperature shift (due to high dose rates of ion irradiation), neutron damage can be surrogated using ion irradiation.

1. The microstructure, microchemistry and mechanical properties of ion irradiated samples are in good agreement with that produced by in-core neutron irradiation under the relevant conditions.
2. In ion irradiated steel strained at 300 °C, localization of the deformation is the primary deformation mode. Increase in slip line spacing (hence, degree of localization of deformation) with increasing dose has been reported in neutron, proton irradiated sample.
3. Proton irradiation could be used to study the IGSCC susceptibility of irradiated material. However, no data available regarding the possibility of using heavy ion irradiation to study the cracking susceptibility of irradiated austenitic stainless steel.

1.5. CONCLUSIONS

Austenitic stainless steel was considered to be immune to SCC and hence, has been the prime choice as structural material for PWRs. Exposure to aqueous medium results in formation of Cr rich protective inner layer which imparts corrosion resistance to steel. Susceptibility of austenitic stainless steel to SCC in PWR has recently been observed, especially in material with work hardening and in the presence of dynamic straining.

In addition to cold work, irradiation can enhance the susceptibility to SCC. Indeed, it is a special kind of SCC called Irradiation Assisted Stress Corrosion Cracking which is known to occur under the complex coupling of susceptible material, stress state, irradiation and corrosive environment (Figure 1-50).

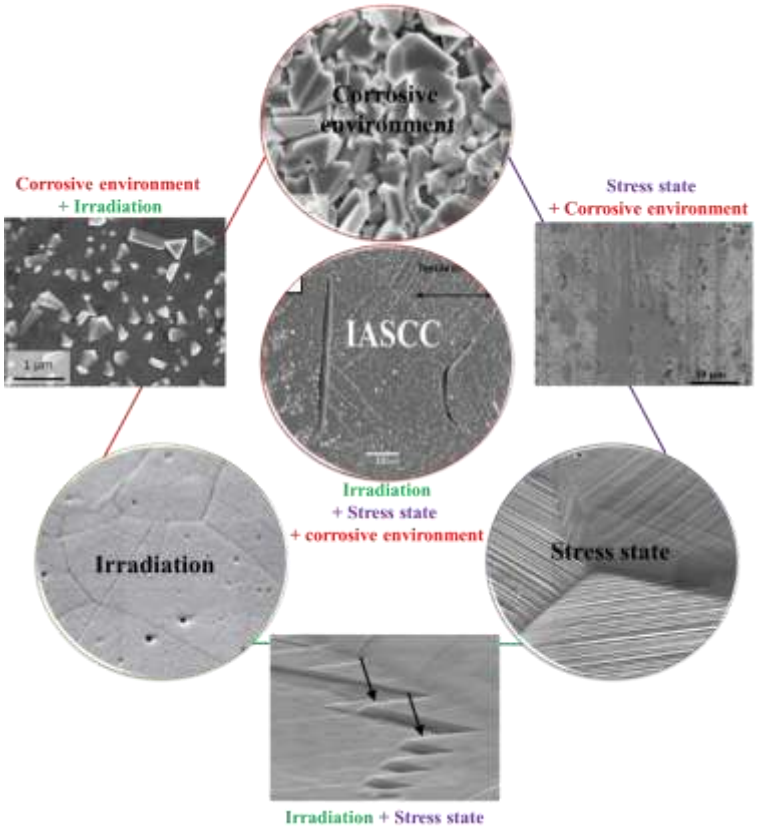

Figure 1-50 : Schematics representing the consequences of coupling of various parameters. Coupling of all four parameters i.e. susceptible material, irradiation, stress state and corrosive environment leads to IASCC.

In PWR, core internals are exposed to high energy particles like neutrons, protons, electrons, heavy ions and alpha particles. Exposure of core internals to the high neutron flux results in formation of point defects in the microstructure thereby, inducing changes in the mechanical properties such as hardening, ductility loss, irradiation creep, IASCC

and potentially swelling. Since 80's, several cases of failure of austenitic stainless steel PWR core internals especially baffle-former bolts have come up. In order to understand the phenomenon of IASCC, few studies have been conducted on neutron irradiated SS 304L austenitic stainless steel.

Post irradiation annealing studies have shown that neither RIS, nor irradiation induced microstructure nor irradiation hardening are sole capable to initiate IASCC. Potential lies in the deformation mode and these factors could serve as the secondary contributors. Studies conducted on neutron irradiated baffle former bolts of PWR revealed the cracks were intergranular in nature and could be a consequence of dislocation based mechanism justifying the findings of post annealing studies. Slip bands are the dominant deformation features observed in irradiated steel at 300 °C. Interaction of these bands with grain boundaries is of great importance especially in concern to crack initiation in irradiated material. When a band interacts with free surface or grain boundary, it results in the formation of steps. These steps are characterized by step height, width and spacing and can give quantitative and qualitative information on the degree of localization of deformation in the material.

Besides, localized deformation, corrosive environment is a necessary condition for intergranular cracking. Irradiation can influence the water chemistry either by radiolysis or by changing the oxidation kinetics at the metal surface. Radiolysis in hydrogenated water cannot result in significant change in corrosion potential and hence, is not a primary issue. Defects induce by irradiation can influence the oxidation kinetics. Changes in the inner layer thickness and Cr enrichment was observed in irradiated samples compared to unirradiated as the diffusion of Cr was enhanced by the defects in former. Some studies suggest an increase in thickness while others, on contrary, suggests a decrease in thickness of inner layer post o irradiation. But all suggests an increase in Cr enrichment in inner layer of irradiated samples and justify it by reporting enhancement of diffusion of Cr by the irradiation induced defects. Higher enrichment of Cr in inner layer of irradiated sample suggests that the material is more protective after irradiation. As the effect of irradiation (beneficial or detrimental) on oxide formation is not yet clear, it remains an open topic for investigation.

To extend the literature and have better understanding of the underlying mechanism of IGSCC, it is necessary to conduct the test on irradiated material over a wide range of dose and in variety of conditions (loading conditions, environmental conditions etc.), which is hardly feasible with neutron irradiation within a single laboratory. As a consequence, ion irradiations have been used to surrogate neutron damage. Using correct temperature shifts, ion irradiation can serve as an efficient tool to isolate the effect of various parameters in IASCC. Indeed, proton irradiation has been successfully used in several studies to investigate the cracking susceptibility of material under different environments (PWR,

inert environments). However, no study has used heavy ion irradiation for the purpose mainly because of its low penetration depths in material. On the basis of understanding of presently available literature, efforts have been made in this study to explore the underlying potential of heavy ions by investigating few aspects of IGSCC of irradiated austenitic stainless steel in corrosive environment.

REFERENCES

1. M. F. McGuire, “Stainless steels for Design Engineers”, ASM International, USA (2008).
2. O. Raquet, E. Herms, F. Vaillant, T. Couvant, “SCC of cold worked austenitic stainless steels in PWR conditions”, Adv. Mater. Sci. 7 (2007) 33 – 45.
3. L. Tribouilloy, F. Vaillant, J-M. Olive, M. Puiggali, “Stress Corrosion Cracking on cold worked austenitic stainless steels in PWR conditions”, Adv. Mat. Sci. 7 (2007) 61 – 69.
4. T. Couvant, F. Vaillant, J. M. Boursier, D. Delafosse, “Effect of strain-path on stress corrosion cracking of AISI 304L stainless steel in PWR primary environment at 360°C”, in proceedings of Eurocorr 2004 (2004).
5. D. Féron, E. Herms, B. Tanguy, “Behavior of stainless steel in pressurized water reactor primary circuits”, J. Nucl. Mat. 427 (2012) 364 – 377.
6. S. M. Bruemmer, E. Simonen, P. M. Scott, P. L. Andersen, G. S. Was, J. L. Nelson, “Radiation-induced material changes and susceptibility to intergranular failure of light water reactor core internals”, J. Nucl. Mat. 274 (1999) 299 – 314.
7. Stress Corrosion Cracking in Light Water Reactors: IAEA Nuclear energy series, No. NP-T-3.13 (2011).
8. M. F. McGuire, “Stainless steels for Design Engineers”, ASM International, USA (2008).
9. P. Marshall, “Austenitic stainless steels: Microstructure and mechanical properties”, Elsevier Applied Science Publisher LTD. (1984).
10. D. Peckner, M. Burnstein, “Handbook of stainless steels”, McGraw-Hill Publishing, (1977).
11. F.B. Pickering, “Physical metallurgical development of stainless steels”, in proceedings of the Conference on Stainless Steels 84 (1984) 2.
12. “Standard specification for chromium and chromium-nickel stainless steel plate, sheet, and strip for pressure vessels and for general applications”, ASTM Designation A 240/A 240M – 15a, Annual Book of ASTM Standards, vol. 01.03, American Society for Testing and Materials, (2015).
13. I. Karaman, H. Sehitoglu, Y. I. Chumlyakov, H. J. Maier, “The deformation of low stacking fault energy austenitic steels”, JOM 54 (2002) 31 – 37.
14. T. Angel, “Formation of martensite in austenitic stainless steels”, J. Iron Steel Inst. (1954) 165-174.
15. L. Remy, “Kinetics of FCC deformation twinning and its relationship to stress strain behavior”, Mat. Sci. Eng. 36 (1978) 47 – 63.
16. T. S. Byun, N. Hashimoto, K. Farrell, “Deformation mode map of irradiated 316 stainless steel in true stress – dose space”, J. Nucl. Mat. 351 (2006) 303 – 315.
17. W. Karlsen, G. Diego, B. Devrient, “Localized deformation as a key precursor to initiation of intergranular stress corrosion cracking of the austenitic stainless steels employed in nuclear power plants”, J. Nucl. Mat. 406 (2010) 138-151.
18. E. Schmid, W. Boas, “Plasticity of crystals”, F.A. Hughes, 1950.

19. C. M. Branco, L. G. Rosa, “Advances in fatigue science and technology”, Springer (1989).
20. A. W. Thompson, “Current status of the role of hydrogen in stress corrosion cracking”, Mater. Sci. and Engg. 43 (1980) 41 – 46.
21. D. C. Belo, M. Walls, N. E. Hakiki. J. Corset, E. Picquenard, G. Sagon, D. Noel, “Composition, structure and properties of the oxide films formed on the stainless steel 316 in primary water type PWR environment”, Corr. Sci. 40 (1998) 447 – 463.
22. B. Stellwag, “The mechanism of oxide films formation on austenitic stainless steel in high temperature water”, Corr. Sci. 40 (1998) 337 – 370.
23. S. Perrin, L. Marchetti, C. Duhamel, M. Sennour, F. Jomard, “Influence of irradiation on the oxide film formed on 316L stainless steel in PWR Primary water”, Oxid. Metals 80 (2013) 623 – 633.
24. T. Terachi, K. Fujii, K. Arioka, “Microstructural characterization of SCC crack tip and oxide film for SUS 316 stainless steel in simulated PWR primary water at 320 °C”, J. Nucl. Sci. and Tech. 42 (2005) 225 – 232.
25. T. Terachi, T. Yamada, T. Miyamoto, K. Arioka, K. Fukuya, “Corrosion behavior of stainless steel in simulated PWR Primary water – Effect of chromium content in alloys and dissolved hydrogen”, J. Nucl. Sci. and Tech. 45 (2008) 975 – 984.
26. N. E. Hakiki, S. Boudin, B. Rondot, D. C. Belo, “The electronic structure of passive film formed on stainless steel”, Corr. Sci. 37 (1995) 1809 – 1822.
27. D. H. Lister, R. D. Davidson, E. McAlpine, “The mechanism and kinetics of corrosion products release from stainless steel in Lithiated High Temperature Water”, Corr. Sci. 27 (1987) 113 – 140.
28. R. Soulas, “Effet de la cristallographie sur les premiers stades de l’oxydation des aciers austénitiques 316 L”, PhD Thesis, Université de Grenoble (2012).
29. R. L. Tapping, R. D. Davidson, E. McAlpine, D. H. Lister, “The composition and morphology of the oxide films formed on type 304 stainless steel in Lithiated high temperature water”, Corr. Sci. 26 (1986) 563 – 576.
30. S. Cissé, L. Laffont, B. Tanguy, M-C. Lafont, E. Andrieu, “Effect of surface preparation on the corrosion of austenitic stainless steel 304L in high temperature steam and simulated water”, Corr. Sci. 56 (2012), 209-216.
31. S. Ghosh, M. K. Kumar, V. Kain, “High temperature oxidation behavior of AISI 304L stainless steel: Effect of surface working operations”, App. Surf. Sci. 264 (2013) 312 – 319.
32. A. Herbelin, T. Couvant, L. Legras, D. Delafosse, G. Ilbevare, “Oxidation of austenitic stainless steels in PWR primary water”, in proceedings of Eurocorr 2009, (2009) 1592 – 1608.
33. G. Was, “Fundamentals of Radiation Materials Science: Metals and Alloys”, Springer, (2007).
34. K. N. Lyon, T. J. Marrow, S. B. Lyon, “Influence of milling on the development of stress corrosion cracks in austenitic stainless steel”, J. Mat. Proc. Tech. 218 (2015) 32 – 37.

35. P. L. Anderson, F. P. Ford, “Life prediction by mechanistic modeling and system monitoring of environmental cracking of Iron and Nickel alloys in aqueous system”, Mat. Sci. and Engg. A103 (1988) 167 – 184.
36. D. Crawford, G.S. Was, "The role of grain boundary misorientation on the intergranular cracking behavior of Ni-16Cr-9Fe in 360°C argon and high purity water," Metall. Trans. A 23A (1992) 1195-1206.
37. V. Y. Gertsman, S. M. Bruemmer, “Study of grain boundary character along intergranular stress corrosion crack paths in austenitic alloys”, Acta Mater. 49 (2001) 1589 – 1898.
38. W. M. Kane, C. J. McMahon, “Part II: Effects of Grain-Boundary Structure on the path of cracking in polycrystals”, Matls Sci. & Eng. A 507 (2009) 61-65.
39. S. Ghosh, V. P. S. Rana, V. Kain, V. Mittal, S. K. Baveja, “Role of residual stress induced by industrial fabrication on stress corrosion cracking susceptibility of austenitic stainless steel”, Mat. Desg. 32 (2011) 3823 – 3831.
40. S. Ghosh, V. Kain, “Microstructural changes in AISI 304L stainless steel due to surface machining: Effect on its susceptibility to chloride stress corrosion cracking”, J. Nucl. Mat. 403 (2010) 62 – 67.
41. M. R. Gilbert, S. L. Dudarev, D. Nguyen-Manh, S. Zheng, L. W. Packer, J. Ch. Sublet, “Neutron induced dpa, transmutation, gas production, and helium embrittlement of fusion materials”, J. Nucl. Mat. 442 (2013) S755 – S760.
42. “Irradiation-Assisted Stress Corrosion Cracking Behavior of Austenitic Stainless Steels Applicable to LWR Core Internals”, Argonne National Laboratory, NUREG/CR-6892, ANL-04/10, 2006.
43. O. K. Chopra, “Degradation of LWR core internal materials due to neutron irradiation”, NUREG/CR-7027, ANL-10/11, 2010.
44. “Development of Radiation Resistant Reactor Core Structural Materials”, 51st IAEA General Conference, (2007).
45. C. Dethloff, “Modeling of helium bubble nucleation and growth in neutron irradiated RAFM steels”, KIT Scientific Publishing, (2012).
46. “Standard practice for neutron radiation damage simulation by charged particle irradiation”, ASTM Designation E 521-89, Annual Book of ASTM Standards, vol. 12.02, American Society for Testing and Materials, (1989).
47. G. S. Was, J. T. Busby, T. Allen, E. A. Kenik, A. Jenssen, S. M. Bruemmer, J. Gan, A. D. Edwards, P. M. Scott, P. L. Andersen, “Emulation of neutron irradiation effects with protons: validation of principle”, J. Nucl. Mat. 300 (2002) 198 – 216.
48. R. E. Stoller, M. B. Toloczko, G. S. Was, A. G. Ceertain, S. Dwaraknath, F. A. Garner, “On the use of SRIM for computing radiation damage exposure”, Nucl. Instrum. and Met. Phy. Res. B 310 (2013) 75 – 80.
49. S. J. Zinkle, P. J. Maziasz, R. E. Stoller, “Dose dependence of the microstructural evolution in neutron irradiated austenitic stainless steel”, J. Nucl. Mat. 206 (1993) 266 – 286.

50. D. Edwards, E. Simonen, S. M. Bruemmer, "Evolution of fine scale defects in stainless steels neutron irradiated at 275 °C", J. Nucl. Mat. 317 (2003) 13 – 31.
51. P. J. Maziasz, "Overview of microstructural evolution in neutron irradiated austenitic stainless steels", J. Nucl. Mat. 205 (1993) 118 – 145.
52. C. Pokor, Y. Bréchet, P. Dubuisson, J. P. Massoud, A. Barbu, "Irradiation damage in 304 and 316 stainless steels: experimental investigation and modeling. Part I: Evolution of the microstructure", J. Nucl. Mat. 326 (2004) 19 – 29.
53. D. Edwards, E. Simonen, S. M. Bruemmer, P. Efsing, "Microstructural evolution in neutron irradiated stainless steels: comparison of LWR and Fast reactor irradiations", in proceedings of 12th international conference on Environmental degradation of materials in nuclear power systems – water reactors (2005).
54. Y. Yang, Y. Chen, Y. Huang, T. Allen, A. Rao, "Irradiation microstructure of austenitic steels and cast steels irradiated in the BOR 60 reactor at 320 °C", in proceedings of 15th international conference on Environmental degradation of materials in Nuclear Power Systems – Water Reactors (2011).
55. A. Renault, J. Malaplate, C. Pokor, P. Gavoille, "TEM and EFTEM characterization of solution annealed 304L stainless steel irradiated in PHENIX, up to 36 dpa and at 390 °C", J. Nucl. Mat. 421 (2012) 124 – 131.
56. D. Féron, "Nuclear corrosion science and engineering", Woodhead Publishing, (2012).
57. D. Edwards, E. Simonen, F. A. Garner, L. R. Greenwood, B. M. Oliver, S. M. Bruemmer, "Influence of irradiation temperature and dose gradients on the microstructural evolution in neutron irradiated 316 SS", J. Nucl. Mat. 317 (2003) 32 – 45.
58. A. Renault, C. Pokor, J. Garnier, J. Malaplate, "Microstructure and grain boundary chemistry evolution in austenitic stainless steels irradiated in the bor-60 reactor up to 120 dpa", in proceedings of 14th international conference on Environmental degradation of materials in nuclear power systems 2009.
59. Y. Miwa, T. Tsukada, H. Tsuji, H. Nakajima, "Microstructure of type 316 model alloys neutron irradiated at 513 K to 1 dpa", J. Nucl. Mat. 271&272 (1999) 316 – 320.
60. K. Fukuya, K. Fujii, H. Nishioka, Y. Kitsunai, "Evolution of microstructure and microchemistry in cold worked 316 stainless steels under PWR Irradiations", J. Nucl. Sci. and Tech. 43 (2006) 159 – 173.
61. B. Radiguet, A. Etienne, P. Pareige, X. Sauvage, R. Valiev, "Irradiation behavior of nanostructured 316 austenitic stainless steel ", J. Mat. Sci. 43 (2008) 7338.
62. R. E. Stoller, G. R. Odette, "A comparison of the relative importance of helium and vacancy accumulation in void nucleation", in proceedings of 13th international symposium on Radiation induced changes in microstructure (1986).
63. P. J. Maziasz, "Some effects of increased helium content on void formation and solute segregation in neutron irradiated type 316 stainless steel", J. Nucl. Mat. 108 & 109 (1982) 359 – 384.

64. R. E. Stoller, A.V. Barashev, S. I. Golubov, "Low temperature swelling in LWR internal components: current data and modeling assessment", Light Water Reactor Sustainability Program, ORNL/LTR-2012/390.
65. K. J. Stephenson, G. S. Was, "Comparison of the microstructure, deformation and crack initiation behavior of austenitic stainless steel irradiated in-reactor or with protons", J. Nucl. Mat. 456 (2015) 85-98.
66. K. Ehrlich, N. H. Packan, "Voids resulting from fast neutron irradiation of a stabilized stainless steel", J. Nucl. Mat. 46 (1973) 77 – 85.
67. H. R. Brager, F. A. Garner, "Dependence of void formation on phase stability in neutron irradiated type 316 stainless steel", in proceedings of 9th International symposium on Effects of radiation on structural materials 1978.
68. P. G. Tipping, "Understanding and mitigation ageing in nuclear power plants: Materials and operational aspects of plant life (PLiM)", Woodhead Publishing series in energy 2010.
69. M. Horiki, M. Kiritani, "Microstructural evolution in low dose neutron irradiated Fe-16Ni-15Cr alloy", J. Nucl. Mat. 212-215 (1994) 246-251.
70. M. Zouari, "Modélisation par dynamique d'amas des évolutions microstructurales et du gonflement sous irradiation dans les aciers inoxydables austénitiques", PhD Thesis, Université de Grenoble (2012).
71. G. S. Was, S. M. Bruemmer, "Effects of irradiation on intergranular stress corrosion cracking", J. Nucl. Mat. 216 (1994) 326 – 347.
72. G. S. Was, J. T. Busby, "Role of irradiated microstructure and microchemistry in irradiated assisted stress corrosion cracking", Phil. Mag. 85 (2005) 443 – 465.
73. P. Scott, "A review of irradiation assisted stress corrosion cracking", J. Nucl. Mat. 211 (1994) 101 – 122.
74. A. J. Jacob, G. E. C. Bell, C. M. Shepherd, G. P. Wozadlo, "High temperature solution annealing as an IASCC mitigating technique", in proceedings of 5th international conference on Environment degradation of materials in Nuclear Power Systems – Water Reactors (1992) 917.
75. A. J. Jacobs, R. E. Clausing, L. Heatherly, R. M. Kruger, "Irradiation assisted stress corrosion cracking and grain boundary segregation in heat treated type 304 SS" in proceedings of 14th international symposium on Effects of radiations on materials (1989) 424.
76. A. Etienne, "Etudes des effets d'irradiation et de la nanostructuration dans des aciers austénitiques inoxydables ", PhD Thesis, Université de Rouen (2009).
77. O. K. Chopra, A. S. Rao, "A review of irradiation effects on LWR core internal materials – IASCC susceptibility and crack growth rates of austenitic stainless steels", J. Nucl. Mat. 409 (2011) 235 – 256.
78. E. A. Kenik, K. Hojou, "Radiation induced segregation in austenitic stainless steels", J. Nucl. Mat. 1331 (1992) 191 – 194.

79. G. S. Was, J. P. Wharry, B. Frisbie, B. D. Wirth, D. Morgn, J. D. Tucker, T. R. Allen, "Assessment of radiation induced segregation mechanism in austenitic and ferritic-martensitic alloys", J. Nucl. Sci. and Tech. 411 (2011) 41 – 50.
80. T. R. Allen, J. I. Cole, E. A. Kenik, T. Yoshitake, G. S. Was, "Analyzing the effect of displacement rate on radiation induced segregation in 304 and 316 stainless steels by examining irradiated EBR-II components and samples irradiated with protons", J. Nucl. Mat. 376 (2008) 169 – 173.
81. N. Hashimoto, E. Wakai, J. P. Robertson, "Relationship between hardening and damage structure in austenitic stainless steel 316LN irradiated at low temperature in the HFIR", J. Nucl. Mat. 273 (1999) 95 – 101.
82. L.E. Thomas and S.M. Bruemmer, "Analytical transmission electron microscopy characterization of stress corrosion cracks an irradiated type 316 stainless steel core component", in proceedings of Fontevraud 5 International Symposium (2002): Contribution of materials investigation to the resolution of problems encountered in pressurized water reactors (2002) 1037 – 1048.
83. C. Bailat, F. Gröschel, "Deformation mode of proton and neutron irradiated stainless steels", J. Nucl. Mat. 276 (2000) 283 – 288.
84. S. Kotrechko, V. Dubinko, N. Stetsenko, D. Terentyev, X. He, M. Sorokin, "Temperature dependence of irradiation hardening due to dislocation loops and precipitates in RPV steels and model alloys", J. Nucl. Mat. 464 (2015) 6–15.
85. C. Pokor, Y. Bréchet, P. Dubuisson, J. P. Massoud, X. Averty, "Irradiation damage in 304 and 316 stainless steels: experimental investigation and modeling. Part II: Irradiation induced hardening", J. Nucl. Mat. 326 (2004) 30 – 37.
86. G. E. Lucas, "The evolution of mechanical property change in irradiated austenitic stainless steels", J. Nucl. Mat. 206 (1993) 287 – 305.
87. K. V. Tsay, O. P. Maksimkin, L. G. Turubarova, O. V. Rofman, F. A. Garner, "Microstructural defect evolution in neutron irradiated 12Cr18Ni9Ti stainless steel during subsequent isochronous annealing", J. Nucl. Mat. 439 (2013) 148 – 158.
88. J. T. Busby, M. C. Harsh, G. S. Was, "The relationship between hardness and yield stress in irradiated austenitic and ferritic steels", J. Nucl. Mat. 336 (2005) 267 – 278.
89. H. Nishioka, K. Fukuya, K. Fujii, Y. Kitsunai, "Deformation structure in highly irradiated stainless steels", J. Nucl. Sci. and Tech. 45 (2008) 274 – 287.
90. Z. Jiao, G. S. Was, "Localized deformation and IASCC initiation in austenitic stainless steels", J. Nucl. Mat. 382 (2008) 203 – 209.
91. Z. Jiao, G. S. Was, "Impact of localized deformation on IASCC in austenitic stainless steels", J. Nucl. Mat. 408 (2011) 246 – 256.
92. K. Farrell, T. S. Byun and N. Hashimoto, "Deformation mode maps for tensile deformation of neutron irradiated structural materials, J. Nucl. Mat. 335 (2004) 471.
93. J. I. Cole, S. M. Bruemmer, "Post irradiation deformation characteristics of heavy ion irradiated 304L SS", J. Nucl. Mat. 225 (1995) 53.

94. Z. Jiao, J. T. Busby, G. S. Was, "Deformation microstructure of proton irradiated stainless steels", J. Nucl. Mat. 361 (2007) 218 – 227.
95. G. S. Was, "Localized deformation as a primary cause of irradiation assisted stress corrosion cracking", University of Michigan Report – DE – FG07 – 05ID14703 (2009).
96. T. N. Agaev, "Effect of irradiation on preliminarily radiation – oxidation – treated stainless steel", Met. Sci. and Heat Treat. 51 (2009) 49 – 51.
97. Y. Nemoto, Y. Miwa, Y. Kaji, T. Tsukada, "Effect of ion irradiation and implantation of H and He on the corrosion behavior of austenitic stainless steel", J. Nucl. Mat. 43 (2005) 313 – 317.
98. M. Dumerval, "Effet des défauts d'implantation sur la corrosion des aciers inoxydables austénitiques en milieu primaire des réacteurs à eau pressurisée", PhD. Thesis, Université de Grenoble, (2014).
99. K. Fukuya, H. Nishioka, K. Fujii, Y. Kitsunai, "Characterization of surface oxides formed on irradiated stainless steels in simulated PWR primary water", in proceedings of Fontevraud 8 international symposium (2014): Contribution of materials investigations and operating experience to LWRs' safety, performance and reliability, (2014).
100. G. S. Was, B. Alexandreanu, J. Busby, "Localized deformation induced IGSCC and IASCC of austenitic alloys in high temperature water", Key Eng. Mat. J. Nucl. Mat. 261 (2004) 885 – 892.
101. K. Takakura, K. Nakata, M. Ando, K. Fujimoto, E. Wachi, "Lifetime evaluation for IASCC initiation of cold worked 316 stainless steel's BFB in PWR primary water", in proceedings of 13th international conference on Environmental degradation of materials in nuclear power system – water reactors (2007).
102. C. G. Rhodes, A. W. Thompson, "The composition dependence of stacking fault energy in austenitic stainless steels", Met. Trans. A. 8A (1977) 1901 – 1906.
103. R. E. Schramm, R. P. Reed, "Stacking fault energies of seven commercial austenitic stainless steels", Met. Trans. A. 6A (1975) 1345 – 1351.
104. K. Fukuya, M. Nakano, K. Fujii, T. Torimaru, Y. Kitsunai, "Separation of microstructural and microchemical effects in irradiation assisted stress corrosion cracking using Post-Irradiation Annealing", J. Nucl. Sci. and Tech. 41 (2004) 1218 – 1227.
105. J. T. Busby, G. S. Was, E. A. Kenik, "Isolating the effect of radiation induced segregation in irradiation assisted stress corrosion cracking of austenitic stainless steels", J. Nucl. Mat. 302 (2002) 20 – 40.
106. R. Katsura, J. Morisawa, S. Kawano, B. M. Oliver, "Post irradiation annealing effect on helium diffusivity in austenitic stainless steels", J. Nucl. Mat. 329 – 333 (2004) 668 – 672.
107. M. C. Hash, L. M. Wang, J. T. Busby, G. S. Was, "The effect of hardening source in proton irradiation assisted stress corrosion cracking of cold worked type 304 stainless steel", in proceedings of 21st international symposium on effects of radiation on materials, (2004).
108. K. Fukuya, H. Nishioka, K. Fujii, Y. Kitsunai, "Characterization of IASCC crack tips in highly irradiated stainless steels", in proceedings of ICGEAC (2009).

109. E. A. West, G. S. Was, "Strain incompatibilities and their role in intergranular cracking of irradiated 316 L stainless steel", J. Nucl. Mat. 441 (2013) 623 – 632.
110. K. Fukuya, H. Nishioka, K. Fujii, T. Miura, T. Torimaru, "An EBSD examination of SUS 316 stainless steel irradiated to 73 dpa and deformed at 593 K", J. Nucl. Mat. 417 (2011) 958 – 962.
111. G.S. Was, R.S. Averback, "Radiation damage using ion beams", Elsevier, 2012.
112. G. S. Was, T. Allen, "Radiation induced segregation in multi component alloys: effect of particle type", Mater. Charact. 32 (1994) 239 – 255.
113. L. K. Mansur, "Theory of transitions in dose dependence of radiation effects in structural alloys", J. Nucl. Mat. 206 (1993) 306.
114. R.D. Carter, D. L. Damcott, M. Atzmon, G. S. Was, E. A. Kenik, "Effects of proton irradiation on the microstructure and microchemistry of type 304 L stainless steel", J. Nucl. Mat. 205 (1993) 361 – 373.
115. B. H. Sencer, G. S. Was, M. Sagisaka, Y. Isobe, G. M. Bond, F. A. Garner, "Proton irradiation emulation of PWR neutron damage microstructures in solution annealed 304 and cold worked 316 stainless steels", J. Nucl. Mat. 323 (2003) 18 – 28.
116. M. Millier, "Fragilisation des aciers inoxydables austénitiques sous irradiation: évolution de la microstructure et amorçage de la corrosion sous contrainte assistée par l'irradiation en milieu REP", PhD Thesis, Mines Paris Tech, (2012).
117. G. S. Was, "Recent developments in understanding irradiation assisted stress corrosion cracking", in proceedings of 11th international conference on Environmental degradation of materials in nuclear power system – water reactors (2003).
118. M. Bertrand, "Caractérisation du gonflement et de la microstructure des aciers représentatifs des internes inférieurs de REP par irradiations aux particules chargées" First year thesis progress report, CEA (2005).
119. T. Miura, K. Fujii, H. Nishioka, K. Fukuya, "Effect of hydrogen on interaction between dislocations and radiation induced defects in austenitic stainless steels", J. Nucl. Mat. 442 (2013) S735 – S739.
120. T. Miura, K. Fujii, K. Fukuya, Y. Ito, "Characterization of deformation structure in ion irradiated stainless", J. Nucl. Mat. 386 – 388 (2009) 210 – 213.
121. Z. Jiao, G. S. Was, T. Miura, K. Fukuya, "Aspects of ion irradiations to study localized deformation in austenitic stainless steels", J. Nucl. Mat. 452 (2014) 328 – 334.
122. A. Lupinacci, K. Chen, Y. Li, M. Kunz, Z. Jiao, G. S. Was, M. D. Abad, A. M. Minor, P. Hosemann, "Characterization of ion beam irradiated 304 stainless steel utilizing nanoindentation and Laue microdiffraction", J. Nucl. Mat. 458 (2015) 70 – 76.
123. T. Miura, K. Fujii, K. Fukuya, K. Takashima, "Influence of crystal orientation on hardness and nanoindentation deformation in ion irradiated stainless steels", J. Nucl. Mat. 417 (2011) 984 – 987.
124. J. D. Hunn, E. H. Lee, T. S. Byun, L. K. Mansur, "Helium and hydrogen induced hardening in 316 LN stainless steel", J. Nucl. Mat. 282 (2000) 131 – 136.

CHAPTER 2. MATERIAL INVESTIGATION

2.1. INTRODUCTION

Majority of the core internals are made up of either SA 304L SS (eg. baffle former plates) or CW 316 SS (eg. baffle former bolts). Observation of baffle bolts (CW 316 SS) cracking during their service period emphasized the need of investigation of IASCC. The behavior (microstructure, microchemistry and mechanical properties) of these two materials (Figure 2-1) post irradiation has been observed to follow same trend [1, 2], with 304 being more susceptible to IASCC. Besides, the microstructure of Solution Annealed material is easier to characterize compared to Cold Worked material simply because density of initial dislocations present in the former is much lower compared to latter (~ 10^{11} m^2 in SA and ~ 10^{14} – 10^{15} m^2 in CW material). Hence, the choice of SA 304 L (where L stands for low carbon content) as the study material was made.

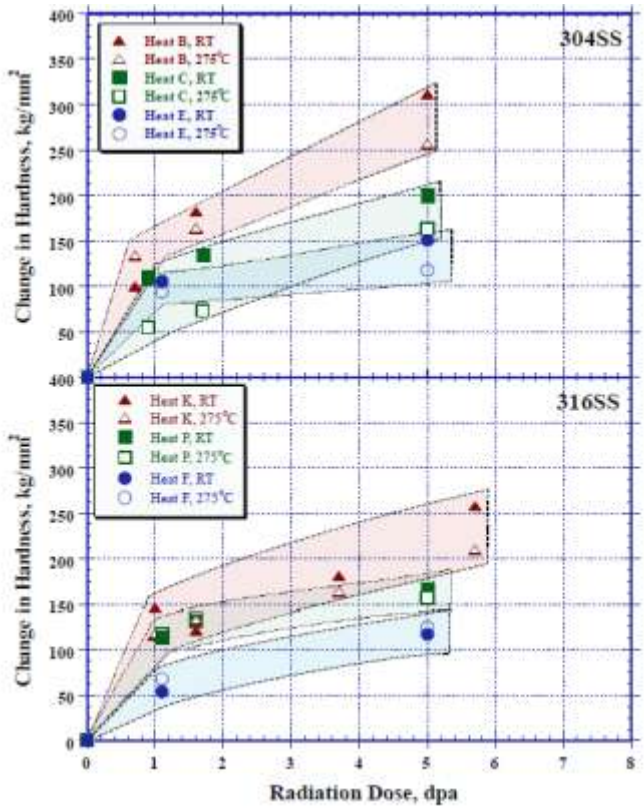

Figure 2-1: Comparison of the increase in hardness observed in 304 SS and 316 SS post neutron irradiation in a BWR at 275 °C [2].

Low carbon steel (with carbon content < 0.03 wt %) is generally preferred as lower carbon content improves the corrosion resistance of the material by minimizing the formation of chromium carbides (which leads to the chromium depletion at the grain

boundaries). As SA 304 L is generally used in the nuclear industry, the industrial grade SA 304 L was used in this study.

IASCC is a complex degradation phenomenon resulting from the simultaneous occurrence of various events. It is generally described as the enhancement of Inter – Granular (IG) SCC of the material with irradiation. As it is difficult to observe all the influencing parameters at the same time, the underlying mechanism of this degradation phenomenon still remains unclear. In addition, working with neutron irradiated material is quite troublesome. Hence, as an alternative, IASCC in laboratories is mimicked by straining the material in PWR simulated environments post to the ion irradiations (especially proton). As only persistent effects (such as irradiation induced microstructure) are considered as the key contributors in IASCC, mechanical tests post to irradiation are great options. Ion irradiations are generally performed at higher temperature and are an established tool to imitate irradiation induced defects [see § 1.4].

With the same background, irradiation was carried out on the SA 304 L with different ions and damage doses to fulfill different objectives. Proton irradiated SS has deformation microstructures and deformation mode similar to neutron irradiated SS and hence, has been the first preference. However, proton is not favorable to attain higher doses owing to long irradiation times and activation of sample post to irradiation. To fix this problem, self-ion (Fe) irradiation was conducted. The prime objective of these irradiations was to reproduce damage equivalent to neutron irradiation (at PWR relevant temperatures) in terms of microstructure and mechanical properties.

In this chapter, different techniques used to achieve the goal are described. In the beginning, a complete description of the reference state of the material is provided. An overview of the irradiations conducted with the justification of choice of various conditions and parameters is given as well. Qualitative and quantitative assessments of irradiation induced damage were done. Comparison with literature has been provided in the last section of the chapter to ascertain the reproduction of neutron (and/or ion) damage. It was necessary as it will help to draw an analogy with neutron and ion literature when comparing the susceptibility of the material (discussed in following chapters).

2.2. MATERIAL UNDER STUDY

The SS 304L belongs to 300 series austenitic stainless steel as per AISI standards. It was provided in the form of rolled rectangular plate by CEA, SCCME (Service de Corrosion et du Comportement des Matériaux dans leur Environnement) after solution annealing. At room temperature, the equilibrium state of SA 304L consists of mixed biphasic austenite (γ) and ferrite (δ) along with carbides of type Cr_7C_3 and $Cr_{23}C_6$. Annealing is generally performed to homogenize castings, and to relieve stresses from cold working. Annealing

not only allows recrystallization of the work hardened grains but also places chromium carbides (precipitated at grain boundaries) back into solution. Hence, to obtain a stable austenitic structure, following heat treatment was performed:

1. Solution annealing at 1050°C for 30 minutes.
2. Rapid cooling with Helium.

This heat treatment was performed in order to erase the thermo-mechanic history resulted from the rolling and preparation of sheets and hence, to eliminate the residual stresses from the material.

2.2.1. CHEMICAL COMPOSITION

The chemical composition of the material used, as obtained using ICP-AES (Inductively Coupled Plasma Atomic Emission Spectroscopy) and GDMS (Glow Discharge Mass Spectrometry), is stated in Table 2-1:

	Cr	Ni	Mn	Si	Mo	C	S	P	Pb	W	Zr	Mg	Co	Cu	V	Ti	Fe
SS 304 L Used	18.75	8.55	1.650	0.450	0.020	0.012	0.002	0.010	8ppm	0.035	12ppm	0.003	<0.05	0.240	0.015	<0.05	Bal
AISI Specifications	18 - 20	8 - 12	-	<1	<2	<0.03	<0.03	<0.045	-	-	-	-	-	-	-	-	Bal

Table 2-1: Chemical composition of SS 304 L (in wt %) [4].

The analyses were done as part of previous study [4]. The composition observed is in good accordance to the AISI specifications. A very small percentage of nitrogen was added to improve toughness, weldability and also to promote austenite temperature even at room temperature. However, its low percentage made it impossible to detect.

Based on chemical composition, stacking fault energy (SFE) could be calculated using different formulas that have been reported in literature [5 – 7]. Three different formulas however were used to calculate the SFE (based on chemical composition in wt %) in this study and have been listed below.

Pickering formula: $\mathrm{SFE}\ (\mathrm{mJ/m^2}) = 25.7 + 2 * (\mathrm{Ni\%}) + 410 * (\mathrm{C\%}) - 0.9 * (\mathrm{Cr\%}) - 77 * (\mathrm{N\%}) - 13 * (\mathrm{Si\%}) - 1.2 * (\mathrm{Mn\%})$ …….. (II.1)

Brofman and Ansell: $\mathrm{SFE}\ (\mathrm{mJ/m^2}) = 16.7 + 2.1 * (\mathrm{Ni\%}) - 0.9 * (\mathrm{Cr\%}) + 26 * (\mathrm{C\%})$ ……. (II.2)

Schramm and Reed: $\mathrm{SFE}\,(\mathrm{mJ/m^2}) = -53 + 6.2 * (\mathrm{Ni\%}) + 0.7 * (\mathrm{Cr\%}) + 3.2 * (\mathrm{Mn\%}) + 9.3 * (\mathrm{Mo})$ ……... (II.3)

Using Pickering formula, a value of 23 mJ/m² was obtained while equation 2 and 3 yielded values of 18 mJ/m² and 19 mJ/m² respectively. This indicates that the SFE of the material ranged between 18 mJ/m² to 23 mJ/m², and corresponds well with the SFE range of the austenitic stainless steels. However, in this study the SFE value obtained using Pickering formula will be used to maintain the consistency with the previous study [4].

2.2.2. SAMPLE FABRICATION

Material was provided in the form of a 500 x 330 x 30 mm^3 SA 304L rectangular plate. From this plate, a parallelepiped was taken from ¼ to ¾ thickness of the plate (~30 mm thick) to avoid edge effects. From each such parallelepiped, two different geometries of samples were fabricated. Machining of some of the samples was done along RT (rolling-transverse direction) while for others it was along TR direction (Figure 2-2).

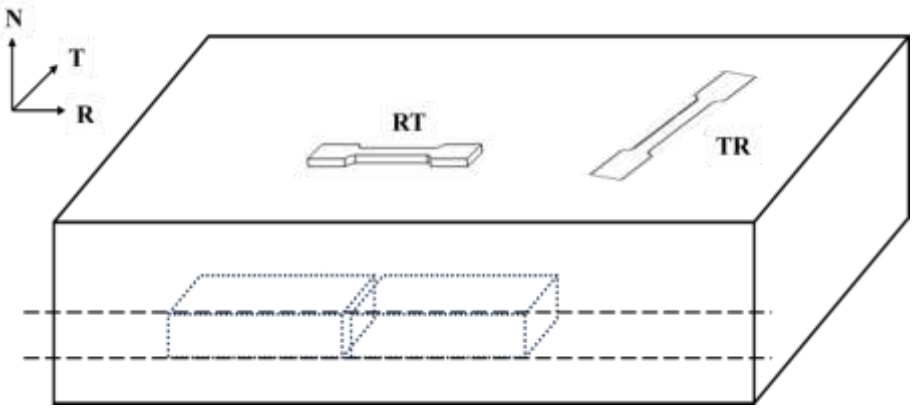

Figure 2-2: Schematic to illustrate the original position of parallelepiped used to make samples (blue dashed parallelepiped) and orientation of sample machined along RT and TR directions from the parallelepiped in the 304L SS plate.

Two different geometries of sample used included tensile samples which were used to perform mechanical tests and flat bars were used to characterize the microstructure, perform hardness and oxidation tests. The dimensions of these samples are provided in appendix A.1.1.

2.2.3. MICROSTRUCTURE

The microstructure of the material is biphasic consisting majorly of austenite phase along with ferrite phase (~ 2 – 6%). The austenite grains were equiaxed while the ferrites were in the form of lamella oriented in the rolling direction (R). The mean size of the grains was obtained to be 27 µm using standard NF EN ISO 643: 200304 norm. The analysis

was done as a part of previous study and the procedure has been reported in [4]. Detailed information on the microstructure is presented in the section below.

2.2.3.1. EBSD ANALYSIS

EBSD analysis was performed using JEOL JSM 7001F Field Emission SEM at 30 kV in "in lens" mode in CEA Saclay. The acquisition was done with Brucker software, and for post treatments the HKL software was used.

Inverse Pole Figure (Figure 2-3) obtained using EBSD revealed the presence of grains of γ face-centered cubic austenitic and δ ferrite phase of simple body-centered cubic structure. In the Figure 2-3, grains oriented parallel to the crystallographic direction <111> or close to this orientation are coloured blue, those parallel to the <001> and <101> are red and green respectively. EBSD analysis estimated the mean austenite grain size to be 28 ± 2 µm for the material used which is in good agreement with the value obtained using standard norm. A value of 27 µm was used as the mean austenite grain size value to maintain the consistency with the previous study.

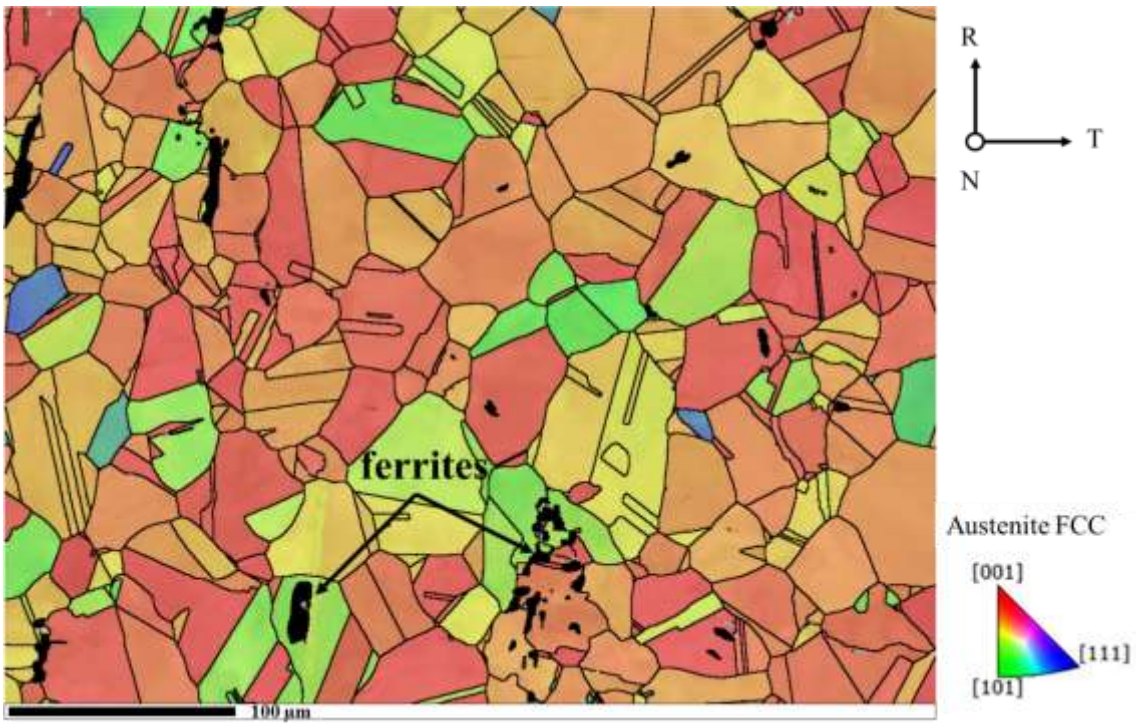

Figure 2-3: IPF cartography indicating the austenite grain orientation along with ferrite phase (in black) in the SS 304L under study.

Indexed ferrite grains are shown in black in Figure 2-3. The δ ferrite grains were observed to be lamellar in nature and their distribution was anisotropic within a face as well as from a face to another (Figure 2-4).

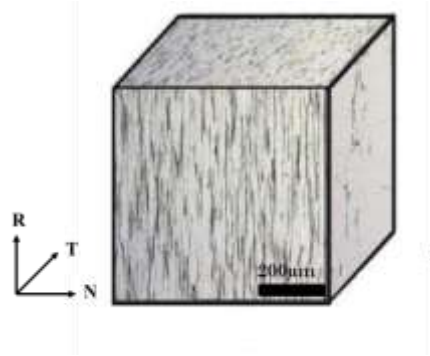

Figure 2-4: View of the 3 faces indicating the anisotropic distribution of δ ferrite in the material used [4].

A volume fraction of 2.5% for the amount of δ ferrite residual was obtained using EBSD. The detailed analysis performed as a part of previous study revealed that the volume fraction was of the order of 8 % on the surface RN, 4% on NT and 1% on the RT. Based on the respective Ni and Cr equivalent contents (% at Ni_{eq} = 11.8, % at Cr_{eq} = 18.82), the average amount of δ ferrite residual estimated using Schaeffler diagram [8] was ~ 6% (Figure 2-5). In total, material was believed to contain 2 – 6 % δ ferrite. Ferrite being harder than the austenite can lead to mismatch of strain at the austenite – ferrite interface resulting in deformation inhomogeneity. However, a recent study [9] has proved that presence of ferrite neither enhances nor suppresses the cracking suggesting its presence will not affect the cracking susceptibility of the material during corrosion tests conducted later in this study.

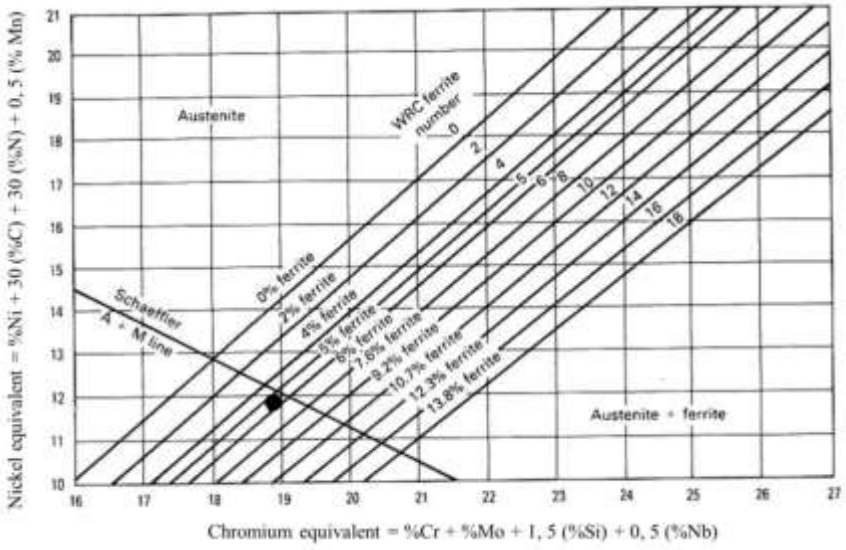

Figure 2-5: Estimation of the amount of ferrite using revised Schaeffler diagram (1990) [8]. The black circle indicates the SS 304 L grade under study [4].

Machining of some of the samples, used in this study, was done along RT direction while for others it was TR (Figure 2-2). The orientation of ferrite with respect to loading

direction was thus, different for the two conditions. Going by above argument, machining done in two different directions should not have any consequential effect on the cracking susceptibility of the material.

In a polycrystalline material, the grains are generally randomly oriented. The difference in the crystallographic orientation between two grains is defined as the misorientation between these grains. On comparing the distribution of the uncorrelated disorientation (two measurement points taken randomly on the surface observed) with the theoretical distribution of MacKenzie for a randomly texture polycrystal, the texture of the material can be characterized. This analysis, done in previous study, revealed that the material under study is non-textured [4].

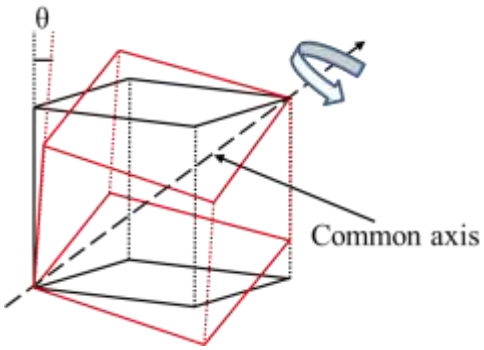

Figure 2-6: Schematic illustrating the misorientation between two grains.

The misorientation between two grains is represented by a (smallest) rotation along the common axis which brings both the grains in perfect matching and hence, is defined by the rotation axis and angle (Θ) (Figure 2-6). Choosing it as criteria, the grain boundaries were classified in two categories: Randomly High Angle Grain boundaries (RHABs) with angle of misorientation $\Theta > 15°$ and Low Angle Grain Boundaries (LAGBs) with angles between 5° and 15° ($5° < \Theta < 15°$). The distribution of angle of disorientation of grain boundaries is presented in the Figure 2-7. The results suggested that majority of the grain boundaries (92 %) belonged to the RHABs category.

The grain boundaries were further categorized as general and special (or coincidental site lattice) boundaries depending on the density of coincident sites. A coincident site is a site where atomic positions of two neighboring grains coincide on superimposition. These sites are spread regularly throughout the whole superimposition and create a super lattice called coincidental site lattice (CSL). The value of reciprocal of density of coincident sites (Σ) could be calculated using the equation (II.4) and each value specifies the relation between two grains unambiguously.

$$\Sigma = \frac{number\ of\ coincident\ sites\ in\ an\ elementary\ cell}{total\ number\ of\ lattice\ sites\ in\ an\ elementary\ cell} \quad \text{..... (II.4).}$$

For example, Σ1 represents a perfect lattice without any coincidental sites while Σ3 corresponds to a twin boundary in FCC structures.

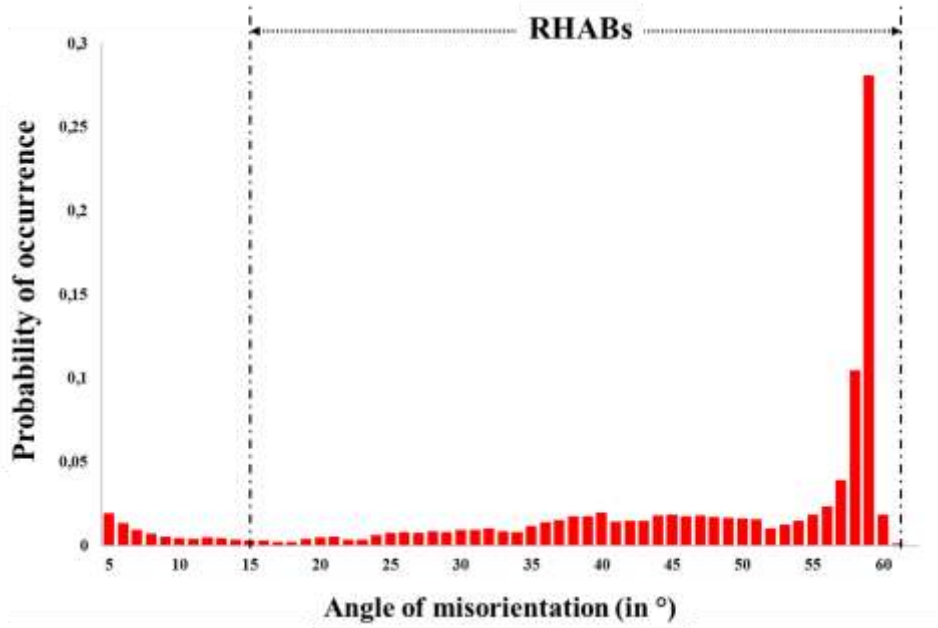

Figure 2-7: Grain boundaries misorientation profile for virgin material obtained using EBSD analysis.

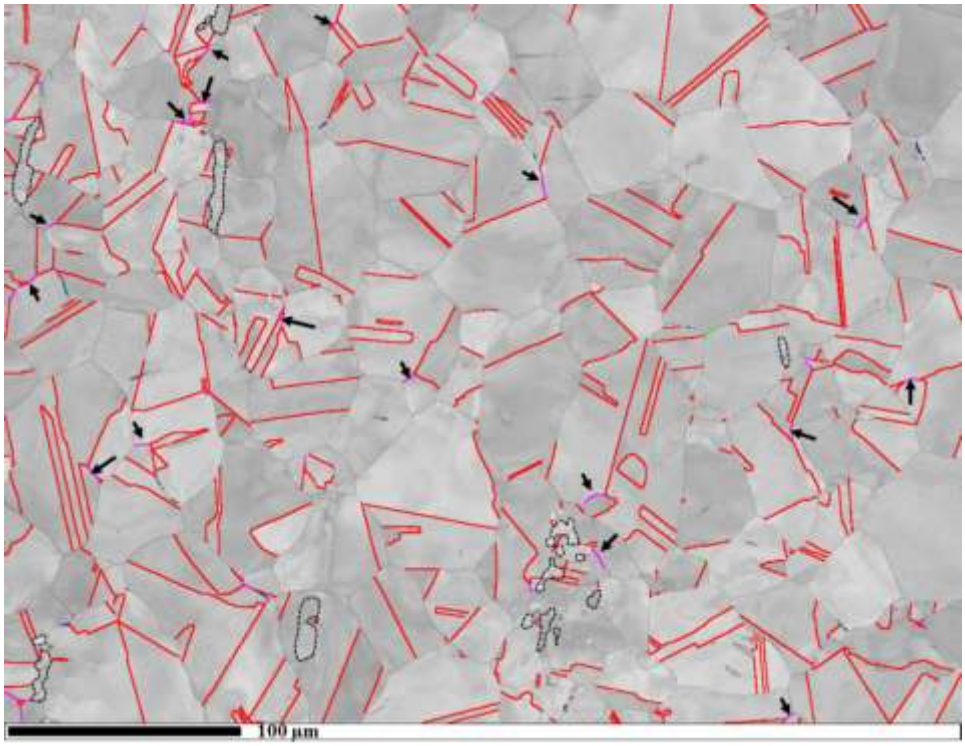

Figure 2-8: EBSD image (post treatment with HKL software) indicating the presence of CSL boundaries in the material. In red are Σ3, in pink are Σ9 types (marked by black arrows) of CSL boundaries. Black dashed contours represent the δ ferrite and rests are the austenite grains.

Based on this categorization, it was observed that 45 % of the boundaries were special boundary (in red in Figure 2-8), Σ3 to be precise, suggesting that the material was highly twinned. A very small amount (~ 1%) of Σ9 was observed as well.

2.2.3.2. TEM OBSERVATIONS

The microstructure of the material (prior and post to irradiation and corrosion tests) was characterized using JEOL 2010 and JEOL 2100F HRTEM (High Resolution Transmission Electron Microscope) operated at 200 kV and equipped with EDS spectrometer, available at UMS Castaing (Toulouse, France).

Sample preparation is of great importance for Electron microscopy as the quality of the images observed under microscope depends on the quality of sample prepared. To prepare the TEM foils, bars were manually ground to 60 – 80 µm and pre-thinned to near electron transparency using dimple grinder. Precision Ion Polishing System (PIPS) was finally used to make electron transparent TEM foils to characterize the extreme surface (or sub – surface).

The initial microstructure of the material consisted of austenite grains and few ferrite grains. Two different morphology of the ferrite was observed namely, elongated and ovoid (Figure 2-9). The EDX analysis revealed that these grains were enriched in Chromium and depleted in Ni (to almost half of its original matrix value). The diffraction pattern, further, indexed these grains as ferrite which crystallized in cubic centered system with cell parameter, a = 2.886 Å. Few MnS precipitates and carbides were observed as well.

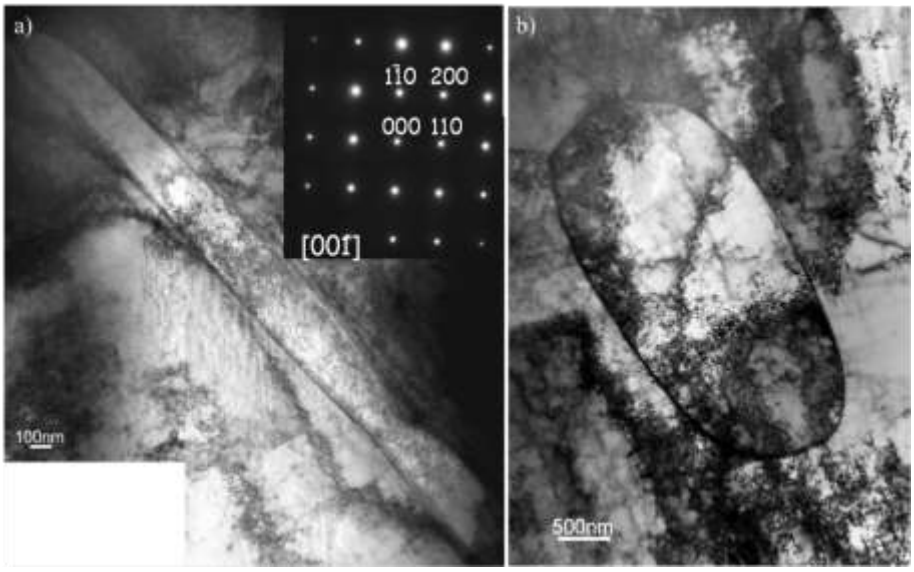

Figure 2-9 : BF TEM images of the ferrite with a) elongated b) ovoid morphology along with associated diffraction pattern.

Moreover, even after rapid cooling in helium, a little precipitation persists. So, few carbides were observed at inter- and intra-granular positions in the material. The diffraction pattern associated indexed these carbides as Cr_7C_3 (Figure 2-10) in orthorhombic cell with Pnma space group and cell parameters a = 4.53 Å, b = 7.01 Å, c = 12.14 Å.

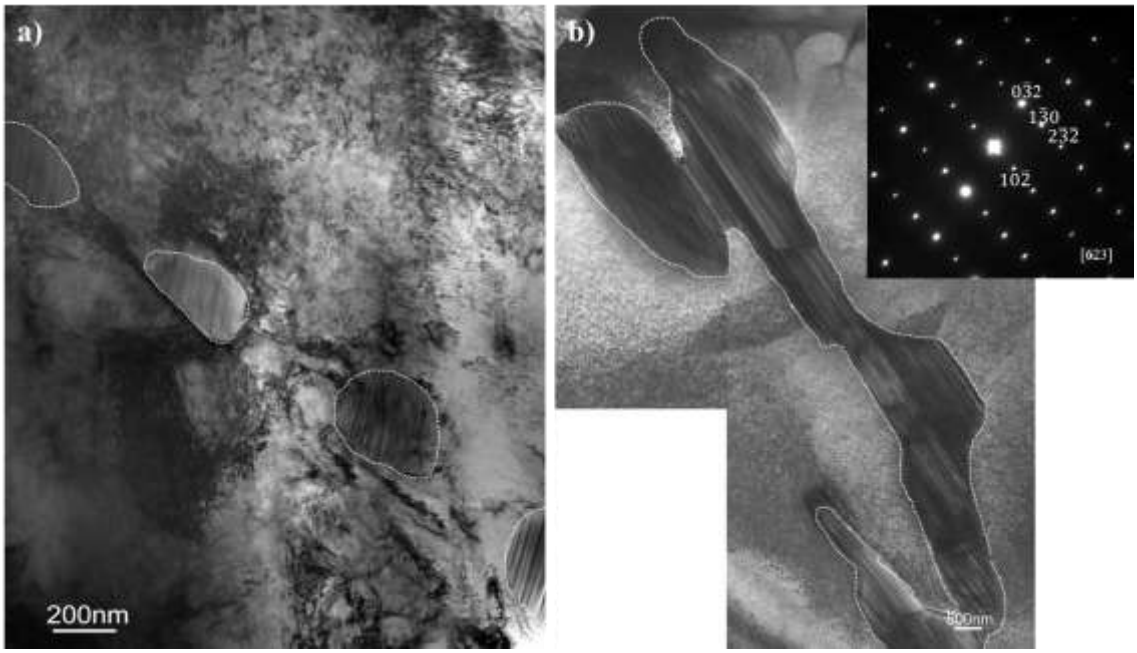

Figure 2-10 : BF TEM images (with associated diffraction pattern in inset) of Cr_7C_3 carbides (outlined using white dashed lines) observed in the material.

Few MnS precipitates were observed as well. These were observed at the intra-granular positions and were enriched in manganese and sulphur. The diffraction pattern on these precipitates along the zone axis [111] indexed them as MnS in cubic centred phase with the Pm-3m space group and cell parameter a = 5.217 Å.

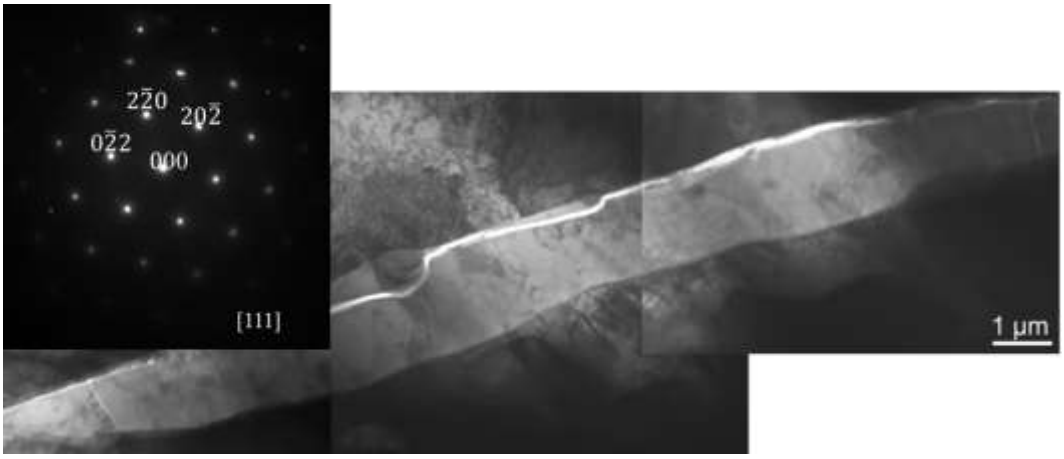

Figure 2-11 : BF TEM image of MnS precipitate (with associated diffraction pattern in inset) observed in the material.

In this study, two different surface preparation techniques namely, mechanical polishing and vibratory (or vibro) polishing were used. The microstructure of the material (at the extreme surface) prior to any irradiation or corrosion test, characterized using TEM, has been reported below.

Mechanically polished sample:

Mechanical polishing is a widely used sample preparation technique in which, samples are polished manually using SiC sandpapers. In this study, samples were polished up to # 4000 grit (starting from # 600 grit) SiC sandpapers followed by polishing using up to ¼ µm diamonds paste to achieve a mirror like surface finish prior to any irradiation or test.

Bright Field (BF) and Dark Field (DF) TEM images of the sub – surface of the mechanically polished sample are shown in Figure 2-12 revealing the presence of nanograins in the material. The associated diffraction pattern indexed these nanograins to be of FCC phase (i.e. nano austenite grains) and their size ranged between 20 and 200 nm. The extent of nanograins in the material is dependent on the final polishing step. Previous study has reported to observe nanograins extending upto a depth of 0.5 – 1 µm in the SA 304L material post to mechanical polishing. It was found to be true for this study as well. So it was assumed that the zone extended upto a maximum depth of 1µm in the sub surface. Presence of nanograins made observation of any sort of dislocations, twins extremely intricate.

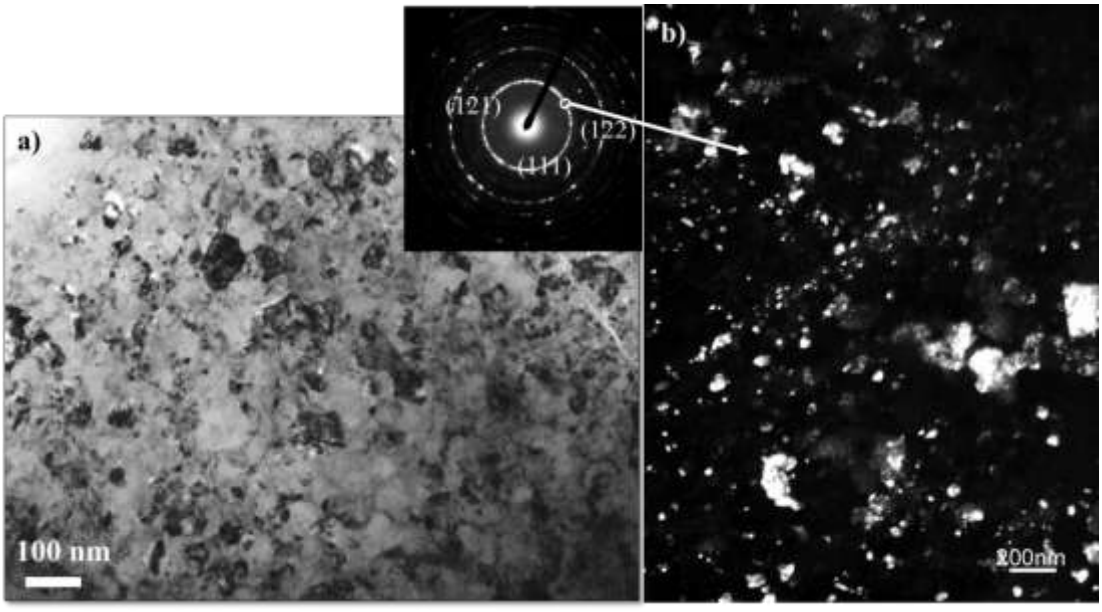

Figure 2-12 : a) Bright Field b) Dark Field TEM image (along with diffraction pattern) of mechanically polished sample indicating the presence of nanograins in the subsurface of the material.

Vibratory polished sample:

The other surface preparation technique used in this study was vibratory polishing. In this technique, an additional step of polishing on a vibratory table using colloidal silica (0.04 µm) polishing suspension was carried out post to mechanical polishing. The detailed procedure is given in appendix A.1.2.1.

The objective of using this technique was to eliminate the surface hardened layer induced by mechanical polishing. As that layer extended upto a depth of 0.5 – 1 µm, decision of removing 2 µm from the surface was taken for the sake of assurance.

A trial test was performed on one sample. In this test, 2 indents were made on the sample. The sample was then polished for 20 hours in colloidal silica suspension. Difference in the depth of indents before and after polishing gave an estimation of the thickness removed in 20 hours. These calculations yielded that 9 hours of polishing is required to remove 2 µm so polishing time of 9 hours was used for rest of the samples. The polisher runs automatically with no user intervention required unless the sample slips off from the holder (in which case it needs to be re-adhered and placed back on the polisher). Once polished, samples were removed from the polisher and rinsed thoroughly using ultrasonic cleaning.

After polishing, TEM characterization of the sub-surface of the material revealed the presence of standard and expected size austenite grains with few ferrite grains (Figure 2-13a) as have been reported in initial microstructure. This suggests that this surface preparation technique, indeed removed the surface hardened layer from the material. The microstructure revealed the presence of few twins (Figure 2-13b) and dislocation.

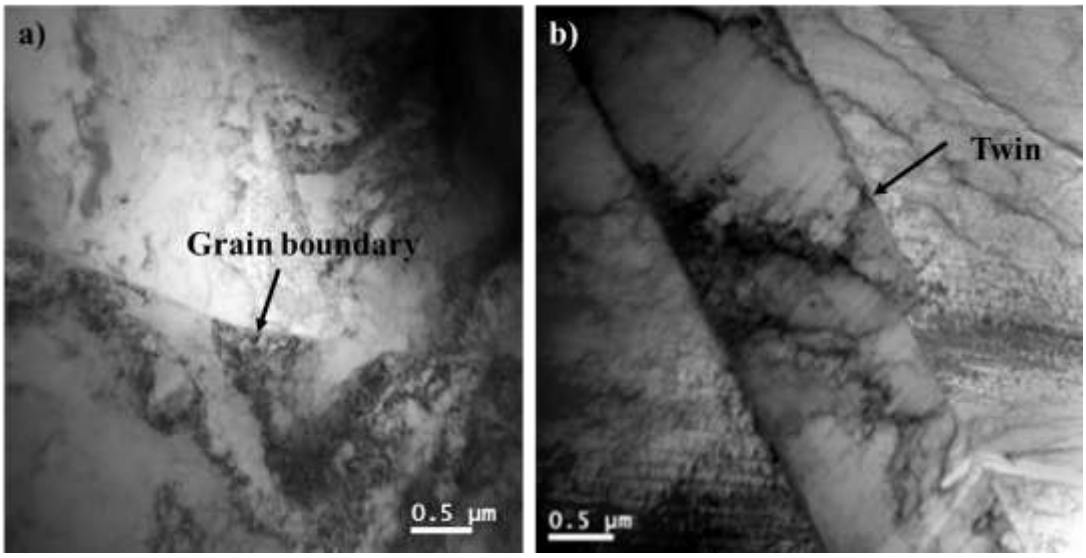

Figure 2-13: a) Austenite grains b) twins observed in the vibratory polished virgin material.

2.2.4. MECHANICAL PROPERTIES

2.2.4.1. HARDNESS

The hardness of the virgin material was estimated using both conventional method and nano indentation testing using continuous stiffness measurement techniques.

In the conventional Vickers hardness measurement method, five indents were made on the material using 30 kg load at room temperature. This test yielded a value of 200 ± 30 H_v. The indents were made at a depth of 220 µm, suggesting that the value obtained corresponded to the bulk value and was independent of the surface finish. Using the correlation, σ_U (in MPa) = H_v / 0.33, the tensile strength of the material computed was 606 ± 91 MPa.

In addition, nano-indentation testing technique was employed to estimate the hardness of the material. With this technique, it was possible to estimate the hardness for small depths which was of interest for the irradiated sample. Hence, to have a reference value for comparative study it was used for unirradiated sample as well. In this technique, a Berkovich tip (three sided pyramid which is self-similar and has a half angle of 65°) with a tip radius of about 50 nm was used. The nano-indenter was calibrated against fused silica before each indentation run to allow for cross comparison between samples and indenters. In total 15 indents at an indenter depth of 6 µm were made along the entire length of the sample. Indents were a minimum of 1 mm (Figure 2-14a) apart from each other to ensure no interaction of the plastic zone around the indents.

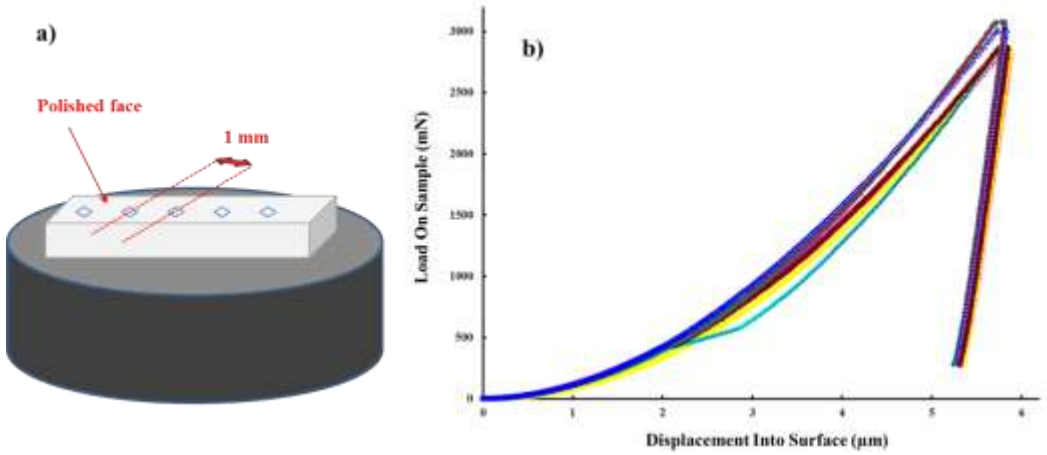

Figure 2-14: a) Schematic to illustrate the placement of indents on the samples b) Example of Load – displacement profiles obtained for various indents made during nano indentation test.

In the nano indentation testing technique, a typical load–displacement curve (Figure 2-14b) is obtained for each indent from which the hardness could be estimated. A

decrease in hardness with increasing indentation depth is generally observed (Figure 2-15a). Nix and Gao established a relation (eq. II.5) between micro-indentation hardness H and the indentation depth d for a sharp, conical indenter, based on the Taylor dislocation model and model of geometrically necessary dislocations underneath a sharp indenter tip [10].

$$\left(\frac{H}{H_0}\right)^2 = 1 + \frac{d^*}{d} \quad \text{..... (II.5)}$$

Where, H is the measured hardness at the depth of d, H_0 is the hardness at infinite depth (i.e., macroscopic hardness or bulk hardness) and d* is a characteristic length which depends on the material and the shape of indenter tip. This relation is based on self-similar deformation field underneath the sharp indenter and the parameters H_0 and d* accounts for the size effects. It predicts a linear relation between H^2 and 1/d corresponding to a straight line in H^2 versus 1/d plot with H_0 being the intercept value on hardness axis (Figure 2-15b). But some deviations have been reported in literature owing to factors such as tip radius of indenter etc., especially for d < 100 nm. As all the tests in this study were done at depths higher than 100 nm, linear relation given by Nix Gao relation will be considered. The extrapolated values (Figure 2-15b) from these curves correspond to the bulk hardness value of the material and are independent of indent size, hence, only extrapolated values will be used in this study to calculate the equivalent Vickers hardness values for different conditions using the relation,

$$H_V = 0.0945\, H_0. \quad \text{..... (II.6)}$$

Where H_0 is the Berkovich hardness value and H_V is the equivalent Vickers hardness value [11].

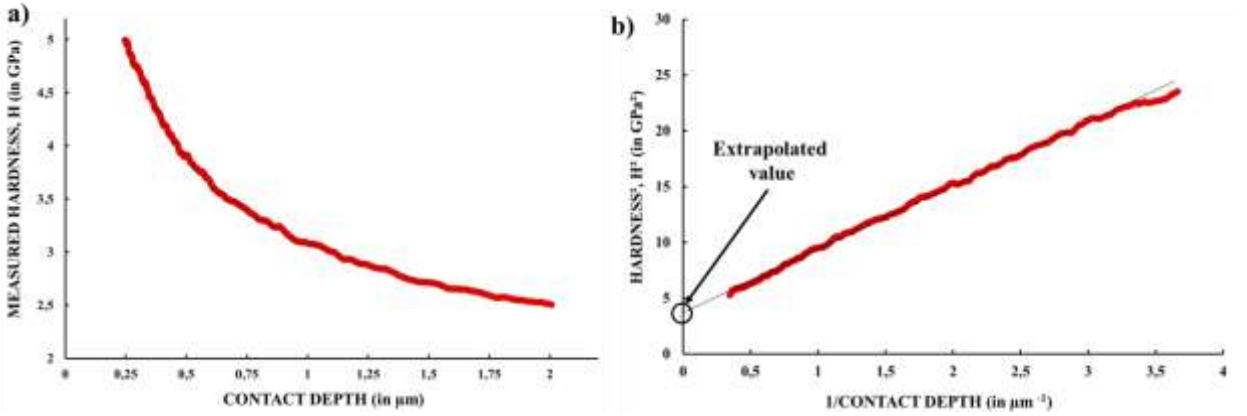

Figure 2-15: Examples of a) Hardness profile b) Corresponding Hardness² versus 1/d (or Nix – Gao) graph illustrating the estimation of extrapolated value, plotted for indents made on sample during nano indentation test.

The Nix Gao plot obtained for the tests conducted on unirradiated vibratory polished SA 304L SS samples is shown in Figure 2-16. A trend of decrease in hardness square (or simply hardness, H) with indentation depth, in consistency with Nix – Gao relation, was observed. For 1/d > 4 μm^{-1} (or d < 0.25 µm), some nonlinearities were observed in the profiles which could be attributed to surface artifacts.

The extrapolated H_0^2 (square of bulk hardness value) obtained from the different tests conducted on the material was 4.1 ± 0.5 GPa^2 (Figure 2-16). This yielded an equivalent Vickers hardness value of 191 ± 11 H_V for vibro polished virgin material which was in good agreement with the value obtained from conventional test. This value will be used as the reference value for comparative studies done later in this study. As the tests were done on three different machines, small differences in the H_0 values were obtained. These differences are incorporated within the error defined. The reason for these differences remains unknown and hence for comparative studies, only results from single machine will be used.

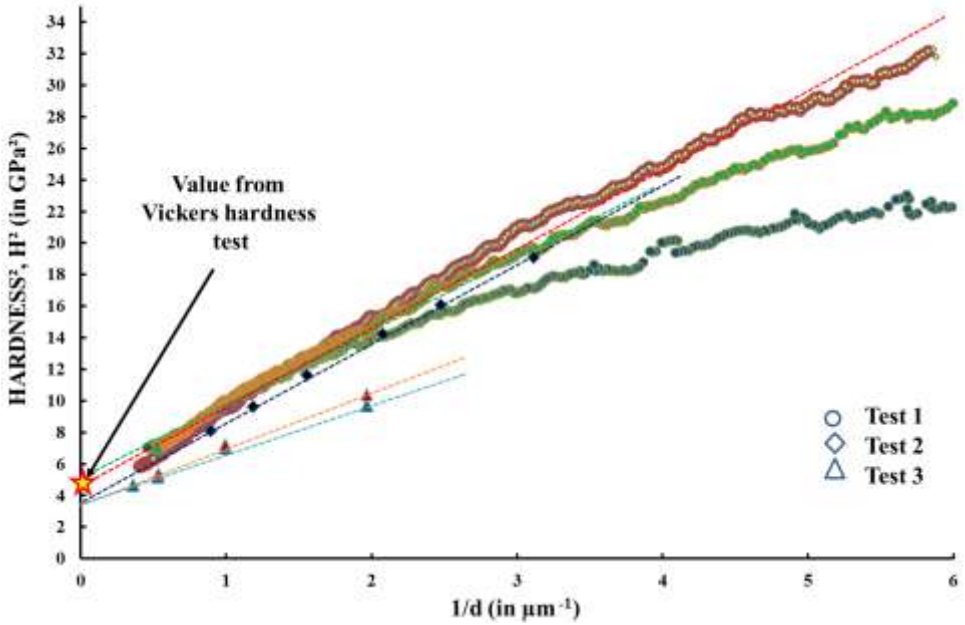

Figure 2-16: Nix and Gao plot of the vibro-polished material obtained from nano-indentation hardness tests performed on different machines. Value obtained from conventional Vickers test (after converting it to berkovich hardness value) is indicated as star in the figure.

Note that the hardness value obtained for a given indent at a depth d doesn't correspond to the actual value at that point but is contributed by a plastic zone extending upto 7d [12]. For instance, the hardness value obtained for indent depth of 0.25 µm (or 1/d = 4 μm^{-1}) is the value contributed by a plastic zone extending to a depth of 1.75 µm. This is not an issue when dealing with vibro polished unirradiated material. However, special precautions are required when calculating the hardness value in mechanically polished samples and in irradiated samples (which will be dealt later in §2.3.3.1).

In mechanically polished samples, a surface hardened layer exists which may extend upto a depth of 0.5 – 1 µm. Hardness value of this layer is different from value for the material beneath it. Hence for all the indents made at d > 0.25 µm, the material beneath surface hardened zone will start contributing and its contribution will increase with increasing d (or decreasing 1/d). And for all d ≥ 1 µm, the entire contribution will be from the material beneath. Justifying this argument, a significant decrease in hardness value of these samples was observed up to the indentation depth of 1µm (Figure 2-17a). And beyond this depth, the value is similar to that of vibro polished sample.

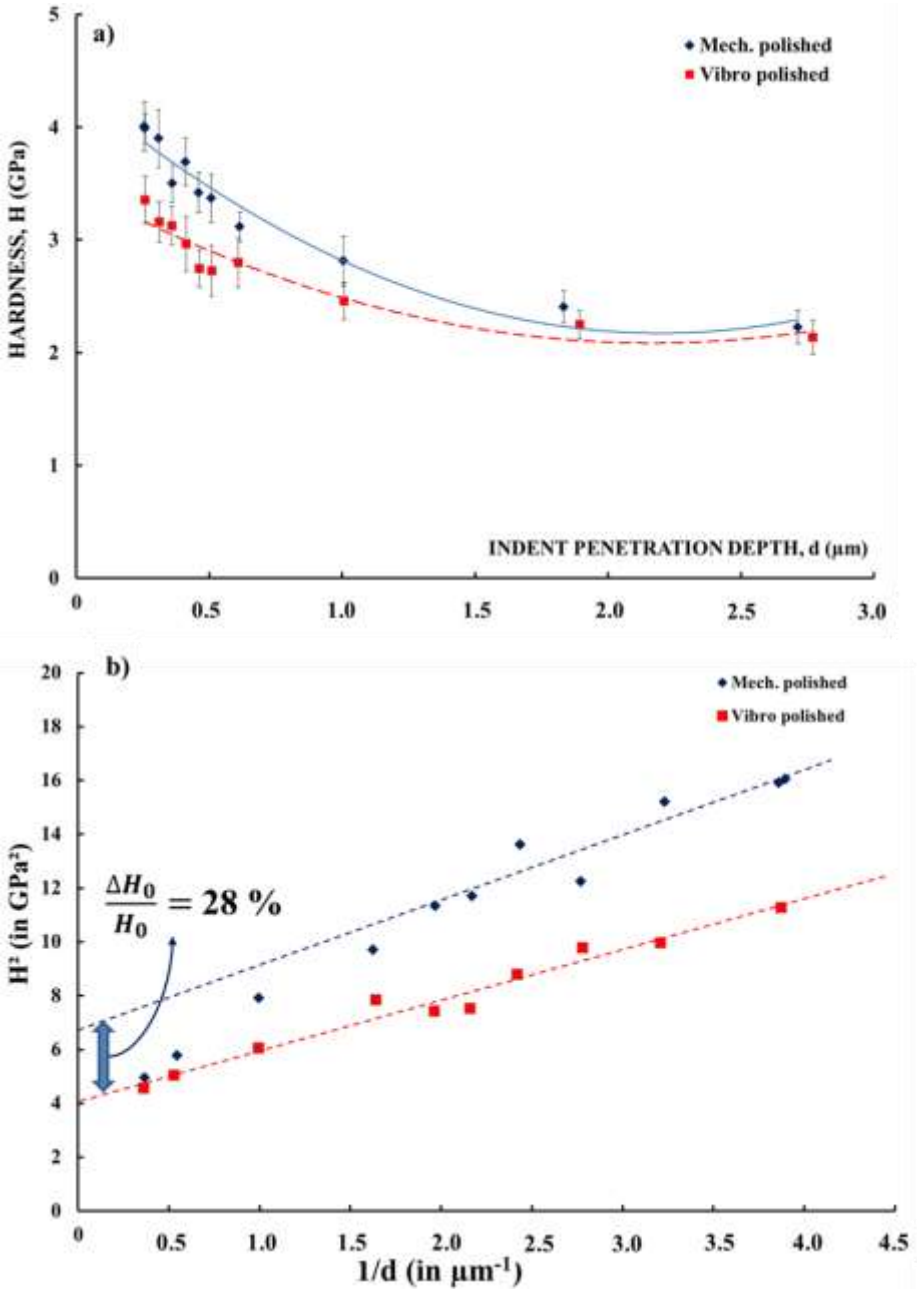

Figure 2-17: a) Hardness profile b) Nix and Gao plot showing the comparison of values obtained for mechanically polished (blue) and vibratory polished (red) materials using nano indentation test.

Assuming a linear relationship, the extrapolated value from the Nix Gao plots (Figure 2-17b) was evaluated using the data points of 1/d available between 2 and 4. The value thus obtained was 6.7 GPa², yielding an increase of 28 % in the hardness value.

2.2.4.2. TENSILE PROPERTIES

The tensile samples (see §A.1.1) were subjected to tensile loading with a strain rate of $5 \times 10^{-4}\ s^{-1}$. The tests were conducted both in air and in PWR simulated primary water environment.

The test in air was conducted at 20°C and 340°C using INSTRON tensile testing machine, while the test conducted in autoclave were conducted in PWR simulated primary water environment (25 – 35cc/kg H_2 STP, 1000 ppm B, 2 ppm Li) at 340°C using the tensile testing Device CORMET C137. The setup of CORMET consisted of an autoclave with a capacity of 5 liters, a load frame, and a computer driven, 30 kN load train for straining of the samples. Samples were clipped on the sample holder and put in the autoclave. System had temperature sensors to record the temperature during operation. On obtaining the desired temperature and pressure, desired loading condition was conducted. After each test, chemical analysis of the water was carried out to look for the presence of any impurity.

The results for all the tests are presented in the Figure 2-18 and mechanical properties such as 0.2 % proof stress or equivalent yield stress ($\sigma_{0.2\%}$), ultimate tensile strength (σ_{UTS}) of material for different conditions have been summarized in Table 2-2 below.

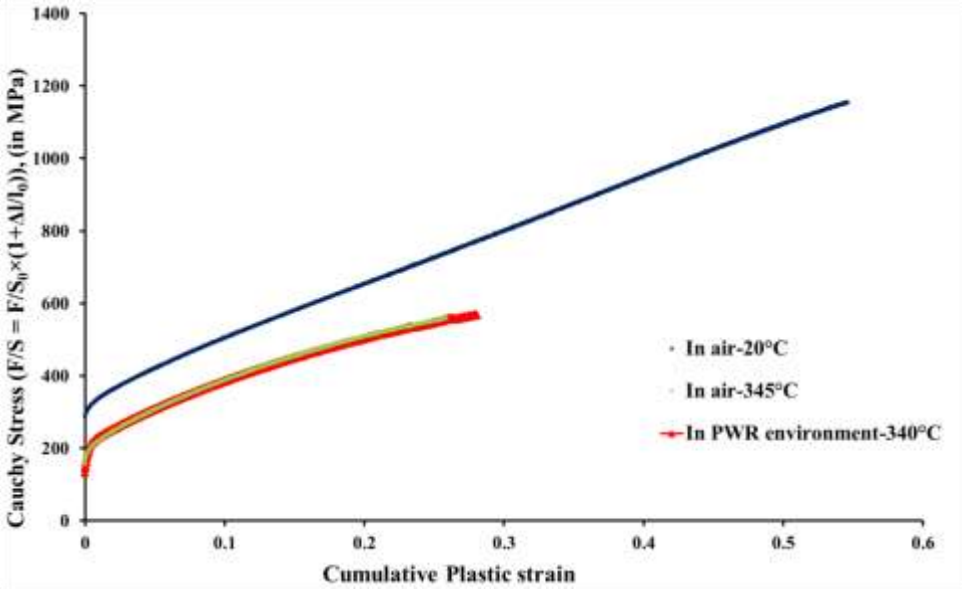

Figure 2-18: Comparison of Cauchy stress – cumulative plastic strain graphs of initial material at 20°C and 340°C in air and at 340 °C in PWR environment.

Condition	$\sigma_{0.2\%}$ (MPa)	σ_{UTS} (MPa)
In air at 20°C	312	675
In air at 340°C	206	432
In autoclave at 340°C	208	428

Table 2-2: Mechanical properties of unirradiated SS 304L observed during tensile test performed in air and autoclave at 20 °C and 340°C.

Decrease in yield strength and ultimate tensile strength was observed on increasing the test temperature indicating the degradation of mechanical properties of material with elevated test temperatures. Also, in the tests conducted at 340 °C in air (in INSTRON) and in corrosive environment (CORMET), no significant difference was observed.

A value of 606 ± 90 MPa for the tensile strength was calculated from the Vickers hardness value of the material which is in good agreement with the value obtained from the tensile test performed in air at 25 °C.

This completes the description of reference state. In the following sections, the irradiation conducted as well as the damage induced post to irradiation in these samples will be discussed.

2.3. IRRADIATED MATERIAL

2.3.1. IRRADIATION CONDITIONS

Two different ions namely, proton and iron were used in this study to perform the irradiations. As both of these have a damage rate higher than that of neutron, a temperature shift was used for both irradiations. The temperature shifts were calculated using the equations (I.9) and (I.10) (see § 1.4). For the dose rates used, the temperatures at which irradiations should be conducted to induce microstructure or microchemistry similar to neutron irradiation (270 – 340 °C) are summarized in the Table 2-3. The temperature chosen for each irradiation in this study was compromise between the two factors.

Similarity with neutron irradiation in	Proton irradiation Temperature (°C)	Fe (/Fe+He) irradiation Temperature (°C)
microstructure	320	368
microchemistry	372	551
Temperature chosen in this study	350	450

Table 2-3: Summary of the ion irradiation temperature required to mimic the neutron equivalent damage.

As evident, the irradiation temperature for heavy ions (Fe /and He) was higher compared to the temperature used for proton irradiation because of the higher dose rates of the former. Further details of these irradiations are given in the following sections.

2.3.1.1. PROTON IRRADIATION

Samples of two different proton irradiation campaigns were used this study. Both of the campaigns were executed at Michigan Ion Beam Laboratory, University of Michigan, US. The first irradiation campaign was conducted on mechanically polished samples using 3.2 MeV protons at 350 °C. In the second campaign, vibro polished samples were irradiated using 2 MeV protons at 350 °C.

For both campaigns, samples (tensile samples and bars) were mounted on a copper stage which was electrically isolated from the beam line (Figure 2-19a). The stage was heated to 350 ± 10 °C using a resistive cartridge heater and cooled using room temperature air owing through cooling lines that penetrate the back of the stage. To provide effective thermal contact between the sample bars and the stage, a thin layer of Indium was placed between the samples and the stage surface. Indium was molten below the irradiation temperature, maximizing the thermal contact between samples and stage. The proton beam (approximately 3 mm in diameter) was rastered across the stage so that about half the total beam current is deposited on the samples and half on the apertures. This rastering ensured that samples at any position on the stage receive the same dose. The Stinger thermal imaging system was calibrated prior to starting the irradiation such that all the points on the samples correspond to same temperature. The sample temperature was controlled to be within ± 10 °C (Figure 2-19b) of the set irradiation temperature by controlling the amount of heating and/or cooling provided to the stage. Experimental parameters were tracked continuously during the irradiation using a PC-based monitoring system [13]. Two different geometries of samples (tensile and bars) were used for the irradiation. Details of these samples are given in appendix A.1.1. For each sample, a section of 10 mm x 2mm corresponded to irradiated zone while the rest of the sample was unirradiated.

Decreasing the energy of proton ions from 3.2 MeV to 2 MeV reduced the activation of the sample and hence, helped to gain some time. Besides, for same time of irradiation, the damage was twice as high for the former compared to latter. The range of protons penetration as calculated using SRIM 2011 [14] was ~ 30 – 40 µm for 3.2 MeV protons while ~ 20 µm for 2 MeV protons (Figure 2-20). The displacement threshold energy (for Fe, Cr and Ni) used for the calculation was 40 eV, which is the recommended value for steel target [15]. The irradiated region in both cases consisted of a constant damage region followed by a sharp irradiation peak. The peak position was 37 µm for 3.2 MeV protons and 19 µm for 2 MeV protons.

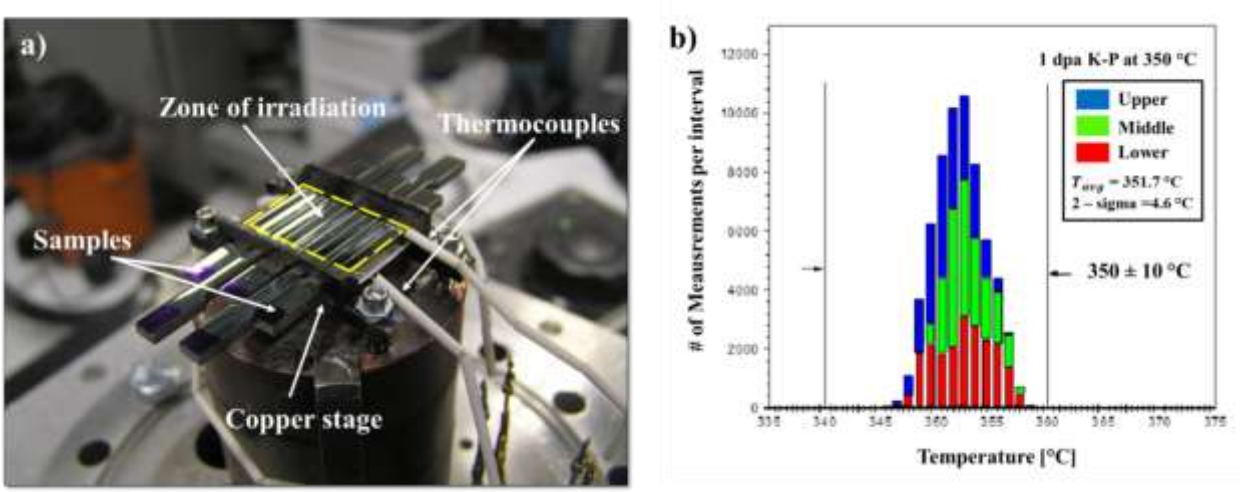

Figure 2-19: a) Samples placed on the copper stage during 2 dpa – H^+ irradiation. Irradiation zone is indicated by yellow dashed square. b) Temperature profile for one of the sample obtained during the irradiation indicating the control of temperature within ± 10 °C.

The first irradiation was performed for two different doses: 1 dpa K–P (with time of irradiation of 95 hours) and 0.25 dpa K–P (with time of irradiation of 20 hours). However, except microstructural characterization, all the tests were done on 1 dpa K–P. The 1 dpa K–P value corresponded to the value at a depth of ~10 µm as the profile was almost flat upto 20µm (Figure 2-20). The samples of this irradiation campaign will be addressed as 1 dpa H and 0.25 dpa H samples based on their respective doses at the surface.

The second irradiation was conducted for 95 hours and implanted a dose of 2 dpa K-P (value at 10 µm) at the surface (Figure 2-20). The samples will be addressed as 2 dpa H samples.

The details of the two irradiation campaigns are given in the Table 2-4.

Sample	Energy (MeV)	Irradiation time (hrs)	Flux (x 10^{14} ions/cm^2/s)	Dose rate (at surface damage) (x 10^{-6} dpa K-P/s)	Dose (at surface) (dpa K-P)	Dose (at Peak) (dpa K-P)	Peak position (µm)
0.25 dpa – H	3.2	20	1.32	3.2	0.25	3	37
1 dpa – H		95	1.35	3.2	1	18	
2 dpa – H	2	95	1.39	5.8	2	30	19

Table 2-4: Different parameters for all proton irradiation campaigns conducted at 350°C ± 10°C.

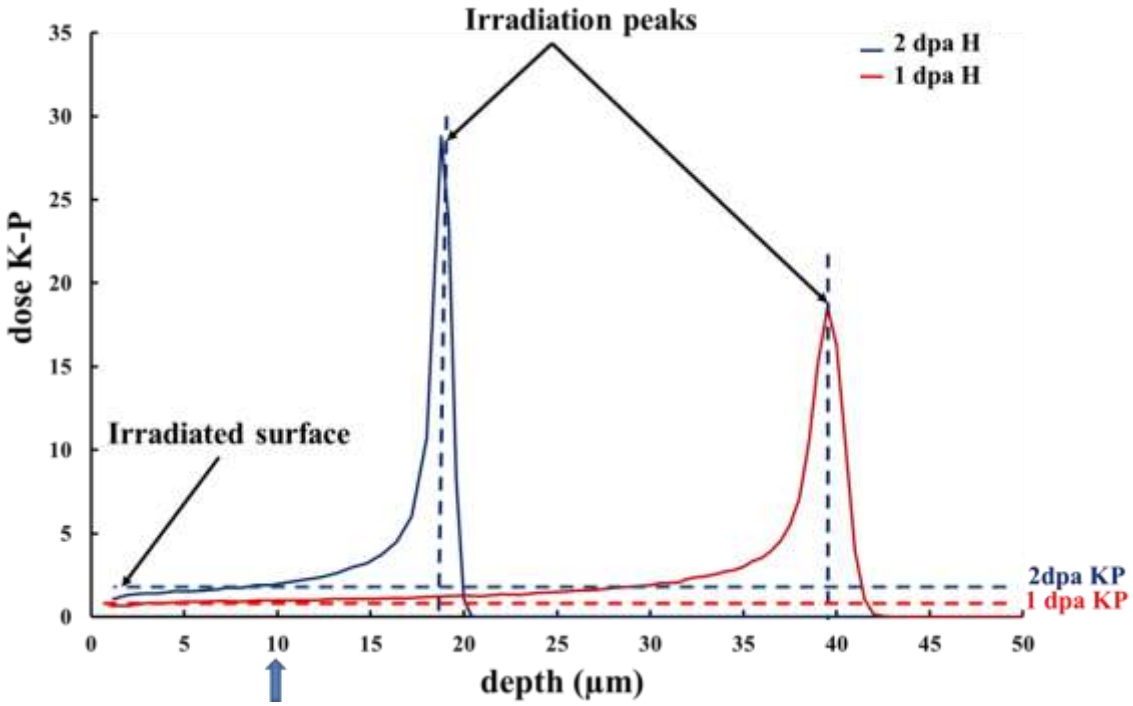

Figure 2-20: Damage profile for 2 dpa H^+ irradiation (using 2 MeV, in blue) and for 1 dpa H^+ irradiation (using 3.2 MeV, in red) in SS 304L obtained using SRIM-2011 under K-P approximation and using threshold displacement energy of 40 eV for Fe, Cr and Ni [15]. The irradiation dose at the 10 µm (indicated by arrow) was considered as the damage at irradiated surface.

2.3.1.2. SELF ION IRRADIATION

Heavy ions irradiation was conducted at JANNuS facility of CEA Saclay (France) using 10 MeV Fe^{5+}. Higher dose rates ($2.7 – 3.4 \times 10^{-4}$ dpa/s) imposed to conduct the irradiation at 450 °C (see § 2.3.1). Three different irradiation campaigns were performed within this framework.

For all campaigns, the samples were mounted on a 304 L SS sample holder which was subsequently placed on the irradiation stage (Figure 2-21a). The position of samples was monitored on a screen with the help of a camera throughout the experiment. Starting from 23 °C, the samples were heated to 450° C ± 20 °C. Temperature was monitored by a two – dimensional infrared thermal imager (FLIR Type SC325) that monitored the surface temperature of the samples during irradiation (Figure 2-21b) [16]. In addition, four thermocouples were used to ascertain the temperature during irradiations, one of which was touching the sample in the irradiated region. The Fe^{5+} beam of proper shape (both in x and y plane) was obtained using different controls of Epiméthée accelerator. Beam centering was done using Niobium doped alumina plate. Like proton irradiation, a raster beam was used to ensure the homogeneous spread of the beam on the sample. The beam was incident on samples at an angle of 15°. Two different geometries of samples (tensile

and bars) were used for the irradiation. Details of these samples are given in appendix A.1.1. For each sample, a section of 10 mm x 2mm corresponded to irradiated zone while the rest of the sample was unirradiated.

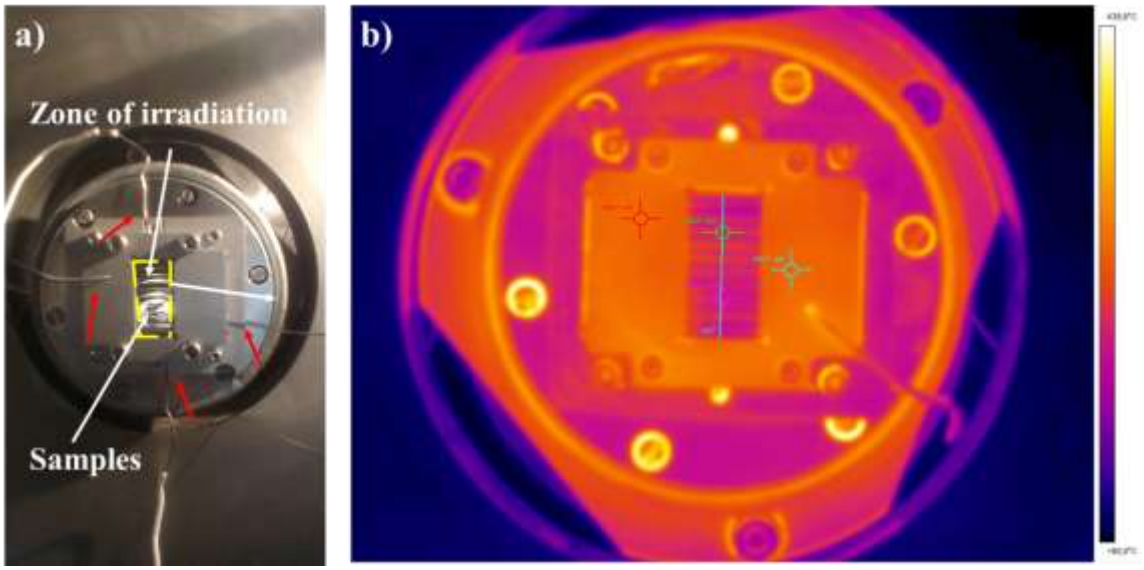

Figure 2-21: a) Samples placed on the irradiation stage during Fe^{5+} irradiation at JANNuS Saclay. Irradiation zone is indicated by yellow dashed square and thermocouples are indicated by red arrows. b) Infra-red heat map indicating the temperature profile during the Fe irradiation

First campaign was conducted on mechanically polished samples. Fe^{5+} flux of 2.6 x 10^{12} ions/cm^2/s for a duration of 8 hours was used which corresponds to a dose of 10 dpa KP at the surface. Samples irradiated in this campaign will be addressed as 10 dpa Fe (mech) irradiated samples. In second campaign, vibro polished samples were irradiated using Fe^{5+} flux of 2.24 x 10^{12} ions/cm^2/s for 5 hours. The dose at the surface of these samples was 5 dpa KP and hence, these samples will be addressed as 5 dpa Fe. In last campaign, like first campaign, Fe flux of 2.6 x 10^{12} ions/cm^2/s was used for a duration of 8 hours. The dose implanted was 10 dpa KP and samples will be referred as 10 dpa Fe samples. Note that the ion flux and time of irradiation used for Fe irradiation was smaller compared to proton irradiation, yet the damage induced was higher. This is due to the higher damage rate of the former.

Using the displacement threshold energy of 40 eV for Fe, Cr and Ni [15], SRIM calculation predicted a penetration depth of ~2.5 µm for 10 MeV Fe ions in austenitic stainless steel. This means that for all these irradiation campaigns the irradiated region in the material extended upto a maximum of 2.5 µm. The irradiated region consisted of continuously varying damage region and an irradiation peak at ~2 µm. Unlike proton irradiation, no region of constant damage exists for Fe irradiation (Figure 2-22).

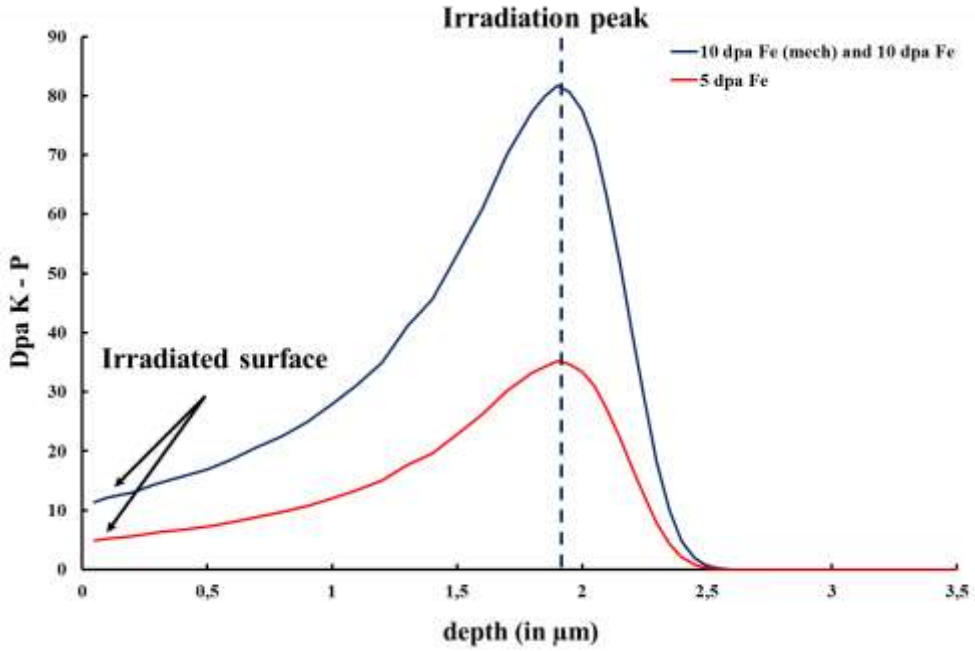

Figure 2-22: Damage profile for 10 dpa (mech), 10 dpa Fe^{5+} irradiation (in blue) and for 5 dpa Fe^{5+} irradiation (in green) in SS 304L obtained using SRIM-2011 under K-P approximation and using threshold displacement energy of 40 eV [15].

The summary of the irradiation campaigns is given in Table 2-5.

Sample	Energy (MeV)	Irradiation time (hrs)	Flux (x 10^{12} ions/cm^2/s)	Dose rate (at surface damage) (x 10^{-4} dpa K-P/s)	Dose (at surface) (dpa K-P)	Dose (at Peak) (dpa K-P)	Peak position (µm)
10 dpa – Fe (meh)	10	8	2.6	3.2	10	75	2
5 dpa – Fe		5	2.24	2.7	5	35	
10 dpa – Fe		8	2.6	3.2	10	75	

Table 2-5: Different parameters for all the iron irradiation campaigns conducted at 450 ± 20 °C.

In addition to these single beam irradiations, one double beam irradiation was conducted on vibro polished samples using 10 MeV Fe^{5+} and 1 MeV He^{+}. The purpose of this irradiation was to facilitate the formation of cavities and bubbles in the material which will help to study their role in the SCC of the irradiated austenitic stainless steel. However, it will not be discussed in this study and the samples of this irradiation will only be used in oxidation studies. He/dpa ratio of 15 appm/dpa was used as it is the upper bound to what the core internals experience in PWRs. The Fe^{5+} and He^{+} flux used were 2.24 x 10^{12} ions/cm^2/s and 2.09 x 10^{11} ions/cm^2/s respectively. The irradiation was conducted for 5 hours. Helium beam was incident on samples with an angle of 15°.

Aluminium degrader of different thicknesses between 0.0 – 2.0 µm were used to homogeneously distribute the Helium in the samples. While travelling through degrader, He^+ ions loses energy. Dependent on the thickness of the degrader, some of the ions are lost due to divergence after scattering in the foils and few others due to straggling in the thick foils. These phenomena were taken in account during the damage profile calculations. Damage implanted in the samples due to He^+ beam was 0.019 dpa which is very low compared to damage implanted by Fe^{5+} (5 dpa). Hence, these samples were considered to have damage of 5 dpa KP solely from iron irradiation and will be addressed as 5 dpa FeHe samples. The damage profile is shown in figure (Figure 2-23).

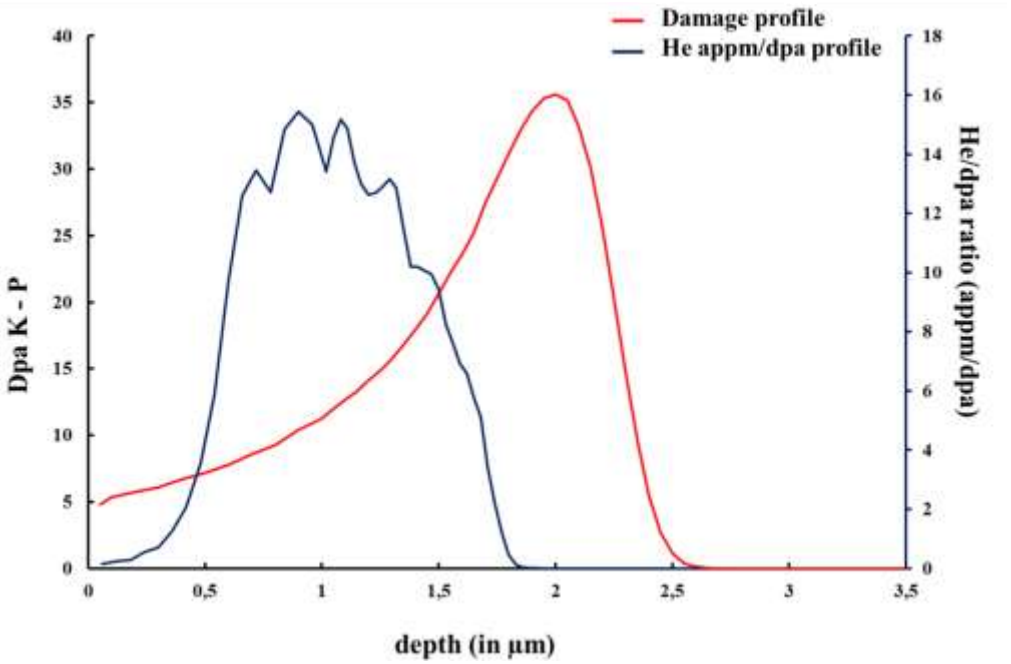

Figure 2-23: Appm/dpa (KP) profile along with Damage profile for 10 MeV Fe ions and 1 MeV He ions in SS 304L obtained using SRIM-2011 under K-P approximation and using threshold displacement energy of 40 eV [15].

Both the ion irradiations were conducted with great precautions. As there was no hot spot or any other issue, it was assumed that all the irradiation campaigns were successful. To verify the assumptions, several tests were conducted which will be described in following sections.

2.3.2. MICROSTRUCTURE CHARACTERIZATION

The microstructural characterization of the irradiated sample was performed using the same TEM as used for unirradiated virgin material. To characterize the irradiated surface, TEM sample preparation was done using PIPS (ion milling) and to characterize the microstructure at the irradiation peak (solely for proton irradiated sample) TEM sample

preparation was done using TENUPOL (chemical etching). Both of the TEM sample preparation techniques have been detailed in appendix A.1.2.2.

The primary defect induced by irradiation in the microstructure is Frank loops. Efforts were made to characterize their presence (both qualitatively and quantitatively). Long established Rel – Rod technique using the diffraction conditions ([011] zone axis with g = ½ (3-11) diffusive line or [001] zone axis with g = 022 streak) was used in TEM. The detail of the process is given in section § A.1.2.2.1. Some studies have reported to observe cavities, irradiation enhanced precipitates ($Cr_{23}C_6$) and irradiation induced precipitates (Ni_3Si and $M_6Ni_{16}Si_7$) at the relevant temperature [10, 17]. Efforts were made to observe these defects as well. To characterize cavities in TEM, over and under focus technique was used.

2.3.2.1. PROTON IRRADIATION

The sub-surface of 1 dpa H samples consisted of a zone of nanograins as these samples were mechanically polished. However, to observe the irradiation induced defects, few microns from the surface was removed during TEM sample preparation. No such issues persisted for 2 dpa – H sample.

Frank loops were present in the microstructure post to proton irradiation. TEM DF images of the four different families of the loops with corresponding diffraction pattern are shown in Figure 2-24. These images were obtained by selecting either of the streaks (indicated by red arrows) presents in the diffraction pattern.

Though the Frank loops were observed in all the samples (at surface doses as well as at irradiation peak doses), cavities were observed only in 1 dpa H sample at irradiation peak dose. The cavities observed were facetted in nature and their spatial distribution was homogeneous. Figure 2-25 shows the DF TEM image of the Frank loops and BF TEM image of the cavities observed at the irradiation peak damage (18 dpa KP) in the 1 dpa H sample.

The quantitative assessment of these defects included the estimation of density and size distribution of the defects. This was done using Visilog software. In the case of Frank loops, the quantification was performed on 3 different images for each dose. To estimate the density of the loops, the mean thickness of the TEM foils used was assumed to be 100 nm. As only the TEM foils of thickness ranging between 70 nm to 150 nm are transparent under TEM, the choice of sample thickness 100 nm is justified. As no actual thickness measurements were performed, the thickness chosen could be a source of error in estimating density. Hence, the error in the density value was estimated by assessing the density using foil thicknesses of 70 nm and 150 nm.

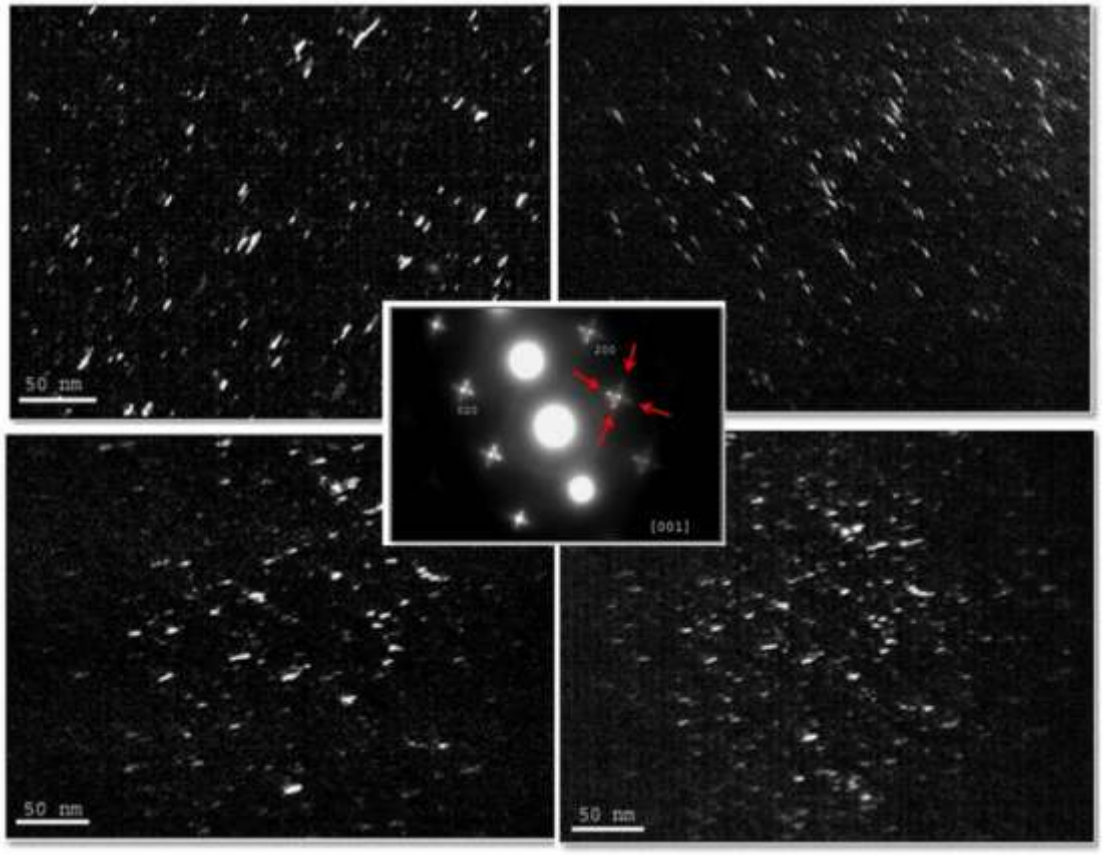

Figure 2-24: Four families of Frank loops observed at a depth of 30 µm (~18 dpa K-P) on 1.0 dpa-H proton irradiated TENUPOL prepared sample along with diffraction pattern.

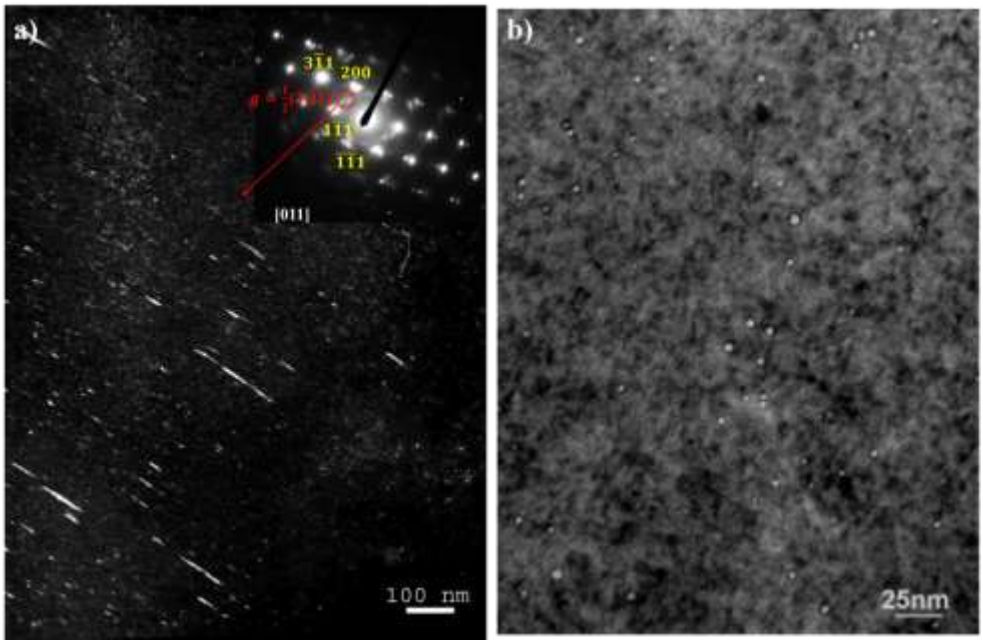

Figure 2-25: a) Dark Field image of the Frank loops observed at the irradiation surface (~ 1 dpa K-P) b) cavities observed at the irradiation peak (~18 dpa K-P) in the 1 dpa-H proton irradiated sample.

The results of the quantitative assessment of the Frank loops are tabulated in Table 2-6.

Sample	Dose (dpa K-P)	Location	Frank loops density (x 10^{22} loops/m^3)	Mean Frank loops size (nm)
1 dpa – H	1	Irradiated surface	1.5 ± 0.6	13.6 ± 4.4
2 dpa - H	2	Irradiated surface	3.6 ± 1.5	13.8 ± 4.8
0.25 dpa – H	3	Irradiation peak	1.6 ± 1.0	18 ± 4
1 dpa – H	18	Irradiation peak	21.0 ± 8.0	4.6 ± 1.6

Table 2-6: Comparison of the irradiated microstructure observed for different doses in proton irradiated samples.

Trend in the loops number density and size may not be clear from the Table 2-6 but when plotted as a function of dpa on a lognormal graph, saturation in density and size was observed which was in accordance with literature (see § 2.3.4). The only exception was the size corresponding to damage of 18 dpa K-P.

The quantitative assessment of cavities yielded a mean density of 3.6 ± 1.45 x 10^{21} cavities/m^3 and a mean size of 2.7 ± 0.1 nm. These quantifications were done on 2 different images and the TEM foil thickness of 100 nm was chosen.

Comparison of these results with the literature is provided in the section § 2.3.4.

2.3.2.2. SELF ION IRRADIATION

All the TEM characterizations, in this case, were done at the irradiated surface as the irradiated zone was just 2.5 µm deep in the material. Like proton irradiated samples, Frank loops were observed in all the samples. However, due to small penetration depth, a strong impact of surface preparation was observed in this case.

Starting with mechanically polished samples (10 dpa Fe (mech.)), post irradiation the subsurface microstructure consisted of nanograins. The size of these nanograins ranged between 100 – 300 nm. The nanograins were present prior to the irradiation as well. However, in irradiated samples, some of the nanograins had a low content of Cr and Ni (EDX chemical composition: 89 at % Fe, 10 at % Cr and 1 at % Ni) compared to the nano austenite grains. The diffraction pattern indexed these grains to be Body Centered Cubic (Im3m space group and a = 2.86 Å). This lead to the conclusion that these grains were martensite (marked as M in Figure 2-26a) depleted in Cr and Ni.

Careful inspection revealed the presence of irradiation induced defects in few nano austenite grains. BF TEM image (on zone axis [011]) of one of the nano austenite grain

containing Frank loops is shown in Figure 2-26b. No irradiation induced defects were observed in martensite grains and hence, quantification of these loops was done by just considering the austenite grains volume. The average density estimated using the TEM foil thickness of 100 nm was $6 \pm 2 \times 10^{20}$ m^{-3} and the average size was 20.3 ± 2.7 nm.

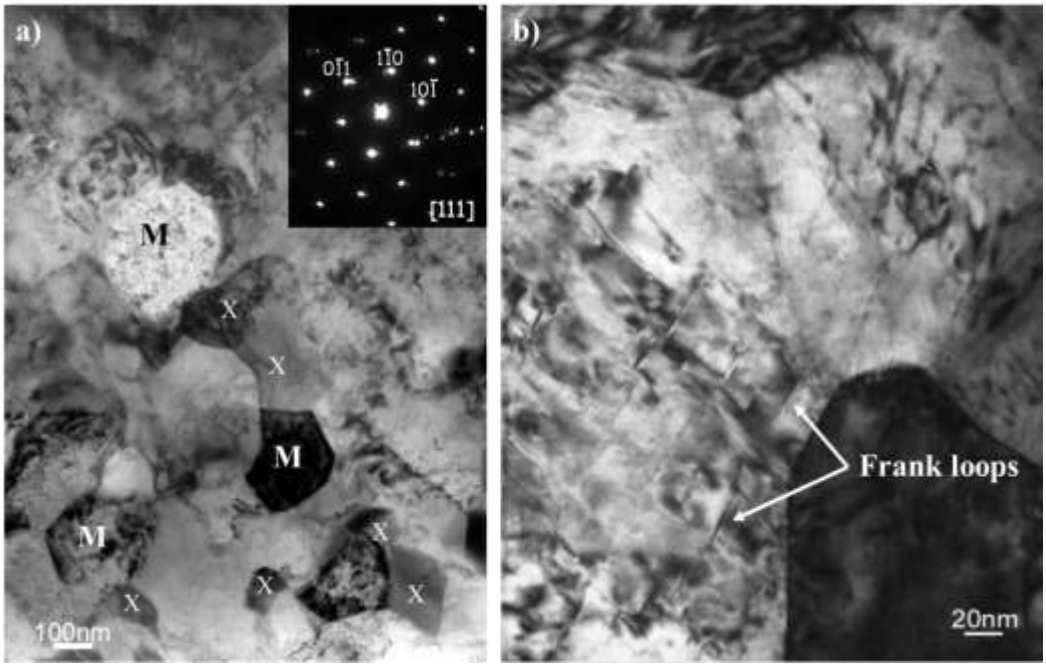

Figure 2-26: Bright Field TEM images showing a) the nano martensite grains (marked as M and $Cr_{23}C_6$ carbides marked as X) along with associated diffraction pattern b) Irradiation induced defects observed in few nano austenite grains in the 10 dpa Fe (mech) irradiated samples.

Frank loops were observed in both 5 dpa Fe (Figure 2-28a) and 10 dpa Fe samples as well. To recall, these samples were vibro-polished and had no nano grains in the subsurface. The DF TEM image (g = ½(3-11) on zone axis [011]) and high resolution BF TEM image of the Frank loops observed in 5 dpa sample is shown in Figure 2-27. In 5 dpa Fe sample, the size of the majority of the loops observed ranged between 6 and 14 nm. The largest loop size observed was 30 nm while no loop smaller than 2 nm was accounted. The size distribution of Frank loops (Figure 2-28b) appeared to be an asymmetric distribution that extended up to 30 nm similar to what has been reported in literature for neutron irradiated SS 304L [18]. The average number density and diameter of dislocation loops observed were $5 \pm 3.1 \times 10^{21}$ m^{-3} and 13.4 ± 1.9 nm respectively.

The results of the quantitative assessments of the irradiation induced Frank loops are summarized in Table 2-7. As evident, the density of the Frank loops was smaller by a factor of ~ 40 in 10 dpa – Fe (mech.) compared to 10 dpa – Fe despite the same dose. This suggests that the nanograins highly suppressed the density of irradiation induced defects. Considering the error in density measurements due to the choice of TEM foil thickness, a

slightly lower density of loops in 5 dpa – Fe sample was observed compared to 10 dpa – Fe sample. Detailed comparison of these results with literature is done in § 2.3.4.

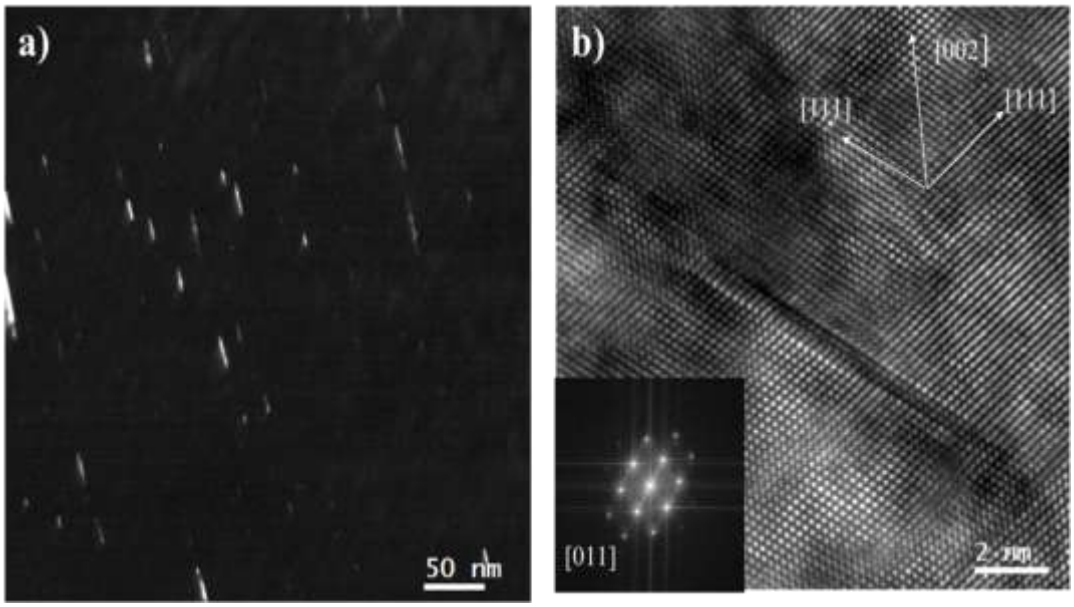

Figure 2-27 : a) Rel-rod DF TEM image b) High resolution BF TEM image along with Fourier transform (inset) of Frank loops observed in 5 dpa Fe sample.

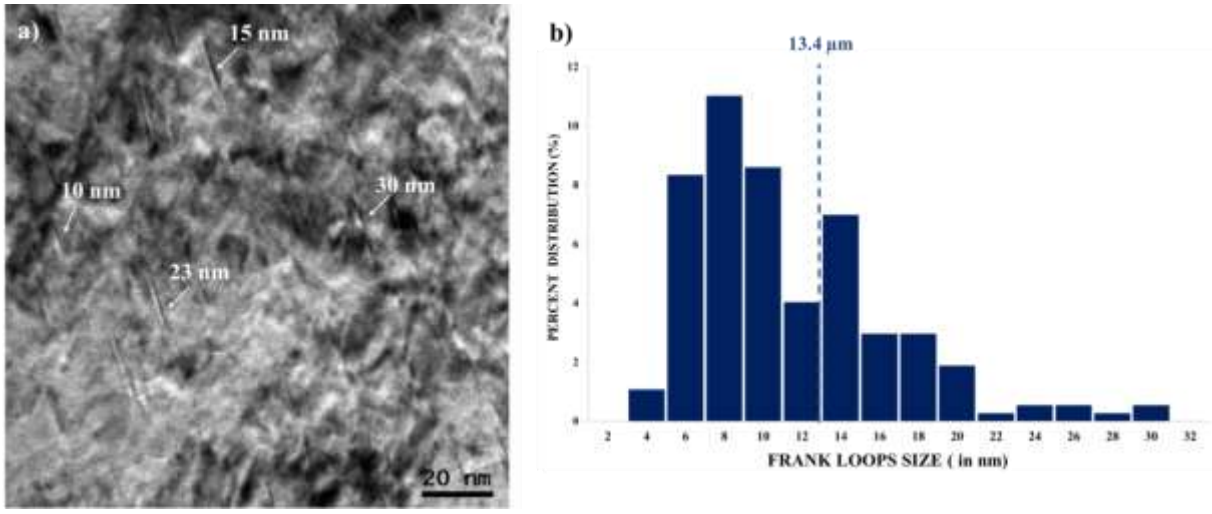

Figure 2-28: a) Bright Field TEM image indicating the size of few Frank loops observed b) size distribution of the Frank loops observed in 5 dpa Fe sample.

Sample	Dose (dpa K-P)	Location	Frank loops density (x 10^{22} loops/m^3)	Mean Frank loops size (nm)
10 dpa – Fe (mech)	10	Irradiated surface	0.06 ± 0.2	20.3 ± 2.7
5 dpa – Fe	5	Irradiated surface	0.5 ± 3.1	13.4 ± 1.9
10 dpa – Fe	10	Irradiated surface	2.55 ± 10.5	14.9 ± 3.6

Table 2-7: Comparison of the irradiated microstructure observed in Fe irradiated samples.

Beside Frank loops, few cavities and irradiation – enhanced carbides (indexed as $Cr_{23}C_6$ in FCC cell with Fm3M space group and cell parameter a = 10.65 Å and marked as X in Figure 2-26) were observed in 10 dpa Fe (mech) sample (Figure 2-29). Cavities were facetted and their size ranged between 8.2 nm to 28.47 nm giving a mean size of 18 nm. Their distribution was highly inhomogeneous. As they were observed only in one or two nano – austenite grains, density estimation was not performed. But no such defects were observed in any other sample. This suggests that the behavior of mechanically polished material to Fe irradiation was different compared to vibratory polished material due to the presence of nanograins in the former.

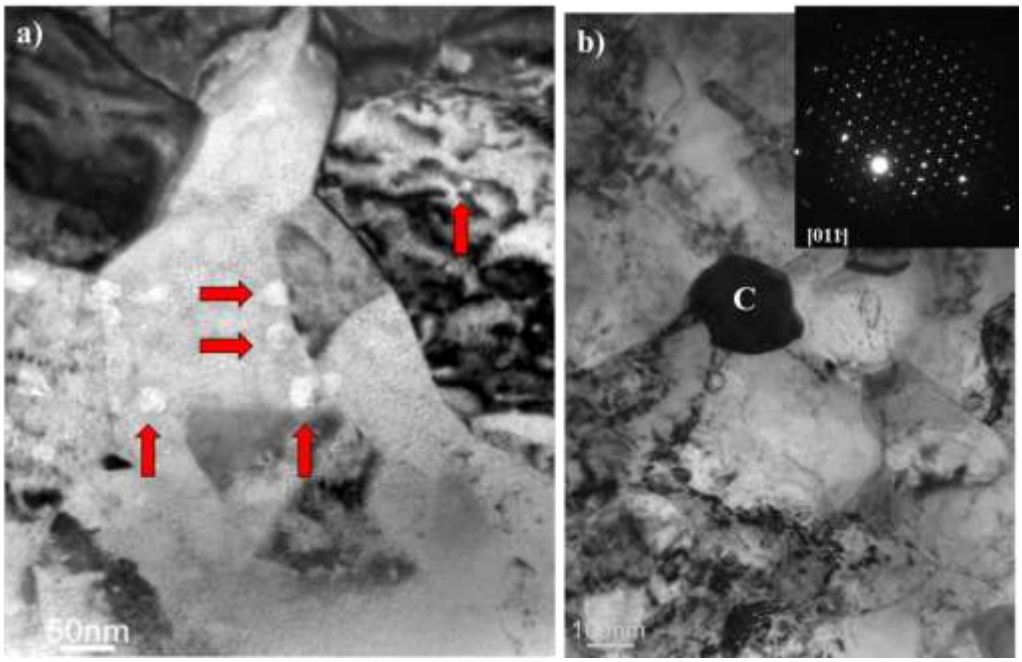

Figure 2-29: BF TEM image of a) cavities observed in a nano austenite grain b) carbides (marked as C) with associated diffraction pattern which indexed it as $Cr_{23}C_6$.

2.3.3. HARDNESS

Owing to the small penetration depths associated to the ion irradiation, nano-hardness testing is generally employed to estimate the irradiation hardening in the material. These tests were done at INP – ENIT Tarbes and SRMP, CEA Saclay.

To testify if this technique could be used in this study, an irradiation damage profile tracing experiment was done on 1 dpa H proton irradiated sample at INP – ENIT Tarbes. For the purpose, sample was mounted using hot compression (upto 200 °C) thermosetting resins. The sample was placed with irradiated face on side (not on top) along with the appropriate mounting resin in a mounting press (Figure 2-30). After hot mounting, sample was polished upto ¼ μm diamond paste. Samples were then mounted on nano indentation machine to make indents. Indents were made along a line slightly tilted (8 – 15 °) with

respect to the edge (Figure 2-31) to increase the number of indents in irradiated region. Starting from the irradiated region, indents were made upto a distance of 100 µm from edge suggesting first few indents were in irradiated region while others were in unirradiated region of the sample. Several tests were conducted to improve the statistics. The hardness was plotted as a function of distance from extreme surface (or irradiation penetration depth) to trace the irradiation damage profile.

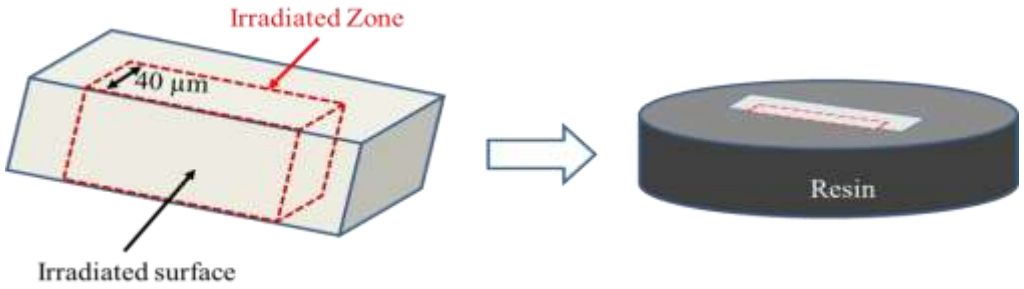

Figure 2-30: Schematic to show the position of the irradiation zone in the resin.

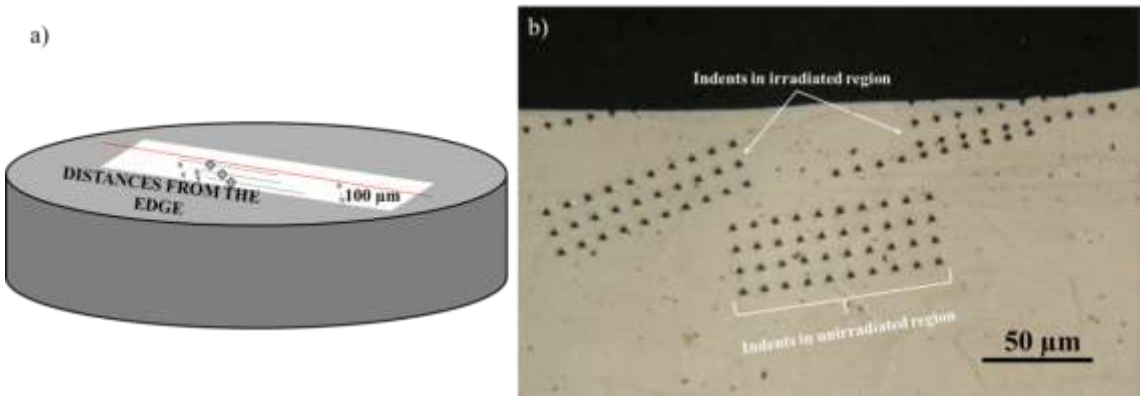

Figure 2-31: a) Schematic to represent the indents made on the sample b) Actual image of the indents made during the nano indentation test to trace the irradiation damage profile.

The damage profile traced using nano indentation test was compared with SRIM calculation and the results are shown in the Figure 2-32. The indents were made at an indent penetration depth of 500 nm which was within the region of surface hardened zone. The hardness for the unirradiated region obtained was between 3 and 4 GPa which corresponds well with the value reported for mechanically polished unirradiated sample. The hardness value for constant dpa (or uniform damage) region was between 5 and 6 GPa indicating a higher value of hardness for irradiated region. This increase in hardness on irradiation is evident in the figure as well. In one of the test, a peak in hardness profile was observed which coincided well with the irradiation peak obtained using SRIM calculations. While in rest of the tests no such peak was observed and the hardness in the irradiation peak region was similar to the hardness corresponding to constant dpa region.

Nevertheless, this test indicates that the nano indentation technique is sensitive to the irradiation hardening and can be employed to estimate the increase in hardness with ion irradiations conducted in this study. The hardness measurement tests were done at INP – ENIT Tarbes and CEA Saclay. The indents were made on the irradiated and unirradiated region of the same sample and the corresponding hardness values were compared to eliminate any surface preparation effect. H^2 versus 1/d graphs were plotted for each condition (irradiated, unirradiated) using the results from the test and the extrapolated values from these graphs were used to calculate the hardness of the irradiated material as well as increase in hardness with irradiation.

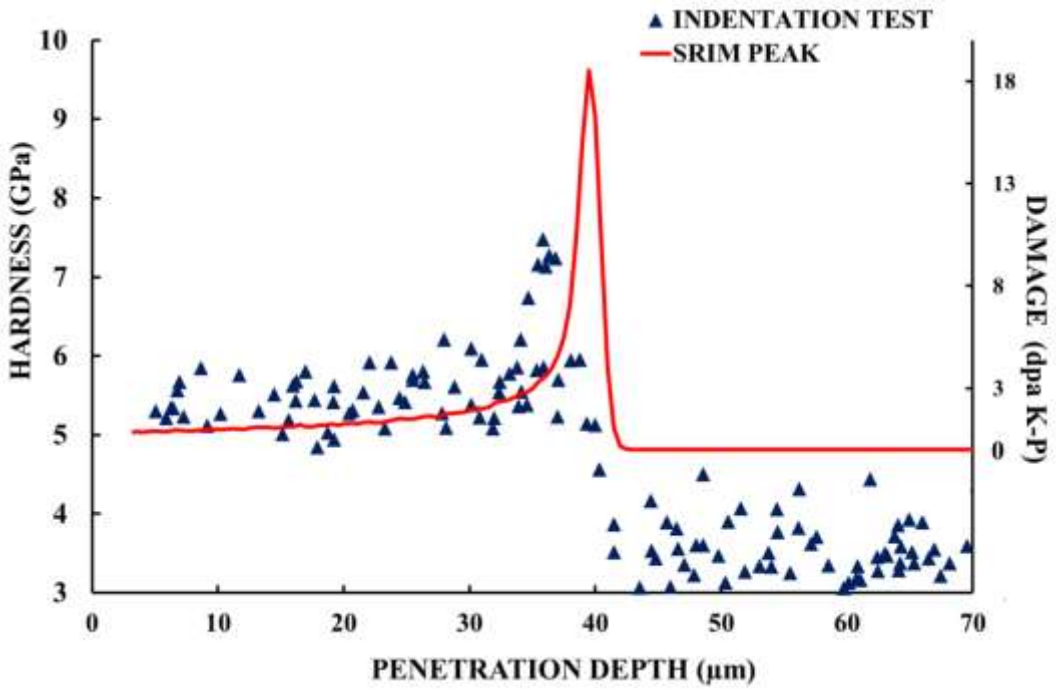

Figure 2-32: Comparison of proton irradiation damage profile traced by continuous stiffness measurement – nano indentation test performed on 1 dpa H sample at a depth of 500 nm with SRIM calculations.

2.3.3.1. NANO-HARDNESS

The Nix – Gao plots for 1 dpa – H and unirradiated material are shown in Figure 2-33. Note that for these hardness measurements, like in unirradiated material, 15 indents were made at a depth of 6 µm. This indicates that the values obtained are not affected by the surface preparation artifacts. From the graph, the extrapolated H^2 value estimated for the irradiated sample was 21 ± 5 GPa^2 while that for unirradiated sample was 4.1 ± 0.5 GPa^2. This indicates an increase of 130 % in hardness corresponding to a dose of 1 dpa K–P (Figure 2-33).

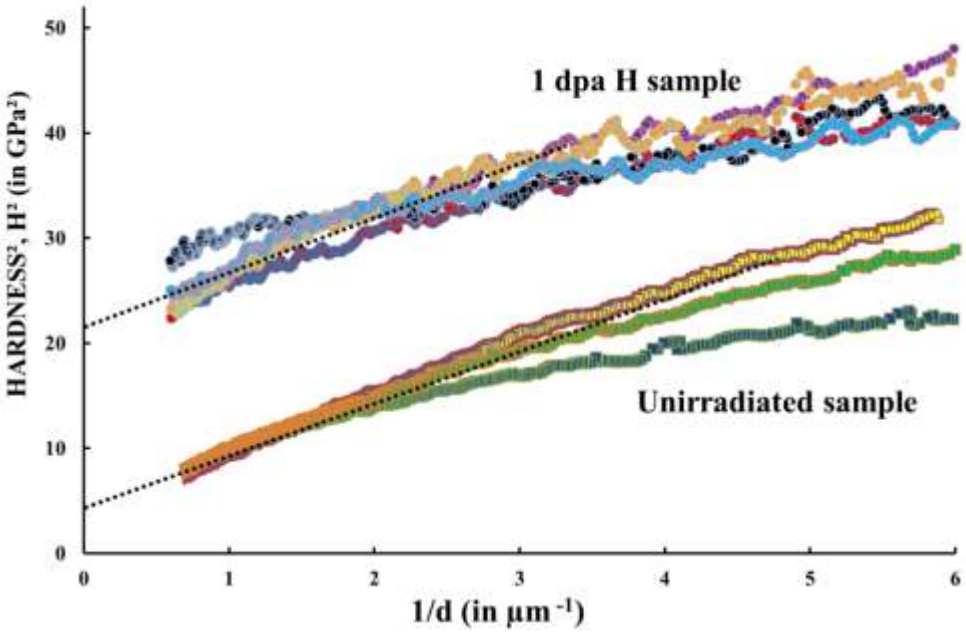

Figure 2-33: Comparison of Hardness profile for unirradiated and 1 dpa – H samples along with fitting lines to assess extrapolated values (black dashed lines) obtained using nano-hardness test.

On 2 dpa – H sample, a grid of 4 lines with 20 indents each were made corresponding to 4 different penetration depths (0.25 μm, 0.5 μm, 1 μm and 2 μm). Figure 2-34 shows a small portion of the indent grids used along with some Load – displacement graphs. The distance between the two consecutive indents and between two lines was 40 μm each. Mean of the 20 values for each indent depth was used as the representative of the hardness for that indent depth. The Nix Gao plot for this sample is shown in Figure 2-35. An increase of 120 % in hardness corresponding to a dose of 2 dpa K–P was obtained. The nano-hardness tests on 1 dpa H and 2 dpa H samples were done on two different machines and hence, comparison of hardness values for the two cases could be somewhat misleading.

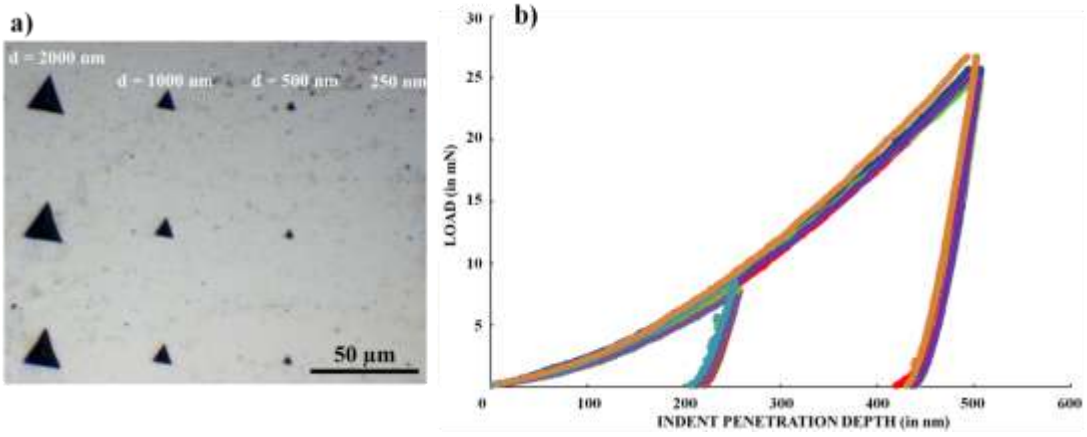

Figure 2-34: a) Image of the nano indent matrix in the unirradiated region obtained using optical microscope b) Evolution of the load as a function of indent penetration depth during nanoharness indentation tests.

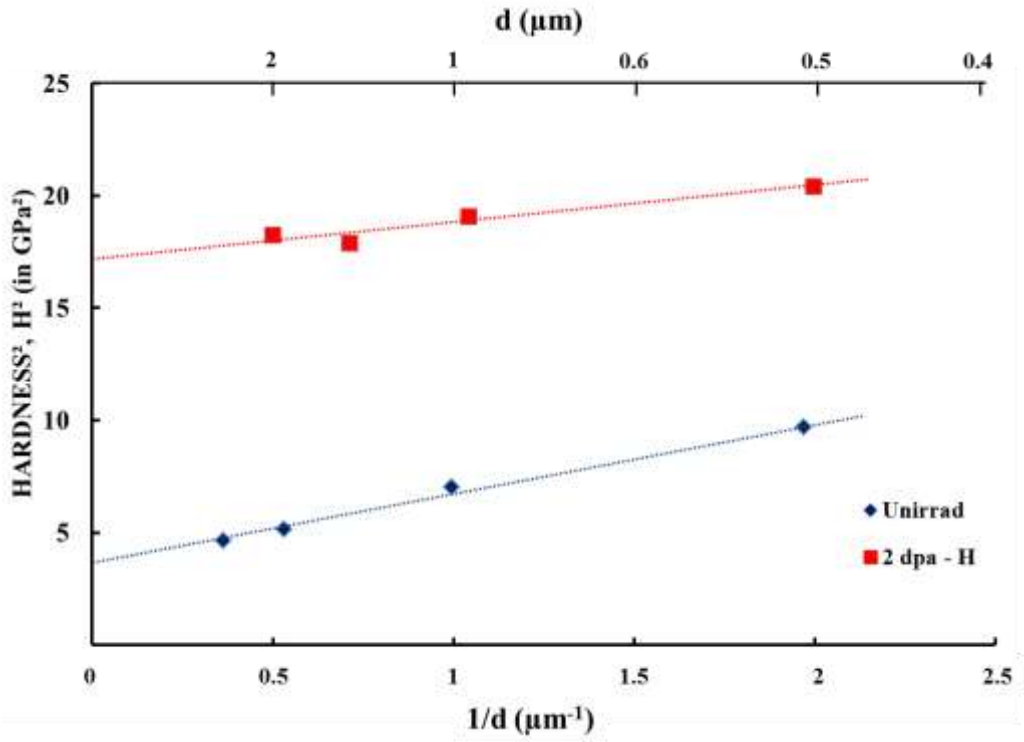

Figure 2-35: Comparison of Hardness profile of 2 dpa H and un-irradiated samples along with fitting lines to assess extrapolated values (black dashed lines) obtained using nano-hardness test.

Similar to the 2 dpa – H sample, nano indentation test was conducted on the Fe irradiated samples. While calculating the extrapolated values for Fe irradiated samples, special attention needs to be paid. As stated before the plastic zone of the indent made at a depth d extends upto 7d. Recent studies have shown that the radius of plastic zone is dependent on the dose. Miura et al. [19] reported to observe a plastic zone extending upto 4d for 10 dpa Fe irradiated austenitic stainless steel material while for the same material in unirradiated state the plastic zone can extend up to a maximum of 10d. Going with this argument, in this study we considered that the plastic zone extends upto 4d for irradiated material and 7d for unirradiated material. The extent of plastic zone is an issue of concern for Fe irradiated samples because, unlike H, the damage profile in these samples consists of a continuously varying damage region followed by a peak at a depth of 2 µm i.e. the net thickness of the material irradiated is just 2.5 µm. Considering a plastic zone of 4d, as soon as this value will exceed 2.5 µm, the unirradiated material beneath will start contributing into hardness value. So for all values of $d > 0.5$ µm, there is a contribution from unirradiated part and this contribution increases with increasing d. This was evident in the hardness profiles (Figure 2-36) plotted for these samples.

Hence, to evaluate the hardness solely for irradiated part, the extrapolated values for Fe irradiated samples were evaluated using the points between $4\ \mu m \geq 1/d \geq 2\ \mu m$. The Nix – Gao plots for Fe irradiated samples are shown in Figure 2-37.

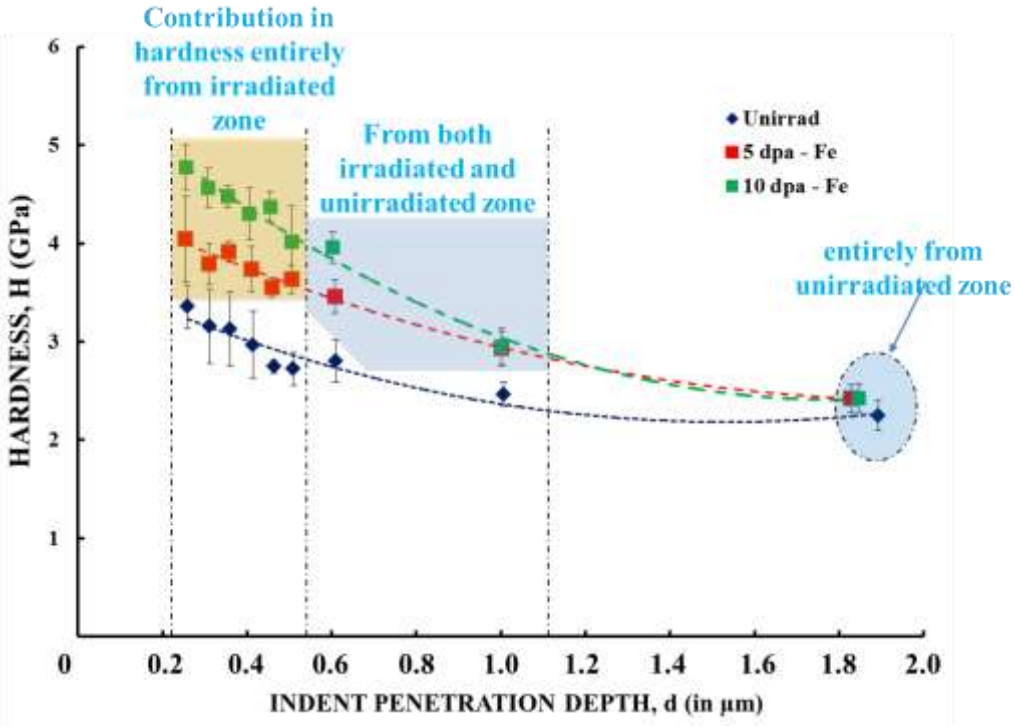

Figure 2-36: Hardness profile showing the comparison of hardness obtained for unirradiated (blue), 5 dpa – Fe (in red) and 10 dpa – Fe (in green) materials using nano indentation test.

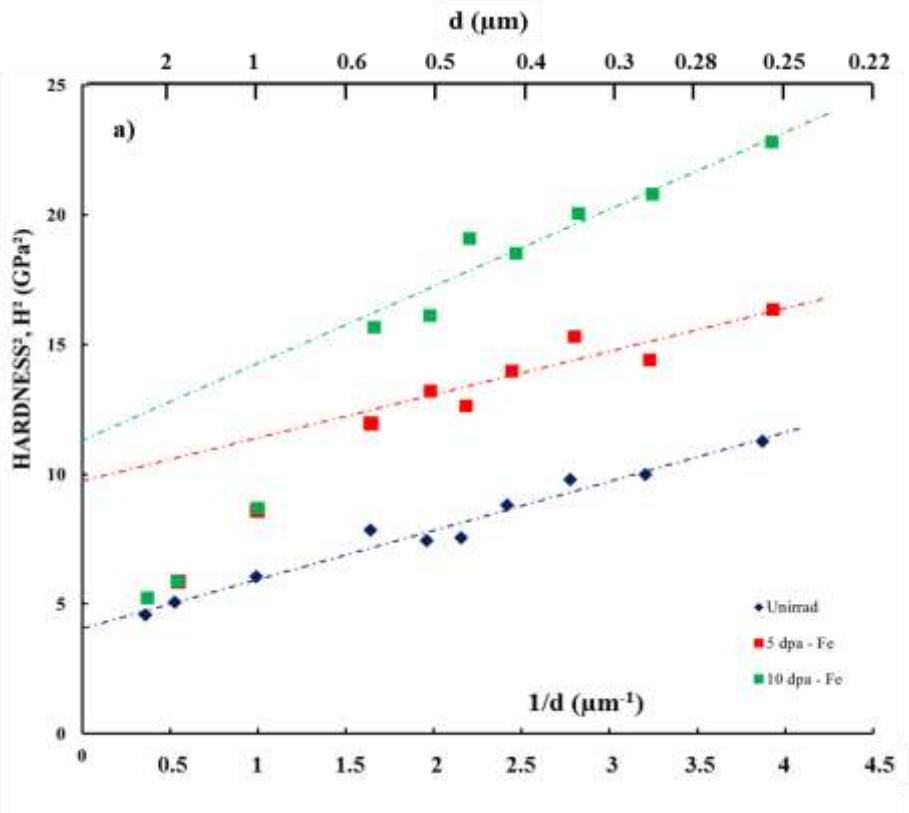

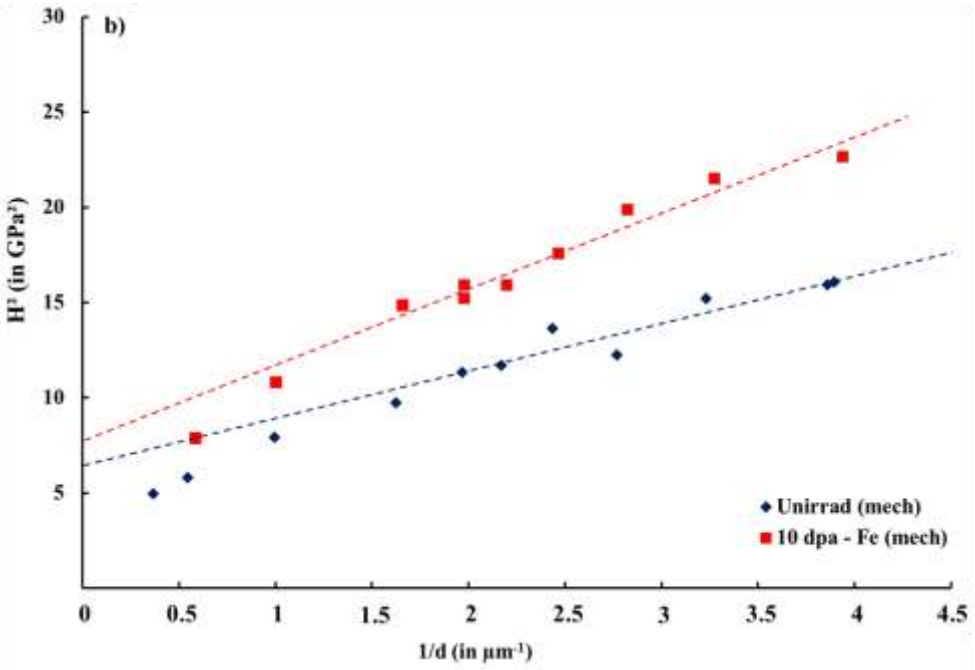

Figure 2-37: Comparison of Nix Gao plots of a) 5 dpa Fe, 10 dpa Fe b) unirradiated and 10 dpa Fe (mech.) samples obtained using nano-hardness test.

An increase of 54 % and 67 % in hardness was observed in 5 dpa – Fe and 10 dpa – Fe samples respectively. As the irradiation induced hardness has been reported to saturate at around 5 dpa, observation of similar increase in hardness despite the dose twice as high is consistent. An increase of just 8% for 10 dpa – Fe (mech) sample was observed.

Irradiation hardening observed for all the conditions has been summarized in the Table 2-8 below.

Sample	Dose at the surface (Dpa K-P)	(ΔH /H) (%)
1 dpa – H	1	130
2 dpa – H	2	120
5 dpa – Fe	5	54
10 dpa – Fe	10	67
10 dpa – Fe (mech.)	10	8

Table 2-8: Comparison of irradiation hardening observed for different doses in material irradiated using different ions.

As proposed by Busby et al. [20], from the measured hardness values the increase in yield strength can be calculated using the relation:

$$\Delta\sigma_y = 3.03\ \Delta H_v \quad \text{..... (II.7)}$$

Besides, the increase in yield strength on irradiation has been attributed to the irradiation induced defects in the microstructure or to be precise the barrier these defects creates in the motion of the dislocations. Hence, increase in yield strength is proportional to the number density and size of these defects. Using dispersed barrier hardening model, the increase in yield strength due to these defects can be calculated using the relation (see section § 1.3.1.3) [1]:

$$\Delta\sigma_y = (\Sigma\Delta\sigma_k^{\,2})^{1/2} \qquad \text{and} \qquad \Delta\sigma_k = \alpha M\mu b(N_k d_k)^{1/2} \quad \ldots\ldots\ldots \text{(II.8)}$$

Using above two relations, it can be deduced that increase in hardness is proportional to the number density of the defects.

$$\Delta H_v = \frac{\alpha M\mu b}{3.03}(N_k d_k)^{1/2} \quad \text{or } \Delta H_v \propto (N_k d_k)^{1/2} \quad \ldots\ldots\ldots \text{(II.9)}$$

Considering only one type of defects (Frank loops), irradiation hardening was plotted as a function of square root of product of density and size of Frank loops observed in the microstructure. The results obtained from the hardness tests conducted on same machine are only taken in account to eliminate effect of any unknown parameter (such as machine performance). A good linear relation between the increase in hardness and product of number density and size of frank loops was obtained.

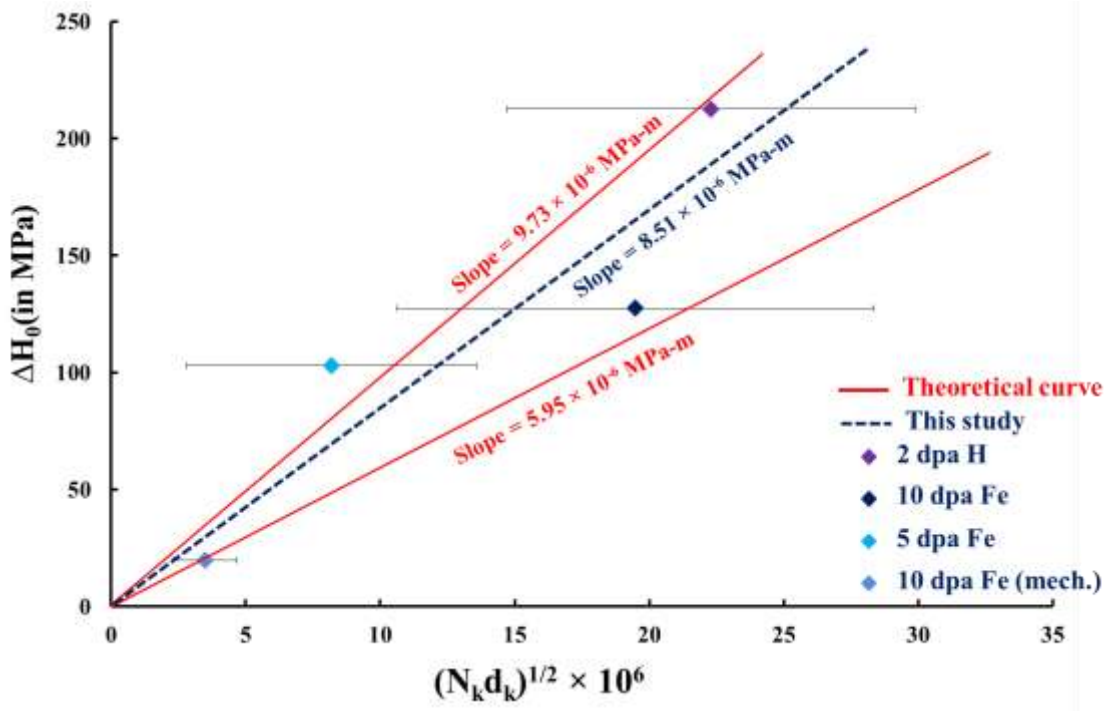

Figure 2-38: Increase in hardness plotted as a function of density of Frank loops for all irradiation doses.

Using the maximum and minimum values of the parameters reported in literature for solution annealed steel irradiated at temperatures > 300 °C, i.e. α = 0.45 and 0.33, M = 3.06, μ = 84,000 and 72,000 MPa, and b = 0.255 and 0.248 respectively, theoretical curves (with slopes: $\{\frac{\alpha M \mu b}{3.03}\}_{max}$= 9.73 × 10^{-6} MPa-m and $\{\frac{\alpha M \mu b}{3.03}\}_{min}$= 5.95 × 10^{-6} MPa-m) are plotted in Figure 2-38 as well for the comparison. Depending on the choice of the parameters, the value of α calculated for the Frank loops contribution in hardness in this study ranged between (0.39 – 0.47) which is in very good accordance to the values reported in literature (0.33 – 0.45) for irradiation temperatures > 300 °C. This implies that eq. II.9 works very well for the irradiated samples used in this study. In fact, using eq. II.9, the observation of smaller increase in hardness in the 10 dpa Fe (mech.) sample compared to 10 dpa Fe sample could be explained on the basis of the observation of density of Frank loops smaller by a factor of 40 in the former despite same dose. A closer look at the graph, however, points out that the increase in hardness in 2 dpa – H sample was much higher compared to 10 dpa – Fe sample despite the observation of only slightly higher density of Frank loops. This might suggest the contribution in hardness from small defects other than Frank loops which were not observed during TEM observations of the samples.

2.3.4. COMPARISON WITH LITERATURE

The ion irradiations were carried out to emulate the microstructure similar to the one obtained from neutron irradiation. To verify the ion irradiation induced microstructure and hardening, comparison with literature was done.

- **Defect density and size comparison**

In literature, the primary microstructural defects reported post to irradiation are Frank loops and cavities. The density and size of Frank loops has been reported to increase with dose initially followed by saturation. The density saturates at around 1 dpa while saturation in size has been reported at 5 dpa for neutron irradiation. Similar trends for ion irradiations have been reported as well. However, the number density and size of the defects is highly dependent on the ion irradiation temperature. In general, number density similar while size slightly lower has been reported for proton irradiation conducted at 340 – 360 °C compared to neutron irradiation 270 – 340 °C.

As stated before, Frank loops were observed post to both ion irradiations conducted in this study. The comparison of Frank loop density and size with literature [9, 17 – 19, 21 – 37] for both ion irradiations is shown in Figure 2-39. Evident from the graphs, the number density of Frank loops observed in proton irradiated samples (this study) was in good accordance with both neutron and ion literature. However, the size was bit larger for the

low doses and slightly lower for higher dose of 18 dpa KP. Though, the values are within the scatter.

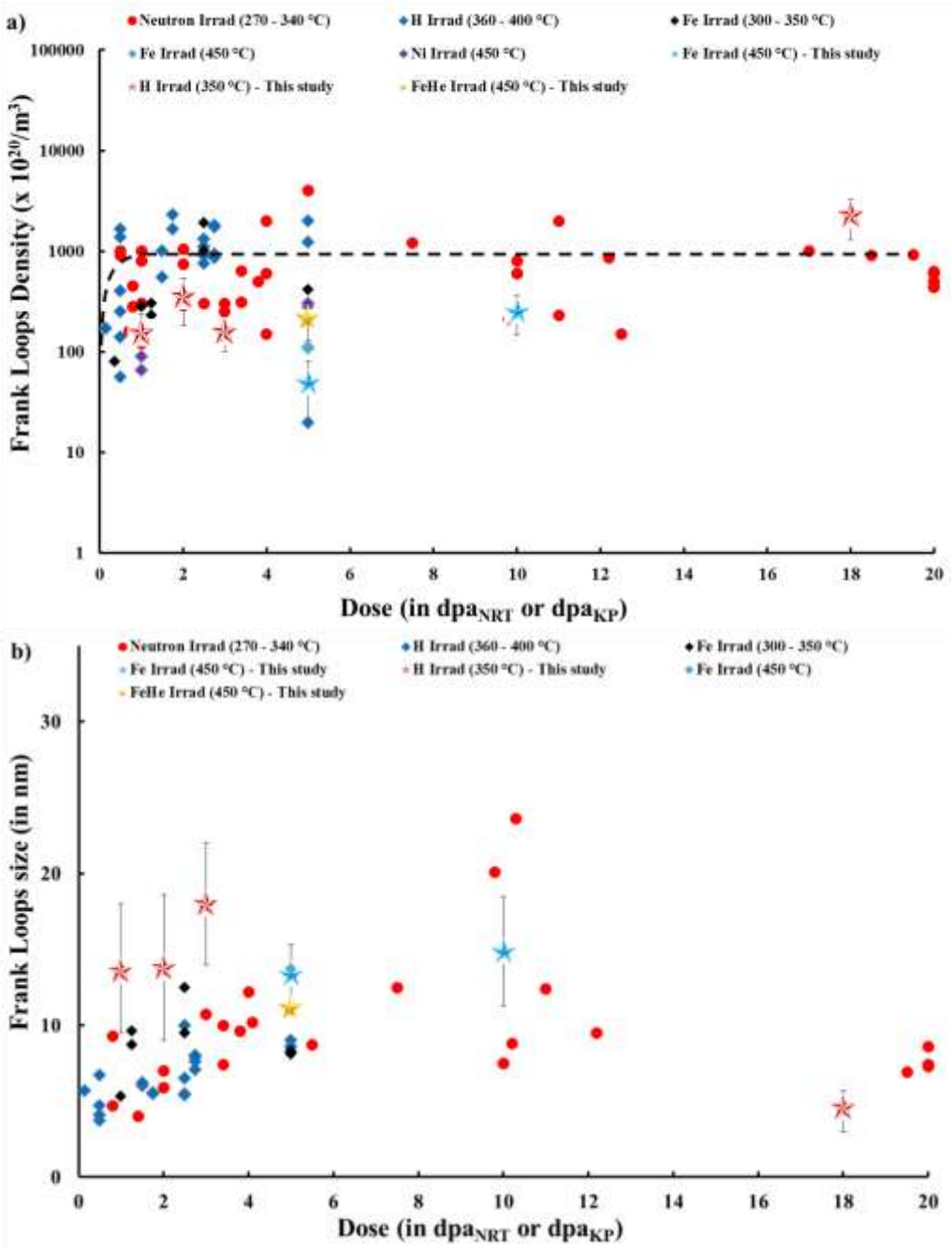

Figure 2-39: Comparison of the Frank loops a) density b) size observed for proton (this study – red star) and iron irradiated (this study – blue stars) samples with neutron, proton and iron literature [9, 17 – 19, 20 – 37].

Frank loop density comparison of 10 dpa Fe sample was in good accordance with neutron and ion literature as well as with the proton irradiation conducted in this study. However, in 5 dpa Fe sample slightly lower density was observed. There could be either of two

explanations for the same: higher irradiation temperature or wrong assessment of density. To have number density of the defects identical to neutron irradiation, Fe irradiation should have been conducted at 370 °C which is lower by 80 °C compared to the irradiation temperature used in this study (450 °C). As irradiation temperature increases the defects density decreases and the defects size increases, this difference in temperature could explains the observation of lower density and slightly higher size of Frank loops in Fe irradiated samples. However, 10 dpa Fe samples were irradiated at 450 °C as well. The density reported in these samples was also lower compared to saturated loop density that has been reported for neutron irradiated material but only by a factor of ~ 5 unlike 5 dpa Fe samples (lower by a factor of 20). This suggests that lower density reported in 5 dpa Fe sample could not have resulted from higher irradiation temperature used. To further verify, Frank loop density measurement was done on 5 dpa FeHe samples. To recall, these samples were also irradiated at 450 °C and the damage induced by He was negligible. On these samples, a density of 2.2×10^{22} loops/m^3 was estimated which is in good accordance to the value estimated for 10 dpa Fe sample and higher than the value for 5 dpa Fe sample. This confirms that the lower density observed in 5 dpa Fe sample is not a consequence of higher irradiation temperature used. The only explanation could be the underestimation of density of defects. Nevertheless, the values obtained for all the samples in this study were within the scatter reported in literature.

In addition, in mechanically polished Fe irradiated sample, the density of the Frank loops observed was lower by a factor of ~ 100 compared to neutron literature. Mechanically polished sample had nanograins and hence, higher fraction of grain boundaries which acts as sinks to these defects. Observation of lower density of defects can be interpreted as annihilation of irradiation induced defects at the sinks.

Beside Frank loops, cavities were observed at the peak damage dose (18 dpa K-P) of 1 dpa H sample. The mean number density of the cavities was $3.6 \pm 1.45 \times 10^{21}$ cavities/m^3. Pokor et al. [25] reported to observe a density of 4.7×10^{21} cavities/m^3 and a mean size of 5.4 nm at 10 dpa in neutron irradiated SA 304 L irradiated at 375 °C in EBR. This value is in good agreement with the value obtained in this study. However, due to different He/dpa ratio it is not recommended to compare the results of Fast reactors and PWR reactors. On comparing the result with the value reported in a study [9] dealing with the proton irradiation of solution annealed 304 at 360°C the value was observed to be lower by a factor of 6. Apart from Frank loops and cavities, few radiation enhanced precipitates were observed only in 10 dpa – Fe (mech.) sample and not in any other samples.

- **Irradiation hardening comparison**

Increase in hardness with increase in dose followed by saturation at 5 dpa has been reported in literature dealing with neutron irradiation. Similar trend has been observed in

proton and heavy ion irradiated samples as well. While the percentage increase in hardness values for proton irradiation have been reported to be in good agreement with neutron literature, the values smaller by a factor of 2 have been reported for heavy ion irradiation.

Post to both ion irradiations, an increase in hardness was observed. The comparison of the same with literature [31, 35 – 40] is reported in the Figure 2-40. An increase of 120 – 130 % was observed in proton irradiated samples which was in good agreement with both neutron and proton literature. The percentage increase observed in Fe irradiated sample was 54 – 67 %, which was lower by a factor of 2 compared to neutron literature but in excellent agreement with the Fe literature. Despite a lower number density of defects in 5 dpa Fe sample, observation of a surprisingly good accordance in hardness with literature suggests that indeed, there was an underestimation of density of Frank loops in 5 dpa – Fe sample.

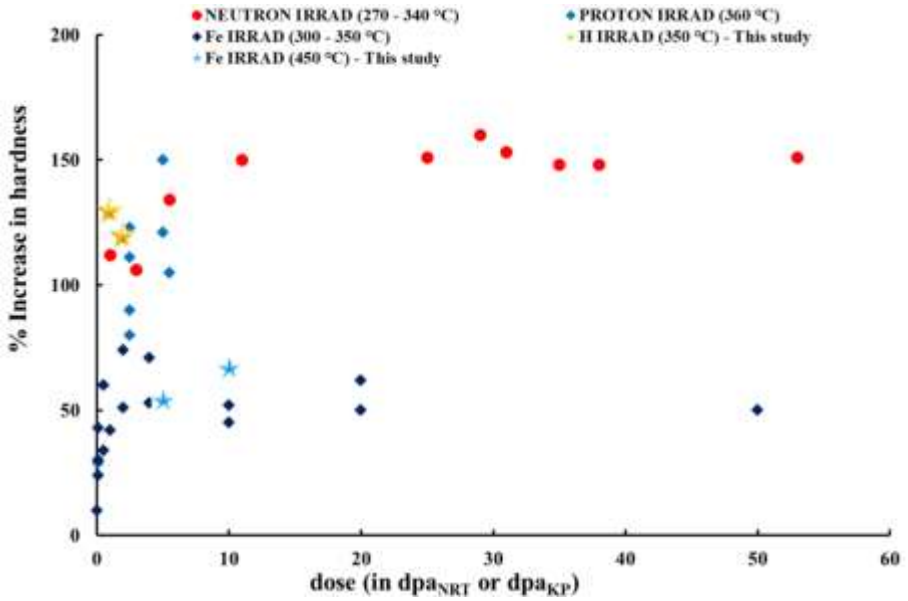

Figure 2-40: Comparison of the irradiation hardening observed in proton (this study – yellow star) and iron irradiated (this study – blue stars) samples with neutron, proton and iron literature [31, 35 – 40].

A linear correlation between measured increase in hardness with irradiation and the square root of the product of number density and size of Frank loops was observed. However, in 2 dpa – H sample and 10 dpa – Fe sample, difference in increase in hardness with irradiation was observed despite similar density of Frank loops. Note that the increase in hardness was assessed considering only one type of defects i.e. Frank loops. But they are not the sole contributors and contribution from all other types of defects (such as cavities, black dots, precipitates, etc.) should also be accounted for. So, the difference in the increase in hardness observed in 2 dpa – H and 10 dpa – Fe could be explained on the basis of contribution in hardness from unknown defects (defects which

were not observed in this study) of size lower than the TEM resolution (i.e. 2 nm). This hypothesis implies that the density of these small unknown defects was higher in 2 dpa – H sample. But the feasibility of this hypothesis needs to be verified using modelling tools such as molecular dynamics, Monte Carlo kinetics and cluster dynamics.

These comparisons concluded that the microstructure and trend in mechanical properties post to ion irradiations were not very different to the ones reported after neutron and ion irradiations.

2.4. CONCLUSIONS

Industrial grade SA 304L was used in this study. The chemical composition of the material was in well accordance to AISI specification. The stacking fault energy for the material was calculated to be 23 mJ/m^2 using Pickering's formula. The initial microstructure of the material was found to contain ~27 μm austenite grains and few ferrite (~ 2.5 – 6 % as per Schaeffler diagram) grains. EBSD analysis further verified these observations. Based on the angle of disorientation (θ) between two consecutive grains, the grain boundaries were divided in two categories: RHABs (Randomly High Angle Grain Boundaries) with $\theta > 15°$ and Low angle grain boundaries with $5° < \theta < 15°$. Majority (92 %) of the grain boundaries in the material were RHABs (Randomly High Angle Grain Boundaries). Further classification of grain boundaries was done based on the number of coincidence site lattices. Observation of 45 % of Σ3 special grain boundaries suggests that the material was highly twinned. The hardness of the material was evaluated using conventional Vickers hardness test as well as nano indentation test and was observed to be 191 ± 11 H_V. Degradation in the mechanical properties of the material with elevated test temperature was observed.

Two different polishing techniques, namely mechanical and vibratory polishing were used. The former induced a surface hardened zone consisting of nanograins of mean size 20 – 200 nm. Presence of these nano grains increased the hardness of the material by 28 %.

Two different ion irradiations were used in this study. Proton irradiation was conducted at 350 °C with dose rate ranging between $3.2 – 5.8 \times 10^{-6}$ dpa/s while the iron irradiation was performed at 450 °C with dose rate ranging between $2.7 – 3.2 \times 10^{-4}$ dpa/s. The irradiation profile for proton irradiation consisted of a zone of constant dpa and an irradiation peak while for iron irradiation consisted of a continuously increasing dpa with an irradiation peak at ~2 μm.

The irradiation induced microstructure for both irradiations consisted of Frank loops. Quantification of these defects was in good accordance with literature for proton

irradiated sample as well as 10 dpa Fe sample. A density smaller by a factor of 20 was observed in 5 dpa Fe irradiated sample compared to literature. This is presumably due to the underestimation of the defect density. Moreover, on comparing the defect density of 10 dpa Fe (mech) sample with literature a difference of a factor of 100 was observed. The smaller density was attributed to the fact that nanograins increased the volume fraction of grain boundaries, hence, enhancing the annihilation of these point defects. Cavities were also observed but just at irradiation peak damage of 18 dpa KP in 1 dpa H irradiated sample. The nano indentation test was used to determine the increase in hardness in ion irradiated sample because of shallow penetration depths of ions in material. The irradiation peak of 1 dpa H sample was traced to verify the possibility of using this technique to estimate hardness of irradiated samples used in this study. The irradiation peak traced was in good accordance with SRIM calculations and hence, nano indentation technique was further used to assess increase in hardness with irradiation. The summary of these results is reported in Table 2-9.

Irrad	Damage (dpa K-P)	Frank loops density (x 10^{22} m^{-3})	Frank loops size (nm)	Increase in hardness (%)
1 dpa – H	1	1.50 ± 0.61	13.6 ± 4.4	130[11]
2 dpa – H	2	3.60 ± 1.50	13.8 ± 4.8	120
5 dpa – Fe	5	0.50 ± 0.31	13.4 ± 1.9	54
10 dpa – Fe	10	2.55 ± 1.05	14.9 ± 3.6	67
10 dpa – Fe (mech)	10	0.06 ± 0.02	20.3 ± 2.7	08

Table 2-9: Summary of irradiation induced microstructure, irradiation hardening observed in the material after proton and iron irradiation.

In conclusion, the microstructure of the material post to irradiation was in accordance with neutron and ion literature. The defects observed were also able to account for the increase in hardness observed in these samples. These results imply that the iron irradiation conditions used in this study successfully reproduced the irradiation damage. Now the challenge is to verify the feasible of using iron irradiation to study the effect of irradiation induced damage on the cracking susceptibility of material under different conditions. This issue has been addressed in the following chapters.

[11] Hardness value obtained from nano indentation test performed on different machine compared to rest.

REFERENCES

1. C. Pokor, Y. Brechet, P. Dubuisson, J.P. Massoud, X. Averty, "Irradiation damage in 304 and 316 stainless steels: experimental investigation and modeling. Part II: Irradiation induced hardening", J. Nucl. Mat. 326 (2004) 30 – 37.
2. G. Was, "Fundamentals of Radiation Materials Science: Metals and Alloys", Springer, (2007).
3. R. S. Pathania, "Characterization of neutron irradiated 300 series stainless steels to assess mechanism of Irradiation Assisted Stress Corrosion Cracking: Volume I: LWR – Irradiated type 304 and 316 SS heats with established IASCC susceptibility", EPRI, (2001), 1001496.
4. S. Cissé "Influence de la localisation de la déformation plastique sur la Corrosion sous Contrainte des aciers inoxydables. Application à l'IASCC des internes de cuve", PhD. Thesis, INP Toulouse and CEA Saclay, 2012.
5. F.B. Pickering, "Physical metallurgical development of stainless steels", in: Proceedings of the Conference on Stainless Steels 84, (1984) 2.
6. P. J. Brofman, G. S. Ansell, "On the effect of carbon on the stacking fault energy of the austenitic stainless steels", Metal. Trans. A, 9A (1978) 879 – 880.
7. R. E. Schramm, R. P. Reed, "Stacking fault energies of seven commercial austenitic stainless steels", Metal. Trans. A, 6A (1975) 1345 – 1351.
8. M. F. McGuire, "Stainless steels for Design Engineers", ASM International, USA (2008).
9. Millier M. "Fragilisation des aciers inoxydables austénitiques sous irradiation : évolution de la microstructure et amorçage de la corrosion sous contrainte assistée par l'irradiation en milieu REP", PhD. Thesis, Ecole Nationale Supérieure des Mines de Saint Etienne, 2014.
10. Y. Huan, F. Zhang, K.C. Hwang, W.D. Nix, G.M. Pharr, G. Feng, "A model of size effects in nano-indentation", J. Nucl. Mat. 54 (2006) 1668 – 1686.
11. A. Lupinacci, K. Chen, Y. Li, M. Kunz, Z. Jiao, G.S. Was, M.D. Abad, A.M. Minor, P. Hosemann, "Characterization of ion beam irradiated 304 stainless steel utilizing nanoindentation and Laue microdiffraction", J. Nucl. Mater. 458 (2015) 70 – 76.
12. J. D. Hunn, E. H. Lee, T. S. Byun, L. K. Mansur, "Helium and hydrogen induced hardening in 316 LN stainless steel", J. Nucl. Mat. 282 (2000) 131 – 136.
13. D. L. Damcott, J. M. Cookson, V. H. Rotberg, G. S. Was, "A radiation effects facility using a 1.7 MV tandem accelerator", Nucl. Instrum. and Meth., B 99 (1995) 780 – 783.
14. R. E. Stoller, M. B. Toloczko, G. S. Was, A. G. Ceertain, S. Dwaraknath, F. A. Garner, "On the use of SRIM for computing radiation damage exposure", Nucl. Instrum. and Meth., B 310 (2013) 75 – 80.
15. "Standard practice for neutron radiation damage simulation by charged particle irradiation", ASTM Designation E 521-89, Annual Book of ASTM Standards, vol. 12.02, American Society for Testing and Materials, (1989).

16. L. Beck, Y. Serruys, S. Miro, P. Trocellier, E. Bordas, F. Leprêtre, D. Brimbal, T. Loussouarn, H. Martin, S. Vaubaillon, S. Pellegrino and D. Bachiller-Perea, "Ion irradiation and radiation effect characterization at the JANNuS-Saclay triple beam facility", J. Mater. Res., 30 (2015) 1183 - 1194.
17. A. Etienne, "Etudes des effets d'irradiations et de la nanostructuration dans des aciers austénitiques inoxydables ", PhD Thesis, Université de Rouen (2009).
18. D. J. Edwards, E. P. Simonen, S. M. Bruemmer, "Evolution of fine scale defects in stainless steels neutron irradiated at 275 °C", J. Nucl. Mat. 317 (2003) 13 – 31.
19. T. Miura, K. Fujii, K. Fukuya, Y. Ito, "Characterization of deformation structure in ion irradiated stainless", J. Nucl. Mat., 386 – 388 (2009) 210 – 213.
20. J. T. Busby, M. C. Harsh, G. S. Was, "The relationship between hardness and yield stress in irradiated austenitic and ferritic steels", J. Nucl. Mat., 336 (2005) 267 – 278.
21. G. S. Was, J. T. Busby, T. Allen, E. A. Kenik, A. Jenssen, S. M. Bruemmer, J. Gan, A. D. Edwards, P. M. Scott, P. L. Andersen, "Emulation of neutron irradiation effects with protons: validation of principle", J. Nucl. Mat. 300 (2002) 198 – 216.
22. S. J. Zinkle, P. J. Maziasz, R. E. Stoller, "Dose dependence of the microstructural evolution in neutron irradiated austenitic stainless steel", J. Nucl. Mat. 206 (1993) 266 – 286.
23. S. M. Bruemmer, E. P. Simonen, P. M. Scott, P. L. Andersen, G. S. Was, J. L. Nelson, "Radiation-induced material changes and susceptibility to intergranular failure of light water reactor core internals", J. Nucl. Mat. 274 (1999) 299 – 314.
24. P. J. Maziasz, "Overview of microstructural evolution in neutron irradiated austenitic stainless steels", J. Nucl. Mat. 205 (1993) 118 – 145.
25. C. Pokor, Y. Bréchet, P. Dubuisson, J. P. Massoud, A. Barbu, "Irradiation damage in 304 and 316 stainless steels: experimental investigation and modeling. Part I: Evolution of the microstructure", J. Nucl. Mat. 326 (2004) 19 – 29.
26. D. Edwards, Ed Simonen, S. Bruemmer, P. Efsing, "Microstructural evolution in neutron irradiated stainless steels: comparison of LWR and Fast reactor irradiations", in Proceedings of 12th international conference on Environmental degradation of materials in nuclear power systems – Water Reactors, (2005).
27. Y. Yang, Y. Chen, Y. Huang, T. Allen, A. Rao, "Irradiation microstructure of austenitic steels and cast steels irradiated in the BOR-60 reactor at 320 °C", in Proceedings of 15th International conference on Environmental degradation of Materials in Nuclear Power Systems – Water Reactors, (2011).
28. A. Renault, J. Malaplate, C. Pokor, P. Gavoille, "TEM and EFTEM characterization of solution annealed 304L stainless steel irradiated in PHENIX, up to 36 dpa and at 390 °C", J. Nucl. Mat., 421 (2012) 124 – 131.
29. A. Renault, C. Pokor, J. Garnier, J. Malaplate, "Microstructure and grain boundary chemistry evolution in austenitic stainless steels irradiated in the BOR-60 reactor up to 120 dpa", in Proceedings of 14th International conference on Environmental degradation of Materials in Nuclear Power Systems – Water Reactors, (2009).

30. Y. Miwa, T. Tsukada, H. Tsuji, H. Nakajima, "Microstructure of type 316 model alloys neutron irradiated at 513 K to 1 dpa", J. Nucl. Mat., 271&272 (1999) 316 – 320.
31. K. Fukuya, K. Fujii, H. Nishioka, Y. Kitsunai, "Evolution of microstructure and microchemistry in cold worked 316 stainless steels under PWR Irradiations", J. Nucl. Sci. and Tech., 43 (2006) 159 – 173.
32. R.D. Carter, D. L. Damcott, M. Atzmon, G. S. Was, E. A. Kenik, "Effects of proton irradiation on the microstructure and microchemistry of type 304 L stainless steel", J. Nucl. Mat., 205 (1993) 361 – 373.
33. Z. Jiao, J. T. Busby, G. S. Was, "Deformation microstructure of proton irradiated stainless steels", J. Nucl. Mat., 361 (2007) 218 – 227.
34. M. Bertrand, "Caractérisation du gonflement et de la microstructure des aciers représentatifs des internes inférieurs de REP par irradiations aux particules chargées" First year thesis progress report, CEA (2005).
35. B. H. Sencer, G. S. Was, M. Sagisaka, Y. Isobe, G. M. Bond, F. A. Garner, "Proton irradiation emulation of PWR neutron damage microstructures in solution annealed 304 and cold worked 316 stainless steels", J. Nucl. Mat. 323 (2003) 18 – 28.
36. K. J. Stephenson, G. S. Was, "Comparison of the microstructure, deformation and crack initiation behavior of austenitic stainless steel irradiated in-reactor or with protons", J. Nucl. Mat., 456 (2015) 85-98.
37. G. S. Was, "Recent developments in understanding irradiation assisted stress corrosion cracking", in proceedings of 11th International conference on Environmental degradation of Materials in Nuclear Power Systems – Water Reactors, (2003).
38. T. Miura, K. Fujii, H. Nishioka, K. Fukuya, "Effect of hydrogen on interaction between dislocations and radiation induced defects in austenitic stainless steels", J. Nucl. Mat., 442 (2013) S735 – S739.
39. Z. Jiao, G. S. Was, T. Miura, K. Fukuya, "Aspects of ion irradiations to study localized deformation in austenitic stainless steels", J. Nucl. Mat. 452 (2014) 3228 – 334.
40. T. Miura, K. Fujii, K. Fukuya, K. Takashima, "Influence of crystal orientation on hardness and nanoindentation deformation in ion irradiated stainless steels", J. Nucl. Mat. 417 (2011) 984 – 987.

CHAPTER 3. IMPACT OF IRRADIATION ON IGSCC OF AUSTENITIC STAINLESS STEEL

3.1. INTRODUCTION

This chapter outlines the work done to study the impact of irradiation on intergranular cracking of austenitic stainless steel. Previously (chapter 2) it has been shown that irradiation modifies the microstructure of material and thereby changing the mechanical properties of material. Increase in hardness observed in irradiated material is an indicator of increase in yield strength with irradiation. Effect of these irradiation induced modifications on cracking susceptibility of vibratory polished ion irradiated SA 304 L is studied in this chapter.

Preliminary step for this is to investigate whether the vulnerability of material changes after both proton (2 dpa – H) and iron (5 dpa – Fe and 10 dpa – Fe) irradiations conducted in this study (§2.3). To achieve this goal, irradiated tensile samples were subjected to SSRT (Slow Strain Rate Test) in simulated PWR primary water (or argon) environment. The tests were interrupted on attaining a plastic strain of 4 %. All these tensile samples (and also irradiated bars) had an irradiated area of 10 mm x 2 mm which corresponded to the irradiated region (Figure 3-1) and rest of the gauge length was unirradiated. Change (increase or decrease) in the cracking susceptibility is quantified in the first part of this chapter by estimating the crack density and mean crack length in the irradiated and unirradiated areas of the samples. Correlation between intergranular cracking, degree of localization and/or (presence of) corrosive environment is shown subsequently.

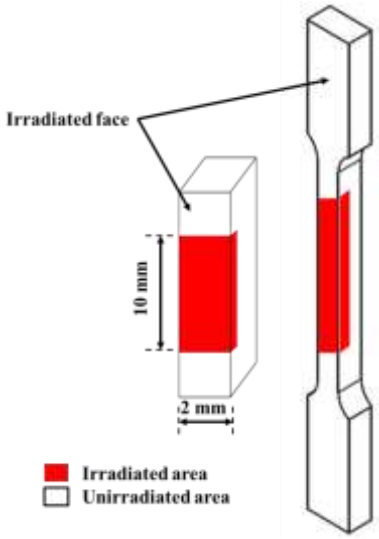

Figure 3-1 : Schematics to represent the irradiated area in the samples and bars.

Second part of this chapter summarizes the oxidation tests conducted on irradiated and unirradiated bars at 340 °C in simulated PWR primary water. The oxide formed on the samples was characterized using SEM (Scanning Electron Microscope) and TEM (Transmission Electron Microscope). Effect of irradiation and different irradiation ions on oxidation was studied and summarized. Though presence of corrosive environment is a necessary condition to observe intergranular cracking of irradiated austenitic stainless steel (except at very high irradiation doses), not enough information is available on the effect of irradiation on oxidation. In this part, efforts are made to have a better overview of the changes irradiation can bring in oxidation of austenitic stainless steel in simulated PWR primary water environment.

In the last part, influence of strain incompatibilities in grains adjacent to the intergranular crack in ion irradiated SA 304L is studied. EBSD analysis was done on the irradiated samples to evaluate strain incompatibilities via Schmid factor (SF) analysis. The dependence of cracking propensity on factors such as grain boundary surface trace inclination with respect to tensile direction, SF and slip continuity at grain boundary was characterized for irradiation and straining conditions used in this study.

3.2. CRACKING OF ION IRRADIATED AUSTENITIC STAINLESS STEEL

The irradiated tensile samples (see §A.1.1) were subjected to Slow Strain Rate Test (SSRT, also called Constant Extension Rate Tensile test, CERT) with a strain rate of 5×10^{-8} s^{-1} upto a plastic deformation of 4 %. The tests were either conducted in simulated PWR primary water environment or in argon environment using the tensile testing Device CORMET C137. To conduct the test in simulated PWR primary water environment, autoclave was filled with primary water (25-35cc/kg H_2 STP, 1000 ppm B, 2 ppm Li). Temperature of the system was raised to reach the test temperature of 340°C and was monitored using PT (Pressure – Temperature) sensor located in the center of the autoclave. The pressure was 155 bars. Prior to straining, environmental conditions were allowed to stabilize for a few hours. On achieving stable conditions, the tensile specimens were strained at a strain rate of 5×10^{-8} s^{-1} upto 4% plastic strain. The displacements were measured by a displacement sensor LVDT (Linear Variable Displacement Transducer) located on the traction line of the autoclave. Load and displacement data was collected by a computerized data acquisition system and recorded every 10 seconds. Water conductivity was measured by water sampling after the test. These analyses confirmed the absence of impurities in the simulated PWR primary water used to conduct the test. The procedure of conducting test in argon environment was identical to that of test conducted in corrosive environment (detailed above) with the only exception of filling the autoclave with argon instead of simulated PWR primary water.

Exposure to simulated PWR primary water resulted in the oxidation of tested samples and hence, formation of oxide crystallites on the surface to be examined. The oxide formed was analyzed using both SEM and TEM (Transmission Electron Microscope). As the oxide crystallites were obstructing the surface analysis of samples, the samples tested in simulated PWR primary water environment were vibratory polished for some time (for e.g. 2 h for 2 dpa H sample) in OPS solution to remove the outer oxide crystals.

The surface of the samples, after re-polishing (except the sample tested in argon), was examined using SEM. SEM images were obtained using FEI Helios 650 NanoLab Dual Beam FIB with an accelerating voltage of 5 kV and a working distance of 14 mm. Plastic deformation leads to the appearance of two prominent features on the surface of the sample; fine slip lines (representing surface off – set or steps) and intergranular cracks which are detailed in the following sections.

3.2.1. QUALITATIVE ANALYSIS

The first prominent feature that was looked for on the surface of the samples post to straining was the cracks. During the SEM surface examination of the gauge length of 5 dpa – Fe sample strained in argon environment, no cracks were found. Whereas, on the 5 dpa – Fe sample tested in corrosive PWR environment, numerous cracks in the irradiated region were observed. This was expected as corrosive environment is a prerequisite condition for intergranular cracking of irradiated austenitic stainless steel. Comparison of the surface of irradiated region of the 5 dpa – Fe samples after SSRT test in inert and corrosive environment shown in Figure 3-2 brings out the role of corrosive environment in enhancing the likelihood of material to crack for the irradiation and straining conditions used in the study.

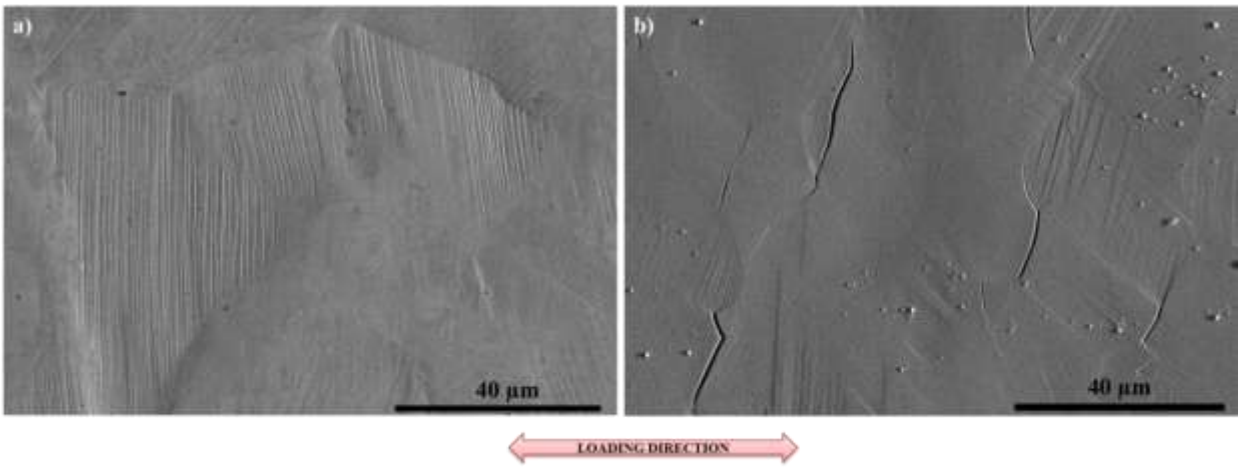

Figure 3-2 : Surface appearance of irradiated region of 5 dpa – Fe sample after SSRT test conducted in a) argon environment b) PWR environment. Loading direction is indicated on the image.

In fact, numerous cracks were observed in the irradiated regions of both iron irradiated (Figure 3-3b) and proton irradiated (Figure 3-3d) samples following straining in corrosive environment. On contrary, major portion of the unirradiated area of these samples was without any crack. However, thorough inspection of the unirradiated region revealed the presence of few small cracks (Figure 3-3a and c). As apparent, these qualitative assessments suggest an increase in the cracking susceptibility of the material with irradiation. However, to ascertain these observations, quantitative assessment was necessary.

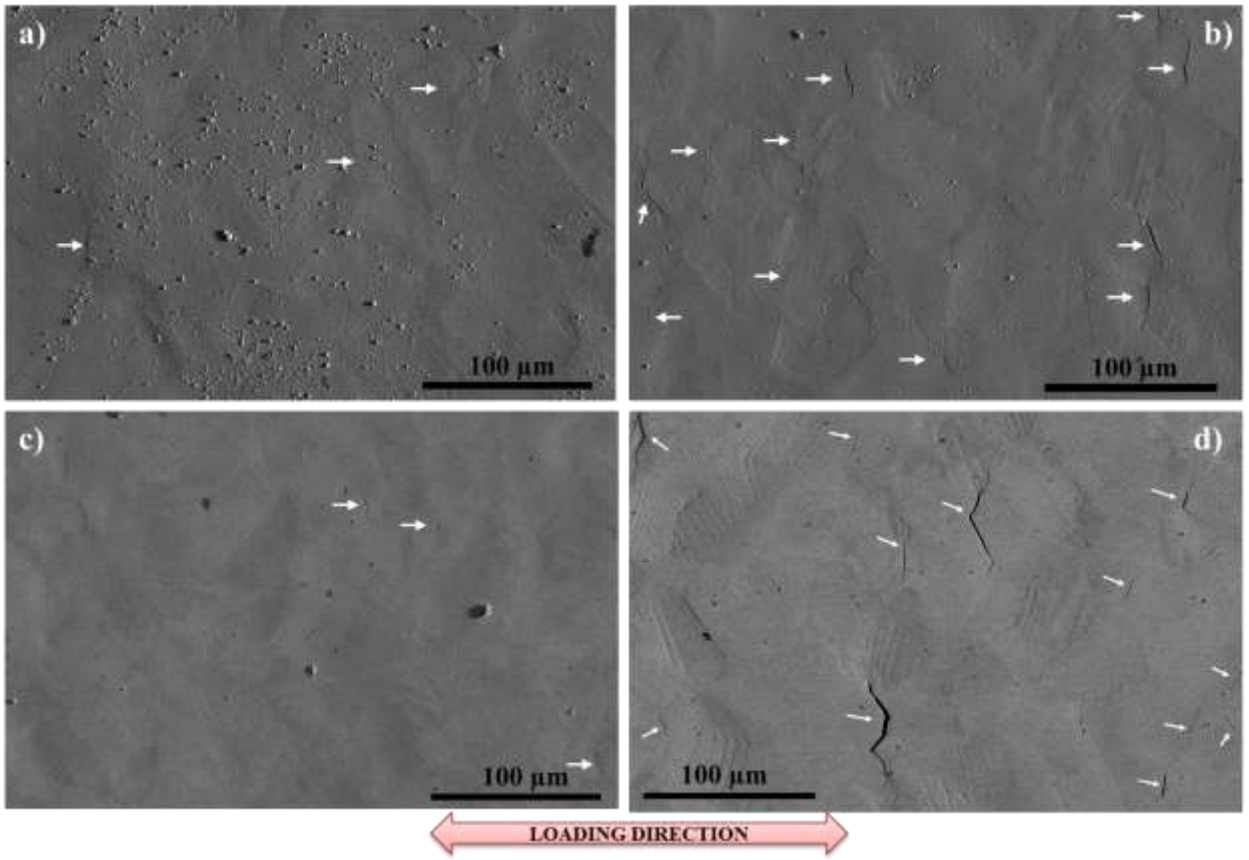

Figure 3-3 : Surface morphology of a) unirradiated region b) irradiated region of 10 dpa – Fe sample and c) unirradiated region d) irradiated region of 2 dpa – H sample after SSRT test conducted in PWR environment. Few of the cracks observed are marked by white arrows. Loading direction is indicated on the image. Images are taken in backscattered electron (BSE) mode.

Evident from Figure 3-3, cracks observed on the samples after SSRT in corrosive environment appeared to follow the grain boundaries suggesting that they were intergranular in nature. However, to ascertain the nature of these cracks, few cartographies of 0.1 mm² area in the irradiated region of the samples (for e.g. Figure 3-4) was obtained using ForeScattered electron (FSE) imaging system of the electron flash EBSD detectors. Due to its high sensitivity to the smallest orientation change, the cartography obtained using FSE included colour contrast to represent different

orientations. Though the information on orientation was just qualitative, it was sufficient to conclude that the nature of the cracks observed on the samples was intergranular.

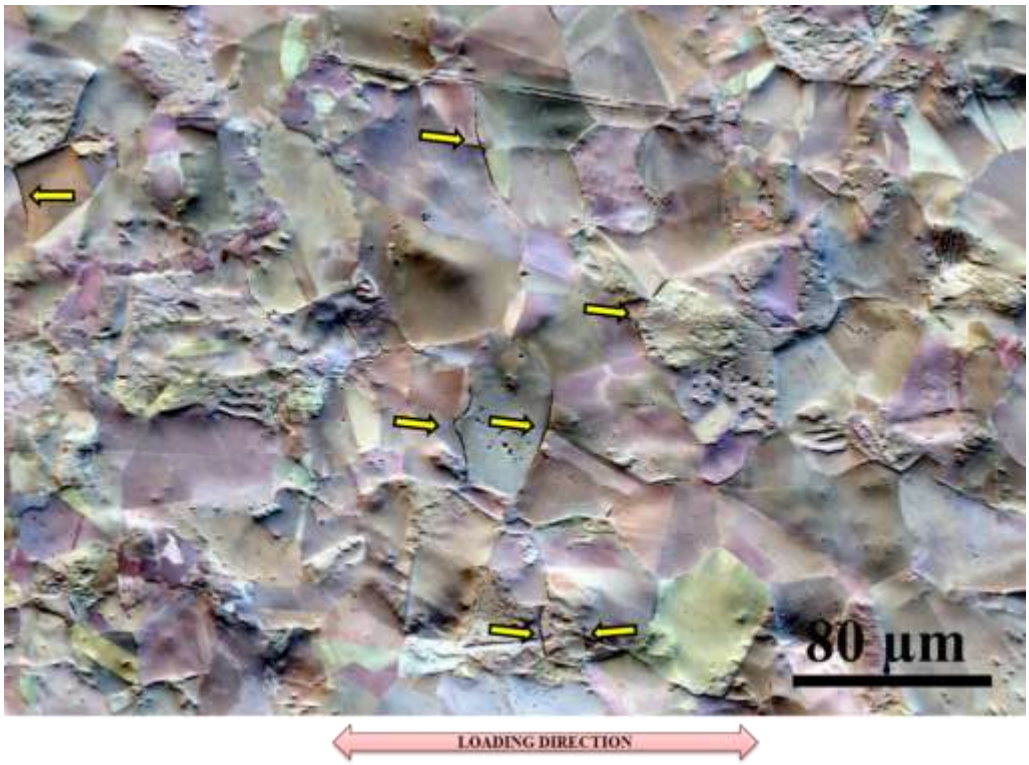

Figure 3-4 : Surface cartography of irradiated areas of 5 dpa – Fe samples obtained using FSE depicting the intergranular nature of the cracks. Few cracks are marked by yellow arrows. Loading direction is indicated on the image.

In addition, EBSD analysis was performed on transverse[12]section FIB samples prepared from the irradiated region of the samples. The thin sample preparation for the purpose was done using conventional FIB lift out procedure using FEI Helios 650 NanoLab Dual Beam FIB. Location of interest was chosen and platinum was coated using electron beam prior to using ion beam to protect the area beneath from being contaminated by the Gallium (Ga) ions (Figure 3-5a). Using a large beam current for fast ion milling, two trenches were milled on either side of the Pt coating. The sample of size 10 x 15 x 7 µm, so prepared, was then mounted on TEM sample holder. It was then polished using successive lower beam currents. Finally, the sample was thinned to 100 nm or less using 1 keV ion beam to minimize the artifacts from sample preparation and hence, to prepare a defect free surface for EBSD analysis. However, during thinning, Ga beam slightly damaged the sample resulting in additional penetration of the crack (marked by red circle in Figure 3-5d). This is known as "channeling effect" of ion beam and to overcome this problem, an additional step of flipping FIB lift sample upside down prior mounting on the TEM sample holder was carried out in successive sample preparations. Post to FIB sample preparation, EBSD was performed on the sample using JEOL JSM 7001F Field

[12] Direction perpendicular to the plane containing the surface trace of the crack.

Emission SEM. The mapping of the samples was done using device on the JEOL microscope. The acquisition was done with Brucker software.

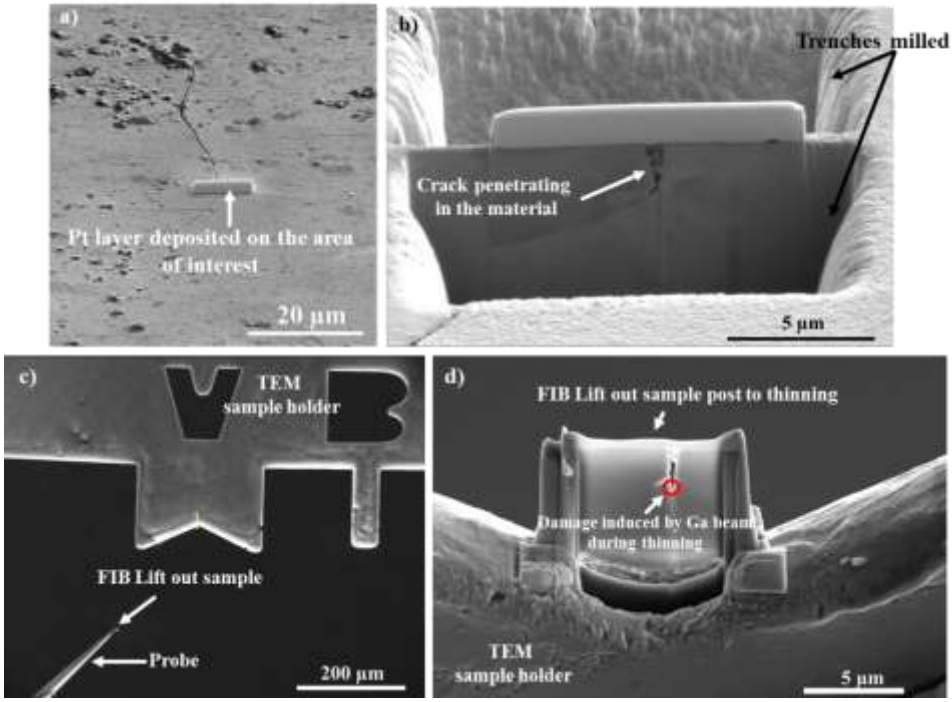

Figure 3-5 : Images to describe the FIB lift out sample preparation procedure used. a) Selecting a crack to be investigated and coating it with Pt deposit b) Milling the trenches on both sides of the crack c) Lifting the FIB prepared sample and gluing it on the TEM sample holder d) thinning of the sample using Ga ion beam.

A crack of length 60 µm was randomly chosen from the irradiated region of 5 dpa – Fe sample (Figure 3-5a). The crack chosen was amongst the largest cracks observed in the irradiated region (see Figure 3-9). Transverse cutting of the crack revealed that the crack followed the grain boundary further implying it was intergranular in nature. Crack penetrated to a depth of 2.2 µm within the material (Figure 3-6a). As the depth of irradiated region was ~ 2.5 µm for this sample, it intimated that the crack arrest occurred in the vicinity of the boundary between irradiated and unirradiated region. In addition, TEM observation of the sample revealed the presence of a BCC phase in the bottom region of the sample (shown in red in Figure 3-6b). EDX analysis of this grain gave a chemical composition similar to that of an austenite grain. It could be linked to deformation induced martensite. Though, formation of deformation induced martensite for $t \geq 300$ °C has been reported to be very rare in unirradiated austenitic stainless steel [1]. A study [2] has reported to observe transformation martensite in irradiated material.

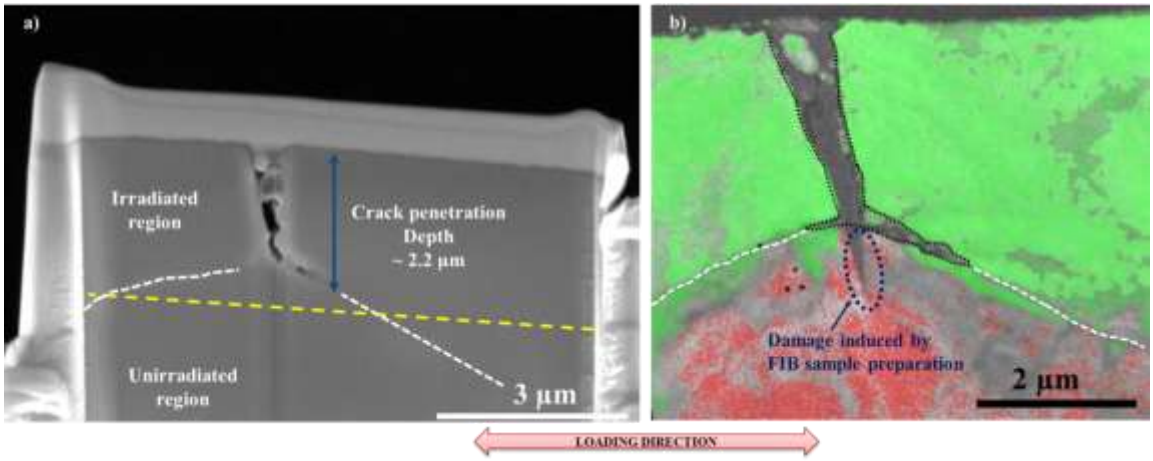

Figure 3-6 : a) SEM image prior to thinning b) EBSD phase orientation map of the FIB sample prepared from 5 dpa – Fe sample. Green indicated the FCC phase while red indicates the BCC phase. Grain boundaries are marked with white dashed lines and crack in b) is marked by black dotted line. Yellow dashed line (in a)) indicates the unirradiated – irradiated interface. Loading direction is indicated in the image.

Observation of intergranular cracks in samples SSRT tested in corrosive environment and no cracks in sample tested in argon environment indicate that the cracking observed in the samples corresponds to IGSCC of the austenitic stainless steel.

3.2.2. QUANTITATIVE ANALYSIS

For comparative studies, quantitative information (i.e. mean crack length and crack density) was necessary which was obtained by scanning an area of 1 mm² (2mm x 0.5 mm) within the middle portion of the irradiated region of the sample using SEM. The scanning was a line by line scanning which consisted of taking images from side to side in a line from top to bottom, much like raster scan. All the images were taken at a same magnification of × 1750 or Horizontal Full Width (HFW) of 118 µm. At this magnification, even small cracks (< 5 µm) were clearly visible. The SEM was used under BSE (Back Scattered Electron) mode rather than SE (Secondary Electron mode) for better visualization of the cracks (Figure 3-7). In BSE mode, there is a marked contrast between the cracks and the surface resulting in a better visibility of cracks in this mode.

The area scanned was recreated by making a photomontage from these images using Photoshop software (Figure 3-8a). From this photomontage, cracks were counted manually to estimate the density of cracks. Photomontage avoided counting of same crack multiple times which was possible if counting was done on all individual images due to the presence of overlapping regions in two consecutive images.

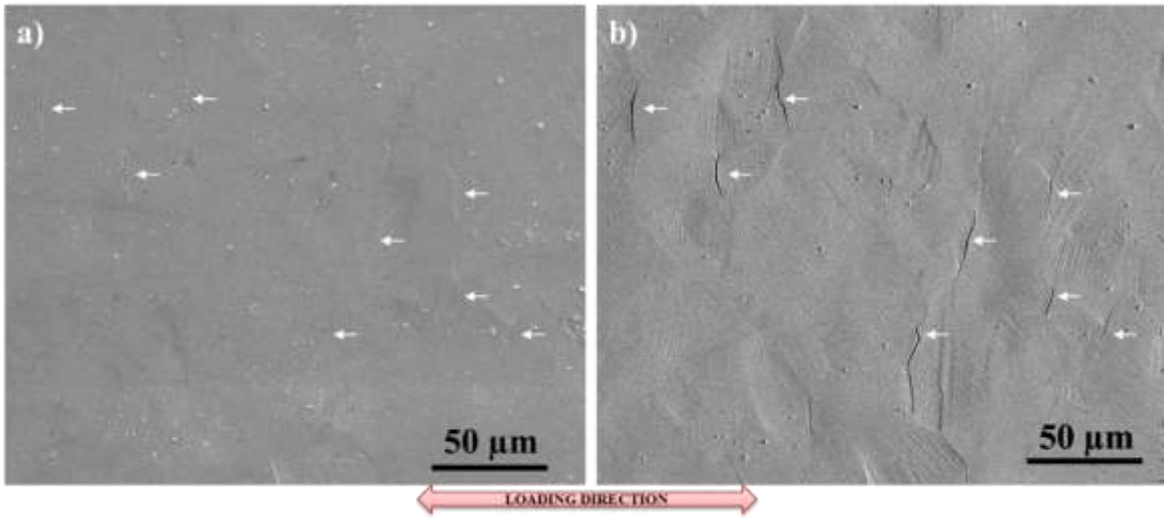

Figure 3-7 : SEM images of the same area of the irradiated zone of strained 5 dpa – Fe sample taken under a) SE mode b) BSE mode. The cracks in the region are marked by white arrows in both images. Loading direction is indicated in the image.

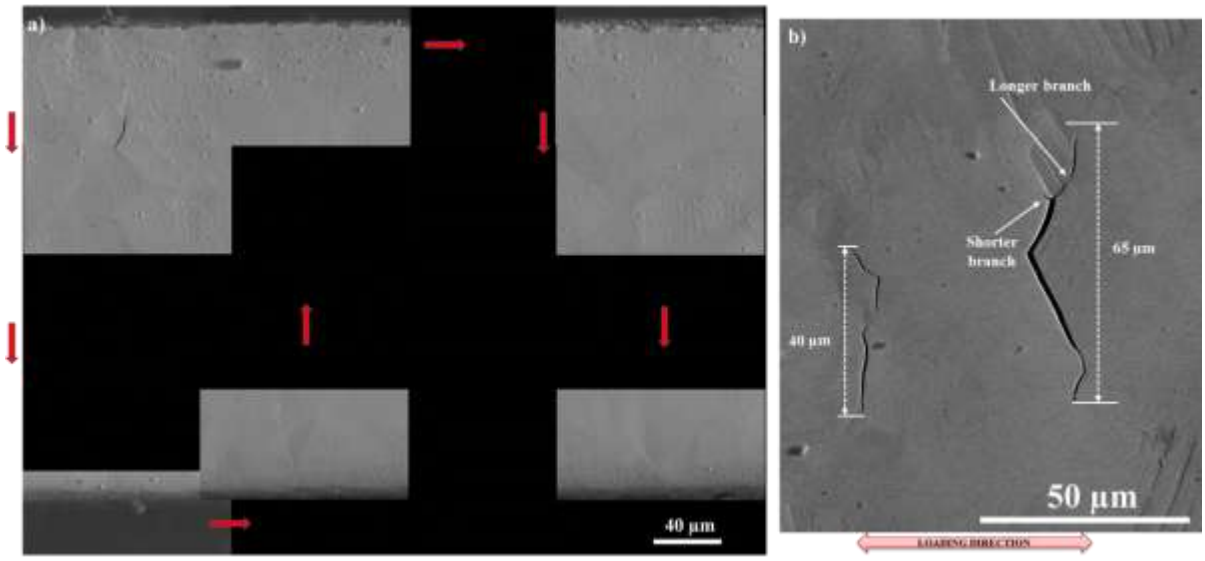

Figure 3-8 : a) Schematics to demonstrate the preparation of the photomontage from the SEM images taken in the irradiated region of the strained samples b) Image to illustrate the criteria chosen to measure the crack length.

The crack density was obtained for two different irradiated areas (of 1 mm² each) scanned on each sample. The mean crack density[13] along with error was estimated from the two values. The crack length of each crack was estimated using imageJ software. The crack length measured was the transverse length between the two ends of the crack and in case of branching, length of the longer side was considered (Figure 3-8b). The data on crack length thus obtained was converted into a crack length distribution profile from which the mean crack length[2] was obtained. The error in the values is the difference in the mean

[13] Values and distributions obtained for two areas were similar and hence, using a mean value is justified.

crack lengths obtained by performing the crack length estimation on the data points obtained for two different areas scanned.

Surface analysis of unirradiated region of 5 dpa – Fe sample revealed the presence of few cracks. Quantitative assessment yielded a crack density of 107 ± 21 cracks/mm². Majority (~ 74 %) of the cracks in this region had length ≤ 15 µm and no crack longer than 30 µm was observed. Mean crack length of 12 ± 2 µm was obtained for this sample. In the irradiated region of the same sample, crack density of 297 ± 25 cracks/mm² was calculated. Ranging from small (< 5 µm) to long (~ 60 µm), cracks of different lengths were observed in irradiated region giving a mean crack length of 17 ± 2 µm. Evidently, an increase in cracking susceptibility of SA 304L post to 5 dpa Fe irradiation was observed. The mean crack length was higher as well in irradiated region of the sample. Comparison of the crack length distributions for the two regions, as shown in Figure 3-9, further verified that irradiation widen the distribution towards the higher crack length value.

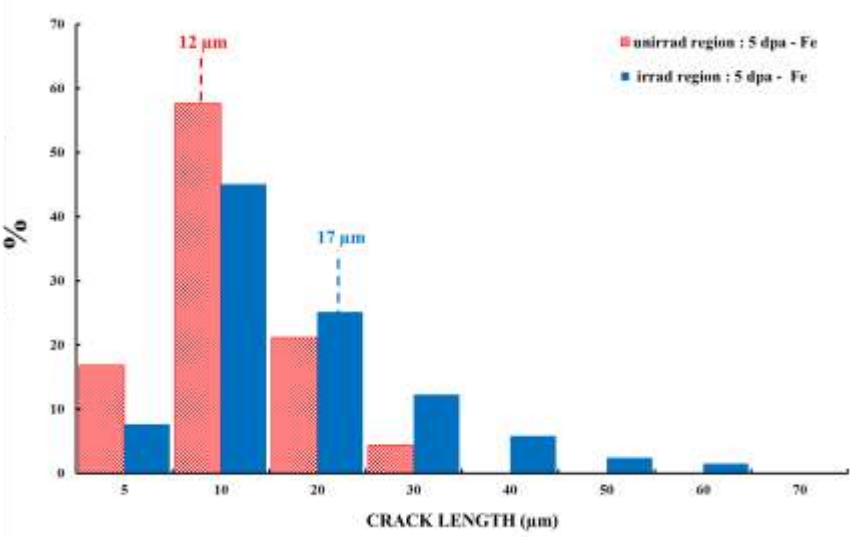

Figure 3-9 : Crack length distributions obtained for unirradiated (in red) and irradiated (in blue) region of 5 dpa – Fe samples. Mean crack length is indicated by dashed line.

To verify the reproducibility of these results, second SSRT test was performed on another 5 dpa – Fe sample. Crack density calculated for unirradiated and irradiated regions of this sample were 91 ± 15 cracks/mm² and 307 ± 23 cracks/mm² respectively. This again implies an increase in the cracking susceptibility of material after irradiation. The values were in good accordance with the result of first test justifying their reproducibility. For 5 dpa – Fe, crack density (mean of the values obtained from two tests) of 99 ± 18 cracks/mm²and 302 ± 23 cracks/mm² for unirradiated and irradiated regions respectively will be used from now onwards.

Similar quantitative analysis was done on unirradiated and irradiated regions of both 10 dpa – Fe and 2 dpa – H samples. The results are summarized in the Table 3-1. Results

for 10 dpa – Fe and 2 dpa – H sample are based on single SSRT test conducted on both samples. Crack density in unirradiated region of 10 dpa – Fe and 2 dpa – H samples were similar but slightly lower compared to 5 dpa – Fe sample. Reason for this difference is unknown.

Sample	Unirradiated region		Irradiated region		% increase in cracking susceptibility with irradiation (in %)
	Crack density (cracks/mm^2)	**Mean crack length (µm)**	**Crack density (cracks/mm^2)**	**Mean crack length (µm)**	
5 dpa – Fe	99 ± 18	12 ± 2	302 ± 23	17 ± 2	205
10 dpa – Fe	64 ± 12	12 ± 2	293 ± 18	16 ± 2	360
2 dpa – H	71 ± 13	12 ± 2	316 ± 30	17 ± 2	345

Table 3-1 : Summary of the quantitative analysis performed in the irradiated and unirradiated regions of 5 dpa – Fe, 10 dpa – Fe and 2 dpa - H samples.

The crack density and mean crack length observed in the irradiated region of all the samples was similar despite the different doses. In the last column of the Table 3-1, percentage increase in cracking susceptibility for all the samples is presented. In all the samples, a strong percentage increase in cracking susceptibility with irradiation was observed which is in agreement to literature [3, 4]. The value of percentage increase was similar for 2 dpa – H and 10 dpa – Fe sample but somewhat lower for 5 dpa – Fe sample. Note that this increase was calculated based on the crack density of unirradiated and irradiated regions. The difference in percentage increase for different samples thus could be explained by the differences in the density of cracks observed in the unirradiated region of these samples. So, from hereafter, only absolute crack density values will be used to compare the irradiated regions of 5 dpa – Fe, 10 dpa – Fe and 2 dpa – H samples. In addition to crack density, the crack length distribution obtained was also remarkably similar for the irradiated region of all the three samples (Figure 3-10).

To summarize, a strong influence of irradiation on the cracking susceptibility of austenitic stainless steel in simulated PWR primary water environment was observed in all the samples. Despite their short penetration depth in material, crack density remarkably similar to that in proton irradiated sample was observed in iron irradiated samples. This implies that iron irradiation could be used as a tool to study the IGSCC of the irradiated austenitic stainless steel. Before this conclusion, however, it is necessary to verify if the cracking mechanism in iron irradiated sample is same as reported for proton (and neutron) irradiated samples in literature [5, 6]. For the purpose, correlation between cracking susceptibility and localized deformation was studied for the iron and proton irradiated samples as higher degree of localized deformation in irradiated material has been

suggested as the main contributing factor in cracking of proton and neutron irradiated samples [5, 6]. The results obtained are detailed in the following section.

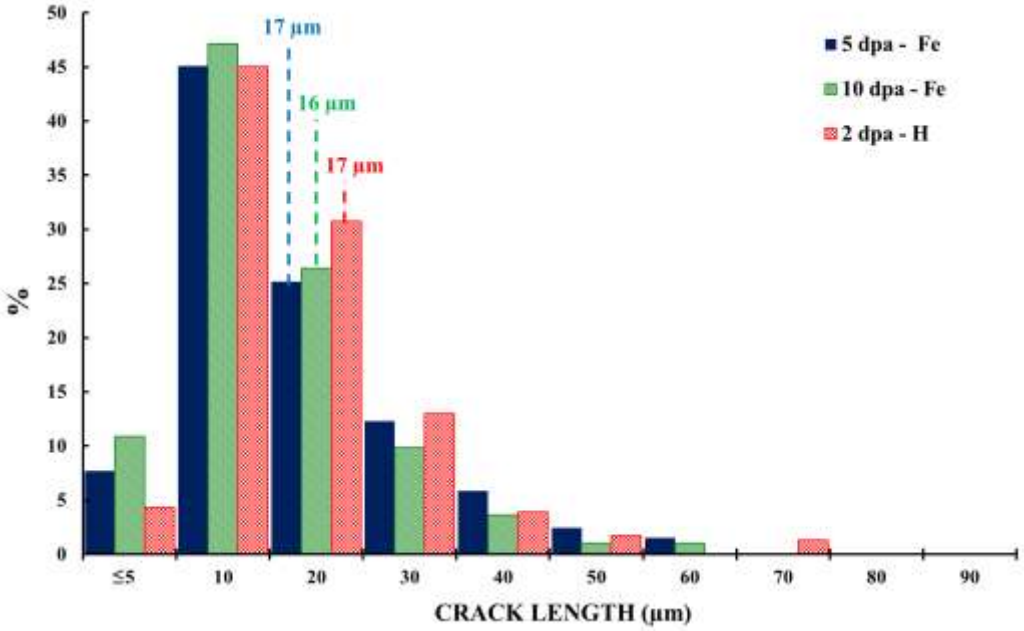

Figure 3-10 : Crack length distributions obtained for 5 dpa – Fe (in blue), 10 dpa – Fe (in green), and 2 dpa – H (in red) samples. Mean crack length for each case is indicated by dashed line.

3.2.2.1. LOCALIZED DEFORMATION

Along with the cracks, the second most prominent feature observed on the surface of the samples post to the loading was slip lines. Surface analysis using SEM confirmed the presence of fine slip lines corresponding to surface steps within grains in both unirradiated and irradiated regions of all the samples. Slip lines in unirradiated region of the samples were hard to observe in the SEM especially at low magnification. While in irradiated regions, they were readily visible. Figure 3-11 demonstrates an example of the slip lines observed in the irradiated region of the 5 dpa – Fe sample and 2 dpa – H sample post to SSRT in simulated PWR primary water and argon environment. Looking at the grains marked 1 – 4 in the Figure 3-11a and 1 – 3 in the Figure 3-11b, it appears that the number of lines per grain varied significantly from grain to grain, with some grains (grain marked 4 in a) and 3 in b)) showing no line at all. This variation of line number density within each grain is linked to the variation of grain orientation relative to the tensile loading and has been reported in previous studies as well (e.g. see [6]).

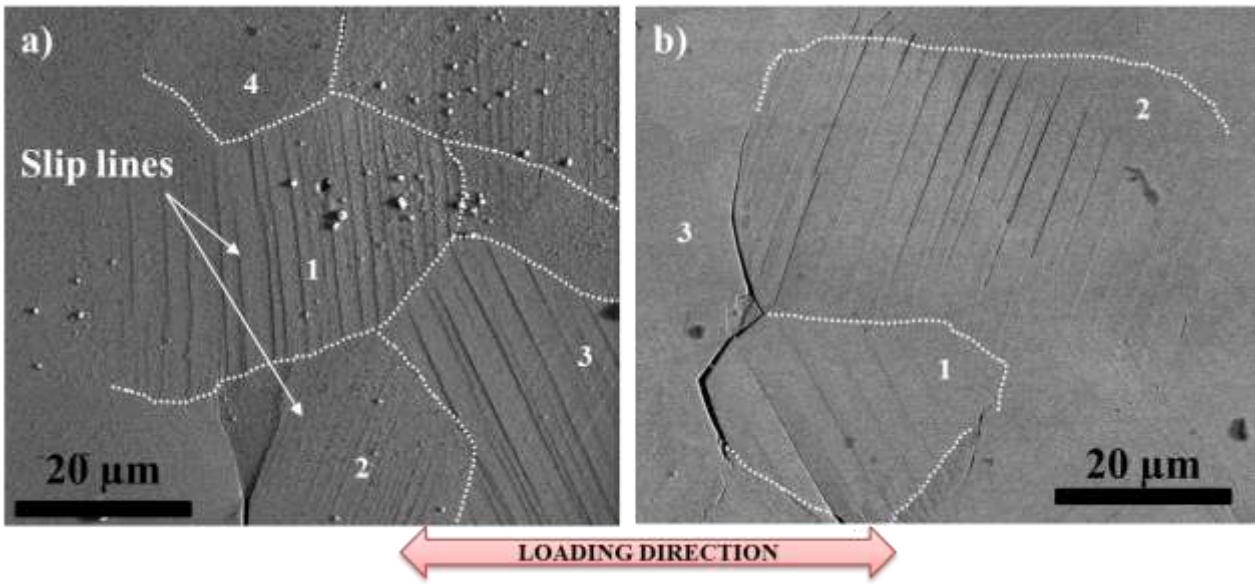

Figure 3-11 : BSE-SEM image of the irradiated region of a) 5 dpa – Fe sample b) 2 dpa – H sample following straining in simulated PWR primary water upto 4 % plastic strain. The presence of slip lines on the surface of the sample is clearly visible. Some of the grain boundaries are marked by white dashed line. Loading direction is indicated in the image.

Slip lines (or surface steps) results from the interaction of deformation bands with the free surface (see §1.3.1.4). In fact, the amount of strain accumulated in deformation bands is proportional to the height of these steps (h) and the spacing (w) between the lines (eq. I.8). Thus, the step height or slip line spacing can provide a good estimation of degree of localization and hence, are efficient quantitative tool for the purpose. In this study, only slip line spacing was used to estimate the degree of deformation. This was done by measuring the distance between the two consecutive slip lines (Figure 3-12) using ImageJ software.

Slip line spacing was computed over 10 SEM images (around 25 grains) for each condition. A range of spacing values were obtained for both unirradiated and irradiated regions of all the samples. Figure 3-13 shows slip line spacing distribution obtained for unirradiated and irradiated zone of the 5 dpa Fe sample. Irradiation appears to have broadened the distribution towards larger values suggesting higher degree of localization in irradiated region compared to the unirradiated. The mean slip line spacing calculated for the unirradiated zone was 0.9 ± 0.2 µm[14] and for the irradiated zone of the 5 dpa Fe irradiated sample was 1.6 ± 0.1 µm. (Figure 3-12 and Figure 3-13). This indicates that the value was higher for the irradiated region of the sample.

[14] Error in the value is the difference in the mean slip line spacing values obtained by repeating the measurements on the same data points.

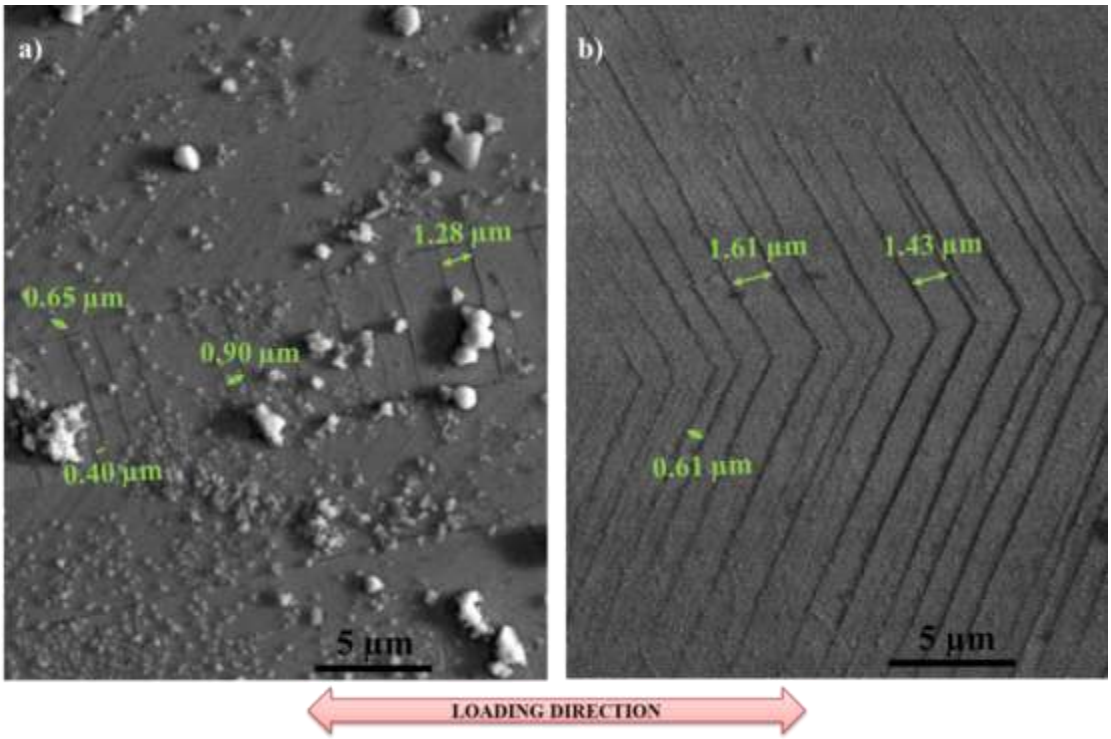

Figure 3-12 : a) SEM images of slip lines observed in a) unirradiated region b) irradiated region of 5 dpa – Fe sample post to 4% plastic straining. The distance measured between two consecutive slip lines was considered as slip line spacing. Spacing between few slip lines is shown by green arrow in the images.

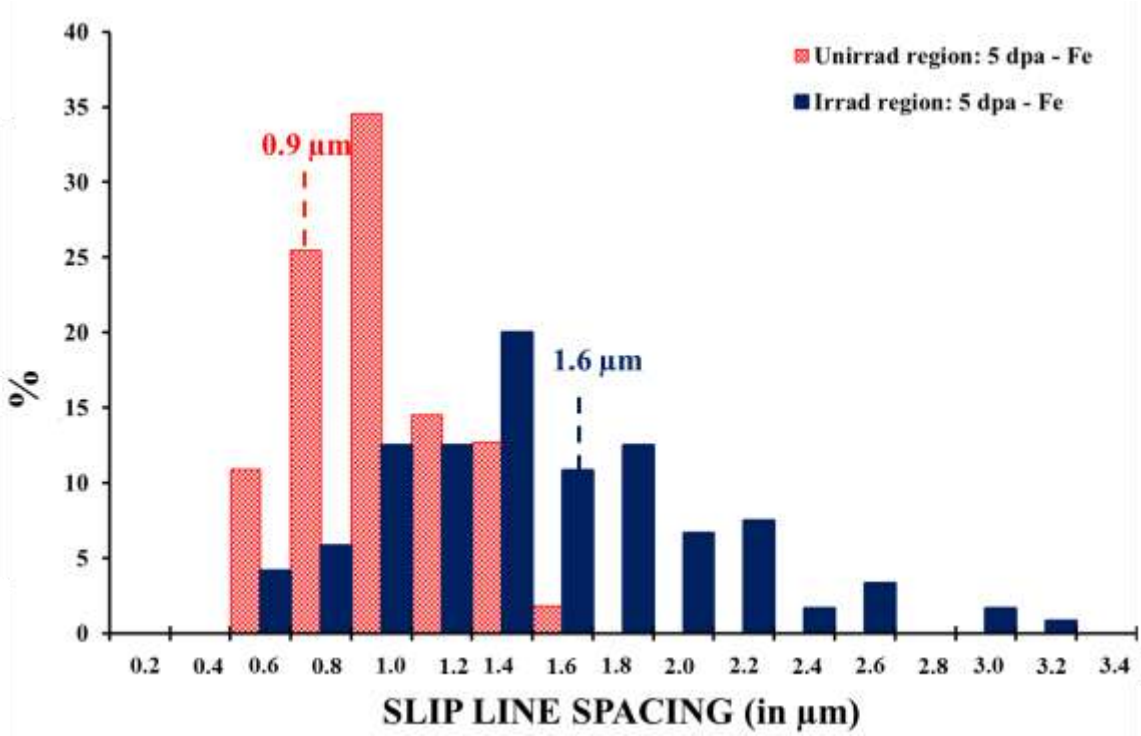

Figure 3-13 : Slip line spacing distribution obtained for unirradiated (in red) and irradiated regions (in blue) of 5 dpa – Fe samples. The mean spacing for each case is indicated by dashes lines.

To ensure, if the increase in spacing value observed is because of irradiation and is not a consequence of difference in line number density for different grain orientation, similar analysis (i.e. computing the spacing for around 25 grains) was done on 5 dpa – Fe sample tested in argon environment. The slip line spacing estimated for the unirradiated and irradiated region of the sample was 0.9 ± 0.2 µm and 1.6 ± 0.1 µm respectively. These values are, indeed, identical to that for 5 dpa – Fe sample tested in simulated PWR primary water environment. The slip line spacing distribution obtained for the irradiated regions of the two samples was similar as well (Figure 3-14). As no effect of environment on spacing is expected, these results justify that the measurements are reproducible. It also implies that the measurements done on 25 grains are sufficient to eliminate any possible effect of grain orientation.

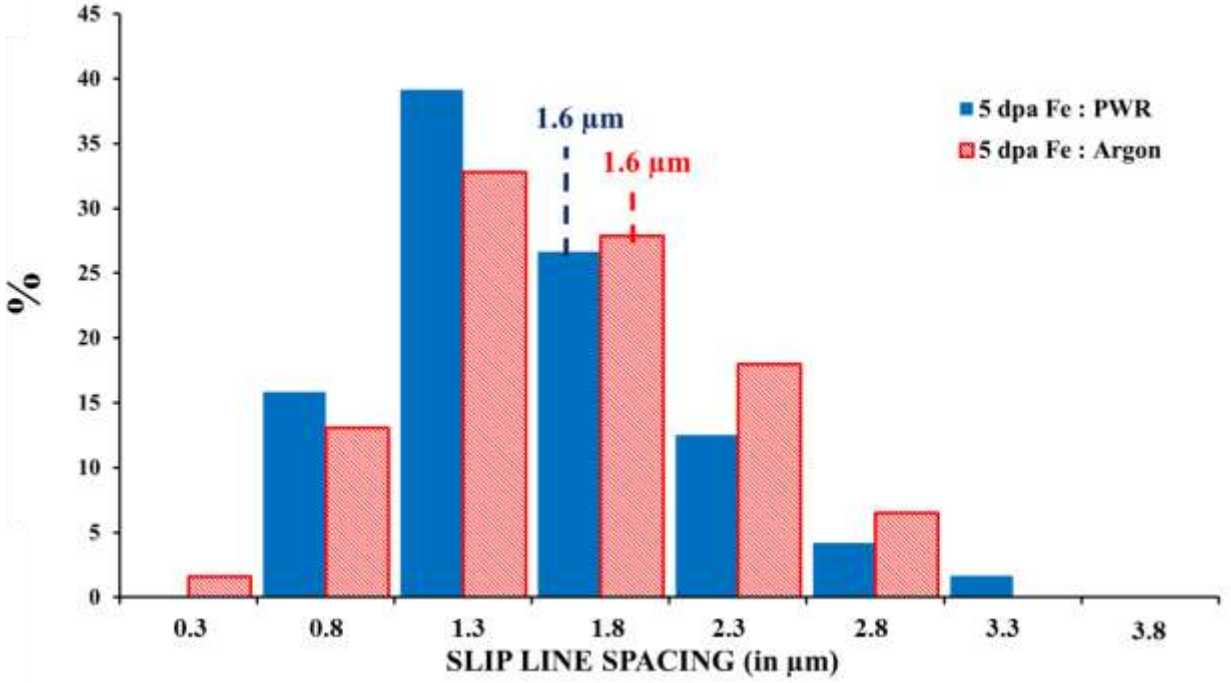

Figure 3-14 : Slip line spacing distribution obtained for 5 dpa – Fe sample - tested in PWR environment (in blue) and tested in argon environment (in green). The mean spacing for each case is indicated by dashed line.

An increase in the slip line spacing with irradiation was observed in 5 dpa – Fe sample. This is in agreement with literature [7] and has been correlated to blocking of some of the slip lines (present in underneath unirradiated material) by irradiation induced damage. Higher spacing observed in the irradiated region of the 5 dpa – Fe sample indicates higher degree of localized deformation.

As expected, the mean slip line spacing estimated for the unirradiated region of different samples (5 dpa – Fe, 10 dpa – Fe and 2 dpa – H) was same i.e. 0.9 ± 0.2 µm. However, the mean slip line spacing in the irradiated region was dependent on the dpa as well as

irradiation ion type. In 10 dpa – Fe sample, mean slip line spacing of 1.7 ± 0.1 µm was observed indicating an increase in the spacing due to irradiation. For the irradiated region, mean spacing value for 10 dpa – Fe sample was similar to that of 5 dpa Fe sample (Figure 3-15). This might indicate saturation in the spacing value at these doses. Indeed, Miura et al. also reported to observe a saturation in slip line spacing for doses around 5 dpa in 2.8 MeV Fe^{2+} irradiated SA 304 SS following deformation upto 2 % plastic with a strain rate of 10^{-7} s^{-1} [8].

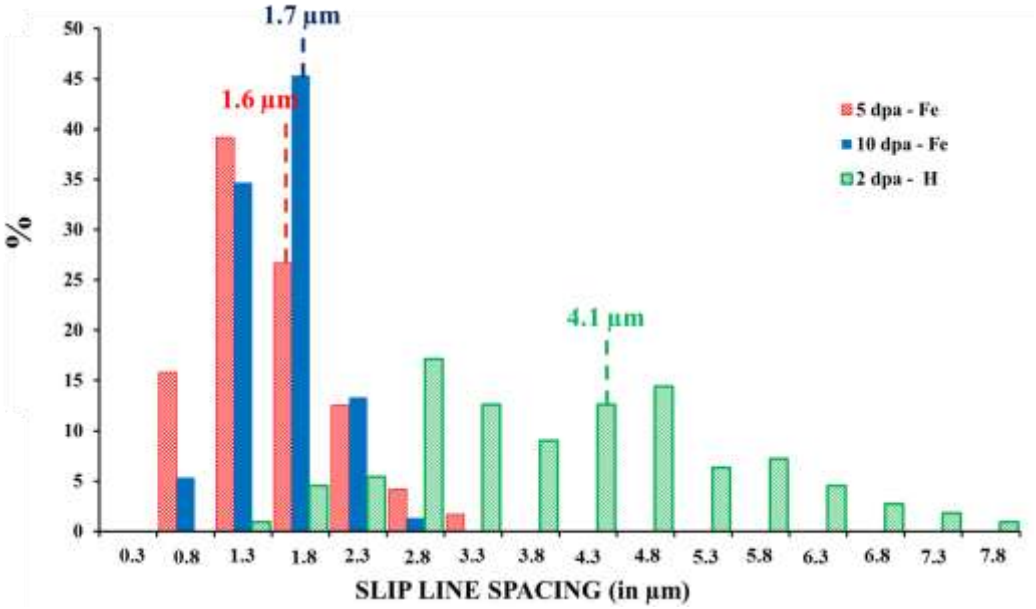

Figure 3-15 : Comparison of slip line spacing distribution obtained for 5 dpa - Fe (in red), 10 dpa – Fe (in blue) and 2 dpa – H (in green) samples following straining in corrosive environment. The mean spacing for each case is indicated by dashed line.

For 2 dpa H sample (Figure 3-15) the mean slip line spacing obtained for the irradiated region was 4.1 ± 0.2 µm, i.e. a significant increase due to irradiation. The mean spacing value is much higher compared to the 10 dpa – Fe and 5 dpa – Fe samples. This difference in mean spacing value is attributed to the different penetration depth of these irradiation beams in the material and is consistent with the findings of Miura [7] and Jiao [9]. These studies have proposed that the damage depth relative to the grain size is of great significance when dealing with ion irradiations (Figure 3-16). They suggested that if the grain is partially irradiated (< 1/3 of the grain, e.g. in case of 10 dpa – Fe sample), some of the slip lines initiating from the unirradiated grain boundaries are blocked by the damage present in the irradiated region. This results in a slight increase of slip line spacing. While if the grain is fully irradiated (or > 1/3 of the grain, e.g. in case of 2 dpa – H sample), widely spaced slip lines are initiating from the irradiated grain boundaries and resulting in higher increase in slip line spacing. Higher spacing implies higher degree of localization in 2 dpa – H sample compared to 10 dpa – Fe sample.

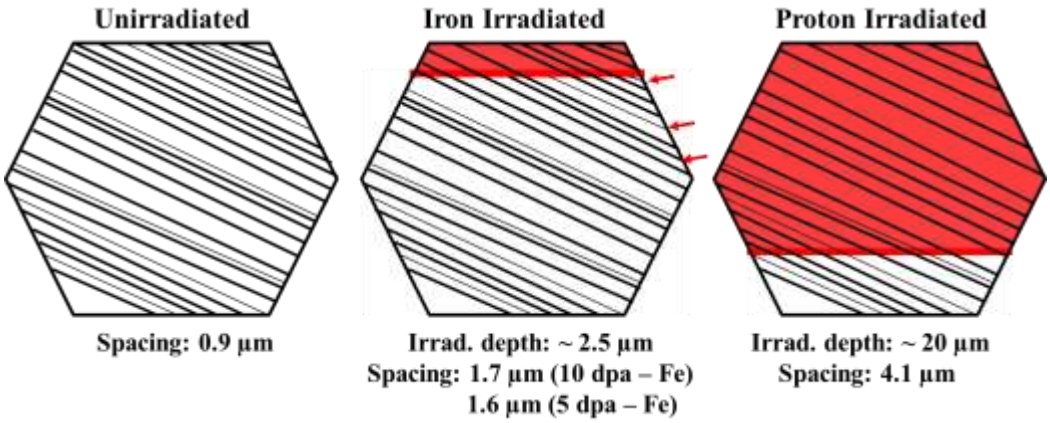

Figure 3-16 : Illustration of effect of irradiation depth on slip line morphologies. Red region represents the irradiated region of the grain. Red arrows point to the slip lines which originated in unirradiated matrix but were blocked by the irradiation damage [extracted from 9].

These results imply an increase in slip line spacing (or degree of localization) with irradiation. This substantiated the increase in cracking susceptibility observed in each case with irradiation except for the 5 dpa – Fe sample tested in inert environment. Despite similar degree of localization, no cracks were observed in 5 dpa – Fe sample tested in argon environment and numerous cracks in sample testes in corrosive environment. Moreover, higher degree of localization was observed for the irradiated region of 2 dpa – H sample compared to 5 dpa – Fe and 10 dpa – Fe samples, yet similar crack density was observed in all the samples following SSRT in simulated PWR primary water environment. These observations indicate that for the irradiation and straining conditions used in this study, localized deformation was not self-sufficient to correlate the intergranular cracking of these samples. It is very plausible that factors such as RIS and oxidation contributed in enhancing the embrittle nature of grain boundaries, thereby, affecting the cracking susceptibility of these samples. RIS and intergranular oxidation were not investigated in this study. But bulk oxidation was studied and is detailed in following sections.

3.2.2.2. CHARACTERIZATION OF OXIDE FORMED ON TENSILE SAMPLES

During SSRT in simulated PWR primary water environment in static autoclave, the tensile samples were exposed to corrosive environment leading to their oxidation during the test. The oxidation time for the sample was 288 hours (or 12 days). A striking difference in the colour of oxide layer formed on the unirradiated and irradiated regions of the 5 dpa – Fe sample was even visible with naked eyes (Figure 3-17). This suggested that the oxide formed on the two regions was different.

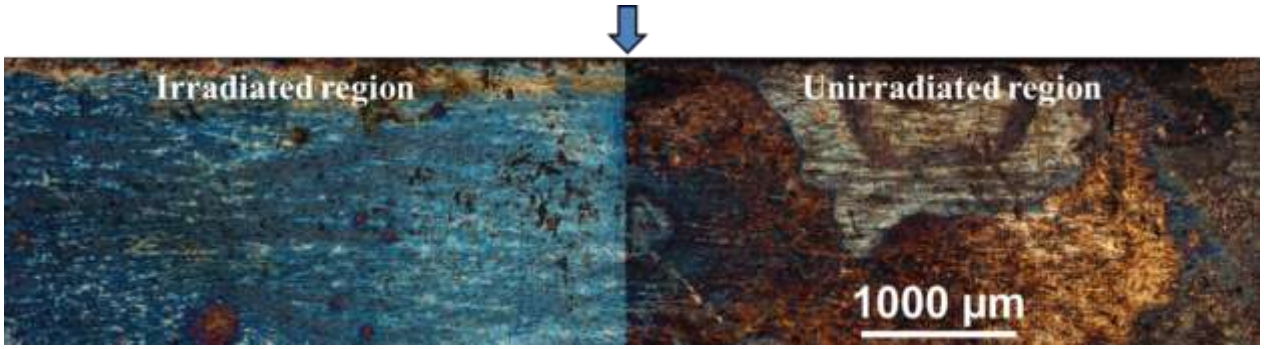

Figure 3-17 : Optical microscope image illustrating the difference in oxide formed on unirradiated and irradiated region of the strained sample. Blue arrow indicates the unirradiated – irradiated interface of the sample.

To account for the differences in the oxide layer formed in the unirradiated and irradiated region of the samples, FIB samples previously prepared by transverse cutting the cracks (see §3.2.1) were analyzed using TEM. The oxide layer formed on both regions was characterized to be a duplex layer consisting of a continuous inner oxide layer and a non-continuous outer oxide layer (Figure 3-18 and Figure 3-19). Several authors [10 – 13] have reported to observe a duplex oxide layer on austenitic stainless steel in simulated PWR primary water environment.

The cross-section shown in Figure 3-18a of the unirradiated region of the strained 5 dpa – Fe sample revealed that the outer oxide layer consisted of crystallites (enriched in Fe) with size ranging from 50 – 150 nm thick. The chromium enriched layer (also called inner layer) at the oxide/substrate interface was 50 – 80 nm thick. Composition of the inner oxide estimated from the EDX profile was 41 at% O, 26 at% Fe, 28 at% Cr and 5 at% Ni. Due to absorption phenomena, the quantification of oxygen is not precise in EDX analysis and hence, the oxygen content was removed from the composition of the inner layer. Thus the chemical composition of inner oxide on unirradiated sample was considered to be 44 at% Fe, 47.5 at% Cr and 8.5 at% Ni. Difference in the contrast of the outer oxide, inner oxide and substrate in TEM images facilitated the marking of outer oxide/inner oxide interface and inner oxide/substrate interface.

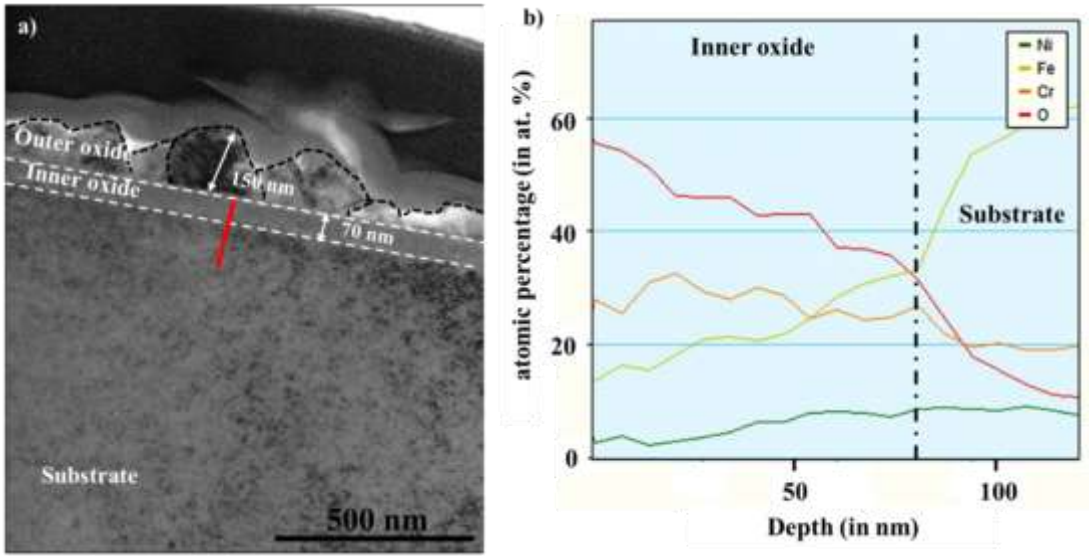

Figure 3-18 : a) Bright Field (BF) TEM image of the oxide layers and substrate observed in unirradiated region of the strained 5 dpa – Fe sample. The inner layer is marked by white dashed line and the outer oxide crystallites are outlined in black dashed line[15]. b) EDX Composition profile of Fe, Cr, Ni and O observed in the inner oxide and the substrate (along the red line in a) in the unirradiated region of strained 5 dpa – Fe sample.

The oxide layer formed in the irradiated region of 5 dpa – Fe sample (shown in BF TEM image in Figure 3.19a) displayed same morphology as was observed on the unirradiated region of the same sample: an outer and an inner oxide. The outer oxide was composed of smaller crystallites (size ranging from 30 – 50 nm) on irradiated region. On orienting one of the crystallite along the [011] zone axis, the Fourier transform (obtained for the HRTEM image Figure 3.19c) indexed the crystallite as spinel of type (Fe, Ni)Cr_2O_4 (space group Fd-3m, a = 8,379 Á). The compact inner oxide (Figure 3.19 d) was 20 nm thick and has a chemical composition of 55 at% Fe, 36 at% Cr and 9 at% Ni. The inner oxide layer formed was thinner and less enriched in Cr in the irradiated region of the sample in comparison to the unirradiated region.

As bulk oxidation (instead of intergranular oxidation) was studied, these results can't be linked to the intergranular cracking observed in unirradiated and irradiated material. However, these results suggest that irradiation modified the oxide formed on austenitic stainless steel. Dumerval [14] also proposed that the process of oxide formation in unirradiated and irradiated material might be different. As not enough information is available about the oxide formation on irradiated material, oxidation tests were conducted in this study to gain some useful insight on the changes irradiation can bring in the formation of oxide layer on material.

[15] Difference in the contrast of the outer oxide, inner oxide and substrate in TEM images facilitated the marking of outer oxide/inner oxide interface and inner oxide/substrate interface.

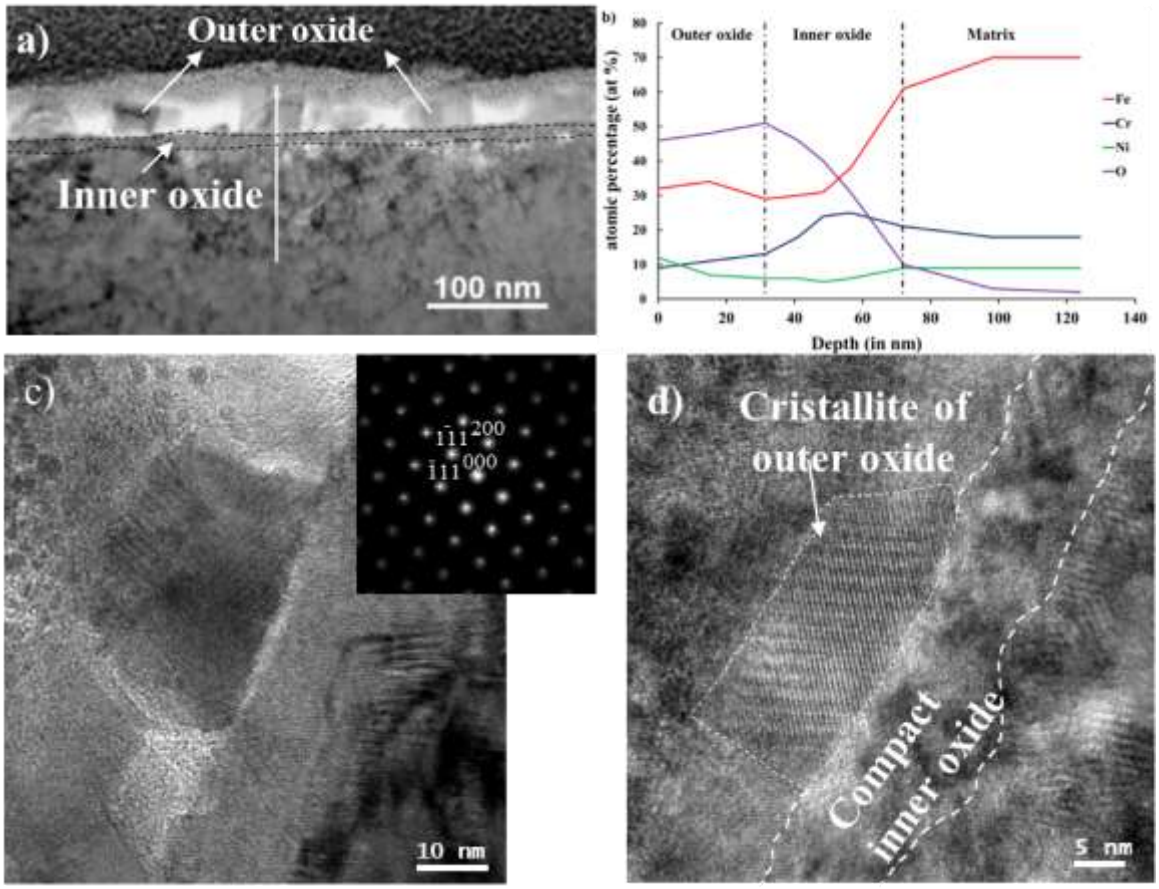

Figure 3-19 : a) BF TEM image of the oxide layers and substrate observed in irradiated region of the strained 5 dpa – Fe sample. b) EDX Composition profile of Fe, Cr, Ni and O observed in the outer oxide, inner oxide and the substrate (along the white line in a)) c) HRTEM images of one of the outer oxide crystallite along with Fourier Transform (in inset). d) HRTEM images of the inner oxide layer. The inner layer is marked by white dashed line and the outer oxide crystallites are outlined in black dashed line.

3.3. OXIDATION OF IRRADIATED AUSTENITIC STAINLESS STEEL

Two oxidation tests on the unirradiated and irradiated vibratory polished bars were conducted in simulated PWR primary water environment in different static stainless steel autoclaves. The first oxidation test was conducted on unirradiated, 5 dpa – Fe and 5 dpa – FeHe samples in a small autoclave of capacity 0.38 L while the second oxidation test was conducted on 5 dpa – FeHe in big autoclave of capacity 5 L. The 5 L autoclave is the autoclave of tensile loading device CORMET C137 used to conduct SSRT in this study (see §3.2). Similar procedure was used for the preparation of autoclave and conduction of both tests. The oxidation tests were conducted at 340 °C and 155 bars for 360 hours.

To suspend the samples in the autoclave, set of bolts, nuts and wire was necessary. For the purpose, oxidized zirconium wire was used to avoid galvanic coupling. The diameter of wire used was 0.5 mm so a hole of diameter 1 mm was drilled close to one of the end of

the bars (unirradiated region of irradiated bars) (Figure 3-20a) to enable the insertion of wire in the samples. The autoclave was filled with primary water (25-35cc/kg H_2 STP, 1000 ppm B, 2 ppm Li). The content of dissolved hydrogen in the water was controlled using Ag-Pd probes. The samples were then suspended in the autoclave using the oxidized zirconium wire, nuts and bolts (Figure 3-20b). The autoclave was sealed. Temperature of the system was then raised to reach the test temperature of 340°C and was monitored using PT (Pressure – Temperature) sensor located in the center of the autoclave. The pressure was 155 bars. Stable temperature and pressure conditions were maintained during the tests.

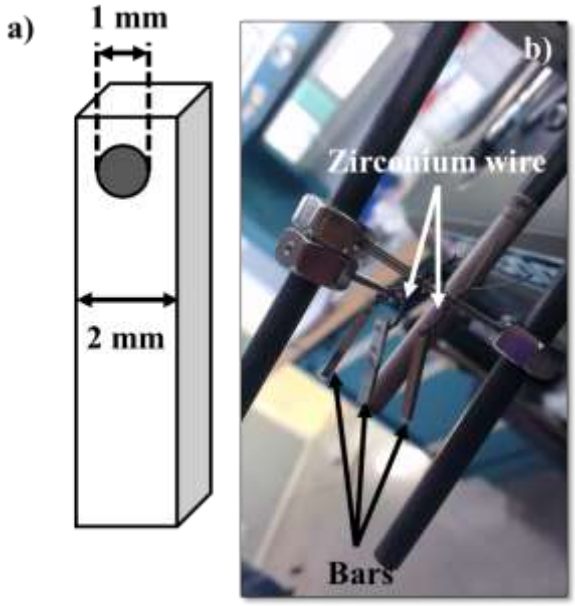

Figure 3-20 : a) Schematics to show the hole made on the bars b) Photograph to illustrate the suspension of bars via zirconium wire. The samples were hanged on two different probes using screw.

As for strained sample, formation of duplex oxide layer was expected on the samples after the oxidation test. To characterize the oxide formed, techniques such as SEM and TEM were used. FEI Helios 650 NanoLab Dual Beam FIB under SEM mode was used to perform the surface analysis of the samples. JEOL 2100F HRTEM (High Resolution Transmission Electron Microscope) operated at 200 kV and equipped with EDS spectrometer was used for in-depth investigations.

3.3.1. EFFECT OF IRRADIATION ON OXIDE FORMED ON AUSTENITIC STAINLESS STEEL

SEM examination of all the samples revealed the presence of oxide crystallites on the surface. Size of these crystallites was different on different samples as well as in the

irradiated and unirradiated region of the same sample. Figure 3-21 serves as an example to disclose the strong impact of irradiation on the morphology of the oxide crystallites observed on the sample after oxidation test conducted in this study. Larger crystallites were observed on the unirradiated sample compared to the irradiated samples (irrespective of irradiation ion). This suggests a decrease in the size of the crystallites with irradiation which is in accordance with literature [13, 14].

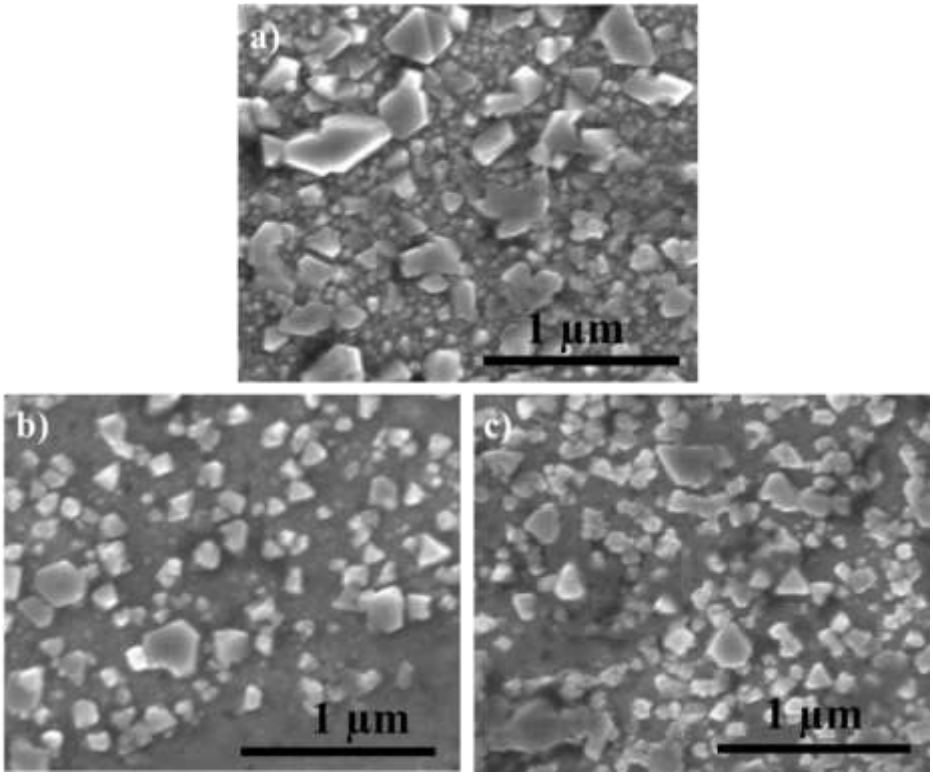

Figure 3-21 : SEM images of the surface of a) unirradiated b) 5 dpa – Fe irradiated c) 5 dpa – FeHe samples demonstrating the effect of irradiation on the morphology of oxide crystallites.

Interestingly in the irradiated region of 5 dpa – Fe sample, islands of oxide crystallites were observed during surface analysis (Figure 3-22). The shape and size of these islands resembled to that of grains in material and hence, their formation could be linked to the effect of crystallographic orientation on oxide formation. In fact, Soulas [10] has previously reported to observe the effect of crystal orientation on unirradiated SS 316 L oxidized in simulated PWR water. However, his tests lasted only for 24 hours which is a much shorter time span compared to 360 h. Note that these islands were observed solely in the irradiated region of 5 dpa – Fe sample and not on any other sample. Presumably, the effect was present on other samples as well but due to long oxidation time (~360 h), the size of oxide crystallites has grown enough to dissipate the difference except in 5 dpa – Fe sample. Not enough information could be attained from surface analysis of these samples to comment on the feasible effects of irradiation on oxide formation. So, cross-

sectional TEM foils were prepared (§ appendix A.1.2.2.2) for subsequent TEM characterizations.

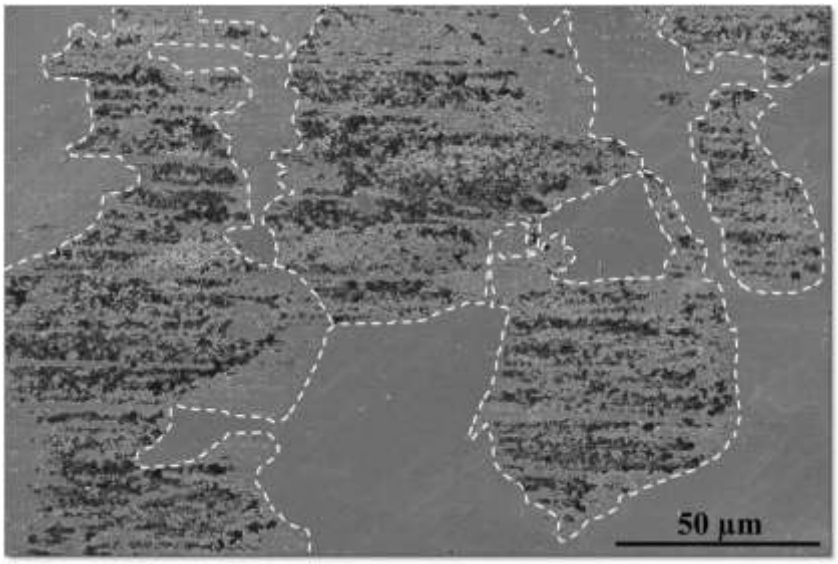

Figure 3-22 : SEM image indicating the plausible impact of grain orientation (in the irradiated region) on the morphology of outer oxide crystallites formed on 5 dpa – Fe sample.

Cross section showing the duplex oxide layer formed on unirradiated sample is reported in Figure 3-23. Outer oxide layer consisted of facetted crystallites of size reaching as high as 100 nm and small crystallites of size ranging between 5 and 20 nm. Small crystallites were distributed between the big crystallites. EDX analysis of facetted crystallites gave a chemical composition of 51 at% of O, 42 at% Fe, 3 at% Cr and 4 at% Ni and electronic diffraction pattern (Figure 3-23b) indexed these crystallites as magnetite $FeFe_2O_4$ phase (space group Fd-3m, a = 8,09 Å). Slightly different chemical composition was obtained for the smaller crystallites. They had lower proportion of iron (32 at% of Fe), a higher proportion of chromium (19 at% of Cr) and somewhat similar percentages of nickel and oxygen in comparison to big crystallites. Small crystallites were indexed as $Fe,NiCr_2O_4$ spinel. The inner layer formed on the sample was 5 – 6 nm thick and had a chemical composition of 56 at% Fe, 34 at% Cr and 10 at% Ni. Fine crystallites present in the inner layer were indexed using the inter-reticular distance of $Fe,NiCr_2O_4$ spinel (space group Fd-3m, a = 8,379 Å) in the Fourier transform of the HRTEM image (Figure 3.23c).

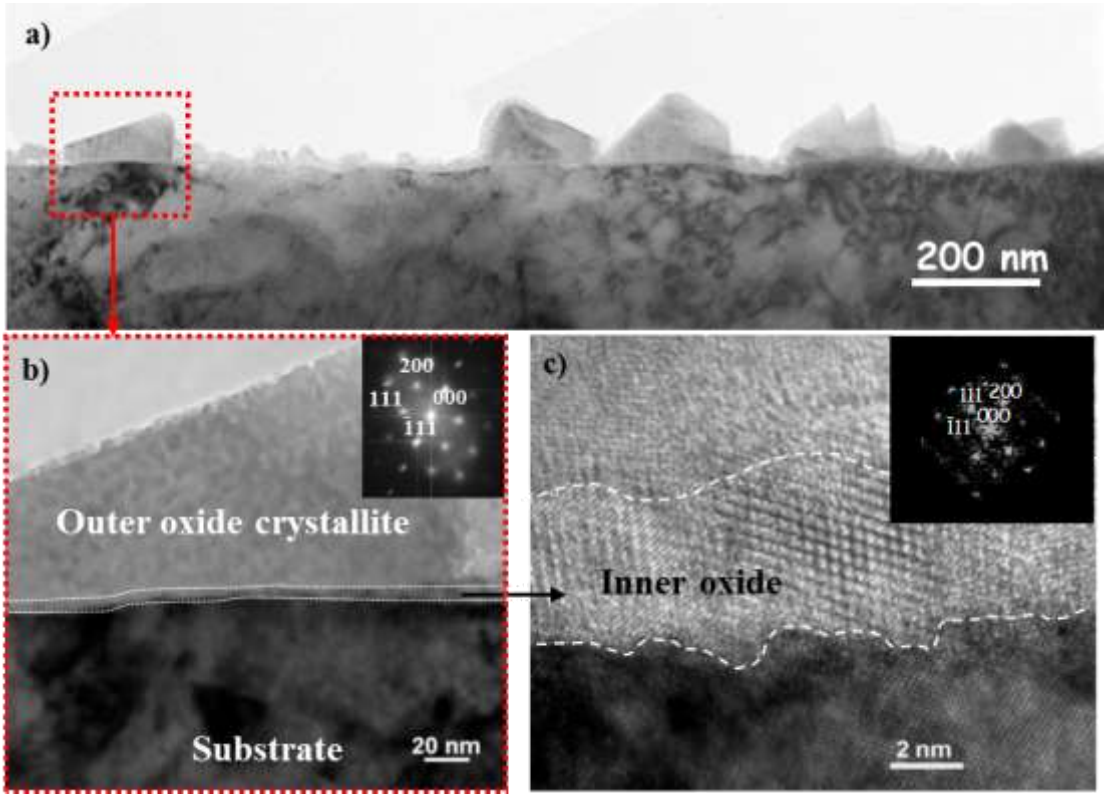

Figure 3-23 : a) BF TEM images of oxide layer observed in unirradiated area b) and of one outer oxide crystallite (marked in red in a)) with the associated SAED pattern[16] along the [011] zone axis. c) HRTEM image of the inner oxide and associated Fourier transform along the [011] axis. Inner oxide is marked by white dashed lines in b) and c).

Duplex oxide layer observed on 5 dpa Fe sample (irradiated region) is shown in Figure 3-24a. Though at low magnifications it was difficult to observe outer oxide crystallites, HRTEM images (Figure 3-24b) confirmed the presence of very small crystallites of size ranging from 1 to 3 nm. To verify these results, three TEM samples were prepared from three different locations. All yielded the same results. Inner layer on this sample was 10 – 20 nm thick. BF STEM image combined with EDX map analysis realized using a aberrated – corrected JEOL JEM-ARM200F Cold FEG microscope equipped EDS/EELS (Figure 3-24c, c_1, c_2, c_3, c_4 and d) gave a chemical composition of 33 at% Fe, 54 at% Cr and 13 at% Ni for the inner layer. EDX profile (Figure 3-24d) also indicated an enrichment of nickel (20% at.) along a distance of 4 nm beneath inner oxide/substrate interface. Beyond Ni enriched zone, substrate rapidly recovered to its normal chemical composition of 69 at% Fe, 21 at% Cr, and 10 at% Ni. Few irradiation induced defects were observed as well in the substrate of 5 dpa – Fe sample (Figure 3-25).

[16] SAED stands for Selected Area Electron Diffraction and is a crystallographic experimental technique to obtain diffraction pattern from the selected part of the specimen.

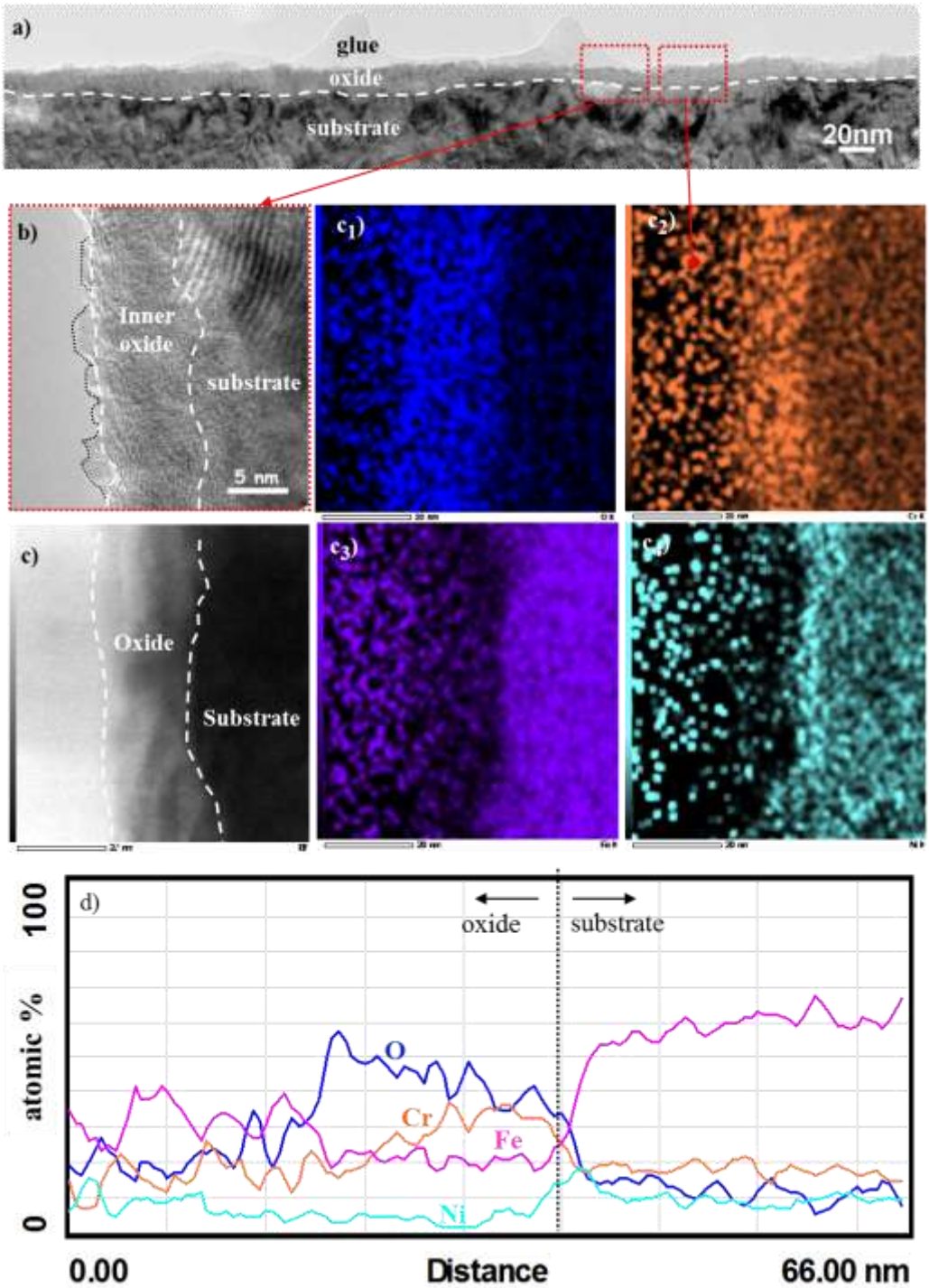

Figure 3-24 : a) Bright field image of the oxide layer observed on the 5 dpa – Fe sample. The two areas used to obtain HRTEM and BF STEM images are marked in red. b) HRTEM image showing the smaller crystallite of the outer oxide (in black dotted line) and the inner oxide (in white dashed line). c) BF STEM images combined with the EDX map analysis of c_1) O c_2) Cr, c_3) Fe and c_4) Ni showing the enrichment at the interface oxide/substrate d) EDX profile of the O, Cr, Fe and Ni in the oxide layers and substrate of the sample.

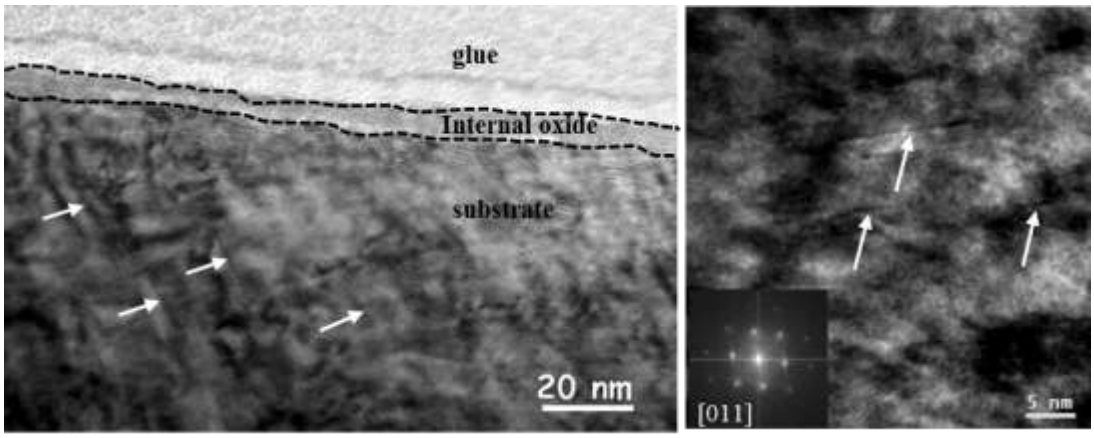

Figure 3-25 : a) Irradiation induced defects observed in the matrix of the oxidized 5 dpa – Fe sample. b) HRTEM image of the defects observed along the [011] axis within the austenite grain of the material. Some of the defects observed are indicated by white arrow and inner layer in b) is marked by black dashed line.

An overview of the oxide layer formed on 5 dpa – FeHe sample is shown in Figure 3-26. Outer oxide on this sample consisted of crystallites of size ranging from 10 to 20 nm whereas the inner oxide layer was a ~ 10 nm thick continuous Cr enriched layer (Figure 3-26a and b). Fourier transform obtained for the HRTEM image of one of the inner oxide crystallite indexed it to be of spinel phase Fe,$NiCr_2O_4$ (Figure 3-26c).

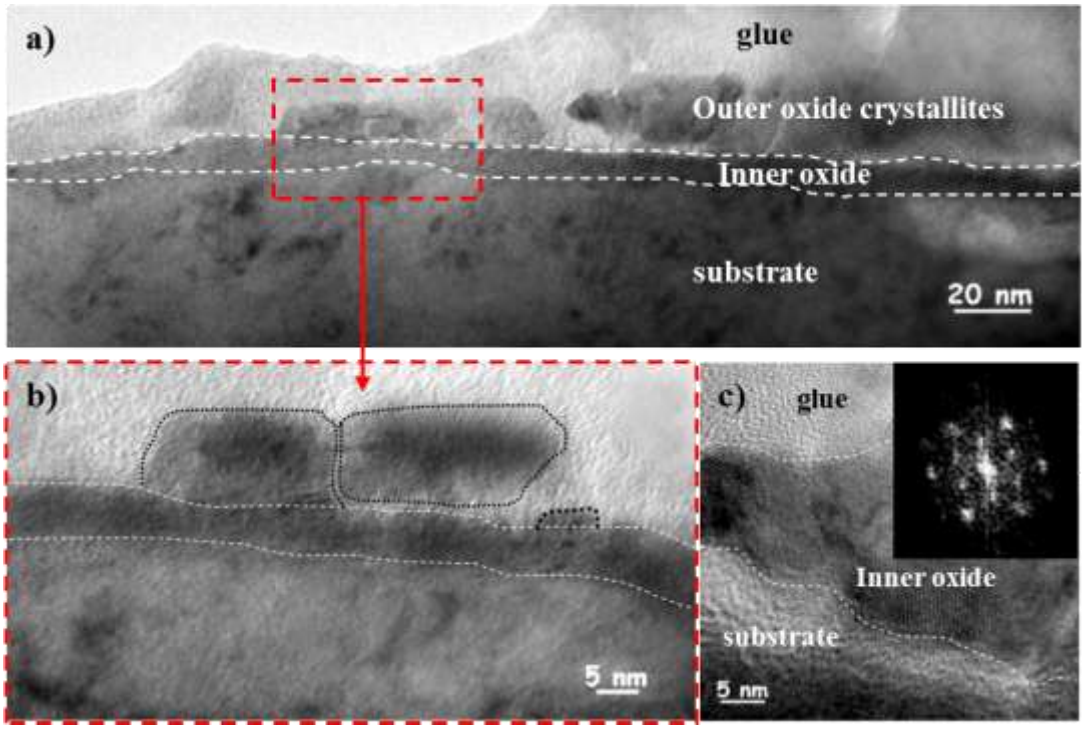

Figure 3-26 : a) BF TEM image b) Zoomed image (red rectangle zone) of the oxides formed on the 5 – dpa FeHe sample. c) HRTEM image of inner layer combined with the Fourier transform (in inset) along the [011] zone axis. The inner layer was indexed to be spinel of type Fe, $NiCr_2O_4$. Outer layer is marked by black dotted line and inner layer by white dashed line.

In comparison to unirradiated sample, size of the outer oxide crystallites was smaller on irradiated 5 dpa – Fe and 5 dpa – FeHe samples (Table 3-2). This is in agreement with the SEM analysis (Figure 3-21). Beside outer oxide, irradiation influenced inner oxide as well. The inner layer in irradiated samples was thicker and more enriched in Cr than in unirradiated sample. Higher enrichment of Cr in the inner layer of the irradiated sample is due to the presence of irradiation induced defects which enhanced the diffusion of Cr and indicates a more protective layer on these samples. These results are contrary to the findings of Perrin [13] and Dumerval [14]. However, in these studies [13, 14] oxidation test was conducted in a corrosion loop and for much longer time. Also, they reported to use mechanically polished sample, which should contain a surface hardened layer [15] (§2.2.3.2) but did not provide any information on the substrate. The contrary finding in this study from [11, 12] could also be due to different surface states prior to oxidation.

In literature, several authors [10 – 14] have also reported to observe a Ni enriched zone beneath the inner layer. Surprisingly, Ni enriched layer was observed only in irradiated 5 – dpa Fe sample. One explanation could be that it was present in all the samples but was very thin and needed a very small probe (using ARM TEM) to be detected. Since, only 5 dpa – Fe was investigated using ARM TEM, it was observed in this sample and not others.

Sample	**Thickness**	
	Outer oxide (nm)	**Inner oxide (nm)**
Unirradiated	20 – 100	5 – 6
5 dpa – Fe	1 – 3	10 – 20
5 dpa – FeHe	10 – 20	8 – 10

Table 3-2 : Thickness of the oxide layers formed on unirradiated, 5 dpa – Fe and 5 dpa – FeHe samples following oxidation in simulated PWR primary water for 360 h.

Conclusively, thicker inner oxide in irradiated samples suggests that diffusion of cations was faster in this layer. And higher Cr content advocates it to be more protective than the inner layer on unirradiated sample. Increase in the thickness of inner layer and enrichment of Cr with irradiation observed in bars was contrary to what was observed on 5 dpa – Fe tensile sample strained in simulated PWR environment (3.2.2.2). There were, however, some differences in the two cases such as the two types of samples (bars and tensile samples) were oxidized for different time in different volume of corrosive media. Besides, tensile sample was strained while bars were not. All of these factors can influence the growth of oxide layers in material.

3.3.2. IMPACT OF VOLUME OF CORROSIVE MEDIUM

To ascertain the possible effect of different autoclaves (to be precise different quantity of corrosive media), 5 dpa – FeHe samples oxidized in small and big static autoclaves were characterized. The morphology of outer oxide formed on these samples showed some differences during surface analysis. SEM images taken in the unirradiated sections of both the samples revealed that the oxide crystallites were smaller on the sample oxidized in the smaller autoclave compared to the samples oxidized in the bigger autoclave (Figure 3-27). Similar observations were made for the irradiated regions of both 5 dpa – FeHe samples (Figure 3-28). To proceed further, the cross sectional TEM samples prepared from the irradiated region of the two samples were characterized using TEM.

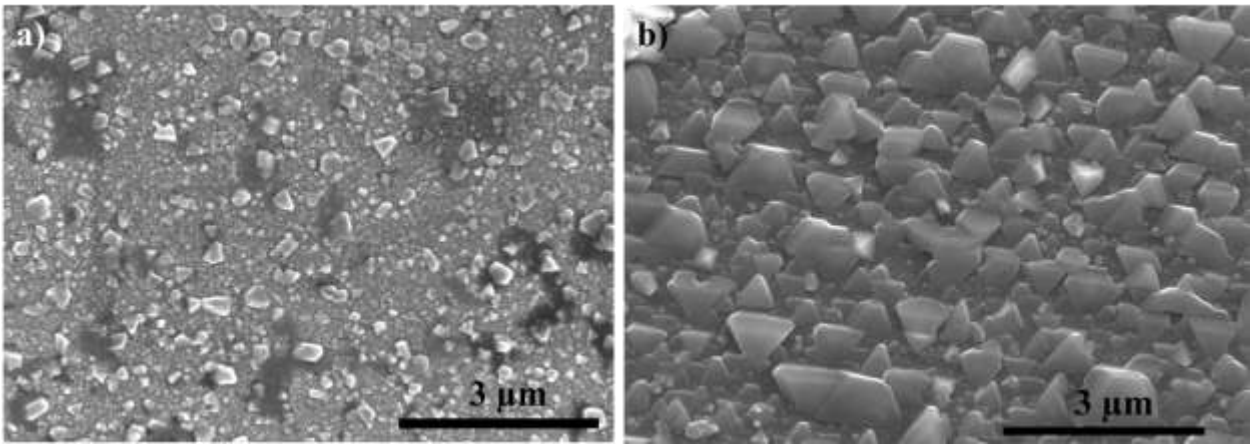

Figure 3-27 : SEM images of the unirradiated region of 5 dpa – FeHe sample post to 360 hours oxidation in simulated PWR primary water environment in a) small b) big autoclave.

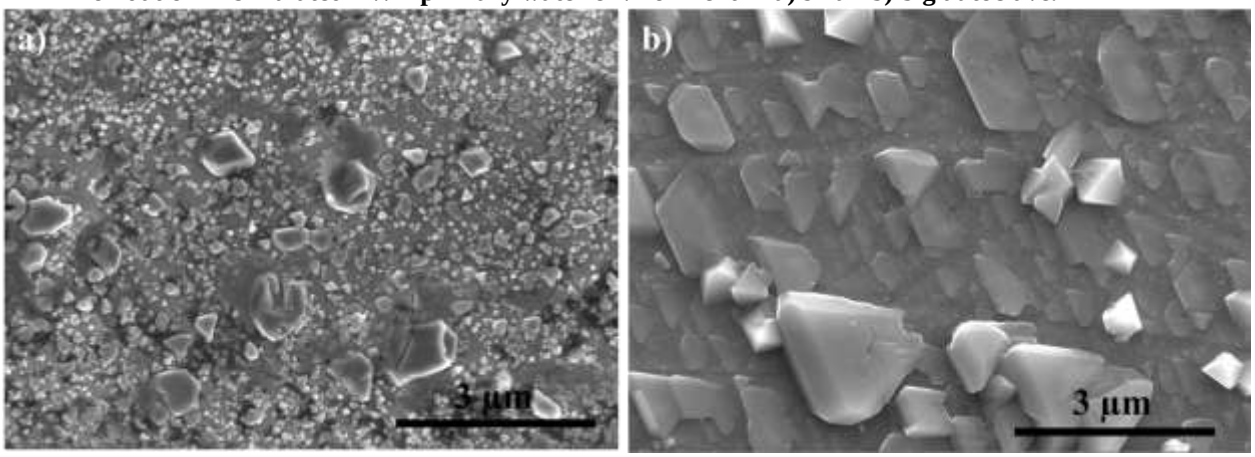

Figure 3-28 : SEM images of the irradiated region of 5 dpa – FeHe sample post to 360 hours oxidation in simulated PWR primary water environment in a) small b) big autoclave.

TEM investigation of the irradiated region of the 5 dpa – FeHe sample oxidized in smaller autoclave disclosed that the outer and inner oxides were 10 – 20 nm and 8 – 10 nm thick respectively (Figure 3-29a). While, on 5 dpa – FeHe sample oxidized in bigger autoclave,

these layers were 15 – 40 nm and 90 – 100 nm thick respectively (Figure 3-29b). This implies that the outer and inner oxides were thicker in sample oxidized in bigger autoclave. As stated before, formation and growth of outer oxide is due to a balance between the re-deposition of iron oxide from media on to the surface and diffusion of Fe, Ni, Cr ions through inner layer. Thicker inner layer observed in the sample oxidized in bigger autoclave suggests that the diffusion of cations was faster which enhanced the dissolution and re-deposition processes. That is why bigger outer oxide crystallites were observed on this sample. Outer oxide layer provides no protection but thicker inner layer suggests that this sample was less corrosion resistant compared to its counterpart tested in smaller autoclave.

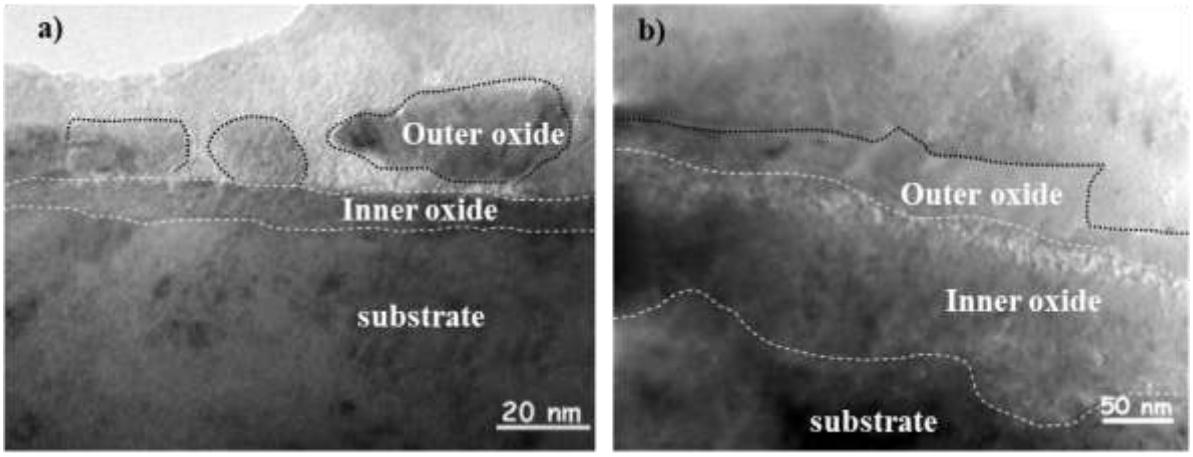

Figure 3-29 : TEM images of the irradiated regions of 5 dpa – FeHe sample post to 360 hours oxidation in simulated PWR primary water environment in a) small b) big autoclave displaying the differences in the outer oxide and inner oxides in the two samples.

Sample	Autoclave	Thickness	
		Outer oxide (nm)	Inner oxide (nm)
5 dpa – FeHe	small	10 – 20	8 – 10
5 dpa – FeHe	big	15 – 40	90 – 100

Table 3-3 : Comparison of the oxide layers observed on 5 dpa – FeHe samples oxidized in simulated PWR primary water for 360 h in different autoclaves.

In conclusion, differences in the oxide formed on the unirradiated and irradiated samples were observed. These results suggest that effect of irradiation on intergranular oxidation of austenitic stainless in corrosive PWR environment should be further investigated to have an insight of the correlation between intergranular oxidation with intergranular cracking of the irradiated material.

3.4. INFLUENCE OF DEFORMATION MECHANISM ON CRACKING MECHANISM OF IRRADIATED AUSTENITIC STAINLESS STEEL

In previous sections, it has been demonstrated that it is possible to study IGSCC of irradiated austenitic stainless steel using heavy ion irradiation. Difference in degree of localization and oxidation with iron irradiation in agreement with literature [9] was observed as well. To further ascertain the possibility of using iron irradiation, more detailed analysis was done by tracking the effect of strain inhomogeneity on the cracking susceptibility of irradiated material. For the purpose, a criterion proposed for proton irradiated stainless steel was used and is detailed in this part of the study.

3.4.1. MORPHOLOGY OF THE CRACKS OBSERVED

Figure 3-30 shows some enlarged SEM images of different configurations of cracks and slip lines observed in the irradiated region of 5 dpa – Fe, 10 dpa – Fe and 2 dpa – H samples. Well open cracks along with small cracks were observed on these samples. Such morphologies of cracks have been reported in different studies dealing with the IASCC cracking of plastically strained irradiated stainless steel, either after neutron irradiation [16], or proton irradiation [6, 17]. It is evident from Figure 3-30 that for most cases, slip lines (represented by black dashed lines) were visible in single direction in a deformed grain. These lines were the trace of the most active slip system in the grain.

Based on the interaction of slip lines with grain boundaries, the crack sites was distinguished into two categories, continuous and discontinuous intersections. If the slip lines are present on either side of the cracked grain boundary, it suggests a transfer of slip from one grain to another and hence, is categorized as continuous interaction. The transmission of slip could be either direct (grains marked 1 and 2 in Figure 3-30a) or via formation of new dislocation source in the adjoining grain at the points where the slip lines of first grain intersects the grain boundary (grains marked 1 and 3 in Figure 3-30a). In discontinuous interaction, the slip lines terminate at the grain boundary without any evident transmission of slip across the boundary (grains marked 1 and 2 in Figure 3-30b). Strangely, in some cases (grains marked 1 and 2 in Figure 3-30c and d), slip lines were observed on either side of the cracked grain boundary but there was neither direct nor indirect transfer of slip across the grain boundary. Consequently, such cases were considered as discontinuous interaction in this study. Recently, McMurtrey and West [17, 18] proposed that in case of discontinuous interaction, dislocations pile up at the grain boundaries resulting in higher stress buildup at the boundaries which increases the susceptibility of the grain boundaries to cracking. In this study, around 50 – 60% of the

total crack sites[17] observed on samples (in both iron and proton irradiated) belonged to discontinuous interaction category while 30 – 40 % belonged to continuous interaction category. These results seem to be consistent with the hypothesis of McMurtrey and West [17, 18].

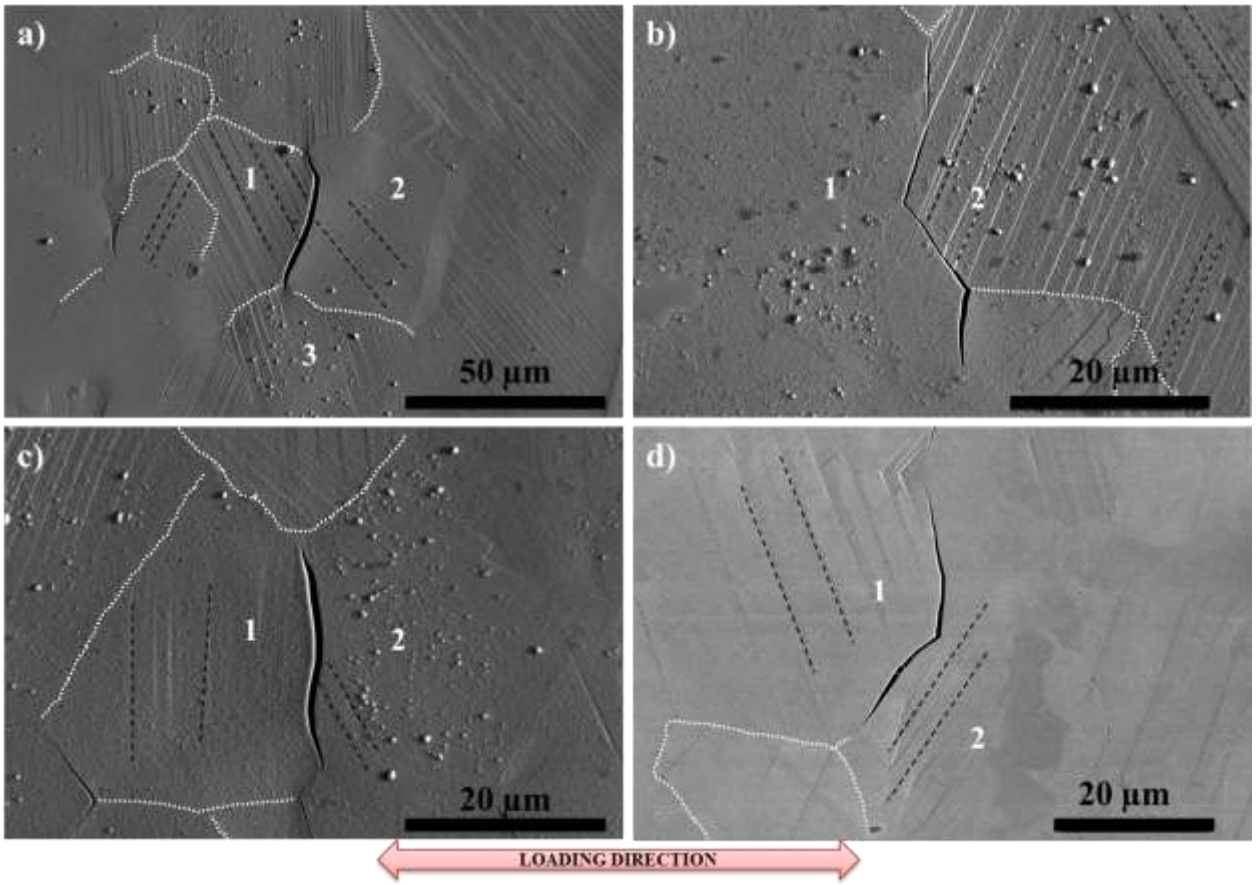

Figure 3-30 : SEM images depicting the various crack sites observed in iron (a – c) and proton (d) irradiated strained samples. a) Exemplify the slip continuity while slip discontinuity is illustrated in b). In c) and d) slip lines were present on both sides of the cracked grain boundary but did not satisfy the definition of continuous interaction. Few grain boundaries are marked by white dashed lines and slip lines are indicated by black dashed lines. Loading direction is indicated in the image.

On rare occasions (≤ 10 %), few cracks without any visible slip line (in the close vicinity of the crack) on either side were observed. Figure 3-31 (grains marked 1 and 2) presents an example of such cracks.

[17] Cracks observed in the 1 mm² area scanned on the samples to estimate the crack density. For example 302 cracks for 5 dpa – Fe sample and 316 cracks for 2 dpa – H sample.

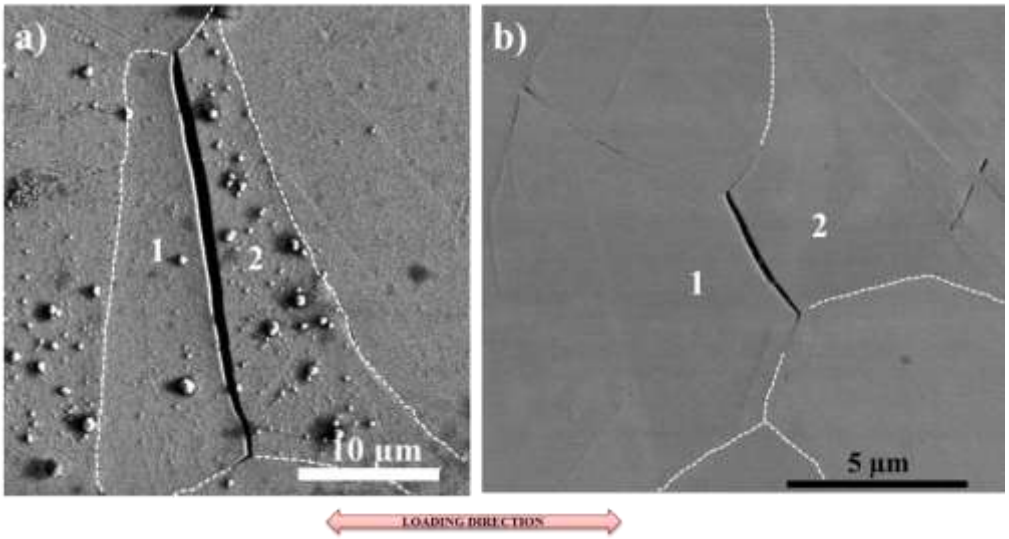

Figure 3-31 : SEM images depicting the crack sites observed in iron (a) and proton (d) irradiated strained samples where no visible slip lines were present on either sides of the cracked grain boundary. Few grain boundaries are marked by white dashed lines. Loading direction is indicated in the image.

Few small and discontinuous cracks were observed as well (Figure 3-32). They appeared to have initiated at the points where slip line intersected the grain boundaries with no transfer of slip in adjacent grain, which is a region of high local stress.

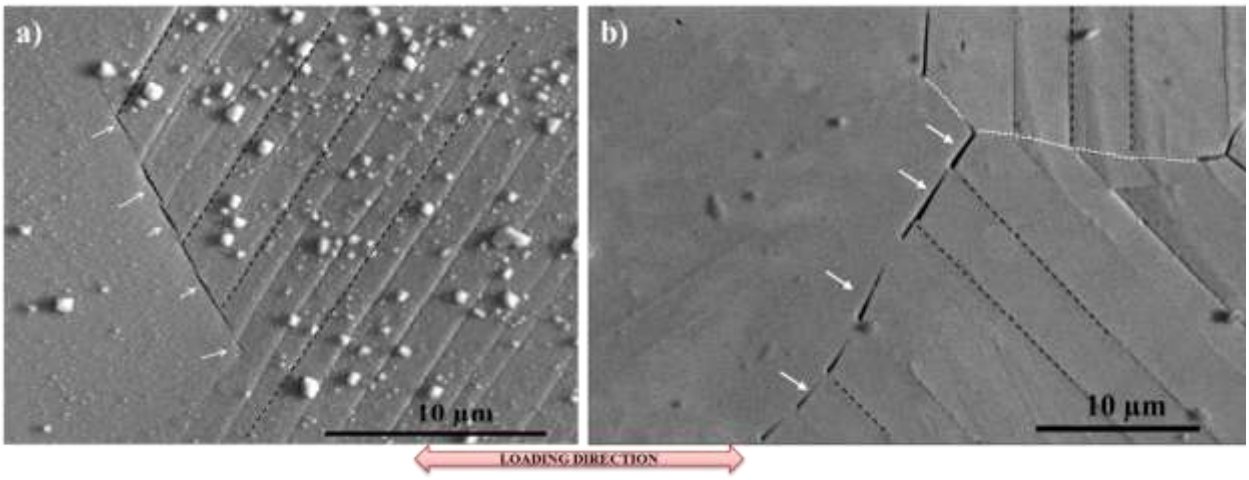

Figure 3-32 : Discontinuous cracks (some indicated by white arrows) observed in the irradiated region of strained a) 5 dpa – Fe b) 2 dpa – H samples. Slip lines are indicated by black dashed slip lines. Loading direction is indicated in the image.

Similar micro-cracks have also been reported in neutron and proton irradiated austenitic stainless steel post to plastic straining in PWR environments [3, 4]. Such discontinuous cracks might appear to be an intermediary step between crack initiation and propagation stage. It could be hypothesized that the points at which slip lines are impingent on grain boundary are crack initiation sites and on increasing the strain, these small cracks will develop into a full uninterrupted crack. However, West [4] conducted a study on 7 dpa

proton irradiated 316L strained in SCW (supercritical water) environment and reported that only 36 % of such interrupted cracks developed in to a single uninterrupted crack on increasing the strain from 5 % to 10 % during sequential test. The author [4] also suggested that majority of these interrupted cracks neither propagated nor increased in density with straining. Hence, in this study, no special attention was given to such crack sites. But they do remain an issue of interest to be investigated further.

3.4.2. VALIDATION OF CRITERION PROPOSED FOR INTERGRANULAR CRACKING

McMurtrey and West [17, 18] recently proposed a criterion for the intergranular cracks observed in the irradiated austenitic stainless steel strained in supercritical water and Boiling Water reactor (BWR) environment. As per the criterion, Randomly High Angle Grain Boundaries (RHABs), which are inclined at high angles (greater than 70°) with respect to tensile direction and adjacent to grains with low Schmid Factor (SF) are more prone to slip discontinuity (i.e. least likely to accommodate strain) and hence, most susceptible to cracking. This criterion was based on the fact that grain boundaries inclined to the tensile axis at high angles will have a high normal stress during straining. Dislocation pileups (due to slip discontinuity) at such grain boundaries will act as an additional stress element thereby, enhancing the propensity of such boundaries to crack. The validity of this criterion for the tests conducted in PWR environment was verified in this study for both iron and proton irradiated samples.

Information on the type of grain boundaries (or their angle of misorientation) was obtained using EBSD post processing software HKL. Surface analysis detailed about the slip continuity and discontinuity. As the Schmid factor for the most active slip system is an accepted indicator of the property of a plastically deformed grain, it was used for the analysis conducted in this study. The information on SF was obtained using EBSD post processing software HKL. The software calculates the SF for all the 12 possible slip systems of austenitic steel with respect to the tensile loading direction and then assigns the grain with SF corresponding to the slip system with maximum resolved shear stress. The software uses different colours to differentiate amongst the different values of SF of grains analysed. Using the categoritation proposed by West et al [18], the values of SF obtained can be sorted into three different categories (or bin) namely High ($0.47 < SF \leq 0.50$), Medium ($0.44 < SF \leq 0.47$) and Low ($SF \leq 0.44$). If one grain belongs to a Low SF category and other to High SF category, they are adressed as LH pair. Based on these three categories, there exist 6 possible combinations of SF for two adjacent grains namely LL, LM, LH, MM, MH, HH.

Before mapping the irradiated regions, SF mapping was done on 3 different small regions (~ 0.1 mm² each) in the unirradiated portion of the 5 dpa – Fe sample after the SSRT test.

Figure 3-33 shows the SF map for one of the region mapped along with SF distribution for the same region. Similar SF distribution was obtained for all the three regions justifying that Figure 3-33 could sufficiently represent the SF distribution in the material. The different colours were used to differentiate amongst the different values of SF of austenite grains analysed. In white is the BCC phase which was not analysed. It was observed (Figure 3-33b) that 39 % of the grains belonged to High SF bin while 31 % and 30 % belonged to Medium and Low SF bin respectively. As austenitic stainless steels are known to be a bit biased towards high value of SF, these observations are consistent.

The SF mapping of the irradiated region of the same 5 dpa – Fe tensile sample is shown in Figure 3-34. An area of 0.1 mm² was analyzed which contained around 273 grains. Like unirradiated region, in this region too higher percentage (40 %) of the grains belonged to the High SF bin compared to Medium (33.5 %) and Low (26.5 %) SF bins. It can be interpreted from this result that the probability of a randomly selected grain belonging to High SF bin (p(H)) was 0.4, while for Medium (p(M)) and Low SF (p(L)) bins was 0.335 and 0.265 respectively, suggesting that they were not equally probably in the area examined. So the probability of a grain boundary to be either of 6 possible types (LL, LM, LH, MM, MH and HH) was calculated keeping the bias in mind. For example, the probability of occurrence of LL was the p(L) × p(L) and probability of occurrence of LM was the 2 × p(L) × p(M)[18]. Incorporating the probability of occurrence, normalized percentage of the type of grain boundary cracked was estimated.

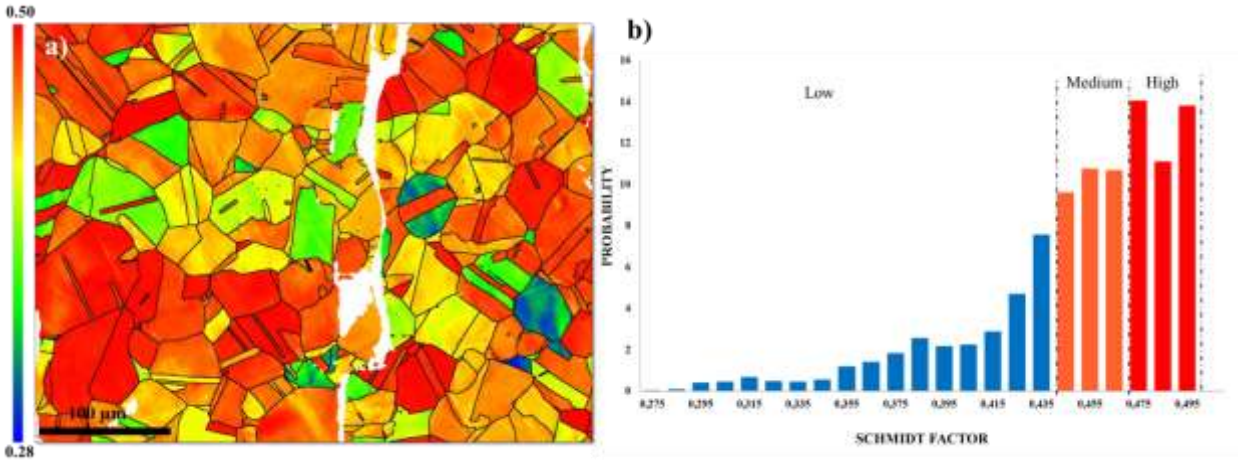

Figure 3-33 : Schmid factor a) map b) distribution obtained on a small area of the unirradiated region of 5 dpa – Fe sample after slow strain rate testing (4 % plastic deformation) in PWR environment. The different colours represent the different Schmid factor value of the grains.

Since, the cracks were not visible on SF map, a cartography of the same area was obtained using ForeScattered electron (FSE) imaging system of the electron flash EBSD

[18] Factor of 2 is included to account for the possibilities of having either LM or ML.

detectors (Figure 3-34b). In addition to qualitative orientation information, the image retained the visibility of surface features (slip lines and cracks) which was an added bonus. Few of the cracks have been indicated by yellow arrows in the Figure 3-34b.

Normalized cracking percentage estimated for each possible grain boundary combination is shown in Figure 3-35. Branched cracks were considered as multiple cracks. For example, a crack branching to two grains is considered as two cracks. As evident, in majority of the cases (84.2 %), at least one of the grain neighbouring, the cracked grain boundary belonged to the Low SF bin. A Low SF grain is reluctant to deformation on loading and hence is more prone to cracking. This is in accordance with the results of Mcmurtrey and West [17, 18]. They further suggested that the factors such as slip continuity and cracked grain boundary orientation with respect to tensile axis are important as well to obtain a refined correlation.

To include factors such as slip continuity and cracked grain boundary orientation with respect to tensile axis, analysis was performed on Figure 3-34b. Using imageJ to measure the angle between the surface trace of cracked grain boundary and tensile axis, it was evaluated that majority (80 %) of the cracked grain boundaries had an inclination greater than 50 ° and around 68 % had an inclination between 70 – 90 ° with respect to tensile axis. Besides, for 75 % of the total of the cracked grain boundaries there existed slip discontinuity i.e. the slip lines were present only on one side, while 17 % of the cracked grain boundaries had slip continuity and the remaining 8 % showed no slip lines on either side. For the ease of understanding, the percentage of cracked grain boundaries observed satisfying particular conditions is shown in Figure 3-36.

Combining all these factors, it could be said that 75 % of the cracked grain boundaries that were inclined at angles ≥ 70 ° with respect to tensile axis and was neighboring at least one Low SF grain, had a discontinuity of slip. McMurtrey and West [17, 18] have suggested that such grain boundaries are unlikely to accommodate the strain and hence, are most susceptible to IASCC. However, the grain boundaries that fulfilled these requirements constituted only 32 % of the total cracked grain boundaries i.e. for the rest 68 % either of the required conditions was not fulfilled. This proposes that these conditions are not necessary for the irradiation conditions used in this study. As the studies of McMurtrey and West [17, 18] dealt with proton irradiated samples, to have a direct correspondence, same characterization was performed on the 2 dpa H samples post to 4 % plastic deformation.

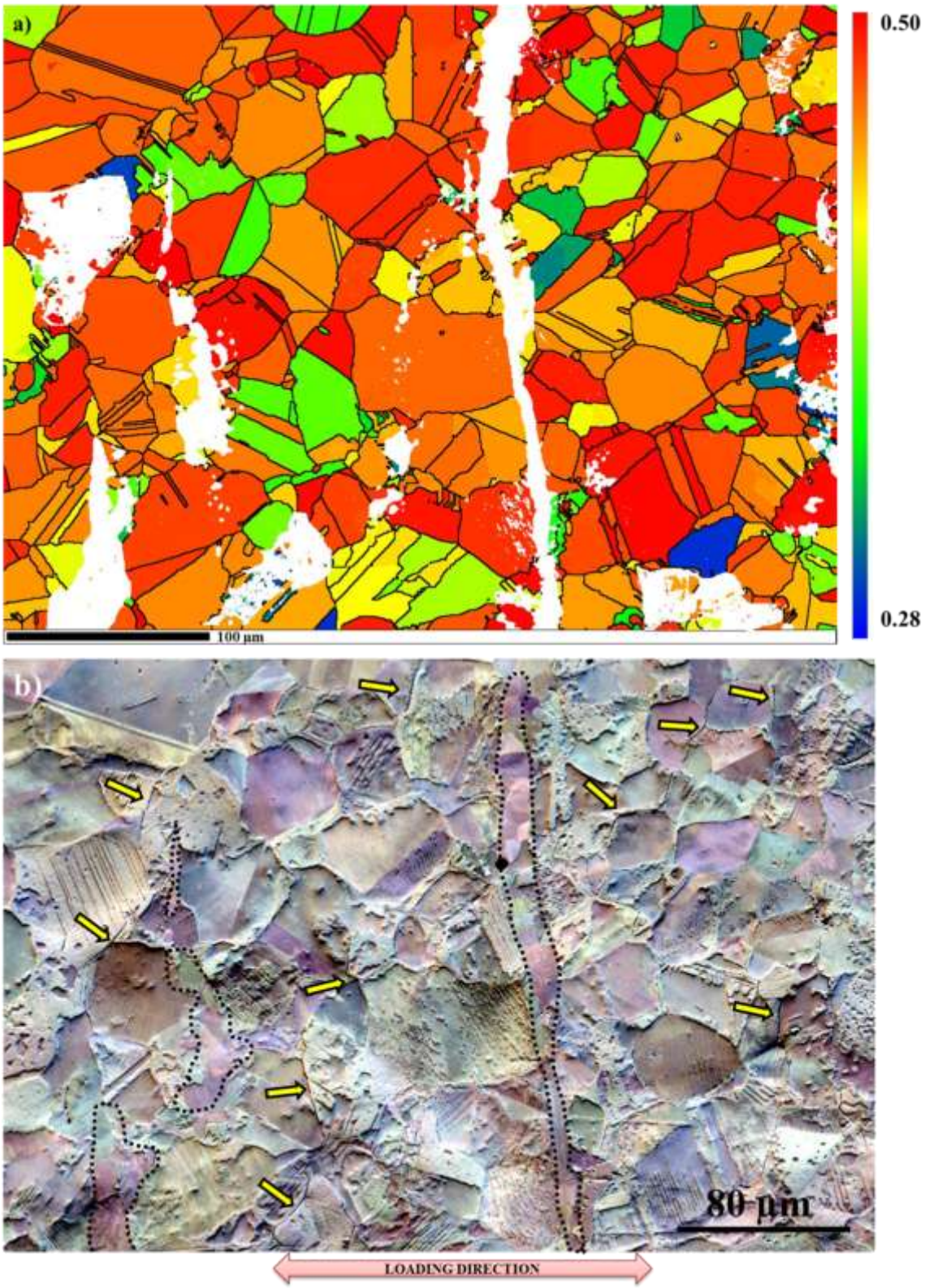

Figure 3-34 : Area of the irradiated region of 5 dpa – Fe sample after slow strain rate testing (4 % plastic deformation) in PWR environment shown as a) Schmid factor map with different colours representing different Schmid factor value of the grains and b) EBSD cartography obtained using FSE. Cracks are indicated by yellow arrow and ferrites are outlined in black.

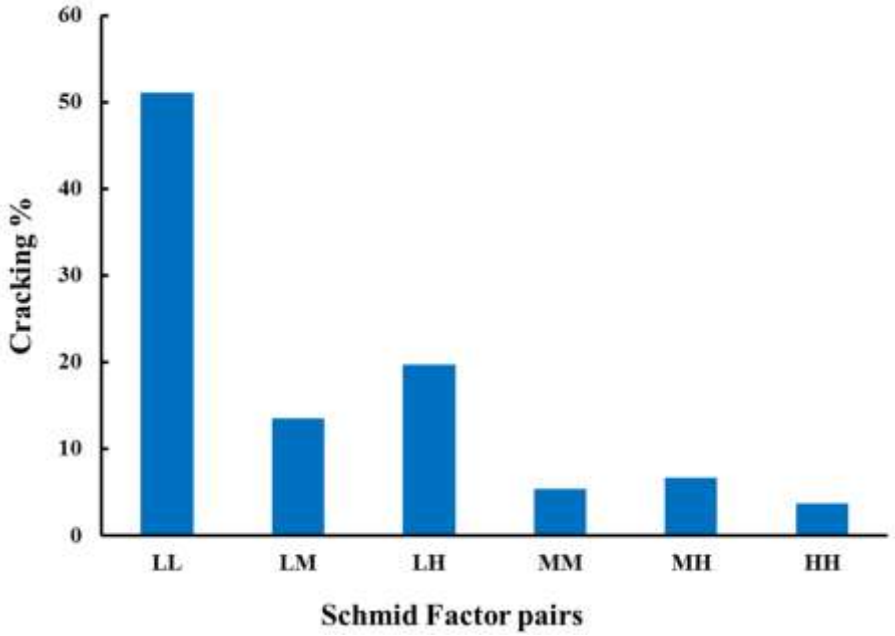

Figure 3-35 : Normalized distribution of Schmid Factor pairs of grains adjacent to the cracked grain boundaries observed in 5 dpa – Fe sample.

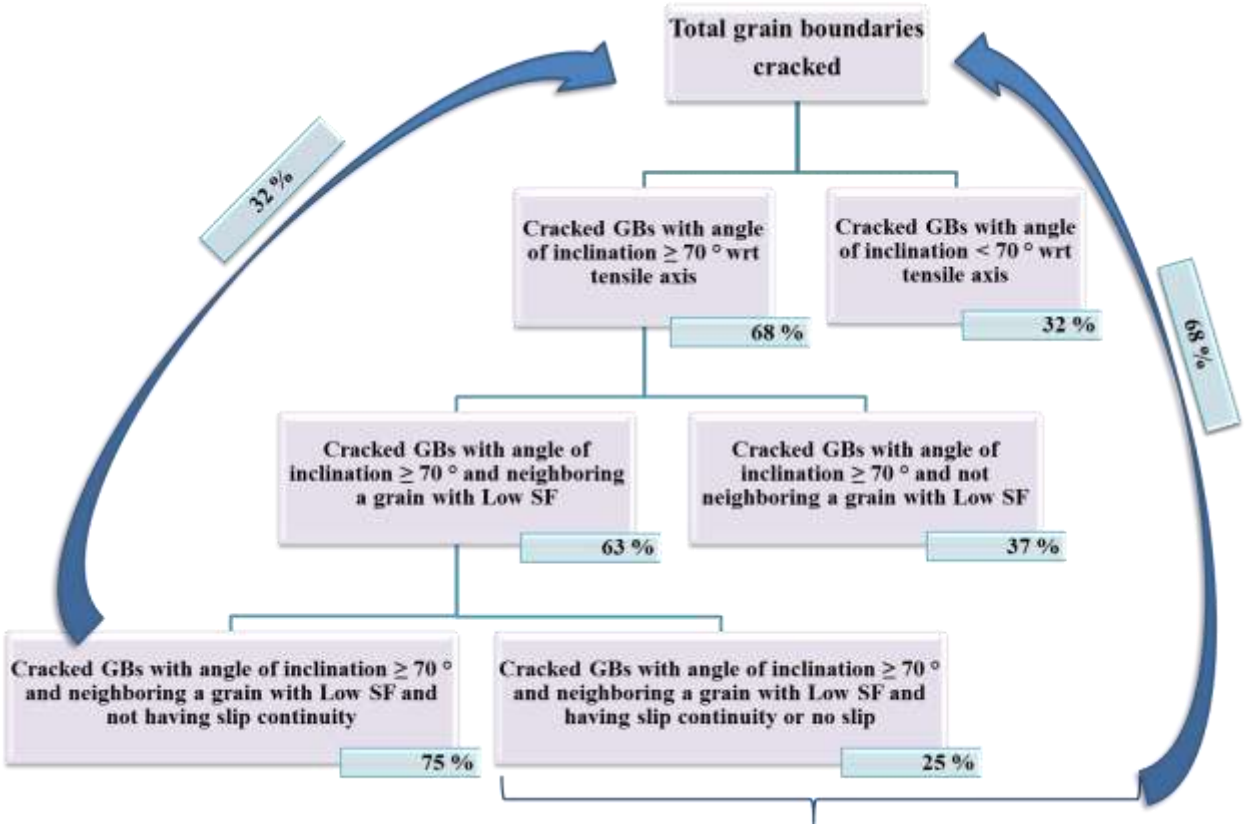

Figure 3-36 : Probability diagram to illustrate the percentage of the cracked grain boundaries observed to satisfy the given conditions in 5 dpa – Fe sample.

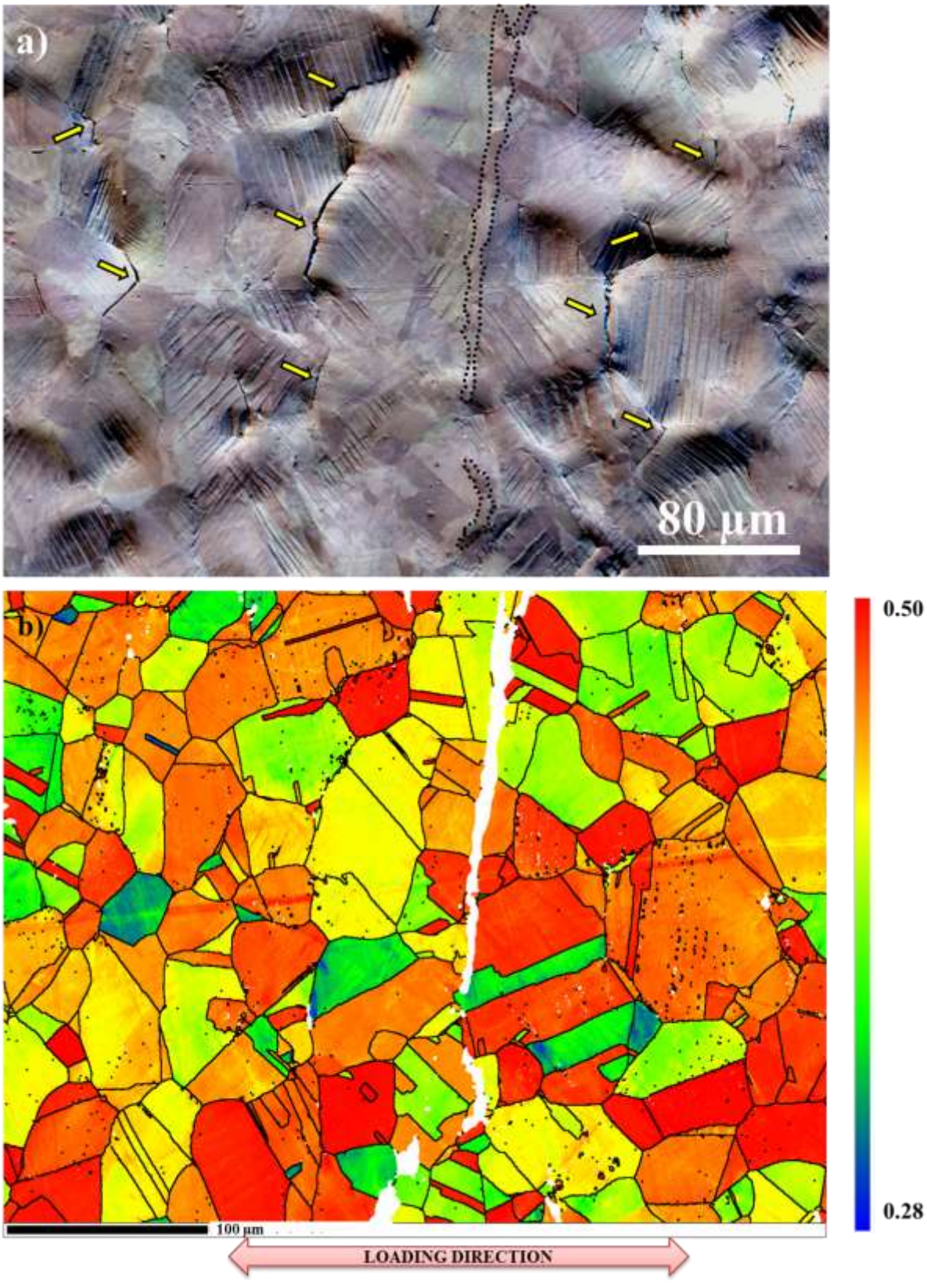

Figure 3-37 : a) EBSD cartography obtained using FSE b) SF mapping after 4% plastic strain in the irradiated area of 2 dpa – H sample. Cracks are indicated by yellow arrow and ferrites are outlined in black.

Figure 3-37 shows the cartography obtained in the irradiated region of the tensile sample using FSE imaging system along with the SF map of the same region. A total of 239 grains were analyzed in 0.1 mm² area. Within this area, 38 % of the grains belonged to the High SF bin while 30 % and 32 % belonged to Medium and Low SF bins respectively. Probability occurrence was calculated in the same manner as for 5 dpa – Fe sample. On this sample as well, majority (83.6 %) of the cracked grain boundaries were associated with Low SF grain (Figure 3-38). In fact, no cracking of the grain boundaries adjoining two High SF grains was observed on this sample.

On taking into consideration, the angle of inclination and slip continuity, it was observed that only 40 % of the total cracked grain boundaries were inclined at angles ≥ 70°, were adjoining at least one Low SF grain and had a discontinuity of slip. This implies that irrespective of irradiation ion used, these conditions were not sufficient to fully describe the cracking criteria in irradiated austenitic stainless steels post to the straining conditions used in this study.

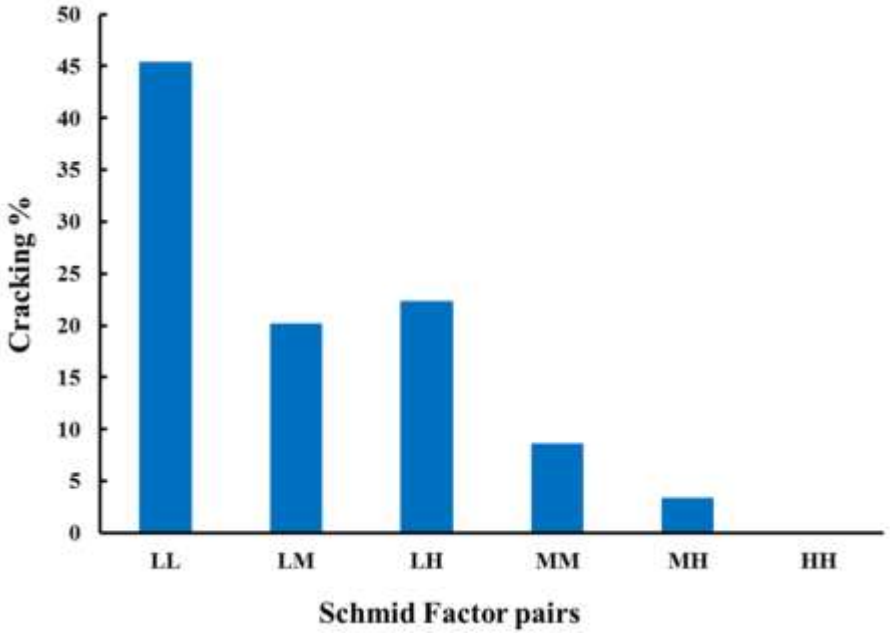

Figure 3-38 : Normalized distribution of Schmid Factor pairs of grains adjacent to the cracked grain boundaries observed in 2 dpa – H sample.

Millier [3] also observed similar conflict of criteria for proton irradiated 304 samples strained to different levels in PWR environment. The author used microextensometry by digital image correlation technique to measure the local deformation fields and reported to observe strong trans-granular heterogeneities localized inside bands which may generate strong stress on the grain boundaries. This led the author to hypothesize that the local stress state has a better reciprocity with cracking susceptibility than local deformation state. However, this hypothesis is yet to be validated.

No detailed investigation on the local stress and strain distribution was conducted in this study. On taking into consideration grain boundaries inclined at angle greater than or equal to 50 °, the correlation between the orientation of grain boundaries with respect to tensile axis and intergranular cracking was improved from 68 % to 90 %. This implies that due to irradiation, boundaries which are not inclined at higher angle with respect to tensile axis become more susceptible to cracking as well. This however needs to be further explored.

3.5. DISCUSSIONS

This chapter summarized the influence of irradiation observed on the cracking behavior of SA 304L. In chapter 2, it has been demonstrated that irradiation altered the microstructure and mechanical properties of material. With this background, the irradiated samples were subjected to SSRT (or CERT) with a strain rate of 5×10^{-8} s^{-1} upto a plastic deformation of 4 % in simulated PWR primary water environment. Results obtained from the tests will be discussed in this section.

- Cracking Susceptibility

On each irradiated sample, some portion of the gauge length was unirradiated. Both the regions of all the samples were analyzed for the presence of cracks. Following straining in inert environment, no cracks were observed on the 5 dpa – Fe sample. Whereas 5 dpa – Fe sample tested in simulated PWR environment had numerous cracks in the irradiated region and few cracks in the unirradiated region. Intergranular nature of the crack was confirmed by performing EBSD analysis on cross-sectional FIB prepared sample. These results justify that the cracking observed on the sample tested in corrosive environment is IGSCC of austenitic stainless steel.

Similar to 5 dpa – Fe sample, numerous cracks were observed in the irradiated region of 10 dpa – Fe and 2 dpa – H samples. Density of cracks was similar for all the three samples and majority of cracks belonged to a length range of 5 and 25 µm. On contrary, few small cracks were observed in the unirradiated region of these samples. One of the longest cracks (~ 60 µm) of the irradiated region of 5 dpa – Fe sample was analyzed to be 2.2 µm deep whereas longest crack (~ 30 µm) of the unirradiated region of sample was found to be just 1 µm deep. To summarize, longer, deeper cracks and in much higher density were observed in irradiated region of the samples compared to their unirradiated counterparts. It could be inferred from these results that cracking was much more severe in irradiated region. This implies that irradiation highly enhanced the IGSCC susceptibility of SA 304L used in this study. It is consistent with the findings of other authors [3, 4].

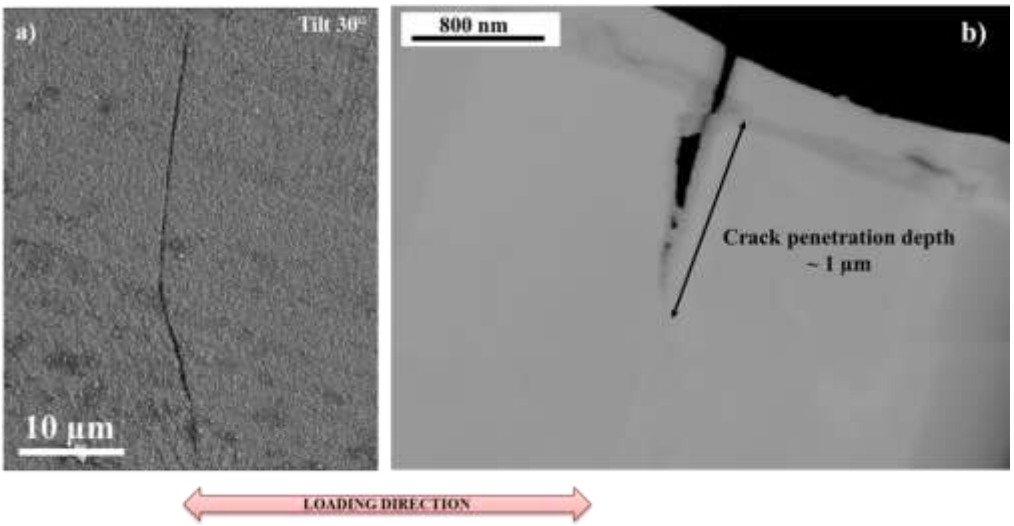

Figure 3-39 : a) SEM image (taken with a sample tilt of 30 °) of the crack chosen from the unirradiated sample to make FIB sample. b) SEM image of the FIB sample prepared by transverse cutting the crack shown in a). Loading direction is indicated in the image.

Previously, no study has investigated the propensity to cracking of iron irradiated material. In literature [3], the crack length distribution for only proton is available. So, the distributions obtained for the iron and proton irradiated samples (irradiated regions only) used in this study were compared with proton literature (2.5 dpa proton irradiated 304 SS successively deformed to 5 % total strain in simulated PWR primary water environment) (Figure 3-40) [3]. Crack length distribution of 2 dpa – H with literature was found to be consistent. Interestingly, the crack length distribution of 2 dpa – H but of all the samples was consistent with the literature, despite different doses and different irradiation ion types. These results imply that the iron irradiated austenitic stainless could be used to study the IGSCC susceptibility of irradiated samples. But at the same time, it is necessary to examine if the mechanism leading to intergranular cracking in iron irradiated material is same as that reported for proton irradiated material or not. In literature, increase in intergranular cracking in consequence of irradiation is generally attributed to the localized deformation or radiation induced segregation (RIS). In this study, RIS was considered to be similar in all the samples[19]. The choice of irradiation temperature for both proton and iron irradiation (§2.3) ensured that the RIS was of the same order of magnitude but no actual measurement was done. Hence, its influence on cracking susceptibility is not discussed here.

[19] RIS is the alteration in grain boundary composition induced by irradiation (§1.3.1.ii). Depletion of Cr at the grain boundaries due to RIS can enhance the susceptibility of the boundaries to intergranular cracking.

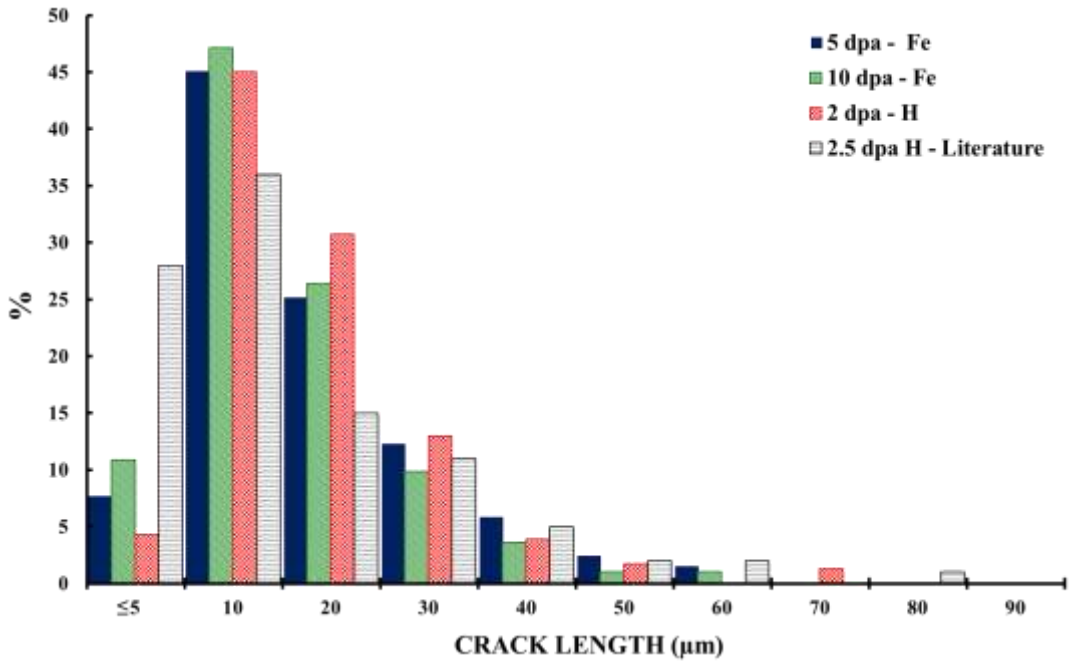

Figure 3-40 : Comparison of crack length distribution obtained for 5 dpa – Fe, 10 dpa – Fe, 2 dpa – H samples (this study) with proton literature.

- Localized deformation

The degree of localization was estimated by measuring the inter-line spacing of two consecutive slip lines observable on the surface of the strained samples. Slip lines in unirradiated region of the samples were difficult to observe while they were readily visible in irradiated region. Spacing in the irradiated region was higher than the corresponding unirradiated region of the samples. The increase in spacing with irradiation is consistent with literature. Miura et al. [7] studied the slip line in helium irradiated SA 304 SS using TEM and found that some of the slip lines originating from the substrate (unirradiated) are blocked by the damage present in irradiated region leading to an increase in slip line spacing. Higher degree of localization correlates with the higher cracking susceptibility observed in ion irradiated SA 304L. The increase in slip line spacing with irradiation could be correlated to the increase in hardness observed in these samples with irradiation. The mean slip line spacing for 5 dpa – Fe and 10 dpa – Fe sample strained in corrosive environment was observed to be similar suggesting saturation in spacing value around 5 dpa. This is in accordance to the findings of Miura et al [6]. It could be associated with the fact that the irradiation induced modifications in microstructure and mechanical properties saturates around 5 dpa.

However, the mean slip line spacing for 2 dpa – H sample was observed to be much higher compared to the value in 5 dpa – Fe and 10 dpa – Fe samples despite its lower dose. This difference is attributed to the different penetration depths (or to be precise

damage depth relative to the grain size) of two ions in the material [8, 9]. For this study, the value of damage depth relative to the grain size was 0.09 (< 0.33) for iron irradiated samples indicating that majority of the slip lines observed on the surface of the irradiated sample originated in the underlying unirradiated material. Whereas in proton irradiated sample, the ratio was 0.74 (> 0.33) suggesting nucleation of channels in the irradiated region independent of underlying unirradiated material was dominant process.

Interestingly, despite higher degree of localization (or higher spacing value) in 2 dpa – H sample compared to 5 dpa – Fe and 10 dpa – Fe sample, the crack density in the irradiated region of all of these samples was similar. This implies that grain boundaries in iron irradiated samples were more embrittle compared to that in proton irradiated sample. This could be due to either RIS or due to oxidation. Moreover, mean spacing was identical for 5 dpa – Fe sample tested in corrosive environment and 5 dpa – Fe sample tested in inert environment meaning same degree of localization in the two cases. Yet no intergranular cracks were observed in latter which further highlighted that corrosive environment played a crucial role in enhancing the cracking susceptibility of iron irradiated material used in this study. Unfortunately, not enough data is available on the effect of irradiation on the oxidation of austenitic stainless steel in simulated PWR environment. So, bulk oxidation was investigated in this study to have some insight of the effect of irradiation on oxidation.

- Oxidation

Oxide formed on the 5 dpa – Fe sample due to the exposure to simulated PWR primary water (5 L – static stainless steel autoclave) during the SSRT test was duplex in nature, as has been reported in literature. The outer oxide observed on the unirradiated and irradiated region of the sample consisted of Fe rich crystallites while inner layer consisted of Cr rich spinel of type (Fe, Ni)Cr_2O_4. Oxide layers (outer and inner) formed on the unirradiated region of the sample were thicker compared to the layers formed on the irradiated region. This indicates that irradiation decreased the size of both outer and inner oxide. Cr content in the inner layer of unirradiated sample was higher. Oxide layers are formed by the cationic and anionic diffusion. Fe^{2+} and Ni^{+} cations diffuse outwards from metal and dissolve in media [13]. When media is saturated, they are precipitated on the surface of the metal as outer oxide crystallites (spinel in nature). Growth of the outer oxide crystallites is dependent on the outward cationic diffusion through inner layer. The inner continuous layer (also consisting of spinel), grows inward due to diffusion of oxygen from surface to metal. Thicker inner and outer oxide observed on the unirradiated sample suggests faster diffusion of cation through inner oxide of this sample. And higher Cr content in the inner layer of unirradiated sample could imply that this inner layer was more protective than the inner layer formed on irradiated sample. Though it may seem appealing to correlate protectiveness of inner layer of unirradiated sample with lower

density of intergranular cracks observed on this sample (in comparison to irradiated sample), caution needs to be paid. Firstly, for intergranular cracking, oxidation at the grain boundaries is of particular interest. Faster diffusion of cations and oxygen ions along the grain boundaries compared to bulk diffusion in oxides results in preferential oxidation at grain boundaries. Unfortunately, the grain boundaries studied were cracked grain boundaries and preferential oxidation of grain boundaries could not be observed in the present case. Secondly, irradiation modifies the microstructure and microchemistry of the material which results in generation of point defects in microstructure and RIS. Depletion of Cr at the grain boundaries due to RIS in irradiated material can increase the oxidation rate at grain boundaries making them more embrittle. This result in formation of oxide layer on irradiated material different than that formed on unirradiated materials. Besides, cracking in irradiated material is not solely because of oxidation but a combination of various factors. So these results can't be used to justify the exact role of oxidation in intergranular cracking observed but to ameliorate the current understanding of oxidation process.

Surprisingly, oxidation test conducted on unirradiated and irradiated bars revealed an opposite trend as observed for the 5 dpa – Fe tensile sample. That is, an increase in the thickness of inner layer and Cr enrichment with irradiation was observed in bars oxidized in 0.38 L autoclave. There were few differences between the two cases namely, duration of test, volume of corrosive medium and stress. Increase in inner layer thickness with duration of test, application of stress has been reported in literature for unirradiated material. However, not much is known for irradiated state. To study the effect of volume of corrosive environment on irradiated samples, 5 dpa – FeHe bars oxidized in 5L autoclave and 0.38 L autoclave each were examined. With increase in volume of corrosive media, an increase in inner layer thickness of irradiated material was observed. However, effect of time and applied stress could not be examined in this study.

Interestingly, some differences in the morphology of outer oxide crystallites formed on 10 dpa – Fe and 2 dpa – H bars oxidized in big autoclave for 360 h were noticed. As apparent in the Figure 3-41 crystallites of wide range of sizes were observed on 10 dpa – Fe sample while on 2 dpa – H sample majorly medium sized crystallites (in comparison to 10 dpa – Fe) were observed. It is difficult to comment on the density of crystallites in two samples. Crystallites on 10 dpa – Fe sample showed a strong effect of crystallographic orientation of underneath grain while the oxide on 2 dpa – H sample was rather uniformly distribute. In fact, effect of crystallographic orientation on outer oxide crystallites was also visible on 5 dpa – Fe sample oxidized in smaller autoclave. These differences suggest the possible effect of different irradiating ions on oxide formation. Though the density of irradiation induced Frank loops was similar in the 10 dpa – Fe and 2 dpa - H samples, perhaps the point defects which could not be detected in TEM analysis played an important role in influencing the formation of oxide layers on these samples or this might

just be a consequence of different degree of RIS in samples. Cross section TEM investigation of these samples is necessary to precisely study the effect of ion types on the thickness and Cr enrichment of inner oxide. Previously, Dumerval [14] has also reported to observe differences in the oxide formed on xenon irradiated and proton irradiated samples and concluded that irradiation induced defects play a vital role. Note that the samples studied in that study were oxidized for 600 h at 325 °C on 316 SS in a corrosion loop. Nevertheless, lack of information in this field suggests that more studies are needed to be conducted to understand the process of oxide formation and factors affecting its formation in irradiated austenitic stainless steel material.

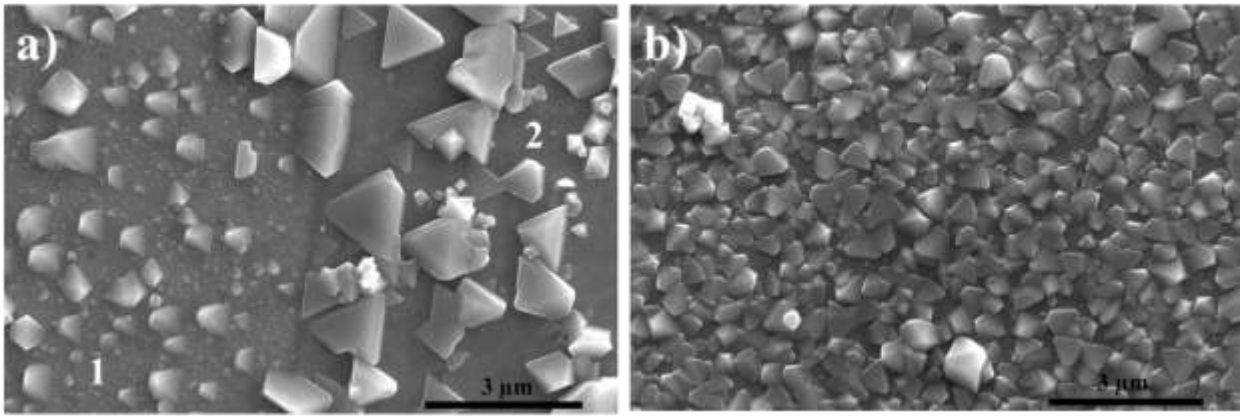

Figure 3-41 : TEM images of the irradiated regions of a) 10 dpa – Fe b) 2 dpa – H samples displaying the difference in the morphology of outer oxide observed on two sample after 360 h oxidation test in 5L autoclave. Grains marked 1 and 2 in a) show the effect of crystallographic orientation of underneath grain on the morphology of outer oxide crystallite formed.

From these results, it is apparent that irradiation increased the degree of localization and modified the oxide formation in SA 304L. These changes (excluding the effect of RIS in this study) could lead to grain boundaries being more embrittle in irradiated material resulting in higher density of cracks compared to unirradiated material. However, within the irradiated region not all the grain boundaries cracked indicating there must be some conditions to be fulfilled by a grain boundary to crack.

- Cracking Criterion

As stated before, cracks and slip lines were observed in the gauge length of tensile samples following SSRT test. Based on the interaction of slip lines with grain boundaries, crack sites were categorized into two categories: continuous interaction (transfer of slip across the boundary) and discontinuous interaction (no evident transmission of slip across the boundary). Amongst all the cracked grain boundaries observed, 30 – 40 % belonged to continuous interaction while 50 – 60 % belonged to discontinuous category. Around 10 % belonged to the category where no slip lines were observed on either side of the cracked grain boundary. In case of discontinuous interaction, the high stress buildup at the grain

boundary occurs due to dislocation pile up which increases the susceptibility of the grain boundary to cracking and hence, slightly higher number of cracks sites belonged to this category. These results are consistent with the findings of McMurtrey [19]. But based on these results, it could be conclude that discontinuous interaction is not a sufficient criterion.

McMurtrey and West [17, 18] proposed that in the irradiated austenitic stainless steel strained in supercritical water and BWR (Boiling Water reactor) environment, RHAB grain boundaries which are inclined at higher angles (greater than 70 °) with respect to tensile direction and adjacent to grains with low Schmid Factor (SF) are more prone to slip discontinuity (i.e. least likely to accommodate strain) and hence, most susceptible to cracking. The criteria was verified on 5 dpa – Fe and 2 dpa – H samples for the irradiation and straining conditions (in PWR environment) used in this study. It was found that amongst the total cracked grain boundaries, only 30 – 40 % fulfilled this criterion. This means that for the rest 60 – 70 % of the cracks, either of the condition was not satisfied suggesting these conditions are not necessary conditions to explain IGSCC of irradiated austenitic stainless steel in PWR environment. Millier [3] has previously reported to observe similar results and hypothesize that the local stress state has a better reciprocity with cracking susceptibility than local deformation state. But this hypothesis is yet to be validated.

Finally, all the above results suggests that not only proton but iron irradiation can also be used to study the cracking susceptibility of irradiated austenitic stainless steel.

3.6. CONCLUSIONS

The vibro polished irradiated SA 304L stainless steel samples were used to study the impact of irradiation on the IASCC susceptibility of the material. As IASCC is the irradiation enhanced SCC, irradiation, stress and environment are the prerequisite conditions. Impact of irradiation on the microstructure of the material has been described previously (see § 2.3). Irradiated and unirradiated samples were subjected to SSRT with a strain rate of 5×10^{-8} s^{-1} upto a plastic deformation of 4 % in stainless steel autoclave. This resulted in the appearance of slip lines and intergranular cracks in the gauge length of the samples tested in corrosive environment. No cracks were observed on the 5 dpa – Fe sample strained in inert environment. Quantitative assessments performed in the unirradiated and irradiated regions (both proton and iron irradiated) of the samples strained in PWR environment revealed that the irradiation highly enhanced the crack density. The mean crack length in material was higher as well for the irradiated samples compared to unirradiated sample. Increase in degree of localization (accounted by slip line spacing measurements) was observed with irradiation in all the samples which

correlates with the higher cracking susceptibility. Degree of Localization was higher in 2 dpa – H sample compared to 10 dpa – Fe sample. Hence, a similar density of cracks was observed in the two samples despite different doses. However, no cracking despite same degree of localization in case of 5 dpa – Fe samples tested in argon suggested that for the irradiation and straining conditions used in the study, localized deformation was not self-sufficient to initiate the cracks in the material.

To characterize the effect of corrosive environment, TEM investigation of FIB prepared samples was conducted. Oxide formed on both the samples was duplex in nature consisting of a Fe rich outer oxide and Cr rich continuous inner oxide. The outer oxide crystallites were bigger on unirradiated sample. Inner oxide was thicker as well on this sample. Higher Cr enrichment in the inner layer formed on unirradiated sample suggested the inner oxide was more protective on unirradiated sample. This is in accordance to the lower density of cracks observed in the irradiated region of the sample. However, no direct correlation could be drawn as only bulk oxidation was studied. To further investigate the effect of irradiation on oxidation kinetics, oxidation test was conducted on unirradiated and irradiated bars in stainless steel autoclaves in simulated PWR water at 340 °C for 360 hrs. Tests revealed that the outer oxide crystallites were bigger on unirradiated sample. A thicker and more Cr enriched inner layer was observed in irradiated sample. Difference in the morphology of outer oxide, thickness of inner oxide, enrichment of Cr was observed for different irradiation ions and different volume of corrosive media. As majority of these results were based on single TEM observations, they did not accounted for the effect of grain orientation. This suggests that further work needs to be done in this field to have concluding results.

Though the exact role of oxidation is not clear, it has been demonstrated that presence of corrosive environment and degree of localization influences the IGSCC susceptibility of irradiated as well as unirradiated austenitic stainless steel. To understand the cracking mechanism, several crack sites were investigated. Based on the interaction of slip lines with grain boundaries, these sites were categorized as continuous and discontinuous interactions. Around 50 – 60 % of the total crack sites characterized belonged to discontinuous interaction while 30 – 40 % belonged to continuous interaction. This suggests that grain boundary across which transfer of slip does not occur has more chances of cracking. In few (≤ 10 %) crack sites, no slip lines were observed in the vicinity of the cracked grain boundaries. Apart from these crack sites, few interrupted small cracks were observed as well. Criterion proposed by McMurtrey and West [18, 19] was then validated for the tests conducted on ion irradiated austenitic stainless steel in PWR environment. For the purpose, an area of 0.1 mm² in the irradiated region of both iron and proton irradiated samples was analyzed using EBSD. It was observed that a very small fraction of the total cracked grain boundaries fulfilled the conditions of criterion which included angle between the surface trace of cracked grain boundary and loading

direction greater than 70 °, cracked grain boundary neighboring at least a grain with low SF and lastly slip discontinuity. This suggested that the criterion is not sufficient to describe the cracking mechanism. A better criterion needs to be worked on.

From all the results of this chapter, it could be deduced that iron irradiation was able to signify impact of irradiation on all parameters (such as crack density, localized deformation, oxidation kinetics) with similar trends as observed after proton irradiation and as has been reported post to neutron and proton irradiation in literature. This means Fe irradiation can be used for IASCC susceptibility studies despite its shallow penetration depths in austenitic stainless steel.

REFERENCES

1. T. S. Byun, N. Hashimoto, K. Farrell,"Temperature dependence of strain hardening and plastic instability behaviors in austenitic stainless steels", Acta Mat. 52 (2004) 3889 – 3899.
2. M. N. Gussev, K.G. Field, J. T. Busby, Hashimoto, "Strain induced phase transformation at the surface of an AISI – 304 stainless steel irradiated to 4.4 dpa and deformed to 0.8 % strain", J. Nucl. Mat. 446 (2014) 187 – 192.
3. M. Millier, "Fragilisation des aciers inoxydables austénitiques sous irradiation: évolution de la microstructure et amorçage de la corrosion sous contrainte assistée par l'irradiation en milieu REP", PhD Thesis, Mines Paris Tech, (2014).
4. E. A. West, "Influence of local stress and strain on intergranular cracking of 316L stainless steel in supercritical water", PhD Thesis, University of Michigan, (2010).
5. Z. Jiao, G. S. Was, "Impact of localized deformation on IASCC in austenitic stainless steels", J. Nucl. Mat. 408 (2011) 246 – 256.
6. Z. Jiao, G. S. Was, "Localized deformation and IASCC initiation in austenitic stainless steels", J. Nucl. Mat. 382 (2008) 203 – 209.
7. T. Miura, K. Fujii, K. Fukuya, Y. Ito, "Characterization of deformation structure in ion irradiated stainless", J. Nucl. Mat. 386 – 388 (2009) 210 – 213.
8. T. Miura, K. Fujii, H. Nishioka, K. Fukuya, "Effects of hydrogen on interaction between dislocations and radiation-induced defects in austenitic stainless steels", J. Nucl. Mat. 442 (2013) S735 – S739.
9. Z. Jiao, G. S. Was, T. Miura, K. Fukuya, "Aspects of ion irradiations to study localized deformation in austenitic stainless steels", J. Nucl. Mat. 452 (2014) 3228 – 334.
10. R. Soulas, "Effet de la cristallographie sur les premiers stades de l'oxydation des aciers austénitiques 316 L", PhD Thesis, Université de Grenoble (2012).
11. D. H. Lister, R. D. Davidson, E. McAlpine, "The mechanism and kinetics of corrosion products release from stainless steel in lithiated high temperature water", Corr. Sci. 27 (1987) 113 – 140.
12. J. Robertson, "The mechanism of high temperature aqueous corrosion of stainless steels", Corr. Sci. 32 (1991) 443 – 465.
13. S. Perrin, L. Marchetti, C. Duhamel, M. Sennour, F. Jomard, "Influence of irradiation on the oxide film formed on 316 L stainless steel in PWR Primary water", Oxidation of Metals 80 (2013) 623 – 633.
14. M. Dumerval, "Effet des défauts d'implantation sur la corrosion des aciers inoxydables austénitiques en milieu primaire des réacteurs à eau pressurisée", PhD. Thesis, Université de Grenoble, (2014).
15. S. Cissé, L. Laffont, B. Tanguy, M-C. Lafont, E. Andrieu, "Effect of surface preparation on the corrosion of austenitic stainless steel 304L in high temperature steam and simulated water", Corr. Sci. 56 (2012), 209-216.

16. H. Nishioka, K. Fukuya, K. Fujii, Y. Kitsunai, “Deformation structure in highly irradiated stainless steels”, J. Nucl. Sci. and Tech. 45 (2008) 274 – 287.
17. M.D. McMurtrey, G.S. Was, L. Patrick, D. Farkas, “Relationship between localized strain and irradiation assisted stress corrosion cracking in austenitic alloy”, Current Opinions in Solid State and Mater. Sci. 19 (2015) 305 – 314.
18. E. A. West, G. S. Was, “Strain incompatibilities and their role in intergranular cracking of irradiated 316 L stainless steel”, J. Nucl. Mat. 441 (2013) 623 – 632.
19. M.D. McMurtrey, G.S. Was, L. Patrick, D. Farkas, “Relationship between localized strain and irradiation assisted stress corrosion cracking in austenitic alloy”, Mater. Sci. Eng. A 528 (2011) 3730 – 3740.

CHAPTER 4. EFFECT OF SURFACE FINISH ON THE CRACKING SUSCEPTIBILITY

4.1. INTRODUCTION

Different surface finishes results in different modifications in the microstructure at subsurface of the material. For example, in chapter 2 it has been shown that subsurface of mechanically polished SA 304L consisted of surface hardened area comprising of nanograins [1]. Whereas the microstructure of vibratory polished SA 304L consisted of standard – size grains with no affected layer at the surface. Difference in the density of irradiation induced defects was also observed as a consequence of this different resulting microstructure. This raises a question of relation between surface finish and the cracking susceptibility of irradiated material as IGSCC initiation is a surface phenomenon. For unirradiated austenitic stainless steel, it has been demonstrated that presence of surface hardened layer increases the internal stresses thereby increasing the susceptibility to intergranular cracking in different corrosive environments [2, 3]. But there is a lack of study in literature demonstrating the effect of surface finish on the cracking susceptibility (or IGSCC) of the irradiated materials in PWR environment. Moreover, the material used in core internals of PWR should have a surface hardened layer due to machining. But majority of the studies conducted in laboratories to investigate the cracking susceptibility of the ion irradiated material employs electro polished samples. These samples are free of any surface hardened layer. In order to be able to link the laboratory results with the actual PWR scenario, it is mandatory to have information on the possible effect of surface finish on IGSCC and different contributing factors of IGSCC. In this chapter, efforts were made to address this issue by incorporating materials with two different surface finishes namely, mechanically polished (i.e. material with surface hardened layer [1]) and vibratory polished (i.e. material with standard-sized-grains).

Samples that will be used for the purpose include unirradiated vibratory polished, unirradiated mechanically polished, 10 dpa – Fe (mech.) and 10 dpa – Fe samples. Sample preparation techniques and irradiation conditions are described in Appendix A.1.2.1 and § 2.3.1.2 respectively. In 10 dpa – Fe sample entire irradiation depth was within standard sized grains. Whereas in 10 dpa – Fe (mech.) sample, surface hardened layer was present on the surface of standard-sized-grained material because of which some portion (mainly the irradiated surface) of the irradiated area was within the recrystallized area (Figure 4-1). SSRT (Slow Strain Rate Test) in simulated PWR primary water environment was conducted on 10 dpa – Fe and 10 dpa – Fe (mech.) samples. Tests were interrupted on obtaining a plastic strain of 4%.

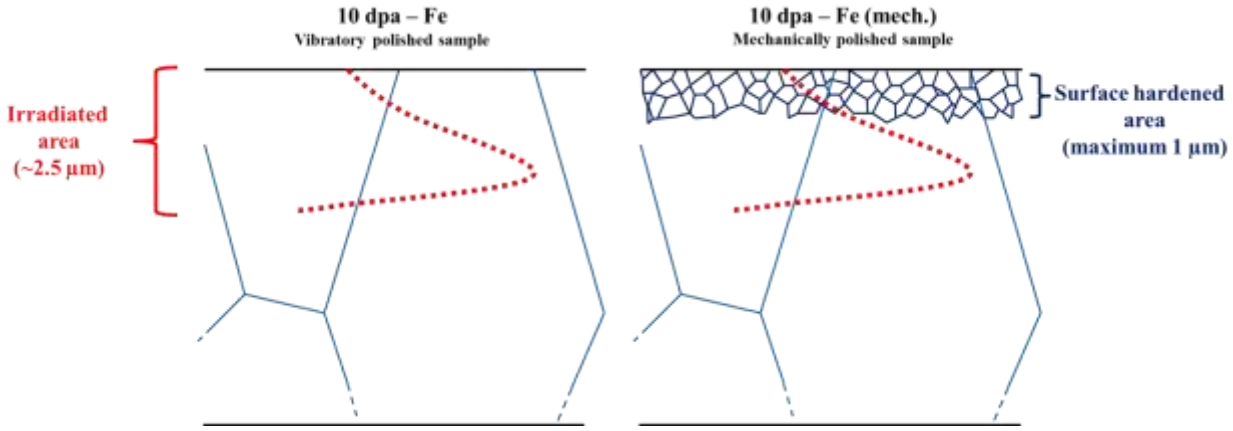

Figure 4-1 : Schematics illustrating the extent of irradiated area in 10 dpa – Fe and 10 dpa – Fe (mech.) sample. Damage profile is shown in red (in dots) and grain boundaries are shown in blue.

First part of this chapter details the changes in the propensity to cracking observed in vibratory polished and mechanically polished material after iron irradiation. It includes comparing the crack densities for unirradiated[20] and irradiated material and for different surface finishes. Factors such as localized deformation and oxidation kinetics were examined and are detailed subsequently. Degree of localization was estimated by calculating the spacing between adjacent slip lines. Oxidation test was conducted on unirradiated and irradiated samples in stainless steel autoclave at 340 °C in simulated PWR primary water environment. The oxide formed on the samples was characterized using SEM (Scanning Electron Microscope) and TEM (Transmission Electron Microscope). Effects of different surface finishes and irradiation on oxide formation are discussed in last section.

4.2. IMPACT ON CRACKING SUSCEPTIBILITY

The irradiated tensile samples were subjected to Slow Strain Rate Test with a strain rate of 5×10^{-8} s^{-1} upto a plastic deformation of 4 %. Tests were conducted at 340 °C in simulated PWR primary water environment. Details of the tests are given in § 3.2. After straining, the surface analysis of the samples was performed using FEI Helios 650 NanoLab Dual Beam FIB under SEM mode. Results of these surface analyses are detailed in the following sections.

4.2.1. QUALITATIVE ANALYSIS

Numerous intergranular cracks were observed in the irradiated region of the 10 dpa – Fe sample during SEM surface analysis of the gauge length of the sample following straining. The unirradiated region of the sample was observed to contain few cracks.

[20] Unirradiated region of irradiated tensile samples.

Surface morphology of the unirradiated and irradiated regions of 10 dpa – Fe sample sufficiently represented the drastic difference in intergranular crack density observed in the two regions. SEM surface analysis done on 10 dpa – Fe (mech.) sample also revealed the presence of few cracks in unirradiated region. Intergranular cracks in the irradiated region of the sample were observed as well. As could be seen in Figure 4-2, it was difficult to assess from qualitative surface analysis of the sample if irradiation modified the cracking susceptibility of the material in any manner.

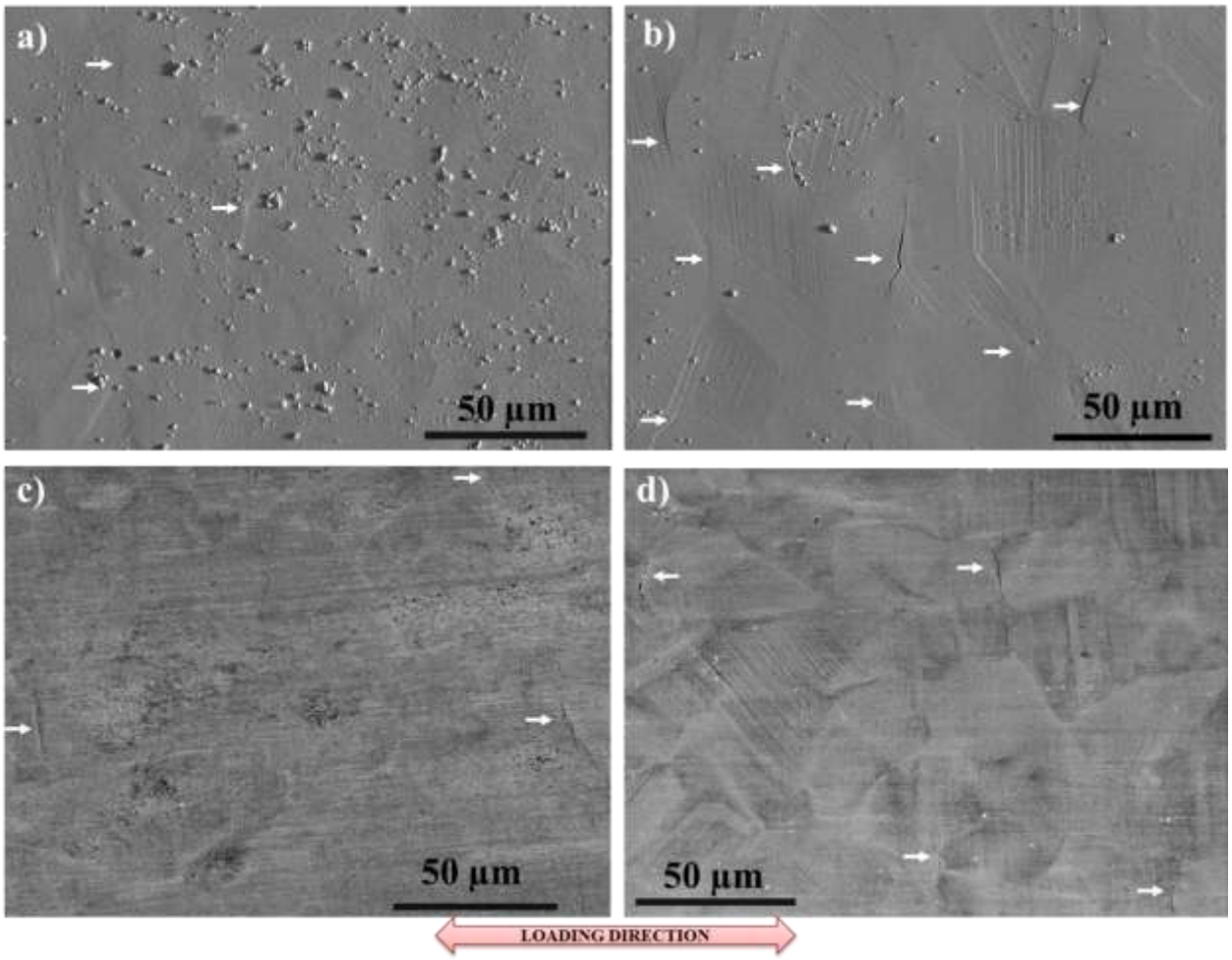

Figure 4-2 : SEM images taken under BSE (Back Scattered Electron) mode in a) unirradiated b) irradiated regions of 10 dpa – Fe sample and c) unirradiated d) irradiated regions of 10 dpa – Fe (mech.) sample[21] after straining. Cracks are marked by white arrows. Loading direction is indicated in the figure.

Comparison of the irradiated regions of the samples suggested that the crack density was much higher in 10 dpa – Fe sample than in 10 dpa – Fe (mech.). Cracks in the irradiated region of 10 dpa – Fe sample also appeared to be wider (opening of the crack). For clarification, SEM images with higher resolution are shown in Figure 4-3. Though

[21] The samples were not re-polished after the SSRT test to remove oxide layer developed on the surface. Presence of this layer somewhat deteriorated the quality of images captured.

quantitative assessment was done to obtain crack density and crack length distribution, no assessment of width and depth of cracks was done in this study.

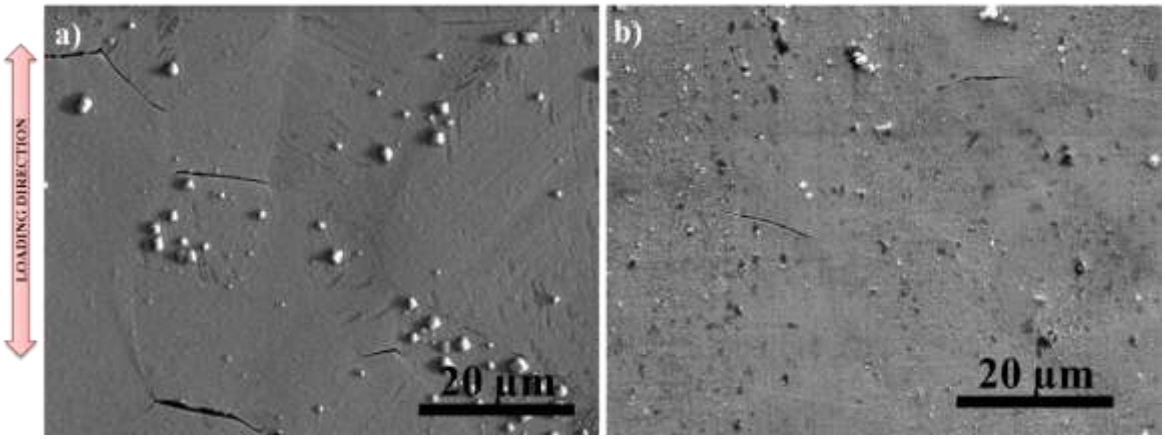

Figure 4-3 : Crack micrographs of irradiated region of a) 10 dpa – Fe (taken in BSE mode) b) 10 dpa – Fe (mech.) (taken in SE mode) samples after straining to 4% plastic strain in simulated PWR environment. Loading direction is indicated in the image.

4.2.2. QUANTITATIVE ANALYSIS

For quantitative information, crack density and crack length distributions calculations were performed in the same manner as described in §3.2.2. It included taking SEM images at high resolution (i.e. Horizontal Full Width of 118 µm) along 1 mm² area within the central region of the sample, making a montage of these images using Photoshop software and using ImageJ software to estimate the length of the cracks. The data on crack length thus obtained was converted to a crack length distribution profile which provided the mean crack length. On each sample, 2 areas of 1 mm² were scanned in both unirradiated and irradiated regions. The mean crack density and mean crack length along with error was estimated from the two values[22].

As shown in § 3.2.2, crack density of 64 ± 12 cracks/mm² and 293 ± 18 cracks/mm² was obtained for the unirradiated and irradiated region of the 10 dpa – Fe sample. While the maximum length of cracks observed in the unirradiated region was 30 µm, cracks as long as 60 µm were observed in the irradiated region of the sample. Comparison of the crack length distribution for the two regions indicated that irradiation increased the mean crack length.

From the 1 mm² areas scanned in the central region of the unirradiated portion of the 10 dpa – Fe (mech.) sample, a crack density of 82 ± 6 cracks/mm² was obtained. A large percentage of cracks (around 44 % of the total cracks) had length ≤ 5 µm and a mean crack length of 8 ± 1 µm was obtained for this region. Similar analysis performed in the

[22] Values and distributions obtained for two areas were similar and hence, using a mean value is justified.

irradiated region of the 10 dpa – Fe (mech.) sample gave a crack density of 115 ± 9 cracks/mm² and a mean crack length of 11 ± 1 µm implying a slight increase in crack density with irradiation. Crack length distribution (Figure 4-4) was shifted to higher values for irradiated region in comparison to that for unirradiated region. This indicates that for 10 dpa – Fe (mech.) sample, irradiation increased the crack length. Indeed, in comparison to 44 % (in unirradiated region), only 20 % of the total cracks in irradiated region had a crack length ≤ 5 µm. Also evident from this quantitative data, crack density in 10 dpa – Fe (mech.) sample was marginally higher (~ 40 %) in the irradiated region indicating a trend of increase in cracking susceptibility with irradiation, trend same as that observed in 10 dpa – Fe.

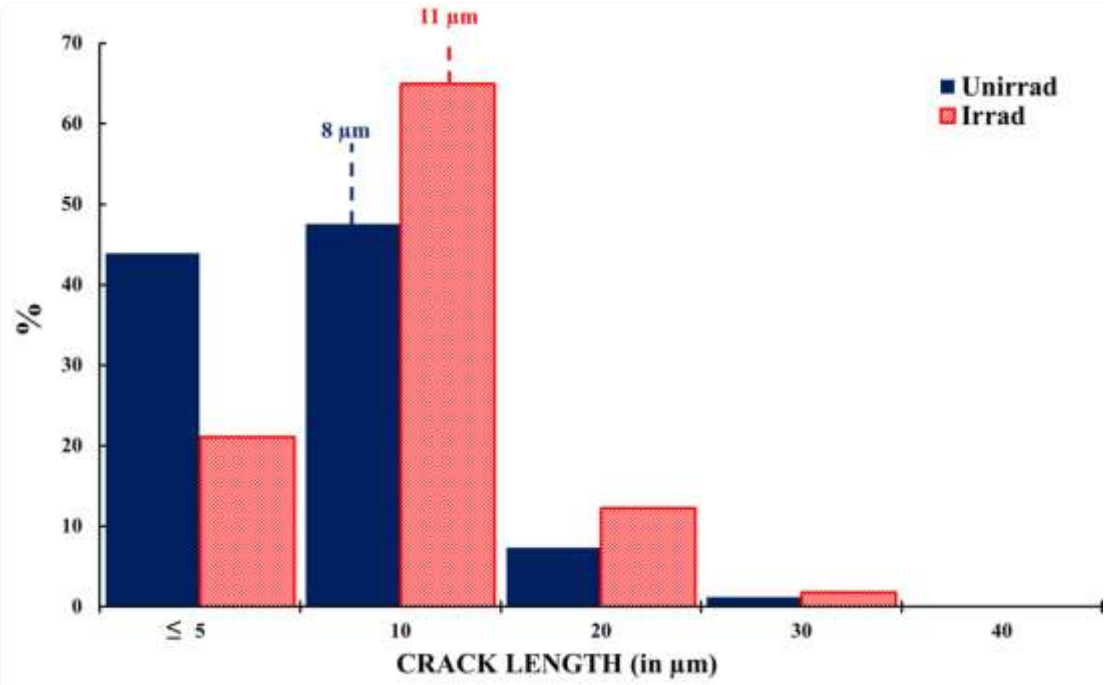

Figure 4-4 : Crack length distribution obtained for the unirradiated (in red) and irradiated (in blue) regions of 10 dpa – Fe (mech.) sample.

Table 4-1 summarizes the results obtained for vibratory polished 10 dpa – Fe sample and for the mechanically polished sample (i.e. 10 dpa – Fe (mech.)). Comparing the crack density in the unirradiated region of the two samples, density slightly higher (~ 28%) was observed for 10 dpa – Fe (mech.) sample. It is attributed to the increase in internal stresses due to surface hardening as has been reported in literature as well [2, 3]. On contrary, in the irradiated region of 10 dpa – Fe and 10 dpa – Fe (mech.) sample smaller crack density and mean crack length values were observed in 10 dpa – Fe (mech.) sample. The possible explanation for this contrary trend observed in unirradiated and irradiated samples is discussed later (in section 4.4). Similar crack length distribution was obtained for the irradiated region of 10 dpa – Fe and 10 dpa – Fe (mech.) samples as is shown in Figure 4-5. Clearly, no crack longer than 30 µm was observed on 10 dpa – Fe (mech.) sample,

unlike on 10 dpa Fe sample. This indicates that the presence of surface hardened layer in irradiated region decreased the crack density as well as shortens the mean crack length.

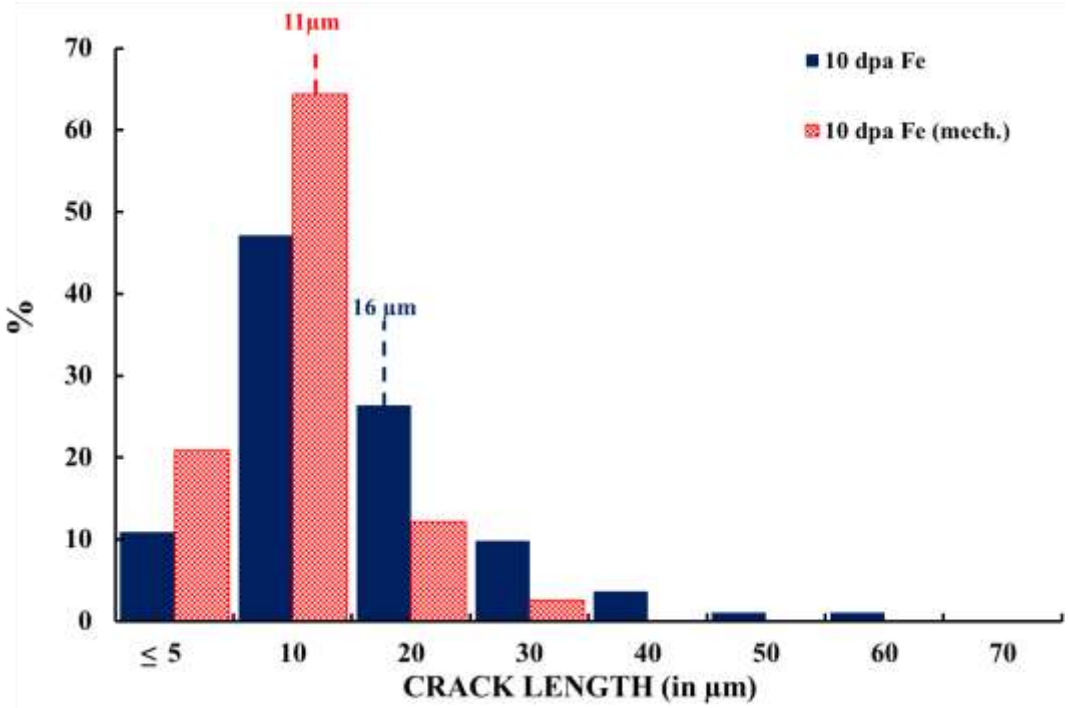

Figure 4-5 : Crack length distribution obtained for the irradiated regions of 10 dpa – Fe (in blue) and 10 dpa – Fe (mech.) (in red).

Sample	Unirradiated region		Irradiated region		% increase in cracking susceptibility with irrad (in %)
	Crack density (cracks/mm²)	Mean crack length (µm)	Crack density (cracks/mm²)	Mean crack length (µm)	
10 dpa – Fe	64 ± 12	12 ± 2	293 ± 18	16 ± 2	360
10 dpa – Fe (mech.)	82 ± 6	8 ± 1	115 ± 9	11 ± 1	40

Table 4-1 : Comparison of the quantitative analysis performed in the unirradiated and irradiated regions of 10 dpa – Fe and 10 dpa – Fe (mech.) samples.

Also, an increase in intergranular cracking susceptibility after iron irradiation was observed for both 10 dpa – Fe (mech.) and 10 dpa – Fe samples. This implies that irrespective of surface state, likelihood of material to intergranular cracking always increases with irradiation. However, cracking was much less severe in irradiated material with surface hardened layer. To have a better overview of these results, it was necessary to acknowledge the effect of surface state on localized deformation and on oxidation state. As done in chapter 3, effect of surface state on localized deformation and hence, its

correlation with the cracking susceptibility of the material was investigated and is detailed in following section.

4.2.3. LOCALIZED DEFORMATION

Surface examination of the gauge length of SSRT tested samples revealed the presence of fine slip lines in unirradiated (Figure 4-6) and irradiated regions of both 10 dpa – Fe and 10 dpa – Fe (mech.) samples. As explained in chapter 3, these lines result when deformation bands intersect the free surface [4]. Quantitative information was acquired by measuring the slip line spacing (i.e. the distance between two consecutive slip lines) using imageJ software. In general, the slip lines in the unirradiated region were more closely spaced than in irradiated region of these samples. To obtain a good statistics, slip line spacing measurements were done on around 25 different grains for each condition. A range of spacing values was obtained (Figure 4-6a), so a distribution was plotted for each condition.

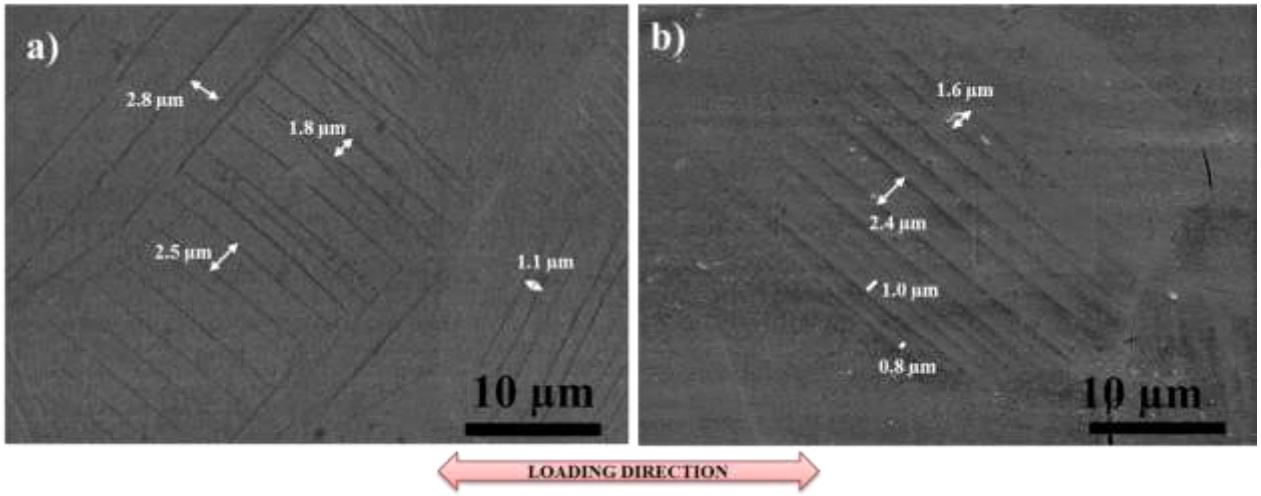

Figure 4-6 : BSE-SEM images of the irradiated region of a) 10 dpa – Fe b) 10 dpa – Fe (mech.) samples demonstrating the slip lines observed on the surface of these sample after straining. Few inter line spacing are indicated by white arrows.

Mean slip line spacing obtained for unirradiated and irradiated regions of 10 dpa – Fe samples were 0.9 ± 0.2 µm and 1.7 ± 0.1 µm respectively. This indicates an increase in slip line spacing with irradiation in agreement to what has been reported in literature [5] for helium ion irradiated SA 304 SS. The slip line spacing distribution was wider as well for the irradiated region indicating that deformation in irradiated region was more localized compared to unirradiated region.

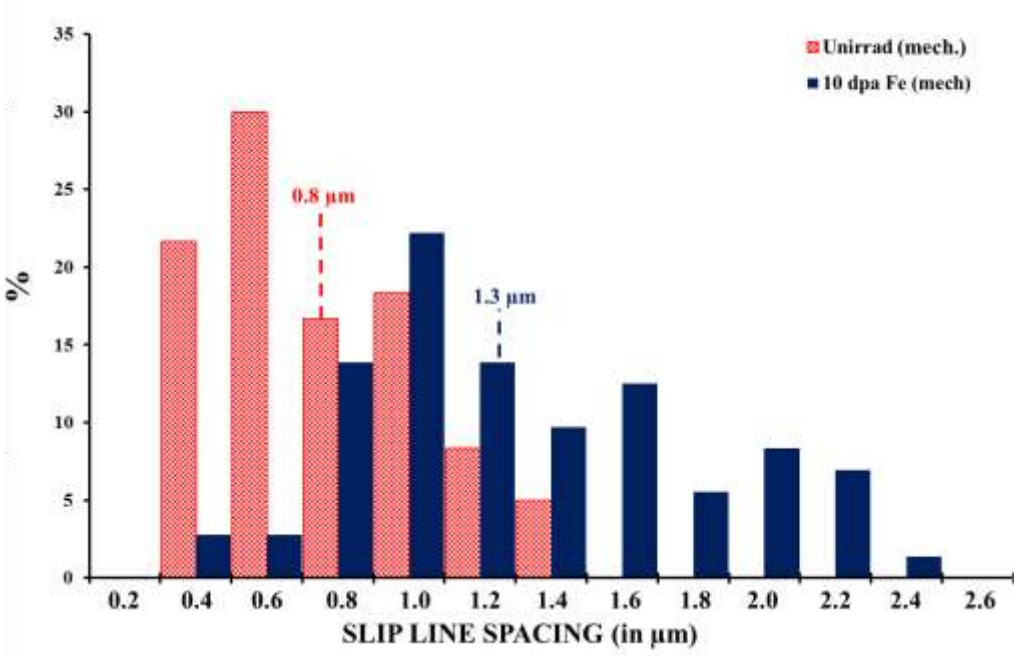

Figure 4-7 : Slip line spacing distribution for the unirradiated (in red) and irradiated (in blue) regions of 10 dpa – Fe (mech.) sample. Mean slip line spacing values for each region are indicated by dashed lines.

Similar analysis conducted on the unirradiated and irradiated regions of 10 dpa – Fe (mech.) sample yielded mean slip line spacing values of 0.8 ± 0.2 µm and 1.3 ± 0.1 µm respectively. An increase in spacing with irradiation was observed in this sample. Comparison of slip line spacing distribution obtained for the unirradiated and irradiated regions of this sample is shown in Figure 4-7. As evident, in comparison to unirradiated region, the distribution for irradiated region was shifted to higher values.

The mean slip line spacing values for the unirradiated regions of 10 dpa – Fe and 10 dpa – Fe (mech.) samples were very similar. Slip line spacing distribution obtained for the two samples was very similar as well (Figure 4-8). Comparison of slip line spacing distribution for the irradiated regions of 10 dpa – Fe and 10 dpa – Fe (mech.) samples is shown in Figure 4-9. The mean spacing value for the sample was higher in comparison to 10 dpa – Fe (mech.) sample. It is also clear from the Figure 4-6 that the slip lines were slightly widely spaced in 10 dpa – Fe sample.

These results suggest no effect of surface hardened layer on slip line spacing value for unirradiated material. On contrary, in irradiated materials, presence of surface hardened layer decreases the value. The correlation of these observations with the cracking susceptibility is discussed in §4.4. Clearly, surface state has an influence on the cracking susceptibility and localized deformation of irradiated material. To answer, whether or not, it can influence the oxidation of austenitic stainless, oxidation test was carried out. The results of this test are detained in following section.

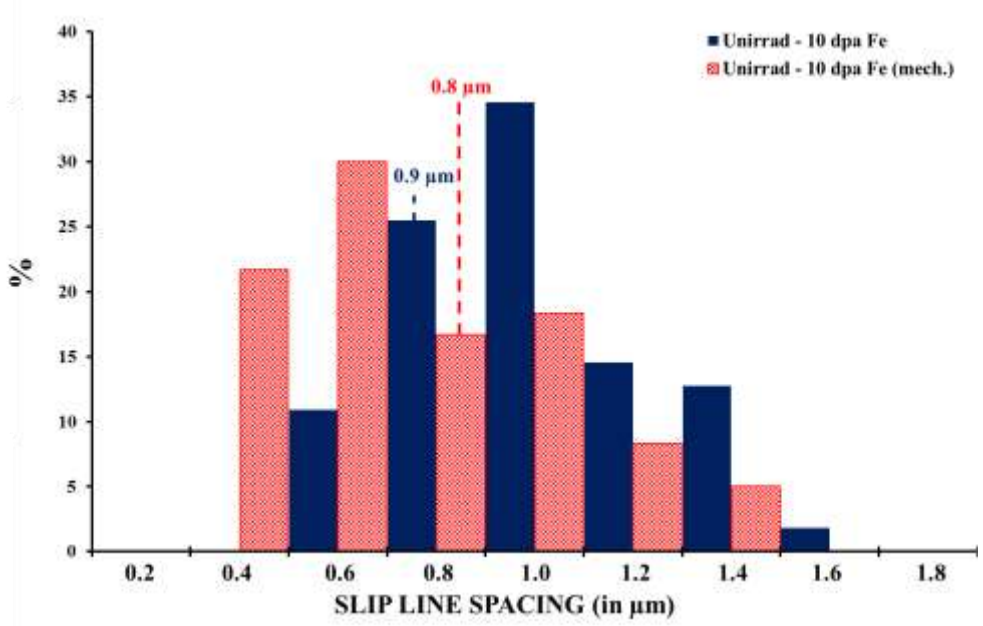

Figure 4-8 : Slip line spacing distribution obtained for the unirradiated region of 10 dpa – Fe (in blue) and 10 dpa – Fe (mech.) (in red) sample. Mean slip line spacing values for each region are indicated by dashed lines.

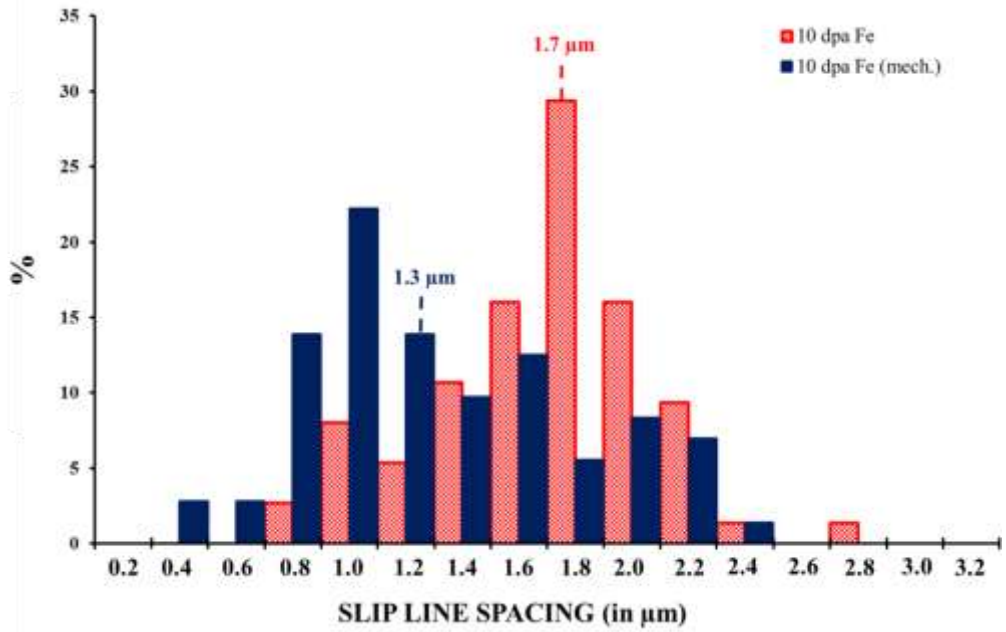

Figure 4-9 : Comparison of the slip line spacing distribution obtained for the irradiated region of 10 dpa – Fe (in red), 10 dpa – Fe (mech.) (in blue) samples. Mean slip line spacing values are indicated by dashed lines.

4.3. OXIDATION KINETICS

Oxidation test on the unirradiated and irradiated bars was conducted in simulated PWR primary water environment in static stainless steel autoclaves of capacity 0.38 L. Samples

that will be addressed in this section include unirradiated vibratory polished, unirradiated mechanically polished and 10 dpa – Fe (mech.)[23] sample. Detailed procedure of the oxidation test is given in §3.3. Test was conducted at 340 °C in simulated PWR primary water environment and continued for 360 h (or 15 days). On completion of the test, oxide formed on the samples was characterized using SEM and TEM (Transmission Electron Microscope). FEI Helios 650 NanoLab Dual Beam FIB under SEM mode was used to perform the surface examination of the samples. JEOL 2100F TEM operated at 200 kV and equipped with EDS spectrometer was used for in-depth investigations. Note that only bulk oxidation will be addressed here and hence, correlation of oxidation with intergranular cracking will not be drawn.

4.3.1. IMPACT OF SURFACE FINISH ON THE OXIDATION OF AUSTENITIC STAINLESS STEEL

To account for the effect of surface hardened layer on the oxide formation, unirradiated vibratory polished and unirradiated mechanically polished samples were examined. SEM surface analysis revealed that the bigger crystallites were observed on vibratory polished sample compared to the mechanically polished sample (Figure 4-10). This implies that the presence of surface hardened layer in mechanically polished sample had an influence on the morphology of outer oxide crystallites formed on the surface of the sample. To investigate further, cross-sectional TEM foils were prepared (§ appendix A.1.2.2.2) from the unirradiated vibratory polished and unirradiated mechanically polished sample and subsequently characterized using TEM.

As demonstrated in § 3.3.1, outer oxide formed on vibratory polished sample consisted of Fe rich facetted crystallites of size ranging between 20 – 100 nm and few small crystallites of size (5 – 20 nm). Big facetted crystallites were indexed as magnetite ($FeFe_2O_4$) with chemical composition of 51 at% of O, 42 at% Fe, 3 at% Cr and 4 at% Ni. Smaller crystallites had slightly higher Cr content and were indexed as $Fe,NiCr_2O_4$ spinel. The continuous Cr enriched inner layer was 5 – 6 nm thick on this sample and the crystallites of this layer were indexed as spinel as well.

[23] Only irradiated regions of the irradiated samples were characterized during oxidation analysis.

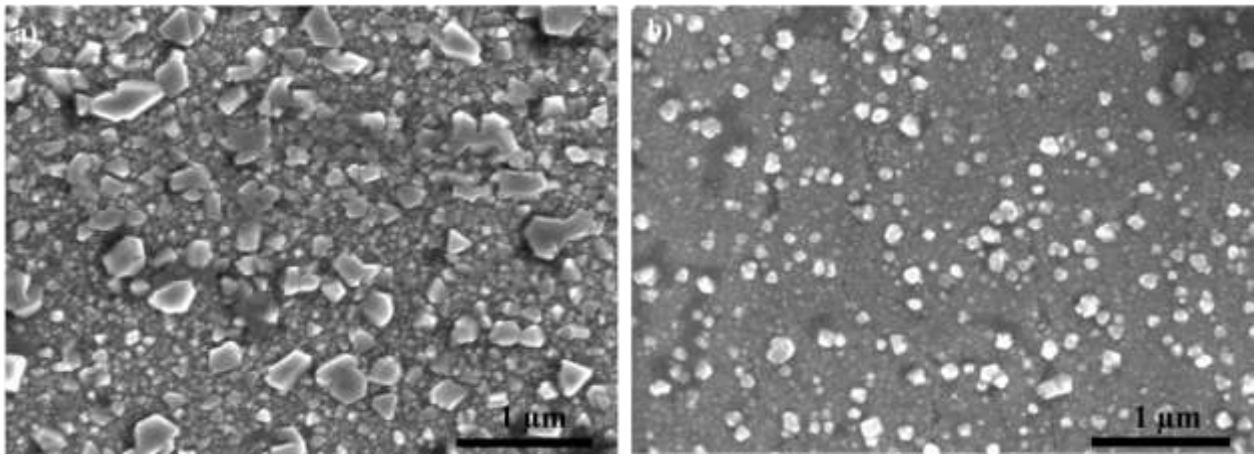

Figure 4-10 : SEM micrographs of a) unirradiated vibratory polished b) unirradiated mechanically polished samples oxidized in 0.38L stainless steel autoclave for 360 h in simulated PWR primary water environment.

The cross-sectional view of the oxide layers observed along a length of 1.2 µm on the unirradiated mechanically polished sample is reported in Figure 4-11a. Like in vibratory polished sample, the oxide formed on the mechanically polished sample is duplex in nature as well indicating that the presence of surface hardened layer did not alter the nature of oxide layers formed. Outer oxide consisted of facetted crystallites whose size ranged between 10 and 35 nm. The chemical composition of these crystallites estimated using the EDX analysis was 19 at% O, 67 at% Fe, 13 at% Cr and 1 at% Ni. The continuous, Cr enriched inner oxide layer observed was estimated to be around 10 – 12 nm thick and had a chemical composition of 16 at% O, 36 at% Fe, 47 at% Cr and 1 at% Ni. The FFTs (Fast Fourier Transforms) obtained for the HRTEM images of both outer and inner oxide layers indexed the crystallites of the two layers to be spinel with composition close to $(Fe,Ni)Cr_2O_4$. The substrate observed beneath the duplex oxide layer consisted of surface hardened layer which extended upto a depth of 650 nm. The chemical composition of few nanograins of this layer was estimated to be 1 at% O, 68 at% Fe, 28 at% Cr and 3 at% Ni using EDX analysis and they were indexed as BCC suggesting they corresponded to ferrite nanograins highly depleted in Ni and enriched in Cr. Details of the duplex oxide layers formed on vibratory polished and mechanically polished samples are summarized in Table 4-2.

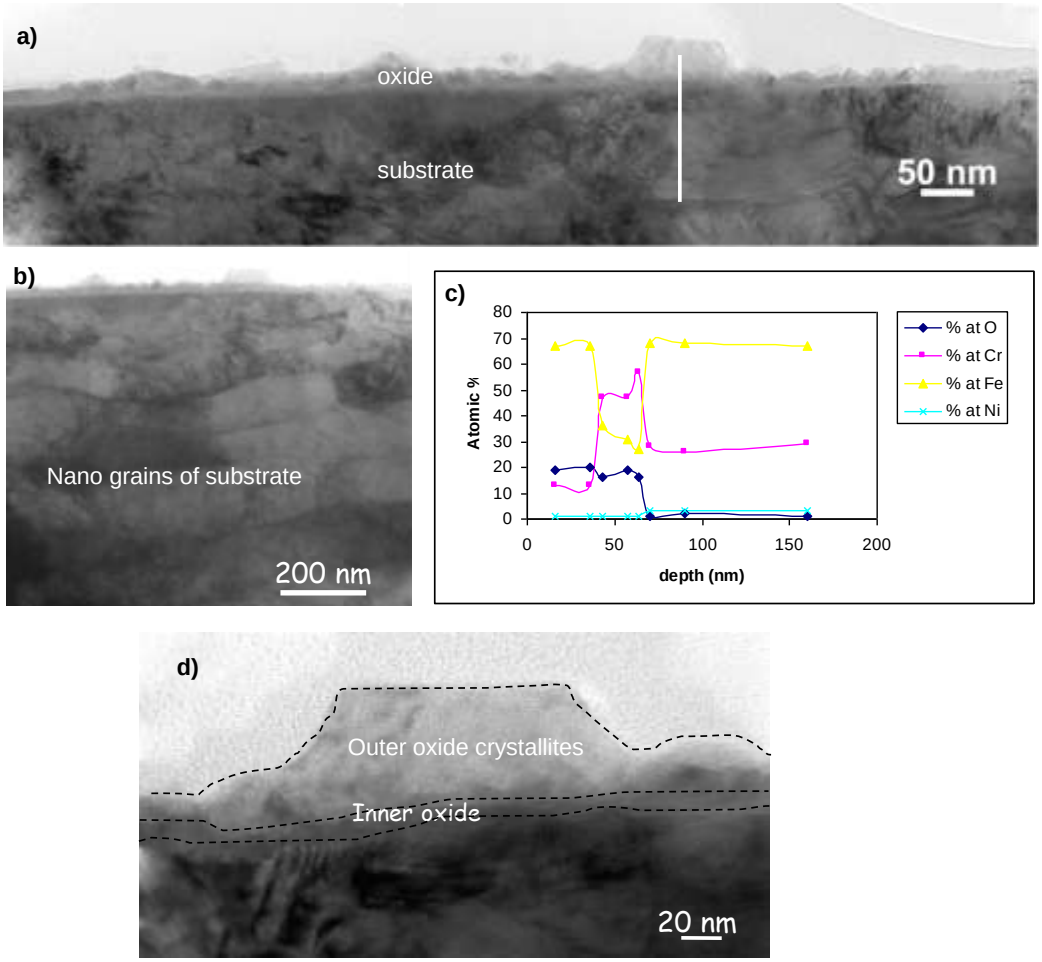

Figure 4-11 : Figure 4-11: BF TEM image of the unirradiated mechanically polished sample of a) the oxide formed, b) the recrystallized area (below the duplex layer) composed of nanograins c) EDX profile showing the evolution of chemical composition along the white line (in a) and d) duplex oxide layer showing the outer and the inner layer.

Sample	Region	Chemical composition			Thickness (nm)
		Cr (relative at. %)	Ni (relative at. %)	Fe (relative at. %)	
Vibratory polished	Outer oxide	6	8	86	20 – 100
		43	9	48	5 - 20
	Inner oxide	48	9	43	5 – 6
	Substrate	21	9	70	–
Mechanically polished	Outer oxide	16	1	83	10 – 35
	Inner oxide	56	1	43	10 – 12
	Substrate (nanograins)	28	3	69	650

Table 4-2 : Comparison of the oxide layers formed on the vibratory polished and mechanically polished unirradiated samples after 360 h oxidation in simulated PWR primary water.

While big crystallites along with few smaller crystallites were observed on vibratory polished sample, only small crystallites were observed on mechanically polished sample. This is in agreement with the SEM observations. Inner layer observed on the vibratory polished sample was thinner (~ 5 – 6 nm) and less enriched in Cr. This implies that the inner oxide layer formed on the unirradiated vibratory polished sample was less protective compared to the layer formed on unirradiated mechanically polished sample. Transport of oxygen and/or metal atoms is faster along grain boundaries compared to diffusion in bulk [6, 7]. Higher volume fraction of grain boundaries in mechanically polished sample would overall enhance the inward diffusion of O and outward diffusion of Fe. This could be one explanation of the observation of thicker inner oxide on the surface of mechanically polished sample. As higher Cr enrichment in the inner layer restricts the growth of outer oxide crystallites so smaller crystallites were spotted on this sample. Note that the nanograins in the substrate were ferrite in case of unirradiated sample and austenite in 10 dpa – Fe (mech.) sample. This implies that the comparison of Cr content of the inner layer in the two samples could be somewhat misleading as the substrate composition was different. Nevertheless, these results demonstrate that the presence of surface hardened layer altered the thickness of oxide layers and Cr enrichment of inner layer.

4.3.2. IMPACT OF IRRADIATION ON OXIDATION OF MECHANICALLY POLISHED AUSTENITIC STAINLESS STEEL

The two samples, i.e. unirradiated mechanically polished and 10 dpa – Fe (mech.) samples were analyzed under SEM which revealed some differences in the morphology of outer oxide crystallites formed on these samples. As illustrated in Figure 4-12 using SEM micrograph, big crystallites along with some small crystallites were observed on the surface of unirradiated sample. On contrary, only a few big crystallites were seen on irradiated sample and it was not possible to comment on the small crystallites as it was difficult to observe them even at higher magnifications.

Detailed in previous section, the size of facetted outer oxide crystallites observed on unirradiated mechanically polished sample ranged between 10 and 35 nm. The inner layer was around 10 – 12 nm thick. Outer oxide crystallites over-laying on the continuous inner layer observed along a length of 1 µm on 10 dpa – Fe (mech.) sample is shown in Figure 4-13. The size of the outer oxide crystallites observed on this sample ranged between 2 – 20 nm. Clearly, the crystallites were very small. Hence, even at very high SEM magnifications, it was very difficult to see the crystallites on 10 dpa – Fe (mech.) sample apart from few big crystallites. EDX TEM analysis gave the chemical composition of these crystallites to be 30 at% O, 42 at% Fe, 23 at% Cr and 5 at% Ni. The inner oxide, on the other hand, was 8 – 15 nm thick and had a chemical composition of 29 at% O, 42 at% Fe, 25 at% Cr and 4 at% Ni. Both inner (Figure 4-13b and c) and outer oxide layer crystallites were indexed to be spinel of type $(Fe,Ni)Cr_2O_4$ using FFTs obtained from the

HRTEM images. And the substrate below the inner layer consisted of surface hardened layer extending upto a depth of 200 – 250 nm. Within this surface hardened layer, chemical composition of few nanograins (present upto a depth of 100 nm from inner oxide – substrate interface) varied between 66-73 at% Fe, 20 at% Cr and 7-14 at% Ni. It indicates a slight enrichment in Ni within this area.

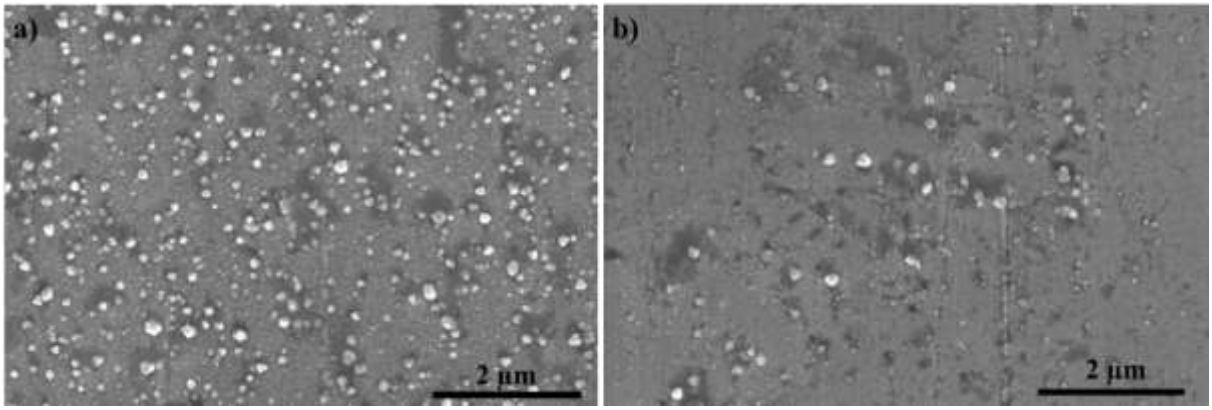

Figure 4-12 : SEM images of the a) unirradiated b) 10 dpa – Fe (mech.) sample illustrating the difference in morphology of outer oxide crystallites observed on the two sample after oxidation in simulated PWR primary water for 360 h.

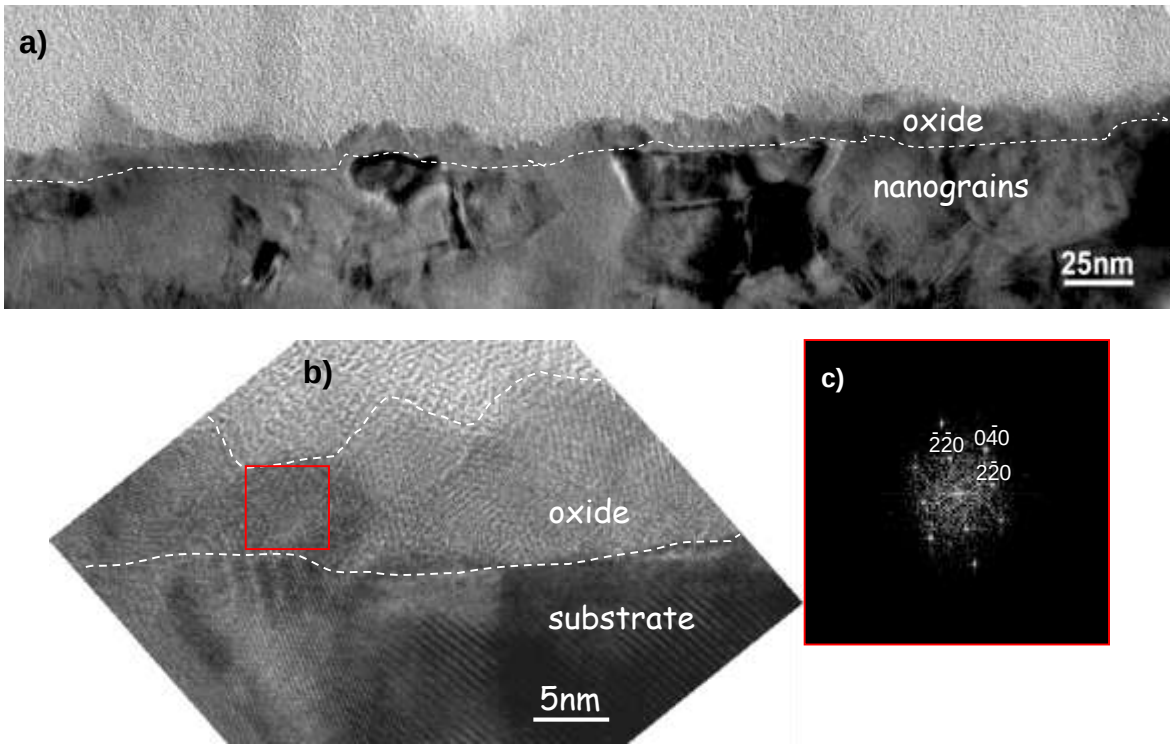

Figure 4-13 : a) BF TEM image of the 10 dpa-Fe (mech.) and b) HRTEM image of the oxides combined with the FFT along the [001] zone axis obtained for the oxide formed on 10 dpa – Fe (mech.) sample.

Table 4-3 summarizes the oxide layers observed on unirradiated mechanically polished and 10 dpa – Fe (mech.) sample. The size of outer oxide crystallites was smaller in irradiated sample indicating decrease in size of crystallites with irradiation. The inner oxide was about the same thickness in the two samples. Inner layer of unirradiated sample was more enriched in Cr making it was more protective compared to its irradiated counterpart. Again, as the oxide layers in unirradiated sample were formed on ferrite nanograins, it is difficult to compare the Cr content of the inner layer formed on the two samples.

Sample	**Region**	**Chemical composition**			**Thickness (nm)**
		Cr (at. %)	**Ni (at. %)**	**Fe (at. %)**	
Mech. Polished Unirrad.	Outer oxide	16	1	83	10 – 35
	Inner oxide	56	1	43	10 – 12
	Substrate (nanograins – Ferrite)	28	3	69	650
10 dpa – Fe (mech.)	Outer oxide	33	7	60	2 – 20
	Inner oxide	36	7	57	10 – 15
	Substrate (nanograins – Austenite)	20	7-14	66-73	200 – 250

Table 4-3 : Comparison of the oxide layers formed on the unirradiated and 10 dpa – Fe (mech.) sample after 360 h oxidation in simulated PWR primary water.

In addition to oxide layers, difference in the depth of the surface hardened layer was spotted in unirradiated sample and 10 dpa – Fe (mech.) sample. It was deeper in unirradiated sample. Formation of surface hardened layer is a consequence of polishing and its depth is unaffected by the irradiation but can influence the oxidation. As reported in previous study [1], larger the recrystallized area, larger the number of grain boundaries available and hence, higher enrichment of Cr in inner layer resulting in a thinner and more protective inner layer. Result obtained in this study appears to be consistent with this hypothesis.

4.4. DISCUSSION

In this chapter, the effect of surface finish (i.e. presence of surface hardened area) on the cracking susceptibility of irradiated material was studied. For the purpose, samples prepared using two different techniques, namely vibratory polishing and mechanical

polishing, were used. While mechanical polishing resulted in the formation of surface hardened layer just beneath the polished surface, vibratory polished samples removed all the surface artifacts created during mechanical polishing. In chapter 2 and 3, it was shown that iron irradiation used in this study is an appropriate tool to emulate the significance of irradiation on microstructure (defect density and size), mechanical properties (hardening) and cracking susceptibility in vibratory polished samples. So to study the effect of surface finish on cracking susceptibility of irradiated material, 10 dpa – Fe and 10 dpa – Fe (mech.) samples were chosen and compared.

The samples were subjected to SSRT upto 4% plastic strain which led to the appearance of cracks and slip lines in gauge section of the samples. To calculate the crack density in unirradiated and irradiated regions of 10 dpa – Fe and 10 dpa – Fe samples (mech.), an area of 1 mm^2 was scanned using SEM in each region of both the samples. An increase in cracking susceptibility with irradiation was observed in both the sample. However, the increase was much lower in 10 dpa – Fe (mech.) sample. Results also demonstrated that the crack density in unirradiated region of 10 dpa – Fe (mech.) sample was marginally higher than in unirradiated region of 10 dpa – Fe sample. To recall, the Vickers hardness of mechanically polished unirradiated sample was higher (by ~ 28 %) compared to vibratory polished unirradiated sample which is in accordance with the higher density of cracks observed in mechanically polished sample. This suggests that presence of surface hardened layer enhanced the cracking susceptibility of the unirradiated material. This is in agreement with other studies [2, 3] conducted on unirradiated material. These studies have suggested that presence of surface hardened layer (induced by surface preparation techniques) results in increase in internal stresses and hence, increase in the susceptibility of material to cracking.

On contrary, in the irradiated regions, the crack density and mean crack length was higher for vibratory polished 10 dpa – Fe sample. Qualitative analysis showed that cracks were wider as well on 10 dpa – Fe sample in comparison to 10 dpa – Fe (mech.). This shows that cracking was severe in vibratory polished sample. In other words, presence of nanograins significantly decreased the cracking susceptibility of irradiated material. The opposite trend observed in the irradiated materials signifies that the cracking susceptibility of irradiated material is dependent on various factors. Effects of increase in hardness, localized deformation, oxidation and RIS are discussed one by one in the following part.

- <u>Increase in hardness</u>

Surface hardened area and irradiation induced point defects are hardening sources. In 10 dpa – Fe sample, only irradiation induced defects contributed in increase in hardness and resulted in an increase of 67 %. Whereas, in 10 dpa – Fe (mech.) sample both factors contributed. While presence of surface hardened layer resulted in an increase of 28 % in

hardness, the increase due to irradiation induced defects was just 8%. Previously (chapter 2), it was shown that the presence of surface hardened layer highly reduced the density of irradiation induced point defects in 10 dpa – Fe (mech.) sample thereby, resulting in a very small increase in hardness with irradiation in comparison to 10 dpa – Fe sample. Even though two factors were contributing in the hardness, the net increase was much lower in mechanically polished iron irradiated 10 dpa – Fe (mech.) sample than its vibratory polished counterpart. This lower increase in hardness is consistent with the observation of lower density of cracks in the 10 dpa – Fe (mech.) sample.

- Degree of localization

Post to straining, slip lines were observed on the surface of the samples. Spacing between these lines as an indicator of degree of localization has been proposed in literature [4], was used in this study. For 10 dpa – Fe and 10 dpa – Fe (mech.) samples, the mean slip line spacing was higher in irradiated region compared to unirradiated region. This implies that irrespective of the surface finish, irradiation enhances the likelihood of material to localized deformation. Higher spacing signifies higher degree of localization and hence, correlates well with the higher density of cracks observed in irradiated region than in unirradiated region in both samples. Comparing the slip line spacing values for the unirradiated regions of the two samples, no significant difference was observed implying no effect of surface hardened layer on slip line spacing for unirradiated material. On contrary, in the irradiated regions of the two samples, spacing value was higher in 10 dpa – Fe sample implying a higher degree of localization in this sample than in 10 dpa – Fe (mech.) sample. Under the hypothesis that localized deformation is linked to intergranular cracking of irradiated material, these results correlate well with the higher density of cracks observed in the irradiated region of the vibro polished sample compared to mechanically polished sample.

- Oxidation

As intergranular oxidation was not studied, a direct correlation of oxidation with cracking susceptibility could not be established. But the oxidation test conducted in this study provided an insight on the effect of surface hardened layer on the oxidation itself. Unirradiated vibratory polished, unirradiated mechanically polished and 10 dpa – Fe (mech.) samples were oxidized in stainless steel autoclave for 360 h. Irrespective of surface state, duplex oxide layer was observed in all the samples. Comparison of the oxide layers formed on unirradiated vibratory and mechanically polished samples indicated that the inner layer formed on vibratory polished sample was thinner and less enriched in Cr making it less protective. Due to the presence of nanograins in the surface hardened layer, the volume fraction of grain boundaries in mechanically polished sample was higher. As the diffusion of oxygen and/or metal atoms is faster along grain

boundaries [6, 7], higher volume fraction of grain boundary would overall enhance the inward diffusion of O and outward diffusion of Fe thereby resulting in thicker and more Cr enriched inner oxide.

Lastly the effect of irradiation on oxidation of the mechanically polished sample was studied. Results indicated that the size of outer oxide crystallites decreased with irradiation. Similar trend was observed in unirradiated vibratory polished and 5 dpa – Fe samples as well. This implies that irradiation reduces the size of outer oxide crystallites. Perrin et al. [8] also reported to observe smaller crystallites on proton irradiated samples compared to unirradiated samples. Note that the authors specified that the use of mechanically polished austenitic steel samples in the study [8], but did not report about the surface hardened layer in the substrate.

In addition, the inner layer formed on the irradiated region of 10 dpa – Fe (mech.) was characterized to have lesser Cr content and thus, was less protective than the layer formed on unirradiated mechanically polished sample. There could be two possible explanations for the observation of lower Cr content in irradiated sample. Firstly RIS in 10 dpa – Fe (mech.) sample which could alter the Cr content at the grain boundaries in irradiated material and thereby affecting the diffusion of elements. Secondly, presence of thicker recrystallized area in unirradiated mechanically polished sample compared to 10 dpa – Fe (mech.). As the preparation of these two samples was done separately, it resulted in somewhat different extent of surface hardened layer in the material. Thicker recrystallized area in unirradiated mechanically polished sample means higher volume fraction of grain boundaries which enhances the diffusion of elements.

Unfortunately, the substrate of unirradiated mechanically polished sample was indexed to contain ferrite grains implying the oxide on this sample was formed on ferrite grains in contrary to austenite grains in unirradiated vibratory polished and 10 dpa – Fe (mech.) samples. This could significantly affect the differences observed on these samples.

- <u>RIS</u>

No RIS measurements were performed in this study. However, in [9] Radiguet et al. have reported that the intergranular RIS occurs with the same intensity in 5 dpa iron irradiated ultra-fine grained material (with a grain size of ~ 100 nm) as in irradiated material with standard – sized grain. As the size of nanograins present in surface hardened layer of 10 dpa – Fe (mech.) sample ranged between 100 – 300 nm, it could be assumed that findings of Radiguet et al. [9] will hold for 10 dpa – Fe (mech.) sample used in this study as well. This implies similar intergranular RIS in 10 dpa – Fe and 10 dpa – Fe (mech.) samples. So, it could be hypothesized that the RIS did not play any significant role in enhancing the propensity of vibratory polished iron irradiated material to cracking. As this

reasoning was deduced from the findings of Radiguet et al. [9], further work is required to justify this hypothesis.

To summarize, presence of surface hardened zone on the surface of the irradiated material highly reduced the density of defects induced after irradiation. This in turn, resulted in a smaller increase in hardness and slip line spacing (or lower degree of localization) with irradiation in material with surface hardened layer than in material with standard sized grains. Nanograins also altered at% of Cr and thickness of inner layer. As a consequence of all these events, likelihood of material to cracking highly diminished in irradiated mechanically polished sample.

In literature, few studies [9 – 11] have reported that irradiation induced damage is significantly smaller in nanograined (or nano crystalline) materials. Radiguet et al. [9] also proposed that nano or ultra-fine grained material may suppress or at least limit IGSCC susceptibility of the irradiated material by suppressing either of the contributing factors. But these propositions were based on microstructural and microchemical evolutions in these materials. Neither study investigated the direct consequence of grain size on cracking susceptibility. More importantly, the machining of core internals of PWRs results in a surface hardened area and presently, no study reports the effect of this surface hardened area (zone of nanograins) on the propensity of the material to cracking upon irradiation. To get the useful insight of this missing link, this study investigated the effect of surface state on cracking susceptibility of irradiated material. Findings of this research work propose that the presence of surface hardened layer can limit the IGSCC in ion irradiated SA 304L. Note that in the case investigated in this study, the depth of irradiated region was slightly higher than the depth of surface hardened layer. However, in case of a baffle former bolt of a PWR, the irradiated region is much deeper[24] than the surface hardened layer. So, it is necessary to confirm the results of this study for the case of irradiation region being deeper than the surface hardened layer, to be able to use them for actual PWR scenario.

4.5. CONCLUSIONS

The objective of this chapter was to study the influence of surface state on the cracking susceptibility of SA 304 L. For the purpose, two different surface finishes were used namely, mechanical polishing and vibratory polishing. Impact of irradiation on the microstructure of 10 dpa – Fe and 10 dpa – Fe (mech.) sample has been described previously (see § 2.3). Cracking susceptibility of these samples was investigated following SSRT test upto 4 % plastic strain in simulated PWR primary water. In both samples, an increase in cracking susceptibility with irradiation was observed. However,

[24] Penetration depth of neutrons is very large in austenitic stainless steel compared to ions (proton or heavy ions).

the percentage increase in cracking susceptibility was much lower in 10 dpa – Fe (mech.) sample. Much higher density of cracks was observed in the irradiated region of 10 dpa – Fe sample than in 10 dpa – Fe (mech.) sample. Mean crack length was higher as well in former. This implies that the presence of surface hardened layer reduced the tendency of irradiated material to cracking.

Following straining, slip lines were observed in the unirradiated and irradiated region of these samples. Again an increase in slip line spacing with irradiation was observed for both the samples. Slip line spacing distributions obtained for irradiated regions were wider compared to unirradiated region in both samples. Slip lines observed in the irradiated region of 10 dpa – Fe sample were more widely spaced than those observed on 10 dpa – Fe (mech.) sample and hence, a higher mean slip line spacing value was observed in the former. Summary of these results is presented in Table 4-4.

Sample	Region	Crack density (cracks/mm^2)	Mean crack length (µm)	% increase in cracking susceptibility with irrad (in %)	Mean slip line spacing (in µm)
10 dpa – Fe	unirradiated	64 ± 12	12 ± 2	360	0.9 ± 0.2
	irradiated	293 ± 18	16 ± 2		1.7 ± 0.1
10 dpa – Fe (mech.)	unirradiated	82 ± 6	8 ± 1	40	0.8 ± 0.2
	irradiated	115 ± 9	11 ± 1		1.3 ± 0.1

Table 4-4 : Summary of quantitative analysis performed in the unirradiated and irradiated regions of 10 dpa – Fe and 10 dpa - Fe (mech.) samples.

Effect of surface hardened layer on oxidation was studied as well. TEM analysis performed on unirradiated vibratory polished and unirradiated mechanically polished sample revealed the formation of duplex oxide layer on two samples. Outer oxide crystallites were smaller while inner layer was thicker in unirradiated mechanically polished. Cr content was also higher in the inner oxide layer formed on the unirradiated mechanically polished sample. The substrate of unirradiated vibratory polished sample consisted of standard sized austenite grains, the substrate of mechanically polished sample consisted of surface hardened layer (containing ferrite nanograins) extending upto a depth of 650 nm. Decrease in size of outer oxide crystallites with irradiation was observed on 10 dpa – Fe (mech.) sample. The inner layer formed on 10 dpa – Fe (mech.) sample was less enriched in Cr in comparison to the layer formed on unirradiated mechanically polished sample suggesting it to be less protective. However, it was difficult to conclude due to the presence of ferrite nanograins in the substrate of unirradiated sample.

Based on these results, it was concluded that the presence of surface hardened layer limits the IGSCC of iron irradiated SA 304L. This result needs to be confirmed for the case with irradiated region much deeper than the surface hardened layer, similar to that for baffle former bolt of a PWR.

REFERENCES

1. S. Cissé, L. Laffont, B. Tanguy, M-C. Lafont, E. Andrieu, "Effect of surface preparation on the corrosion of austenitic stainless steel 304L in high temperature steam and simulated water", Corr. Sci. 56 (2012), 209-216.
2. Stress Corrosion Cracking in Light Water Reactors: IAEA Nuclear energy series, No. NP-T-3.13 (2011).
3. S. Ghosh, V. P. S. Rana, V. Kain, V. Mittal, S. K. Baveja, "Role of residual stress induced by industrial fabrication on stress corrosion cracking susceptibility of austenitic stainless steel", Mat. Desg. 32 (2011) 3823 – 3831.
4. G. S. Was, "Localized deformation as a primary cause of irradiation assisted stress corrosion cracking", University of Michigan Report – DE – FG07 – 05ID14703, (2009).
5. T. Miura, K. Fujii, K. Fukuya, Y. Ito, "Characterization of deformation structure in ion irradiated stainless steel", J. Nucl. Mat. 386 – 388 (2009) 210 – 213.
6. K. Fukuya, H. Nishioka, K. Fujii, Y. Kitsunai, "Characterization of surface oxides formed on irradiated stainless steels in simulated PWR primary water", in proceedings of Fontevraud 8 Contribution of Materials Investigations and Operating Experience to LWRs' Safety, Performance and Reliability Palaisdes, (2014).
7. J. Robertson, "The mechanism of high temperature aqueous corrosion of stainless steels", Corr. Sci. 32 (1991) 443 – 465.
8. S. Perrin, L. Marchetti, C. Duhamel, M. Sennour, F. Jomard, "Influence of irradiation on the oxide film formed on 316 L stainless steel in PWR Primary water", Oxidation of Metals 80 (2013) 623 – 633.
9. B. Radiguet, A. Etienne, P. Pareige, X. Sauvage, R. Valiev, "Irradiation behavior of nanostructured 316 austenitic stainless steel ", J. Mat. Sci. 43 (2008) 7338 – 7343.
10. M. Rose, A. G. Balogh, H. Hahn, "Instability of irradiation induced defects in nanostructured materials", Nucl. Instrum. and Meth. B 127 – 128 (1997) 119 – 122.
11. N. Nita, R. Schaeublin, M. Victoria, "Impact of irradiation on the microstructure of nanocrystalline materials", J. Nucl. Mat. 329 – 333 (2004) 953 – 957.

CHAPTER 5. IMPACT OF LOADING CONDITIONS ON IGSCC OF IRRADIATED AUSTENITIC STAINLESS STEEL IN PWR ENVIRONMENT

5.1. INTRODUCTION

The existing IASCC initiation data available in literature advocates the existence of a stress threshold for a given neutron fluence below which IASCC will not occur in a PWR environment [1, 2]. These assessments are based on the use of constant load on irradiated austenitic stainless steels to obtain an engineering stress – dose threshold (i.e. threshold stress for crack initiation as a function of dose, see Figure 1-34 and Figure 1-35). However, the representability of these tests towards the operating conditions is still to be validated. The thermal stresses that baffle former bolts experience in a PWR during their in-service lifetime (for e.g. during shutdown and startup of reactor for maintenance) is more complex than a constant load as shown in Figure 5-1. It can be described as a low frequency cyclic loading with long hold periods. Temperature varies during cyclic loading leading to stress variation. It raises the questions of the effect of the cyclic loading on the propensity to crack initiation and on crack initiation mechanisms. Few studies [3, 4] suggests that the sudden spikes in load should result in faster crack growth rates (or lower fatigue life) increase in crack initiation. However it is also reported that long hold periods at relatively constant loading provides enough time for the formation of stable oxide films, thereby increasing the fatigue life of (unirradiated) austenitic stainless steel in PWR environment [5]. The existing data for irradiated material is rare and mainly focuses on the crack propagation rates during different loadings implying that the effect of loading path on crack initiation stress threshold of irradiated austenitic stainless steel in PWR environment has not yet been studied in a comprehensive way. Therefore, an effort was made in the present study to have an overview of this problem using iron irradiated austenitic stainless steel.

For the sake of simplicity, the actual complex loading of baffle former bolt has been simplified drastically and in a first approach mimicked by a cyclic loading. To study the role of loading path on crack initiation of iron irradiated SA 304L, it was proposed to compare cyclic and constant loadings. These different loading paths were applied on 5 dpa – Fe samples in PWR environment. The maximum stress chosen for the both the conditions was 300 MPa[25]. An identical pre-straining (rapid loading from 0 MPa to 300 MPa with a strain rate of 5×10^{-4} s^{-1} upto 4 % plastic strain) was used prior to both cyclic and constant loadings. While pre-straining prior to constant loading is a standard way, samples were pre-strained before cyclic loading to have an identical reference state at the

[25] This corresponds to the stress applied to the unirradiated material. Within the irradiated region, the value was estimated to be around 565 MPa ($\sigma_{applied} + \Delta\sigma_{irradiation}$). Note that the value in irradiated region was same for all the samples.

beginning of both the tests. To understand the consequences of this pre-straining, one tensile loading with a strain rate of 5 x 10^{-4} s^{-1} upto 4 % plastic strain was conducted as well.

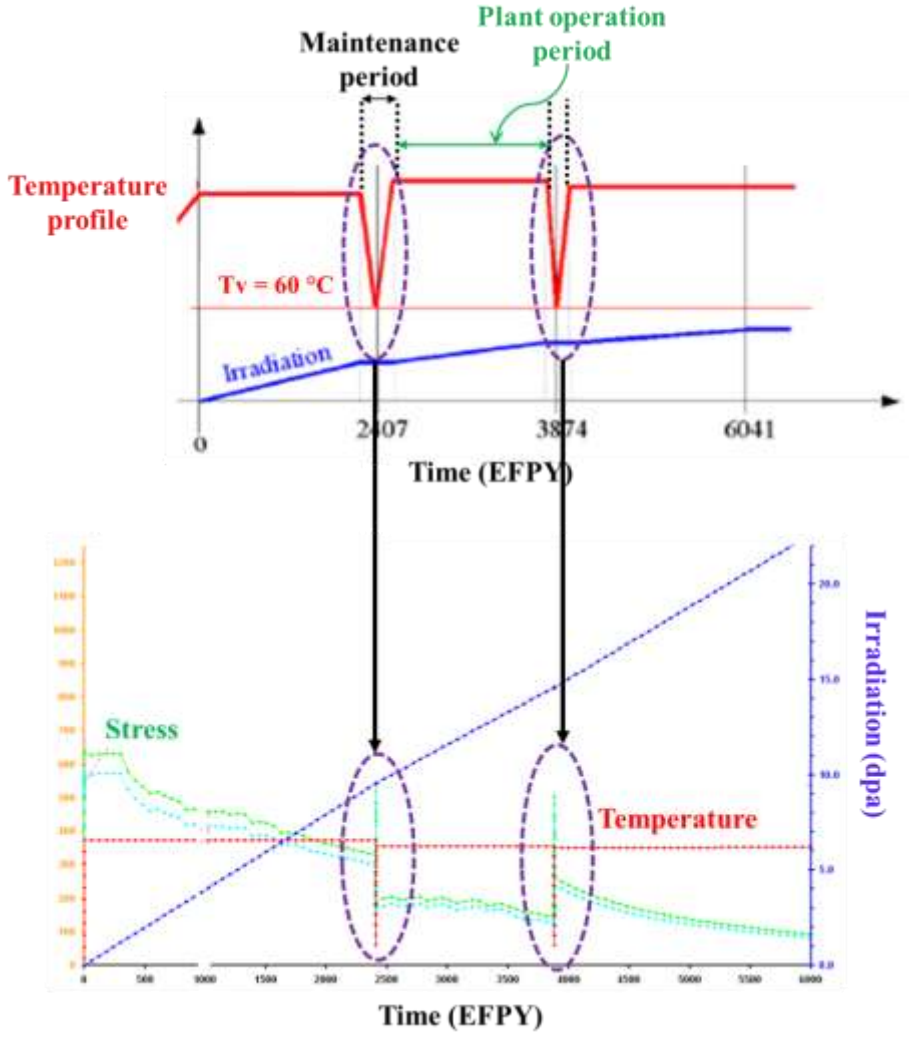

Figure 5-1 : Schematics illustrating the temperature cycle during normal working and maintenance period (source EDF).

The first part of this chapter provides the qualitative and quantitative information on the impact of the loading parameters (i.e. loading rate and loading path) on cracking susceptibility. In the second part, correlation of cracking susceptibility with localized deformation is studied. Only vibratory polished iron irradiated (i.e. 5 dpa – Fe and 10 dpa – Fe) sample are used in this chapter. To help the reader, a subscript is added at the end of the name of the samples (Table 5-1). No subscript for SSRT, _Cy for cyclic loading, _Co for constant loading and _R for tensile straining at 5 x 10^{-4} s^{-1}. For example, 5 dpa – Fe sample which was subjected to cyclic loading is addressed as 5 dpa – Fe_Cy.

Sample	Designation	No. of Tests performed	Type of loading	Test duration (in h)
5 dpa - Fe	5 dpa – Fe_ Cy	1	Cyclic	360
	5 dpa – Fe_ Co	1	Constant	360
10 dpa – Fe	10 dpa – Fe	1	SSRT	240
	10 dpa – Fe_ R	1	Rapid loading	0.07

Table 5-1 : Details about the designation of samples based on the loading condition used. Test duration and number of tests performed on each sample is detailed as well.

5.2. IMPACT OF LOADING CONDITIONS ON CRACKING

Different mechanical loading conditions were conducted on irradiated tensile samples using the same tensile device CORMET C137 attached to a stainless steel autoclave. Procedure of preparation of autoclave was same for all the tests and is described in detailed in § 3.2. Tests were conducted at 340 °C in simulated PWR primary water environment. Pressure in the autoclave during the tests was 155 bars. On attaining stable temperature and pressure conditions, preferred loadings were applied.

The first load condition consisted of applying a cyclic load varying from 20 MPa (σ_{min}) to 300 MPa (σ_{max}) with a frequency of 2 cycles/day. The choice of positive stress cycle was made to replicate the situation of real operating condition. Whereas the choice of frequency of cycles was a compromise between the test time and time necessary for the formation of a stable oxide between loading and unloading sequences. In second loading condition, i.e. constant loading test, load was maintained to 300 MPa upto 360 h. Stress versus time graphs for the two loading conditions is shown in Figure 5-2. These tests were done under load control mode and the plastic strain at the end of both the tests was around 6.5 %. The strain rate during cyclic loading (Figure 5-3) was 2 x 10^{-8} s^{-1}. A slight increase in the strain with time (Figure 5-4) was observed during constant loading condition. Measurements gave a strain rate of order ~ 10^{-9} s^{-1}. Austenitic stainless steels are characterized by a very slow creep rate at PWR relevant temperatures and they are insufficient to promote crack growth [6].

Note that the cyclic and constant loading conditions were applied following a rapid loading sequence from 0 MPa to 300 MPa (in red dotted line in Figure 5-3a and Figure 5-4a) with a strain rate of 5 x 10^{-4} s^{-1}. In other words, samples were pre-strained to 4 % plastic strain prior to cyclic and constant loading. Duration of the pre-straining was around 4 minutes which is much smaller compared to the actual test time.

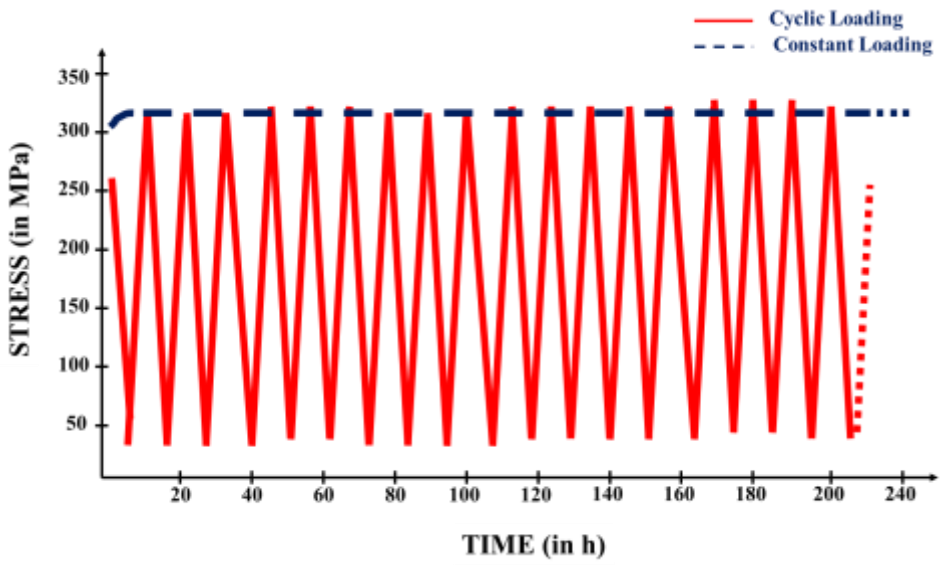

Figure 5-2 : Stress versus time graphs obtained for cyclic (in red solid line) and constant (in blue dashed line) loading conditions used. The tests were conducted at 340 °C in simulated PWR environment.

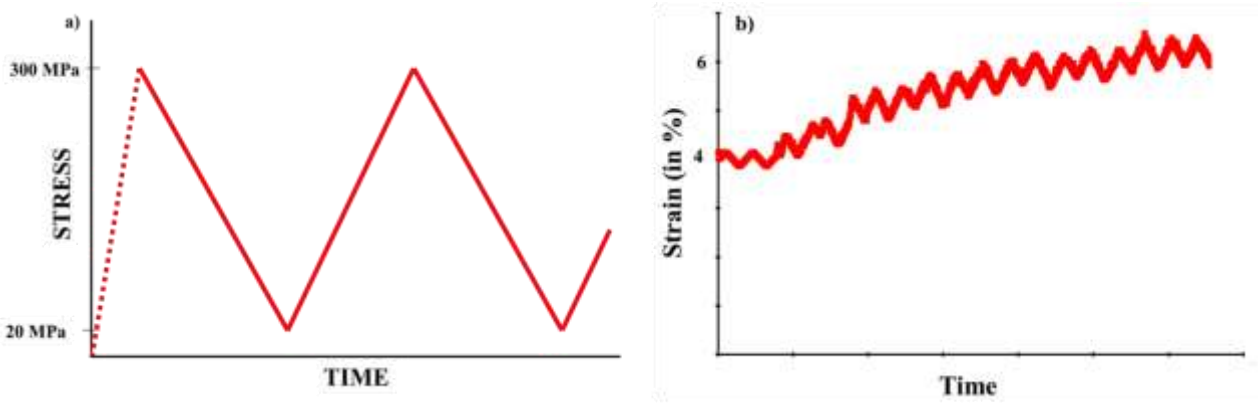

Figure 5-3 : Schematics representing a) the pre-straining condition (in red dotted line) used prior to cyclic loading and b) strain versus time graph obtained for the cyclic loading condition used.

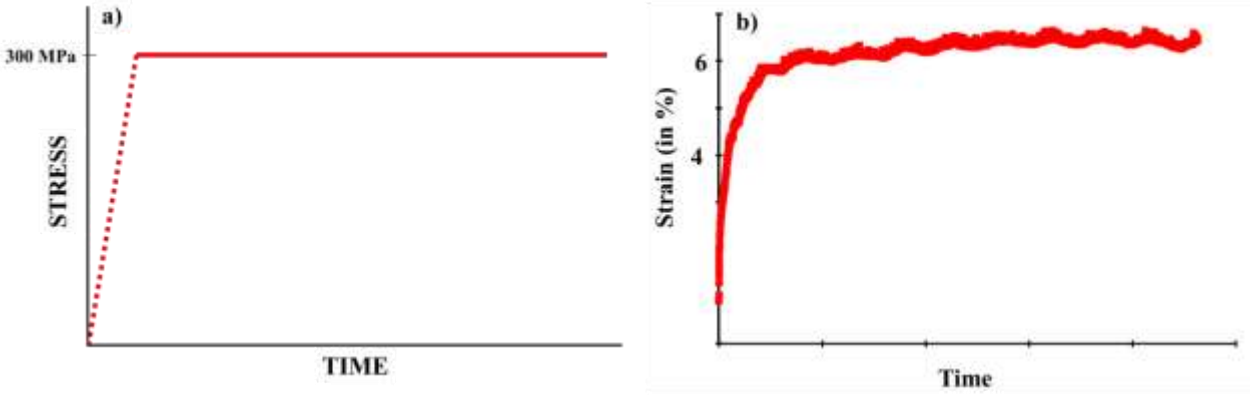

Figure 5-4 : Schematics representing a) the pre-straining condition (in red dotted line) used prior to constant loading and b) strain versus time graph obtained for the constant loading condition used.

For SSRT condition, a strain rate of 5 x 10^{-8} s^{-1} (same as the value used for tests described in chapter 3 and 4) was applied, while a strain rate of 5 x 10^{-4} s^{-1} was applied in rapid (tensile) loading test. Both the tests were interrupted on achieving a plastic strain of 4%. Stress at 4% plastic strain was around 300 MPa in both conditions. True stress – strain curves for both the samples is shown in Figure 5-5.

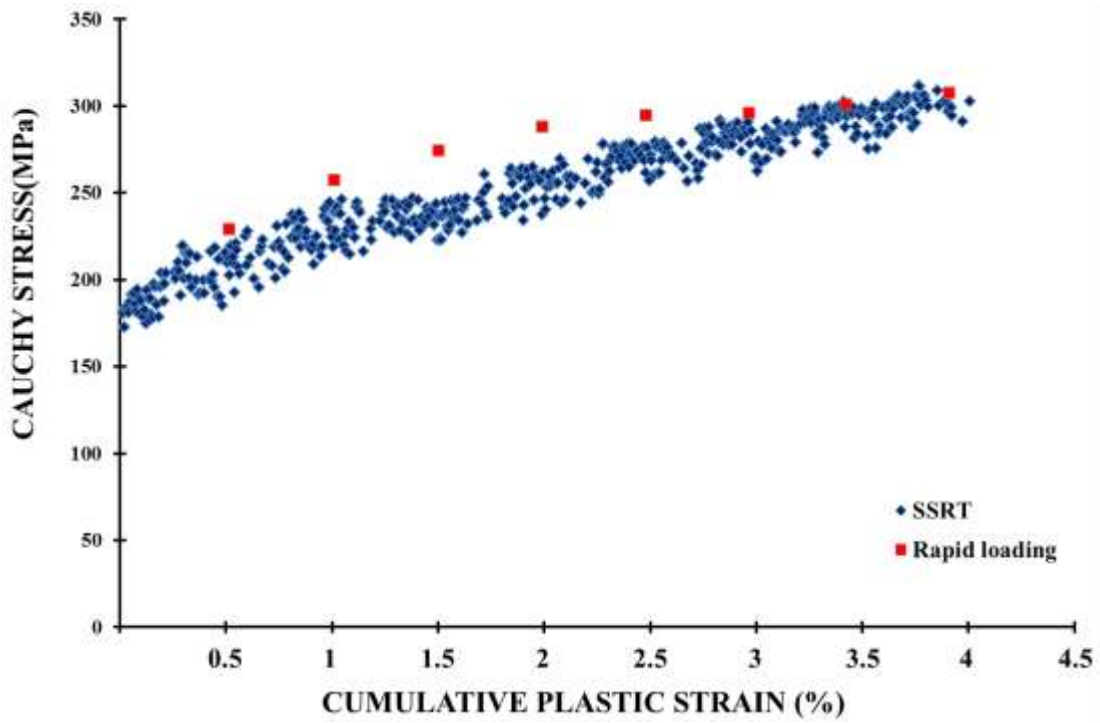

Figure 5-5 : Comparison of true stress - strain graph obtained for SSRT and rapid loading condition used. The tests were conducted at 340 °C in simulated PWR primary water environment.

Following loading, surface of all the samples was analyzed (qualitative and quantitative assessments of cracks and slip lines) using FEI Helios 650 NanoLab Dual Beam FIB under SEM mode. As in previous chapters 3 and 4, it has been demonstrated that irradiation enhances the cracking susceptibility of SA 304L in PWR environment, focus in this chapter was on characterizing only the irradiated region.

5.2.1. QUALITATIVE ANALYSIS

The 5 dpa – Fe tensile samples were subjected to two different loading conditions and subsequently analyzed using SEM. SEM micrographs (Figure 5-6) obtained from the irradiated regions of 5 dpa – Fe_Cy and 5 dpa – Fe_Co samples during surface analysis disclosed the presence of numerous intergranular cracks on all the samples. Qualitative analysis gave an impression that number of cracks on the two samples was same. This will, however be verified in the next section.

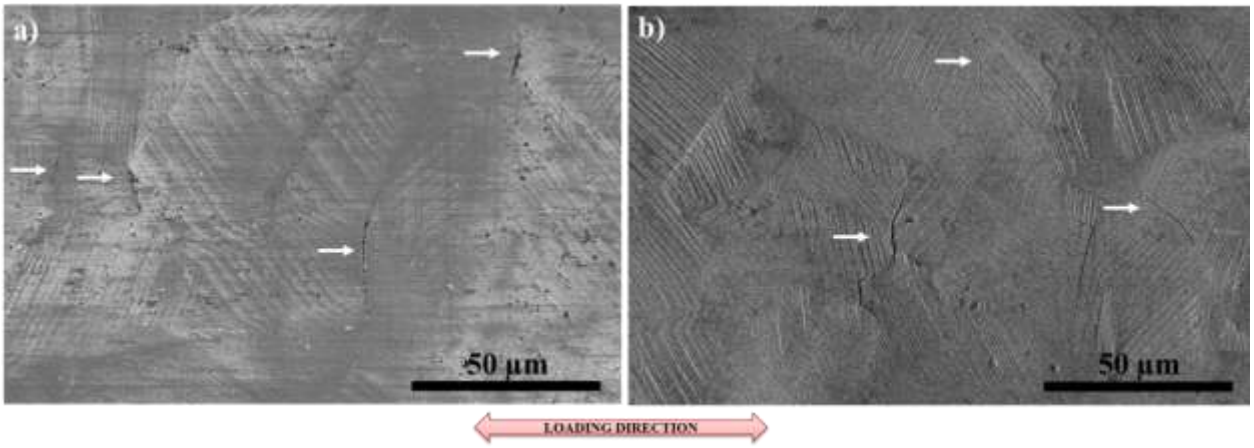

Figure 5-6 : SEM micrographs obtained from the surface of a) 5 dpa – Fe_Cy (in BSE mode) and b) 5 dpa – Fe_Co (in SE mode). Few cracks are marked by white arrows. Loading direction is indicated in the figure.

As stated previously, a pre–straining was applied on the samples before cyclic and constant loading. To understand the impact of this pre-straining, the 10 dpa – Fe samples subjected to rapid tensile loading in simulated PWR primary water environment was analyzed as well. The sample was scanned thoroughly but no cracks were found on the surface of 10 dpa – Fe_R sample. This is in contrary to the observation of numerous cracks on its counterpart 10 dpa – Fe sample subjected to SSRT.

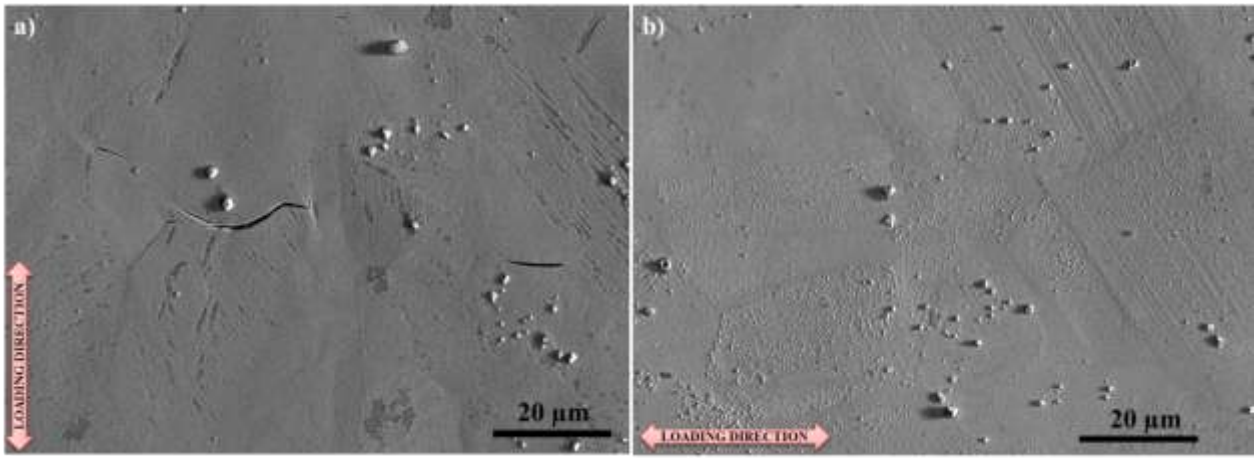

Figure 5-7 : SEM images (taken under BSE mode) of a) 10 dpa – Fe and b) 10 dpa – Fe_R samples after straining. Loading direction is indicated in the micrographs.

The plastic strain at the end of the test for both the cases was 4 % but the time available for oxidation process relative to applied strain was very different. So, it could be hypothesized that the embrittlement of grain boundary due to oxidation was different in the two cases leading to a difference in the propensity of the boundaries to cracking. The hypothesis is detailed in discussions (§5.3). This result implies that loading rate had a

detrimental effect on the intergranular cracking susceptibility of iron irradiated stainless steel used in this study. This is consistent with the findings of Fukuya et al. [7] for 35 dpa neutron irradiated CW 316 SS PWR flux thimble tube.

To summarize the observations of qualitative analysis, presence of intergranular cracks on the surface of the samples following cyclic and constant loading was confirmed. But no cracks were observed on the 10 dpa – Fe_R sample. This could be linked to the lack of embrittlement of grain boundaries in this sample due to small time available for oxidation. This also implies that the cracks observed on samples following cyclic and constant loading were initiated during the loading stage and not during pre-straining. To compare the effect of cyclic and constant loading paths on cracking susceptibility, quantitative data was required. Results of the quantitative analysis are presented in the following section.

5.2.2. QUANTITATIVE ANALYSIS

To obtain information on crack density and crack length distribution, technique employed was identical to the one described in §3.2.2. Due to lack of time, only one 1 mm² area was investigated on each specimen. As shown previously in chapter 3, these measurements are reproducible. No error in the mean crack density and mean crack length values could be obtained.

Detailed quantitative analysis performed on 5 dpa – Fe_Cy sample yielded a crack density of 153 cracks/mm². Within the 1 mm² area scanned on this sample, cracks of different lengths were observed with majority (74 %) of size ≤ 15 µm. No crack longer than 30 µm was observed. A mean crack length of 12 µm was obtained. Similar analysis conducted on 5 dpa – Fe_Co sample gave a crack density of 166 cracks/mm². On this sample as well, around 79 % of cracks were smaller than 15 µm. The mean crack length obtained was 12 µm for this sample.

Evident from this data, the crack density and mean crack length values were similar for 5 dpa – Fe_Cy and 5 dpa – Fe_Co samples. In both cases, majority of the cracks were smaller than ≤ 15 µm and no crack longer than 30 µm was observed. Comparison of crack length distribution (Figure 5-8) obtained for these samples further verify the similarities observed in the two cases. This implies that for the irradiation and loading conditions used in this study, no effect of loading path on cracking susceptibility was observed. This is in contrary to literature [3, 4, 8] where it has been reported that cyclic loading in comparison to constant loading, should enhance the crack propagation in irradiated as well as unirradiated material.

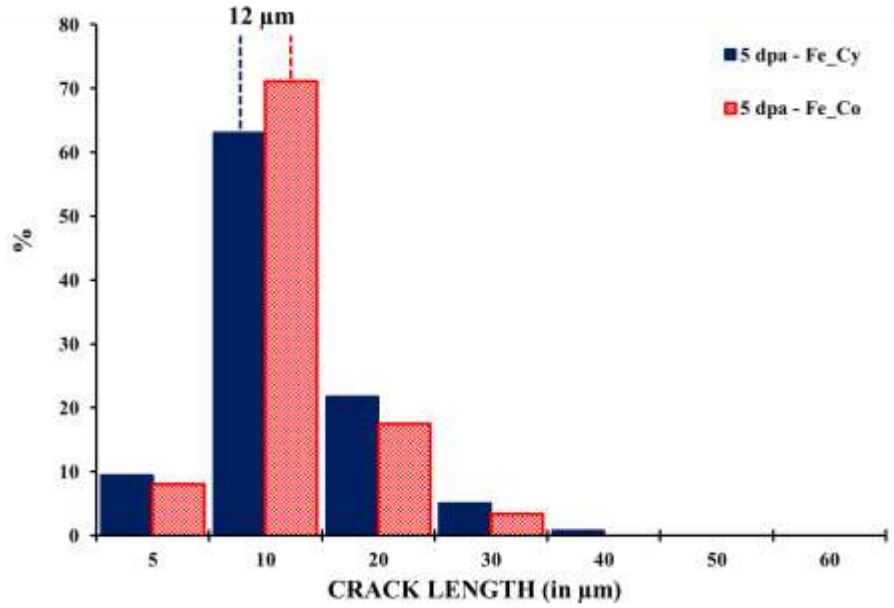

Figure 5-8 : Crack length distributions obtained for 5 dpa – Fe_Cy (in blue) and 5 dpa – Fe_Co (in red) samples.

Intergranular cracking in irradiated austenitic stainless steel is generally attributed to the localized deformation, radiation induced segregation (RIS) and grain boundary oxidation. It is therefore necessary to investigate these factors in 5 dpa – Fe_Cy and 5 dpa – Fe_Co samples to see if the trend opposite to literature observed in this study could be explained on the basis of either of these factors. The 5 dpa – Fe_Cy and 5 dpa – Fe_Co samples were irradiated to same dose and belonged to the same irradiation campaign, level of RIS should be identical in the two samples. Other dominant factor, i.e. localized deformation was studied for the different type of loading paths to have a better understanding of the quantitative data and is detailed in the following section.

5.2.3. LOCALIZED DEFORMATION

Presence of slip lines on both the samples was verified during the surface analysis of gauge lengths of 5 dpa – Fe_Cy and 5 dpa – Fe_Co samples. In fact, in both of these samples, slip lines were observed in majority of the grains. Figure 5-9a serves as an example to represent the surface of 5 dpa – Fe_Co samples following constant loading. Few times, slip lines were visible in multiple directions in a deformed grain in 5 dpa – Fe_Co sample (e.g. grain marked 1 in Figure 5-9b). Same was true for 5 dpa – Fe_Cy sample (grain marked 1 in Figure 5-9c) as well.

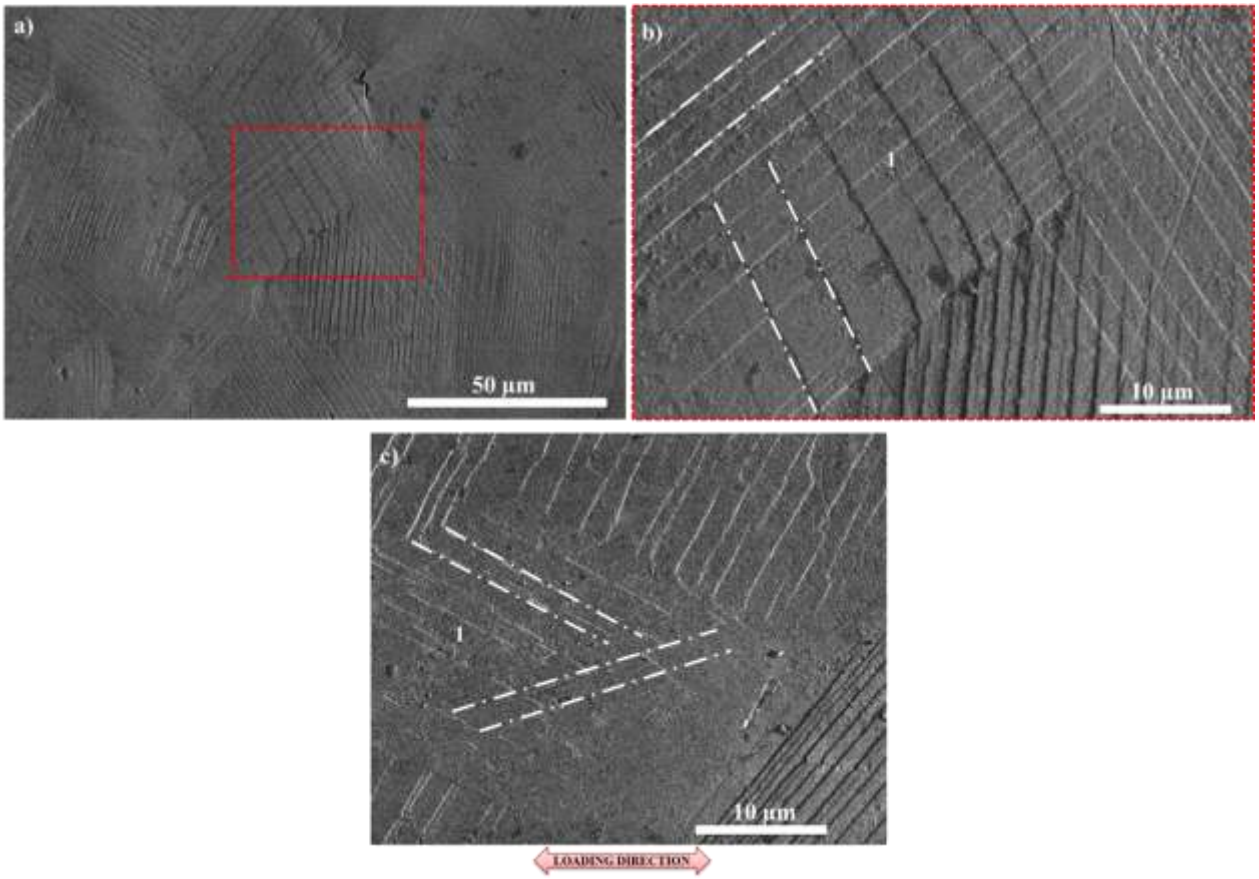

Figure 5-9 : a) BSE SEM image obtained for 5 dpa – Fe_Co sample indicating the presence of slip lines following constant loading. b) Zoomed image of red rectangle in a). c) BSE SEM image obtained for 5 dpa – Fe_Cy sample. Grains marked 1 in b) and c) represents the grain with multiple slip system visible on the surface. Few slip lines of the two slip systems are marked by dotted lines. Loading direction is indicated in the figure.

Quantitative information was acquired by measuring the slip line spacing (i.e. the distance between two consecutive slip lines) using imageJ software. To obtain a good statistics, slip line spacing measurements were done on around 25 different grains for each condition. A range of spacing values was obtained, so a distribution was plotted for each condition. Note that while calculating the spacing, grains with multiple active slip systems were not accounted. This was done to keep the consistency[26] in the method used.

Interestingly, the mean slip line spacing value obtained for 5 dpa – Fe_Cy and 5 dpa – Fe_Co samples was same i.e. 1.6 µm. Indeed, the slip line spacing distribution was very similar for both the samples (Figure 5-10). This implies that the degree of localization was

[26] Previously in chapter 3 and 4, the measurements were done for the predominant slip system (which was marked, or to say readily visible). But in the present cases of visibility of multiple active slip system, it was difficult to ascertain the most active slip system amongst them. So, they were not accounted in measurement.

same as well in the two samples and hence, is in agreement with the similar crack density observed in the two samples.

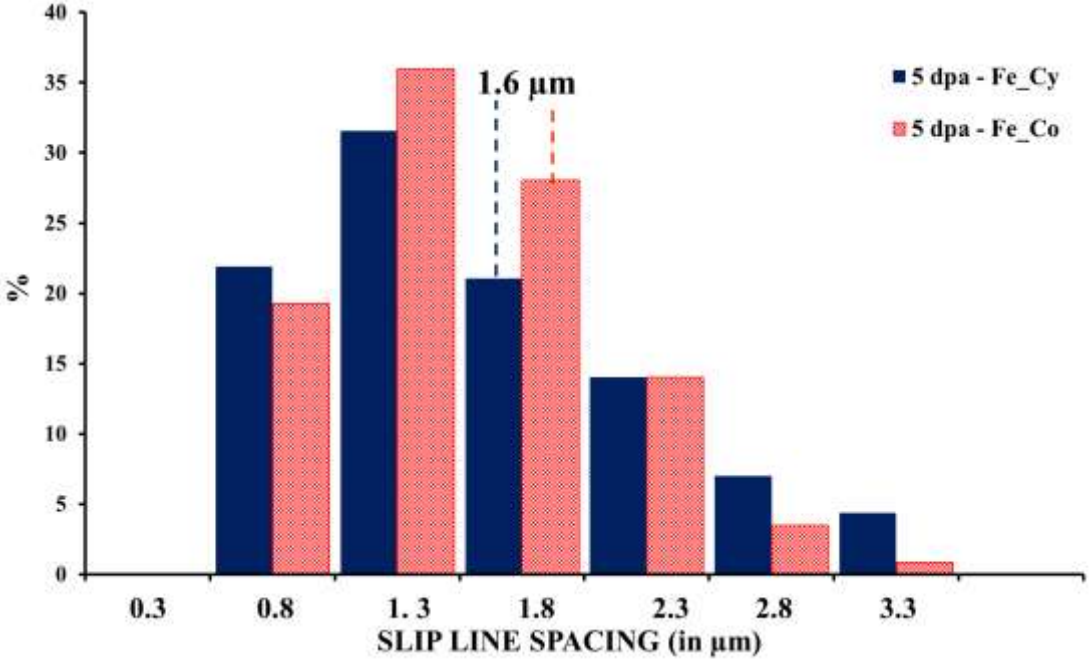

Figure 5-10 : Slip line spacing distribution obtained for 5 dpa – Fe_Cy and 5 dpa – Fe_Co samples.

5.3. DISCUSSIONS

The effect of loading conditions such as loading path, loading rate on the propensity of iron irradiated material was analyzed in this chapter. The results obtained are discussed below.

- Effect of loading rate

One 10 dpa – Fe irradiated sample was subjected to SSRT with a strain rate of 5 x 10^{-8} s^{-1} and another was subjected to rapid tensile loading with a strain rate of 5 x 10^{-4} s^{-1} to study the effect of loading rate. Interestingly, no cracks were observed on 10 dpa – Fe_R sample while numerous cracks were observed on 10 dpa – Fe sample following SSRT. The plastic strain at the end of the test in the two samples was same. This implies that the cracking susceptibility decreases with increasing strain rate. Previously, Fukuya et al. [7] have reported to observe same effect of loading rate on 35 dpa neutron irradiated 15 % cold worked 316 SS material. This observation could be explained by the hypothesis that there was not enough time for environment to initiate cracks in case of faster strain rate. So the susceptibility of material to cracking in corrosive environment with this faster strain rate reached that of material in inert environment. In chapter 3, it was shown that for the iron irradiation conditions used in this study, material was not susceptible to

intergranular cracking in inert environment for even slow strain rates (5×10^{-8} s^{-1}). So, no cracks were observed on the 10 dpa – Fe_R sample. This highlights that to study the IGSCC of ion irradiated SA 304L in corrosive environment, it is necessary to use a strain rate of order ~ $10^{-8} – 10^{-7}$ s^{-1}.

Also, the rapid tensile loading test conducted was identical to the pre-straining (rapid loading from 0 MPa to 300 MPa with a strain rate of 5×10^{-4} s^{-1}) used for cyclic and constant loading conditions used in this study. Though the pre-straining was applied on 5 dpa – Fe tensile samples, results of 10 dpa – Fe_R could be used despite the difference in dose. This is because in chapter 3, it has been shown that the crack density in the irradiated region of 5 dpa – Fe and 10 dpa – Fe following SSRT was similar and same was expected for rapid loading tensile tests. Thus, it could be concluded that the cracks observed in samples (if any) following cyclic and constant loading were initiated during loading and not during pre-straining.

- Effect of loading path

An oversimplified version of the actual complex loading of the baffle former bolt, i.e. cyclic loading, was employed in this study. In addition, constant loading was used as well. The maximum stress was 300 MPa and plastic strain at the end of the test was 6.5 % for both the tests. The comparison between the results of two loading conditions was drawn.

On both, 5 dpa – Fe_Cy and 5 dpa – Fe_Co samples, intergranular cracks were observed in the gauge length following mechanical loadings. Quantification of these cracks suggested that the crack density and crack length distribution for both the cases were similar despite different load paths. Results are summarized in Table 5-2. It could be concluded from these results that for the irradiation conditions and loading conditions used in this study, loading path did not alter the crack initiation and propagation susceptibility of the irradiated material. Or in other words, maximum load applied is a more influential parameter than the loading path.

Sample	Type of loading	Crack density (cracks/mm²)	Mean crack length (µm)
5 dpa – Fe_ Cy	Cyclic	153	12
5 dpa – Fe_ Co	Constant	166	12

Table 5-2 : Comparison of the quantitative analysis performed on iron irradiated samples following different loading conditions.

Previously, Raquet et al. [8] have reported to observed slight crack initiation but no propagation during constant loading tests conducted on unirradiated sample. This led

them to conclude that dynamic loading conditions are prerequisite conditions for IGSCC to initiate and propagate in unirradiated austenitic stainless steel in PWR environment. Also, in [3, 4], it has been reported that the crack growth rate remains constant during constant loading while increases during the application of cyclic loading in neutron irradiated austenitic stainless steel. As the same sample was loaded to different loadings, no information is provided on crack initiation. But it was concluded from these results that there is no propagation (of existing cracks) during constant loading. This is contrary to the observation of same crack length for both cyclic and constant loaded samples in this study. The reason for this opposite trend is not clear. Hence, to have a better understanding of the present result, possible factors contributing in intergranular cracking of the material and their correlation with different loading paths were explored.

Intergranular cracking of irradiated austenitic stainless steel is generally credited to localized deformation and grain boundary embrittlement via RIS or oxidation. Level of RIS in 5 dpa – Fe_Cy and 5 dpa – Fe_Co should supposedly be the same. Localized deformation in the two samples was estimated by measuring the slip line spacing following loading. Interestingly, the mean slip line spacing value and the spacing distribution were very similar as well. Same spacing value implies same degree of localization. This seems to be consistent with the same density of cracks observed in the two samples. But, evolution of oxidation with loading path for iron irradiated austenitic stainless steel in PWR environment is yet to be studied. In literature [5], it has been reported for unirradiated material that during constant loading formation of stable oxide films can occur which should decrease the propagation (and possibly initiation) of cracks under constant loading conditions. However, it has been shown in chapter 3 and 4, irradiation modifies the oxidation of austenitic stainless steel and hence, it is necessary to study the possible response of oxide growth during different mechanical loadings in irradiated material.

- Effect of dose

To study the effect of dose on cracking susceptibility, one cyclic test was performed on 10 dpa – Fe sample (maximum dose available in this study). The crack density and mean crack length obtained for this sample were 172 cracks/mm² and 12 µm respectively. The values were similar to that obtained for 5 dpa – Fe_Cy sample implying no effect of dose on cracking susceptibility of 5 dpa – Fe sample. This is consistent with similar crack density and mean crack length observed in the irradiated regions of 5 dpa – Fe and 10 dpa – Fe sample following SSRT (see §3.2.2).

- Comparison with SSRT

The results obtained for 5 dpa – Fe_Cy and 5 dpa – Fe_Co samples were compared with 5 dpa – Fe (SSRT tested in PWR environment, see §3.2.2) sample as well. Interestingly, the crack density and mean crack length was highest in the 5 dpa – Fe sample following SSRT test. Comparison of the crack length distribution for all the three samples is shown in Figure 5-11. This difference could be associated to the difference in the oxide growth response during different mechanical loadings. Nevertheless, it could be inferred from these results that cracking was much more severe in the sample following SSRT than cyclic and constant loading. And perhaps that is why most of the studies [9 – 11] reported in literature dealing with ion irradiated austenitic stainless steel, uses SSRT to study the IGSCC responses of material.

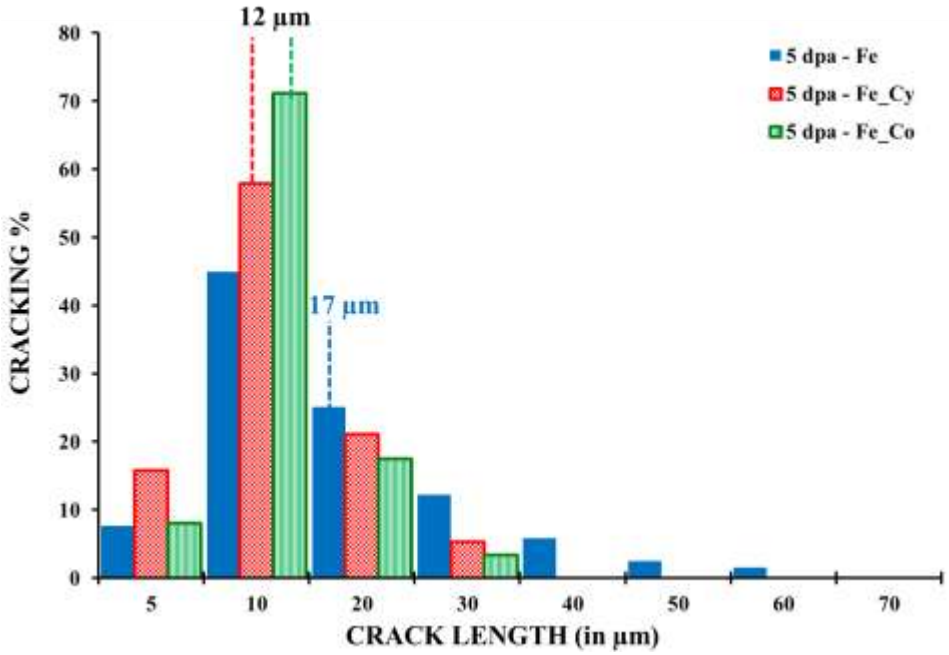

Figure 5-11 : Crack length distributions obtained for 5 dpa – Fe (in blue), 5 dpa – Fe_Cy (in red) and 5 dpa – Fe_Co (in green) samples.

5.4. CONCLUSIONS

A first study of effect of loading path on the cracking susceptibility of iron irradiated SA 304L was proposed in this chapter. To start with, the effect of loading rate was studied by employing two different strain rates. A decrease in cracking susceptibility with increase in strain rate was observed which could be associated to smaller time available for oxidation to embrittle the grain boundaries at higher strain rates. Effect of loading path was studied by using two different loading conditions, namely cyclic and constant loading. An identical pre-straining to 4 % plastic strain using rapid strain rate was employed prior to

cyclic and constant loading to ensure identical reference state at the beginning of both the tests. As no crack initiation in case of rapid loading was observed previously, it was concluded that the cracks initiation took place only during the loading conditions and not during pre-straining used. Similar crack density and crack length distribution was observed in 5 dpa – Fe sample following cyclic and constant loading. This suggested that for the irradiation and loading conditions used in this study, loading path did not impact the cracking susceptibility of material. This is contrary to the results reported in literature [3, 4, 8] suggesting no crack propagation during constant loading. Unfortunately, in literature, all the studies on irradiated samples are dedicated to study the crack propagation rates during cyclic and constant loadings and hence, employ both loading on same sample subsequently one after the other. This implies the need of further studies to investigate the effect of loading paths on crack initiation in irradiated austenitic stainless steel.

In addition, a similar degree of localization was observed in samples after cyclic and constant loading. Considering same level of RIS, these results are in agreement with the similar density of cracks observed in both the samples. It will however, be interesting to investigate the effect of loading path on the growth of oxide layer to see if any difference exists.

REFERENCES

1. K. Takakura, K. Nakata, M. Ando, K. Fujimoto, E. Wachi, "Lifetime evaluation for IASCC initiation of cold worked 316 stainless steel's BFB in PWR primary water", in proceedings of 13th international conference on Environmental degradation of materials in nuclear power system – water reactors (2007).
2. H. Nishioka, K. Fukuya, K. Fujii, T. Miura, "IASCC initiation in highly irradiated stainless steels under uniaxial constant load conditions", J. Nucl. Sci. and Tech. 45 (2008) 1072 – 1077.
3. Y. Chimi, "Final report on the BWR crack growth rate investigation IFA-745", OECD Halden reactor project.
4. O. K. Chopra, "Degradation of LWR core internal materials due to neutron irradiation", NUREG/CR-7027, ANL-10/11.
5. M. Ménard, J. M. Olive, A. M. Brass, I. Aubert, "effects of hydrogen charging on surface slip band morphology of a type 316L stainless steel", in Environment – induced cracking of materials (2008) 179 – 188.
6. A. Herbelin, T. Couvant, L. Legras, D. Delafosse, G. Ilbevare, "Oxidation of austenitic stainless steels in PWR primary water", in proceedings of Eurocorr 2009, (2009) 1592 – 1608.
7. K. Fukuya, H. Nishioka, K. Fujii, T. Torimaru, "Effects of dissolved hydrogen and strain rate on IASCC behavior in highly irradiated stainless steel", J. Nucl. Sci. and Tech. 45 (2008) 452 – 458.
8. O. Raquet, E. Herms, F. Vaillant, T. Couvant, "SCC of cold worked austenitic stainless steels in PWR conditions", Adv. Mater. Sci. 7 (2007) 33 – 45.
9. K. Fukuya, M. Nakano, K. Fujii, T. Torimaru, "IASCC susceptibility and slow tensile properties of highly irradiated 316 stainless steels", J. Nucl. Sci. and Tech. 41 (2004) 673 – 681.
10. K. J. Stephenson, G. S. Was, "Comparison of the microstructure, deformation and crack initiation behavior of austenitic stainless steel irradiated in-reactor or with protons", J. Nucl. Mat., 456 (2015) 85-98.
11. H. Nishioka, K. Fukuya, K. Fujii, T. Miura, "IASCC initiation in highly irradiated stainless steels under uniaxial constant load conditions", J. Nucl. Sci. and Tech. 45 (2008) 1072 – 1077.

CONCLUSIONS AND FUTURE PERSPECTIVES

The purpose of this study was to investigate the intergranular stress corrosion cracking of ion irradiated SA 304L austenitic stainless steel in PWR environment with main focus on some of the open questions related to the impact of irradiation induced microstructure and strain paths on intergranular cracking susceptibility of austenitic stainless steel. Two different ion irradiations were conducted in this study on vibratory polished samples (i.e. samples free of polishing induced surface hardened layer). Proton irradiation was conducted at 350 °C for a dose of 2 dpa and iron irradiation was conducted at 450 °C for doses of 5 dpa and 10 dpa. The choice of irradiation temperature was a compromise to have microstructure and microchemistry similar to that of neutron at PWR relevant temperatures. The microstructure characterized using TEM post to irradiation consisted of Frank loops with size and density in accordance to neutron and ion literature. Increase in hardness with irradiation observed in all the samples showed a linear correlation with the product of number density and size of Frank loops observed. With this background, these pre-irradiated samples were subsequently subjected to mechanical tests. Following information could be inferred from the results of these tests.

- <u>Iron irradiation could be used to study the intergranular cracking of irradiated austenitic stainless steel.</u>

  At low doses (~ 5 dpa), iron irradiated material showed resistant to intergranular cracking in inert environment. Numerous intergranular cracks were observed in both iron irradiated and proton irradiated samples following SSRT in simulated PWR primary water environment. Using iron irradiation it was shown that cracking susceptibility of material following SSRT in simulated PWR primary water increases with irradiation irrespective of irradiation dose and surface state. Increase in cracking susceptibility of material with proton irradiation was observed as well.

  To verify the similarity of the cracking mechanism in iron and proton irradiated samples, degree of localization was investigated. Higher degree of localization (estimated by the mean slip line spacing value) was observed in iron irradiated material compared to unirradiated material. Saturation in slip line spacing value with dose was achieved in iron irradiated material for doses ~ 5 dpa. The degree of localization was lower in iron irradiated samples compared to proton irradiated samples yet a similar crack density was observed in both samples. This suggests the need of information on RIS in iron and proton irradiated samples to further improve the findings of this study as the strength of the grain boundaries could be different between these two types of irradiation due to different level of RIS.

The results of this study highlighted the possibility of using iron irradiation to investigate the IGSCC of irradiated austenitic stainless steel. Majority of the existing data on intergranular cracking of ion irradiated sample is based on the proton irradiation. But the limitation of proton irradiation is the inability to achieve very high doses in short time compared to heavy ions. As proposed in this study, iron irradiation could be used to enhance the present literature especially at higher doses, thereby improving the current understanding of IGSCC of irradiated austenitic stainless steel.

- Criterion proposed for the intergranular cracking of irradiated austenitic stainless steel in BWR environment is not sufficient to address cracking in PWR environment.

Crack sites similar to that reported in neutron and proton literature were observed in iron and proton irradiated samples. Amongst all the cracked grain boundaries analyzed, the percentage of cracked grain boundaries having slip discontinuity was slightly higher compared to cracked grain boundaries having slip continuity. Majority of the cracked grain boundaries investigated were neighboring a low Schmid factor grain in both iron irradiated and proton irradiated samples. However, taking into consideration all the conditions of criterion proposed in literature, a very weak correlation of criterion with cracking was observed. This result doesn't support the use of criterion for addressing intergranular cracking in iron and proton irradiated samples in PWR environment. As only cracked grain boundaries were analyzed in this study. It is proposed to investigate the intact boundaries in order to be able to propose a more suitable criterion.

- Irradiation influences the oxidation of austenitic stainless steel.

Few studies have investigated the oxidation of austenitic stainless steel in PWR environment and even fewer have reported the effect of irradiation on oxidation. To extend the literature, effect of irradiation was studied by performing an oxidation test on unirradiated and irradiated bars for 360 hours in simulated PWR primary water environment. Oxidation led to the formation of duplex oxide layer: outer and inner (or protective) layers on the material. An increase in the thickness of inner layer and Cr enrichment with irradiation was observed in oxidized bars. An opposite trend was however, observed on the tensile sample (oxidized during SSRT). Also, with increase in volume of corrosive media, an increase in inner layer thickness of irradiated material was observed. Material with surface hardened layer also showed difference in oxidation upon irradiation. These results proposed that irradiation influences the oxidation of austenitic stainless steel. As no concluding information on the impact of irradiation on oxide formation and growth could be obtained from this test, further investigation is required. Difference in the morphology of outer oxide on iron and proton irradiated sample was also observed in this study. Study of inner oxide on these samples could provide some information on the impact of different irradiating ions on oxidation. Oxidation test

conducted in this study was used to study the bulk oxidation and suggested the possibility of modification in inner layer thickness and chromium enrichment with irradiation. Extending this study to investigate the effect of irradiation on intergranular oxidation will provide a correlation between oxidation and intergranular cracking observed in this study for different irradiation conditions.

- Surface hardened layer affects the IGSCC resistance of material.

  Two different surface preparation techniques (i.e. vibratory polishing and mechanical polishing) were used to have difference in the subsurface microstructure of the material. Both the samples were irradiated to same dose using iron. Formation of subsurface nanograins in material with surface hardened layer (due to mechanical polishing) results in formation of a much lower (factor of ~ 40) density of defects upon irradiation compared to its vibratory polished counterpart. The subsequent increase in irradiation induced hardening was lower as well. On subjection to SSRT in simulated PWR primary water environment, irradiated mechanically polished sample showed a lower cracking susceptibility than vibratory polished for same loading conditions. These findings propose that the presence of surface hardened layer can limit the IGSCC in ion irradiated SA 304L. At present, this result is limited to the case of irradiation depth slightly deeper than the depth of surface hardened layer in the material. Validation of these results using mechanically polished proton (or neutron) irradiated samples for irradiation depth much deeper than the depth of surface hardened layer in the material condition is required. This will make these results more appropriate to be used for actual PWR core internals scenario (material with surface hardened layer due to fabrication) and will provide a correlation between the cracking observed in laboratories on vibratory polished or electro polished samples and the cracking observed in the PWR core internals.

- In iron irradiated austenitic stainless steel, the cracking susceptibility is not affected by cyclic loading compared to constant loading.

  An oversimplified version of the actual complex loading of the baffle former bolt, i.e. cyclic loading, was employed in this study and the results were compared with that of a constant loading path. At higher strain rates during tensile loading in simulated PWR primary water environment, the time available for oxidation was not sufficient to initiate cracks and the cracking susceptibility of iron irradiated material in corrosive environment approaches that of irradiated material in inert environment. No difference in the cracking susceptibility of iron irradiated material following constant and cyclic loading was observed. This result proposes that the loading path did not impact the cracking susceptibility of iron irradiated samples. This result is in contrary to the literature and needs to be further investigated. Verification of these results using proton irradiation will

provide useful insight on the crack initiation in baffle former bolts of PWR during actual complex loading condition.

APPENDIX 1: SAMPLE MACHINING AND PREPARATION

A.1.1. MACHINING

From the 40 x 20 x 4 mm^3 SA 304L plate, two types of samples, Tensile and bars, were machined using electro spark technique. Figure 0-1a shows the geometry of the samples used.

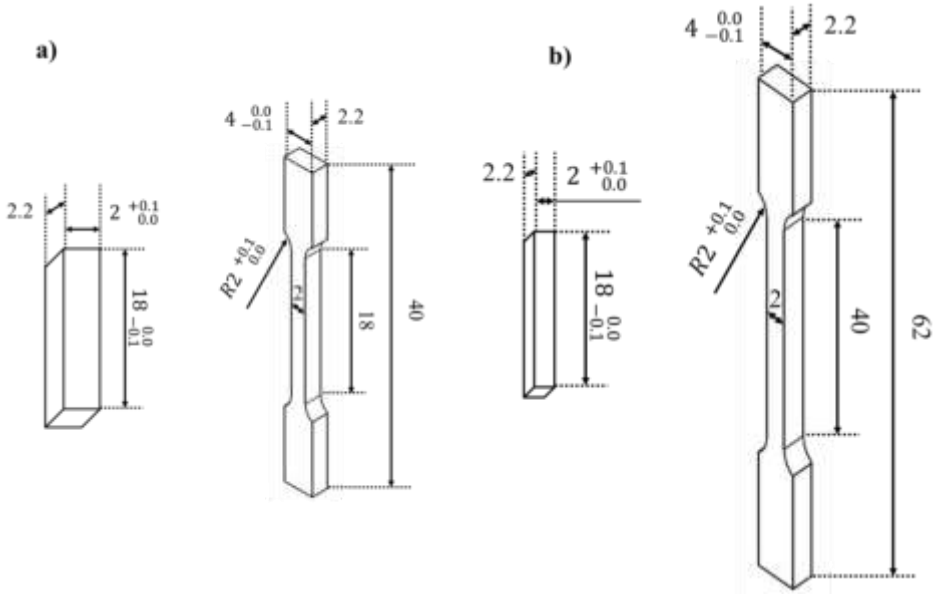

Figure 0-1 : Drawing of the samples (Tensile and Flat bars) a) for all irradiation campaigns b) for 2 dpa H irradiation campaign fabricated with the designated measurements (in mm).

In addition, for 2 dpa H irradiation campaign, some modifications in the dimensions of these samples were done to increase the number of irradiated samples (Figure 0-1b). Except 1 and 0.25 dpa H proton samples (machined in RT), all the samples were machined in TR direction (Figure 0-2).

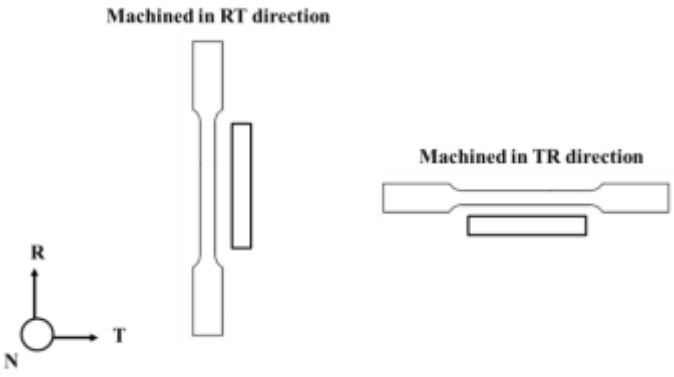

Figure 0-2 : Schematics representing the machining direction of the samples.

A.1.2. SAMPLE PREPARATION

A.1.2.1. IRRADIATION

Before each irradiation campaign, samples were polished on both faces (or sides). First face (or front side) polishing was necessary to have a reproducible, low roughness surface. Second face (or back side) polishing was essential to ensure good thermal contact between the samples and irradiation stage, thereby improving dissipation of heat due to irradiation beam.

The samples were polished using following steps:

- First face was polished using SiC papers of grades # 600, # 1000, # 1200, # 2400 and # 4000.
- Second face was polished using SiC papers of grades # 600, # 1000, # 1200, # 2400 and # 4000.
- Final polishing on second face using 3 µm, 1 µm and ¼ µm diamond paste.
- Final polishing on first face (to be irradiated) using 3 µm, 1 µm and ¼ µm diamond paste.

The polished samples were then rinsed using ultrasonic cleaning and kept safely to protect the polished first surface from scratches. The samples thus prepared are addressed as "mechanically polished samples" in this study.

In some cases, an additional step of vibratory polishing was used for the face to be irradiated and the samples thus prepared are addressed as "vibratory polished samples" in this study. Vibratory polishing was done only on the first face of the mechanically polished samples for 9 hours using following steps:

- The samples were pasted on the stainless steel sample holder (weighing around 200g), using double face tape, with the first face on the top. Tensile samples were polished individually i.e. one sample per sample holder while five bars were pasted on one sample holder for polishing.
- Vibratory polisher was prepared by adhering polishing nap to the polisher. Enough colloidal silica (0.04 µm) polishing suspension was added to cover the nap completely.
- The ensemble of sample and sample holder was then put upside down (sample in the suspension and sample holder at top) on the nap and polished on vibratory table rotating at a speed of 7200 cycles per minute.
- After 9 hours of polishing, samples were thoroughly cleaned using ethanol. To identify the face vibro-polished, an arrow was marked on the side of the samples. Polished samples were then kept safely to protect the polished first surface from scratches.

The thickness of the samples was reduced from 2.2 µm to 1.8 µm.

A.1.2.2. TRANSMISSION ELECTRON MICROSCOPE (TEM)

A.1.2.2.1. MICROSTRUCTURAL CHARACTERIZATION

Bars were used for microstructural characterization both post and prior to irradiation. From a bar, cuboids with diagonal of 3mm and thickness 2mm were cut using diamond wire (Figure 0-3).

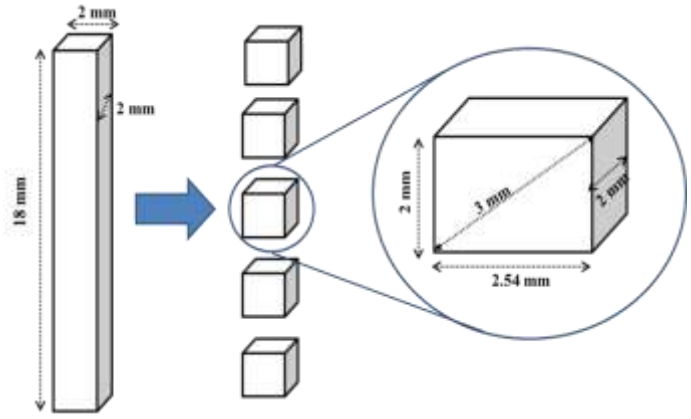

Figure 0-3 : Schematic to show the small cuboids cut from the bars for TEM samples preparation.

The face to be characterized was glued to an aluminium sample holder (irradiated face was glued on holder) using a thermosetting epoxy adhesive (QuickStick 135 Mounting Wax- South Bay Technology). The other face of this sample was polished using abrasive discs of SiC of different grades and diamond papers to reduce the thickness from 2mm to ~ 60 – 80 µm. To make these samples observable under microscope, further thinning was required, which was achieved using two different systems.

- Precision Ion Polishing System (PIPS - GATAN): To characterize the irradiated or polished surface, this system was used. In this, two focused Argon ion beams was used to mill the dimple-ground sample.
- Electrolytic Polishing System (TENUPOL 5 – STRUERS): This was used to make TEM samples for in-depth characterization i.e. characterization at irradiation peak region or at depths few microns away from surface. In this, jet of electrolyte (900 cc of Methanol, 200 cc of Butyl Cellosolve Glycol Ether and 100 cc acetic perchloride) was used for thinning.

The samples at this stage were thin enough to be characterized using TEM.

A.1.2.2.2. OXIDE CHARACTERIZATION

Oxidation tests were performed on bars. To characterize the oxide layers formed, cross-sectional TEM samples were prepared from the bars following oxidation tests. For the purpose, bars were cut (normal to the oxide/substrate interface) in the form of parallelepipeds (Figure 0-4) of dimension 10 mm × 1.7 mm × 0.7 mm using ACUTOM50 diamond wire saw.

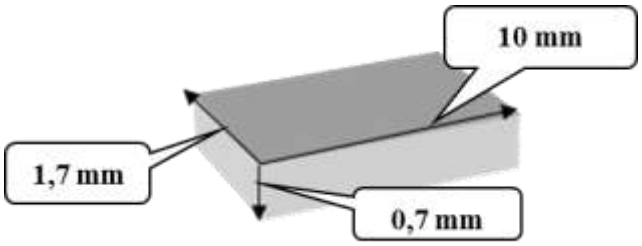

Figure 0-4: Illustration of the parallelepipeds prepared by cutting the sample using diamond wire saw.

The two parallelepipeds were glued together, oxide to oxide using GATAN (G1) epoxy resin. Subsequently, they were embedded in a brass tube of diameter 3 mm using same resin. The sandwich structure was then sliced into 300 µm thick discs using diamond wire saw (Figure 0-5).

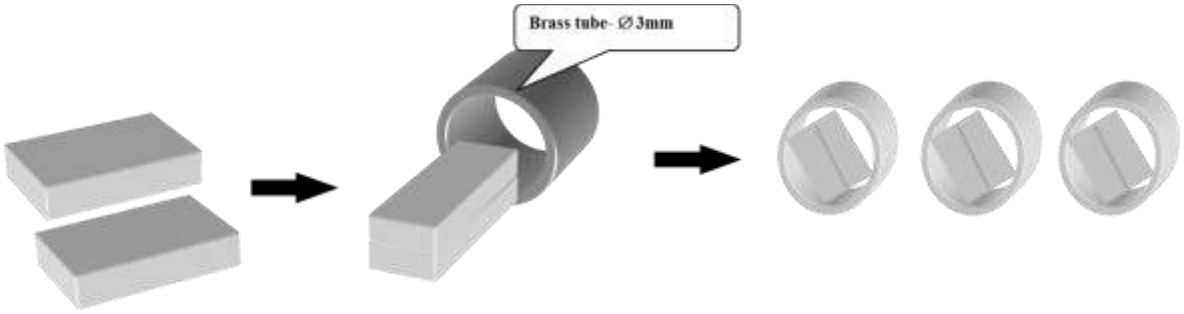

Figure 0-5: Schematics demonstrating the preparation of thin slices from parallelepipeds.

The discs were mechanically polished on both sides on diamond nap (Figure 0-6). Thin discs were subsequently dimpled using a dimpler (South bay technology).

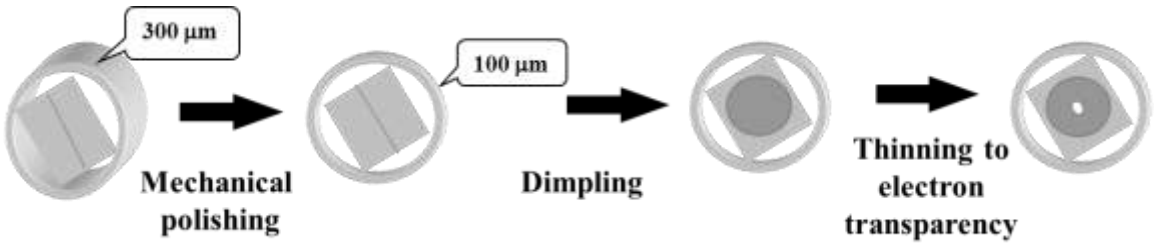

Figure 0-6: Illustration of preparation of electron transparent TEM samples from thin slices.

To make these samples transparent to electrons, ion – milling was done using PIPS – GATAN in which two focused Argon ion beam were incident at low angle (0 – 10°) to create a hole in the sample (Figure 0-6).